

ISSN 0965-0393

IOP

# Modelling and Simulation in Materials Science and Engineering

Volume 8 Number 3 May 2000

**Special Feature: Papers from the Workshop on  
Thermodynamic and Structural Properties of  
Alloy Materials, 20–24 June 1999,  
Oranjestad, Aruba**

---

Online: [www.iop.org/Journals/ms](http://www.iop.org/Journals/ms)

---

DTIC QUALITY IMPROVED 4

20010116 145

Institute of Physics PUBLISHING

# Modelling and Simulation in Materials Science and Engineering

Institute of Physics Publishing is a not-for-profit learned society publisher with a reputation for quality and high standards. It has a comprehensive range of products serving the physics and physics-related communities and in particular is an established leader in the world of scientific journals and is at the forefront of electronic publishing. Authors of journal articles are supplied with 50 free offprints of their articles and there are no page charges. Authors and readers benefit from the rigorous refereeing procedures, prompt publication times and rapid response to research developments, ensuring that the journals are timely, topical and fully validated.

## Journal scope

Electronic structure/properties of materials determined by *ab initio* and/or semi-empirical methods, e.g., quantum chemistry, density functional, tight binding. Atomic level properties of materials, including structural, mechanical, thermodynamic and kinetic properties. Microstructural level phenomena, including grain growth, sintering, dislocation networks, coarsening, texture etc. Continuum-level modelling pertaining to materials, including continuum elasticity/plasticity, fracture mechanics, fluid flow, diffusion, heat transfer, phase transitions etc. Macroscopic process models, e.g. welding, forming, casting, CVD. Modelling behaviour in service, e.g. lifetime predictions, environmental persistence, degradation. The journal particularly welcomes papers treating simulation related to the interpretation of experimental observations and linking synergistically theory and experiment. Data representation, data manipulation, data exchange formats and other aspects of computerization of the structure, properties and processing of materials.

## A brief guide for authors

A submission to *Modelling and Simulation in Materials Science and Engineering* must be the original work of the author(s) and must not be published elsewhere or under consideration for another publication in its submitted or a substantially similar form in any language.

Research Papers should not normally be more than 8500 words in length and must be in English.

Details on how to structure an article, including specific information on figures, tables and references, are available in the booklet *Notes for Authors* (see below).

### How to submit

The following material should be submitted:

1. Three complete copies of the article.
2. One complete set of illustrations suitable for reproduction. Photographic illustrations should be supplied as glossy prints (not negatives or slides).
3. Copies of any unpublished or obscure references that may be necessary for the refereeing process.

### Electronic production

Articles can be published from a wide range of electronic text (TeX (including LaTe<sub>X</sub>, REVTeX, AMS-TeX, etc) source code, wordprocessor (e.g., Word, WordPerfect) files or ASCII files) and graphics formats. Authors are asked to submit hard-copy versions for refereeing as normal and to indicate in their submission letter the formats in which the text and illustrations are available. Further details are available from Institute of Physics Publishing's World Wide Web server ([www.iop.org](http://www.iop.org)) and in the booklet *Notes for Authors* (see below).

### Further details

Authors who are submitting to *Modelling and Simulation in Materials Science and Engineering* for the first time, or who require more details on presentation and style, should consult the booklet *Notes for Authors*, obtainable free of charge from the Journals Publishing Department at the Publishing Office. E-mail requests should be addressed to [notes4au@ioppublishing.co.uk](mailto:notes4au@ioppublishing.co.uk). *Notes for Authors* is also available in electronic format via the World Wide Web server ([www.iop.org](http://www.iop.org)).

### Address for submissions

Dr M I Baskes  
MST-8 G755  
Los Alamos National Laboratory  
PO Box 1663  
Los Alamos  
NM 87545, USA  
**Tel:** (1) 505 667 1238  
**Fax:** (1) 505 667 8021  
**E-mail:** [msmse@lanl.gov](mailto:msmse@lanl.gov)

# REPORT DOCUMENTATION PAGE

Form Approved  
OMB NO. 0704-0188

Public Reporting burden for this collection of information is estimated to average 1 hour per response, including the time for reviewing instructions, searching existing data sources, gathering and maintaining the data needed, and completing and reviewing the collection of information. Send comment regarding this burden estimates or any other aspect of this collection of information, including suggestions for reducing this burden, to Washington Headquarters Services, Directorate for Information Operations and Reports, 1215 Jefferson Davis Highway, Suite 1204, Arlington, VA 22202-4302, and to the Office of Management and Budget, Paperwork Reduction Project (0704-0188) Washington, DC 20503.

1. AGENCY USE ONLY (Leave Blank)	2. REPORT DATE	3. REPORT TYPE AND DATES COVERED Workshop funding June 20 - June 24, 1999	
4. TITLE AND SUBTITLE <b>Theory and modeling of disordered materials (workshop)</b>		5. FUNDING NUMBERS <b>DAAD19-99-1-0265</b>	
6. AUTHOR(S) <b>Professor Gerbrand Ceder</b>			
7. PERFORMING ORGANIZATION NAME(S) AND ADDRESS(ES) <b>Massachusetts Institute of Technology 77 Massachusetts Avenue, Building 13, Room 5056 Cambridge, MA 02139</b>		8. PERFORMING ORGANIZATION REPORT NUMBER <b>2716800</b>	
9. SPONSORING / MONITORING AGENCY NAME(S) AND ADDRESS(ES) <b>U. S. Army Research Office P.O. Box 12211 Research Triangle Park, NC 27709-2211</b>		10. SPONSORING / MONITORING AGENCY REPORT NUMBER <b>ARO40052.1 - MS-CF</b>	
11. SUPPLEMENTARY NOTES The views, opinions and/or findings contained in this report are those of the author(s) and should not be construed as an official Department of the Army position, policy or decision, unless so designated by other documentation.			
12 a. DISTRIBUTION / AVAILABILITY STATEMENT  <b>Approved for public release; distribution unlimited.</b>		12 b. DISTRIBUTION CODE	
13. ABSTRACT (Maximum 200 words)  <b>Structural and chemical disorder form the cornerstone of modern engineering materials. With the support of the Army Research Office a workshop was held that brought together experimentalists and theorists that work on various forms of disorder in metals, oxides and semiconductors. The workshop, held from June 20-24, 1999 in Oranjestad, Aruba, assessed the state-of-the-art of the field and provided a clearer picture of the challenge and possibilities ahead. Proceedings have been published in Modeling and Simulation in Materials Science and Engineering.</b>			
14. SUBJECT TERMS <b>Disorder, order, amorphous, phase diagram</b>		15. NUMBER OF PAGES <b>6</b>	
		16. PRICE CODE	
17. SECURITY CLASSIFICATION OR REPORT <b>UNCLASSIFIED</b>	18. SECURITY CLASSIFICATION ON THIS PAGE <b>UNCLASSIFIED</b>	19. SECURITY CLASSIFICATION OF ABSTRACT <b>UNCLASSIFIED</b>	20. LIMITATION OF ABSTRACT <b>UL</b>

# **FINAL PROGRESS REPORT**

**ARMY RESEARCH OFFICE GRANT DAAD19-99-1-0265**

## **Theory and modeling of disordered materials: Evaluating the challenges for the future**

### **Workshop**

#### **Summary and Objective**

Structural and chemical disorder form the cornerstone of modern engineering materials. With the support of the Army Research Office a workshop was held that brought together experimentalists and theorists that work on various forms of *disorder in metals, oxides and semiconductors*. The workshop, held from June 20-24, 1999 in Oranjestad, Aruba, assessed the state-of-the-art of the field and provided a clearer picture of the challenge and possibilities ahead. *Proceedings* have been published in *Modeling and Simulation in Materials Science and Engineering*.

#### **Workshop, Attendees and Proceedings**

Fourty-two reserachers from the US, Europe and Asia attended the workshop and most stayed for the full four-day program. Presentations covered a wide range of materials, from metals to semiconductors and oxides. Configurational disorder as well as topological disorder was covered, with a substantial interest in amorphous materials and liquids. Some discussions took place on how regular first principles alloy theory (currently almost exclusively used for crystalline materials) could be used to study liquids or metallic glasses. The interaction between experimentalists such as Bill Johnson,

Ricardo Schwartz, Saboungi, Loiseau, Moss, Ardell, Price and theorists led to the definition of several interesting problems for the future. A follow-up workshop will be held in September 2001 and will be organized by Dr Alphonse Finel (ONERA, France), Dr. Ben Burton (NIST) and Dr. Duane Johnson (University of Illinois).

## Attendees:

Alan Ardell, Mark Asta, Ben Burton, John Cahn, Gerd Ceder, Catherine Colinet, Didier de Fontaine, Stefano de Gironcoli, Hugues Dreysse, Francois Ducastelle, Alphonse Finel, Mike Finniss, Brent Fultz, Jeff Hoyt, Bill Johnson, Duane Johnson, Rio Kikuchi, Annick Loiseau, Tetsuo Mohri, Dane Morgan, Simon Moss, Alain Pasturel, David Price, Andrew Quong, Marie-Louise Saboungi, Juan Sanchez, Ricardo Schwarz, Marcel Sluiter, Patrice Turchi, Chris Wolverton, Don Nicholson, Harry Cook, Mathias Ekman, Kristin Einarsson, Cecile Berne, Alex Legris, David Stepp, Eric Wu, Anton Van der Ven, Chris Marianetti, Axel van de Walle,

## Proceedings:

Two copies are attached

## Workshop Program:

### Sunday, June 20<sup>th</sup>

6:30-8:00 p.m. Reception and Registration

### Monday, June 21<sup>st</sup> m

8:50-9:00 a.m. Welcome and Opening Remarks

#### *Alloy Phase Stability* (Chair - D. de Fontaine)

9:00-9:45      **J. Sanchez**, "Computation of Phase Diagrams: From First Principles to Phenomenology"

9:45-10:30      **P. Turchi**, "Ab initio Prediction of Phase Diagrams and Beyond"

10:30-10:50      Coffee Break

#### *Surface Alloys* (Chair - P. Turchi)

10:50-11:35      **M. Asta**, "Thermodynamics of Metallic Surface-Alloy Formation"

11:35-12:20      **S. Moss** (with H. Trenkler), "X-ray Studies of Order-Disorder in V<sub>2</sub>H: from a Continuous Transition in the Surface 'Skin' to a First Order Transition in the Bulk"

12:20-2:00      Lunch

2:00-2:45      **H. Dreysse** (with L. Wille), "Surface Segregation and Heteroepitaxial Growth in Metallic Alloys"

*Alloy Microstructure* (Chair - J. Cahn)  
2:45-3:30      **A. Ardell**, "The Ni-Ni<sub>3</sub>Al Phase Diagram: The Last Word"  
3:30-4:15      **C. Wolverton**, "First-Principles Theory of Large-Scale, Coherent Alloy Morphologies"

4:15-4:35      Coffee Break  
  
4:35-5:20      **A. Finel**, "Dynamical Evolution of Microstructures with Elastic Effects: Phase Field and Atomistic Methods"  
5:20-6:05      **A. Loiseau**, "Order-Disorder Phase Transformations in Co-Pt: Wetting and Development of a Chess-Board Like Microstructure"  
6:05-6:50      **A. Pasturel**, "Ab Initio Study of Transitory Metastable Phases Solidified by Drop-tube Processing"

**Tuesday, June 22<sup>nd</sup>**

*Vibrations in Alloys* (Chair - F. Ducastelle)  
9:00-9:45      **B. Fultz**, "Vibrational Entropies of Alloy Phases"  
9:45-10:30      **A. Quong**, "The Effect of Vibrational Entropy on the Dilute Heats of Solutions of Impurities in Al"  
  
10:30-10:50      Coffee Break  
  
10:50-11:35      **D. Morgan** (with A. van de Walle and G. Ceder), "Lattice Vibrations and Alloy Thermodynamics"

*Amorphous and Liquid Alloys* (Chair - M. Asta)  
11:35-12:20      **D. de Fontaine**, "Topologically Disordered Alloys"  
  
12:20-4:00      Free Afternoon  
  
4:00-4:45      **W. Johnson**, "Microstructure and Property Relationships in Bulk Metallic Glass Forming Alloys"  
4:45-5:30      **J. Hoyt** (with M. Asta), "Obtaining Parameters of the Phase Field Model from Atomistic Simulations"  
  
5:30-5:50      Coffee Break  
  
5:50-6:35      **D. Price** (with J. Corbett, T. Rosenbaum, and W. Howells), "Orientational and Translational Disorder in Zintl Alloys"  
6:35-7:20      **R. Schwartz**, "Lattice Disorder and Amorphization of Intermetallics Caused by Hydrogen Absorption"  
7:20-8:05      **M. Saboungi**, "Clusters or Networks in Zintl Alloys: Thermodynamics and Structure"

**Wednesday, June 23<sup>rd</sup> Caribbean Room**

*Electronic Properties* (Chair - D. Johnson)

- 9:00-9:45      **S. de Gironcoli**, "Structural and Electronic Properties of Wide Gap Semiconductor Alloys"
- 9:45-10:30      **D. Nicholson**, "Electron and Positron States in Amorphous NiPdP"
- 10:30-10:50      Coffee Break
- Oxide Alloys* (Chair - D. Price)
- 10:50-11:35      **G. Ceder**, "Challenges for *Ab-Initio* Alloy Theory in Oxides"
- 11:35-12:20      **B. Burton**, "Thermodynamics of Cation Ordering in  $A(B_{1/3},B'_{2/3})O_3$  Perovskites"

12:20-8:00p.m. Free Afternoon

- 8:00p.m.      Banquet - Speaker: **H. Cook**, "The Value of Things"  
 Location: Sonesta Island. Boats will begin departing at 7:30 from the hotel lobby.

### **Thursday, June 24<sup>th</sup>**

- Statistical Mechanics* (Chair - J. Sanchez)
- 9:00-9:45      **J. Cahn**, "Swallowtails , Mushrooms and All That"
- 9:45-10:30      **C. Colinet**, "Comparison of CVM and Monte Carlo Calculations of Order-Disorder Transformations"
- 10:30-10:50      Coffee Break
- 10:50-11:35      **R. Kikuchi**, "Infinitesimal Lattice-Constant Treatment of Liquid"
- 11:35-12:20      **T. Mohri**, "Pseudo Critical Slowing Down within the CVM and PPM"

12:20-2:00      Lunch

- Metals and Intermetallics* (Chair - C. Wolverton)
- 2:00-2:45      **M. Sluiter**, "*Ab Initio* Calculation of the Structural Transformation in Ca and Sr"
- 2:45-3:30      **M. Finnis**, "*Ab Initio* Predictions of Defect Thermodynamics in NiAl"
- 3:30-3:50      Coffee Break
- 3:50-4:35      **F. Ducastelle**, " $L1_2$ - $D0_{22}$  Competition and Long Period Structures in Pseudobinary (Pt or Pd)<sub>3</sub>V Alloys"
- 4:35-5:20      **D. Johnson**, "Alloy Structural Energy Differences from Experiment and Theory:  
 A                   Lesson from  $Ni_3V$ "
- 5:20-5:40      Concluding Remarks and Adjourn

# Modelling and Simulation in Materials Science and Engineering

Serving the emerging multidisciplinary materials community through original contributions to modelling methods and applications, the journal covers properties, structure and behaviour of all classes of materials at scales from the atomic to the macroscopic.

## Editor-in-Chief

M I Baskes *Los Alamos National Laboratory, NM, USA*  
(msmse@lanl.gov)

## Executive Editorial Board

S Asai *Nagoya University, Japan*  
C R A Catlow *The Royal Institution of Great Britain, London, UK* (richard@ri.ac.uk)  
M Doyama *Teikyo University of Science and Technology, Tokyo, Japan* (doyama@ntu.ac.jp)  
B M Klein *University of California, Davis, USA* (klein@bethe.ucdavis.edu)  
L Kubin *CNRS-ONERA (OM), Chatillon, France* (kubin@onera.fr)  
A Needleman *Brown University, Providence, RI, USA* (needle@an.engin.brown.edu)  
D Pettifor *University of Oxford, UK*  
D J Srolovitz *Princeton University, NJ, USA* (srol@princeton.edu)  
V Vitek *University of Pennsylvania, Philadelphia, USA* (vitek@lrsm.upenn.edu)  
J H Westbrook *Brookline Technologies, Bailston Spa, NY, USA*  
R Zeller *Institut für Festkörperforschung, KFA Jülich, Germany* (ru.zeller@kfa-juelich.de)

## Editorial Board

J B Adams *Arizona State University, Tempe, USA*  
J Bassani *University of Pennsylvania, Philadelphia, USA*  
A Beaudoin *University of Illinois at Urbana-Champaign, IL, USA*  
R Becker *Lawrence Livermore National Laboratory, CA, USA*  
R Benedek *Argonne National Laboratory, IL, USA*  
Y Brechet *LTPCM-ENSEEG, St Martin d'Heres, France*

## Publishing Editor

Tom Spicer

## Publishing Administrator

Julie Stott

## Production Editor

Katie Pennicott

## Advertisement Sales

Chris Manning  
CPL Sales Ltd  
53-54 Sidney Street  
Cambridge CB2 3HX, UK

**Tel:** +44 (0)1223 477411

**Fax:** +44 (0)1223 327356

**E-mail:** chris@campublishers.com

**Web:** www.campublishers.com

P Bristowe *University of Cambridge, UK*  
V Bulatov *Lawrence Livermore National Laboratory, CA, USA*  
B Cantor *Oxford University, UK*  
M Daw *Motorola Inc, Austin, TX, USA*  
J W Evans *University of California, Berkeley, CA, USA*  
S Foiles *Sandia National Laboratories, Livermore, CA, USA*  
C Fong *University of California, Davis, USA*  
H Gao *Stanford University, CA, USA*  
G Gottstein *Institut für Metallkunde und Metallphysik, Aachen, Germany*  
G Grest *Sandia National Laboratories, Albuquerque, NM, USA*  
P Gumbsch *Max-Planck-Institut für Metallforschung, Stuttgart, Germany*  
J Harding *University College London, UK*  
T Isikawa *Nagoya University, Japan*  
K A Jackson *Central Michigan University, Mt Pleasant, USA*  
T Kaxiras *Harvard University, Cambridge, MA, USA*  
M Kohyama *Osaka National Research Institute, Japan*  
Y-w Lu *Tsinghua University, Beijing, China*  
M Ortiz *California Institute of Technology, Pasadena, USA*  
R Phillips *Brown University, Providence, RI, USA*  
C Pisani *Università di Torino, Turin, Italy*  
M Rappaz *EPFL, Lausanne, Switzerland*  
A Rollett *Carnegie Mellon University, Pittsburgh, PA, USA*  
U W Suter *ETH Zurich, Switzerland*  
O Takai *Nagoya University, Japan*  
S Taniguchi *Tohoku University, Japan*  
V Tvergaard *Technical University, Lyngby, Denmark*  
R A Van Santen *Eindhoven University of Technology, The Netherlands*  
P Voorhees *Northwestern University, Evanston, IL, USA*  
M Weinert *Brookhaven National Laboratory, Upton, NY, USA*  
S Yip *Massachusetts Institute of Technology, Cambridge, USA*

## Publishing Office

Institute of Physics Publishing  
Dirac House  
Temple Back  
Bristol BS1 6BE, UK

**Tel:** +44 (0)117 929 7481

**Fax:** +44 (0)117 929 4318

**E-mail:** msms@ioppublishing.co.uk

# Modelling and Simulation in Materials Science and Engineering

Published bimonthly in hard copy and online by Institute of Physics Publishing, Dirac House, Temple Back, Bristol BS1 6BE, UK.

## Institutional subscription information: 2000 volume

For all countries, except the United States, Canada and Mexico, the subscription rate is £279.00 per annual volume. Single-issue price £46.50 (except conference issues/supplements—prices available on application).

Delivery is by air-speeded mail from the United Kingdom to most overseas countries, and by airfreight and registered mail to subscribers in India.

### Orders to:

Order Processing Department  
Institute of Physics Publishing  
Dirac House, Temple Back  
Bristol BS1 6BE, UK

For the United States, Canada and Mexico, the subscription rate is US\$547.00 per annual volume. Delivery is by transatlantic airfreight and onward mailing.

### Orders to:

American Institute of Physics Subscriber Services  
Suite 1NO1  
2 Huntington Quadrangle  
Melville  
NY 11747-4502, USA

Non-institutional subscription rates are also available.

## Back issues

Orders and enquiries for the previous volume should be sent to the subscription addresses given above, and for earlier volumes to: Dawson UK Ltd, Cannon House, Folkestone CT19 5EE, UK.

## United States Postal Identification Statement

*Modelling and Simulation in Materials Science and Engineering* (ISSN: 0965-0393) is published bimonthly by Institute of Physics Publishing, Dirac House, Temple Back, Bristol BS1 6BE, UK in association with the American Institute of Physics, Suite 1NO1, 2 Huntington Quadrangle, Melville, NY 11747-4502, USA. Application to Mail at Periodicals Postage Rates is Pending at Huntington Station, NY, and additional mailing offices. POSTMASTER: Send address changes to: *Modelling and Simulation in Materials Science and Engineering*, American Institute of Physics, Suite 1NO1, 2 Huntington Quadrangle, Melville, NY 11747-4502, USA.

Copyright ©2000 by IOP Publishing Ltd and individual contributors. All rights reserved. No part of this publication may be reproduced, stored in a retrieval system or transmitted in any form or by any means, electronic, mechanical, photocopying, recording or otherwise, without the written permission of the publisher, except as stated below. Single photocopies of single articles may be made for private study or research. Illustrations and short extracts from the text of individual contributions may be copied provided that the source is acknowledged, the permission of the authors is obtained and IOP Publishing Ltd is notified. Multiple copying is permitted in accordance with the terms of licences issued by the Copyright Licensing Agency under the terms of its agreement with the Committee of Vice-Chancellors and Principals. Authorization to photocopy items for internal or personal use, or the internal or personal use of specific clients, is granted by IOP Publishing Ltd to libraries and other users registered with the Copyright Clearance Center (CCC) Transactional Reporting Service, provided that the base fee of \$30.00 per copy is paid directly to CCC, 222 Rosewood Drive, Danvers, MA 01923, USA.

**Articles in *Modelling and Simulation in Materials Science and Engineering* are abstracted in:** INSPEC Information Services; Bulletin Signaletique; Materials Information: Ceramic Abstracts; Engineering Information (Compendex\*Plus); ISI (Science Citation Index, SciSearch, Research Alert, Materials Science Citation Index, Current Contents/Physical, Chemical and Earth Sciences, Current Contents/Engineering, Computing and Technology); Applied Mechanics Reviews; Chemical Abstracts.

©™ The paper used in this publication meets the minimum requirements of American National Standard for Information Sciences — Permanence of Paper for Printed Library Materials, ANSI Z39.48-1992.

## Preface

Structural and chemical disorder are part of almost any engineering material. Their detailed characterization with theoretical and experimental approaches therefore forms the cornerstone of modern materials science and engineering. To assess the state of this field, the Workshop on Thermodynamic and Structural Properties of Alloy Materials was held on 20–24 June 1999 at the Sonesta Hotel in Oranjestad, Aruba. The workshop brought together experimentalists and theorists in the fields of metals, oxides and semiconductors. Particular emphasis was placed on efforts to transfer the success of first-principles modelling of configurational disorder to topological disorder, as occurs in metallic glasses and liquids. Fittingly, the workshop was dedicated to Professor de Fontaine of the University of California at Berkeley, whose influence on the field of order-disorder reactions and first-principles phase diagram calculations has been of key importance to the development of the subject.

The organizers would like to thank the Army Research Office for financial support and the editorial staff of *Modelling and Simulation in Materials Science and Engineering* for working with us patiently on these proceedings.

**Mark Asta, Northwestern University**  
**Gerbrand Ceder, Massachusetts Institute of Technology**  
**Chris Wolverton, Ford Motor Company**  
**Conference Organizers**

# Long-range versus short-range interactions and the configurational energies of $\text{Ba}(B, B')\text{O}_3$ and $\text{Pb}(B, B')\text{O}_3$ perovskites

B P Burton

Materials Science and Engineering Laboratory, Ceramics Division,  
National Institute of Standards and Technology, Gaithersburg MD 20899, USA

Received 16 September 1999, accepted for publication 7 November 1999

**Abstract.** Total energy calculations were performed for three perovskite related ordered supercells in several stoichiometries of  $A(B, B')\text{O}_3$ ; where  $A$  is  $\text{Pb}^{2+}$  or  $\text{Ba}^{2+}$ ;  $B$  is  $\text{Mg}^{2+}$ ,  $\text{Zn}^{2+}$ ,  $\text{Sc}^{3+}$  or  $\text{In}^{3+}$ ; and  $B'$  is  $\text{Nb}^{5+}$ ,  $\text{Ta}^{5+}$  or  $\text{W}^{6+}$ . A striking difference between the Pb and  $\text{Ba}(B, B')\text{O}_3$  systems is that the differences in total energies for Pb-systems span ranges that are consistently smaller than those of the Ba systems. This indicates a reduction in the energetic barriers to disordering in the Pb-systems, which is consistent with experimental observations of consistently higher transition temperatures in the Ba-systems. This trend is explained as a consequence of enhanced Pb–O bonding to underbonded oxygens in  $B^{2+}$ –O– $B^{2+}$  and  $B^{3+}$ –O– $B^{3+}$  environments.

## 1. Introduction

Lead-based  $A(B, B')\text{O}_3$  perovskites ( $A$  is  $\text{Pb}^{2+}$  or  $\text{Ba}^{2+}$ ;  $B$  is  $\text{Mg}^{2+}$ ,  $\text{Zn}^{2+}$ ,  $\text{Sc}^{3+}$  or  $\text{In}^{3+}$ ; and  $B'$  is  $\text{Nb}^{5+}$ ,  $\text{Ta}^{5+}$  or  $\text{W}^{6+}$ ) are widely used as relaxor ferroelectric [1–3] transducers, actuators and multilayer capacitors. Their  $\text{Ba}(B, B')\text{O}_3$  counterparts, particularly  $\text{Ba}(\text{Zn}_{1/3}\text{Ta}_{2/3})\text{O}_3$ , are the premier dielectric resonator materials [4]. Some cation disorder is essential to obtain the relaxor properties of the Pb systems [1, 2], but disorder in the Ba systems can degrade the dielectric ‘quality factor’ by orders of magnitude [5, 6]. As indicated by the experimental data summarized in table 1, B-site ordering in  $A(B, B')\text{O}_3$  perovskites persists to higher temperatures when the  $A$  cation is  $\text{Ba}^{2+}$  rather than  $\text{Pb}^{2+}$ , especially in the  $A(\text{B}_{1/3}\text{B}'_{2/3})\text{O}_3$  systems [5, 7–12, 15–17]. Clearly, the energetics of B-site ordering are dramatically altered by substituting Pb for Ba on the  $A$  sites, and it is not obvious why this should occur. The results presented below suggest that this surprising trend is caused by enhanced Pb–O hybridization between the Pb 6s and the O 2p states of *underbonded oxygens* in  $B^{2+}$ –O– $B^{2+}$  or  $B^{3+}$ –O– $B^{3+}$  environments. This interaction has an inherently many-body character because it depends upon the configuration of the eight B-site ions that surround an  $A$  site. The local symmetry of the B-site configuration dictates that some configurations are conducive to Pb–O bond relaxation and others are not.

All of the  $\text{Ba}(\text{B}_{1/3}\text{B}'_{2/3})\text{O}_3$  systems, adopt the 1:2 crystal structure at low temperatures (a  $B:B':B'$  layer sequence perpendicular to the cubic [111] vector, ([111]<sub>c</sub>)), but the only  $\text{Pb}(\text{B}_{1/3}\text{B}'_{2/3})\text{O}_3$  system that exhibits long-range order is  $\text{Pb}(\text{Mg}_{1/3}\text{Ta}_{2/3})\text{O}_3$ . When maximally ordered, the 1:1 structure with  $\text{Pb}(\text{Mg}_{1/3}\text{Ta}_{2/3})\text{O}_3$  stoichiometry, has two  $B$  sites: one occupied by Ta and the other by a disordered  $\text{Mg}_{2/3}\text{Ta}_{1/3}$  mixture. Thus, the 1:1 structure is a partially ordered, intermediate-temperature phase rather than the  $\text{Pb}(\text{Mg}_{1/3}, \text{Ta}_{2/3})\text{O}_3$  (PMT)

**Table 1.** Experimental data on ordering in  $A(B, B')\text{O}_3$  perovskites.

System	Abbreviation	Observed ordering	Transition temperature	Ref.
Pb(Zn <sub>1/3</sub> , Nb <sub>2/3</sub> )O <sub>3</sub>	PZN	1:1 Short-range order		[7]
Pb(Mg <sub>1/3</sub> , Nb <sub>2/3</sub> )O <sub>3</sub>	PMN	1:1 Short-range order		[8, 9]
Pb(Zn <sub>1/3</sub> , Ta <sub>2/3</sub> )O <sub>3</sub>	PZT	?		[18]
Pb(Mg <sub>1/3</sub> , Ta <sub>2/3</sub> )O <sub>3</sub>	PMT	1:1 $\rightleftharpoons$ Disordered	1350 °C < $T_t$ <sup>a</sup> < 1400 °C	[10]
Ba(Zn <sub>1/3</sub> , Nb <sub>2/3</sub> )O <sub>3</sub>	BZN	1:2 $\rightleftharpoons$ Disordered	1300 °C < $T_t$ < 1350 °C	[15, 16]
Ba(Mg <sub>1/3</sub> , Nb <sub>2/3</sub> )O <sub>3</sub>	BMN	1:2 $\rightleftharpoons$ Disordered	1350 °C < $T_t$ < 1400 °C	[10]
Ba(Zn <sub>1/3</sub> , Ta <sub>2/3</sub> )O <sub>3</sub>	BZT	1:2 $\rightleftharpoons$ Disordered	$T_t \geq 1650$ °C	[5]
Ba(Mg <sub>1/3</sub> , Ta <sub>2/3</sub> )O <sub>3</sub>	BMT	1:2 $\rightleftharpoons$ Disordered	$T_t \approx 1655$ °C	[17]
Pb(Sc <sub>1/2</sub> , Nb <sub>1/2</sub> )O <sub>3</sub>	PSN	1:1 $\rightleftharpoons$ Disordered	1200 °C < $T_t$ < 1220 °C	[19]
Pb(Sc <sub>1/2</sub> , Ta <sub>1/2</sub> )O <sub>3</sub>	PST	1:1 $\rightleftharpoons$ Disordered	1400 °C < $T_t$ < 1560 °C	[2, 20]
Pb(In <sub>1/2</sub> , Nb <sub>1/2</sub> )O <sub>3</sub>	PIN	1:1 $\rightleftharpoons$ Disordered	920 °C < $T_t$ < 950 °C	[11, 12]
Pb(In <sub>1/2</sub> , Ta <sub>1/2</sub> )O <sub>3</sub>	PIT	1:1 $\rightleftharpoons$ Disordered	1070 °C < $T_t$ < 1100 °C	[13, 14]
Ba(Sc <sub>1/2</sub> , Nb <sub>1/2</sub> )O <sub>3</sub>	BSN	1:1 $\rightleftharpoons$ Disordered	1400 °C < $T_t$	[21]
Ba(Sc <sub>1/2</sub> , Ta <sub>1/2</sub> )O <sub>3</sub>	BST	1:1 $\rightleftharpoons$ Disordered	1400 °C < $T_t$	[21]
Ba(In <sub>1/2</sub> , Nb <sub>1/2</sub> )O <sub>3</sub>	BIN	1:1	1200 °C < $T_t$ < 1400 °C	[22, 23]
Ba(In <sub>1/2</sub> , Ta <sub>1/2</sub> )O <sub>3</sub>	BIT	1:1	1200 °C < $T_t$ < 1650 °C	[22, 24]
Pb(Mg <sub>1/2</sub> , W <sub>1/2</sub> )O <sub>3</sub>	PMW	1:1	?	[22]
Ba(Mg <sub>1/2</sub> , W <sub>1/2</sub> )O <sub>3</sub>	BMW	1:1	?	[22]
Pb(Sc <sub>2/3</sub> , W <sub>1/3</sub> )O <sub>3</sub>	PSW	1:1	melts incongruently at 970 °C	[25]
Ba(Sc <sub>2/3</sub> , W <sub>1/3</sub> )O <sub>3</sub>	BSW	1:1	1100 °C < $T_t$	[26]

<sup>a</sup>  $T_t$  is the cation order-disorder transition temperature.

ground state (GS); Ba(Sc<sub>2/3</sub>, W<sub>1/3</sub>)O<sub>3</sub> also exhibits the partially ordered 1:1 structure, as do many other  $A(B_{2/3}, B'_{1/3})\text{O}_3$  perovskites with stoichiometries not considered here [22]. For the  $A(B_{1/2}, B'_{1/2})\text{O}_3$  systems, stoichiometry is consistent with a 1:1 GS, and both Ba and Pb systems adopt the 1:1 structure at low temperatures, and the Ba(B<sub>1/2</sub>, B'<sub>1/2</sub>)O<sub>3</sub> systems consistently exhibit higher cation order-disorder transition temperatures [10, 19, 21]. The A(Mg<sub>1/2</sub>, W<sub>1/2</sub>)O<sub>3</sub> systems also exhibit the 1:1 structure, but no transition temperatures have been reported; given the large difference in formal charges, Mg<sup>2+</sup> against W<sup>6+</sup>, it seems likely that these phases will melt before disordering.

## 2. Total energy calculations

The total energies were calculated for three 15-atom perovskite-based superstructures in each of the eight possible stoichiometries of  $A(B_{1/3}B'_{2/3})\text{O}_3$ , where  $A$  is Pb or Ba;  $B$  is Mg or Zn; and  $B'$  is Nb or Ta (figure 1). The three  $A(B_{1/3}B'_{2/3})\text{O}_3$  superstructures ([111]<sub>1:2</sub>, [110]<sub>1:2</sub> and [001]<sub>1:2</sub>) are derived from ideal perovskite by adding a ( $B:B':B'$ ) layer sequence perpendicular to [111]<sub>c</sub>, [110]<sub>c</sub> and [001]<sub>c</sub>, respectively. Calculations were also performed for the eight  $A(B_{1/2}B'_{1/2})\text{O}_3$  stoichiometries in which  $A$  is Pb or Ba;  $B$  is Sc or In; and  $B'$  is Nb or Ta (figure 2). The three ten-atom  $A(B_{1/2}B'_{1/2})\text{O}_3$  superstructures, [111]<sub>1:1</sub>, [110]<sub>1:1</sub> and [001]<sub>1:1</sub>, are derived by adding  $B:B'$  layer sequences perpendicular to [111]<sub>c</sub>, [110]<sub>c</sub> and [001]<sub>c</sub>. All calculations were performed with the Vienna *ab initio* simulation program (VASP) [27] using ultrasoft Vanderbilt-type [28] plane-wave pseudopotentials with a local density approximation for exchange and correlation energies. Electronic degrees of freedom were optimized with a conjugate gradient algorithm, and both cell constant and ionic positions were fully relaxed; ferroelastic acentric relaxations were not investigated. Valence electron configurations for the pseudopotentials are: Pb, 5d<sup>10</sup>6p<sup>2</sup>6s<sup>2</sup> (Pb<sub>d</sub> version); Ba, 5p<sup>6</sup>6s<sup>2</sup>; Mg, 2p<sup>6</sup>3s<sup>2</sup>; Zn, 3d<sup>10</sup>4s<sup>2</sup>;

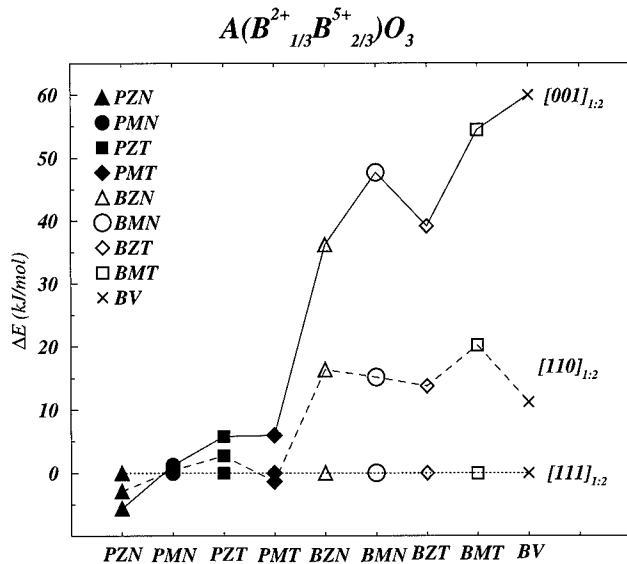


**Figure 1.** Total energies relative to  $E_{[111]_{I2}}$ , for the perovskite-based supercells with compositions  $A(B_{1/3}B'_{2/3})O_3$ , where  $A$  is Pb or Ba;  $B$  is Mg or Zn;  $B'$  is Nb or Ta; and for ionic model of BV [29] (one mole is  $ABO_3$ ).

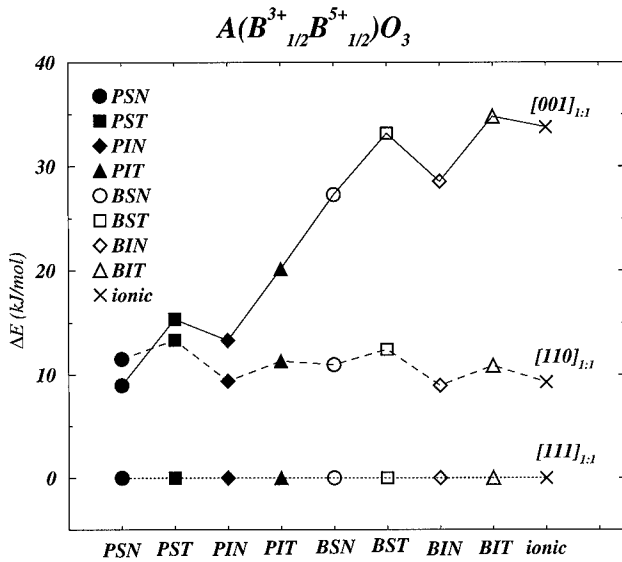


**Figure 2.** Total energies, relative to  $E_{[111]_{I1}}$ , for  $A(B_{1/2}B'_{1/2})O_3$  perovskite-based supercells.

Sc, 3p<sup>6</sup>3d4s<sup>2</sup>; In, 4d<sup>10</sup>5s<sup>2</sup>5p<sup>1</sup>; Nb, 4p<sup>6</sup>5s4d<sup>4</sup>; Ta, 5d<sup>3</sup>6s<sup>2</sup>; W, 5d<sup>4</sup>6s; O 2p<sup>6</sup>. An energy cut-off of 395.7 eV was used, in the ‘high-precision’ option which guarantees that *absolute* energies are converged to within a few millielectronvolts (a few tenths of a kilojoule per mole; one mole of  $ABO_3$ ). To promote cancellation of errors, the formation energies for the  $ABO_3$  and  $AB'O_3$  reference states are calculated for each supercell with K-point meshes:  $5 \times 5 \times 4$ ,  $4 \times 4 \times 10$  and

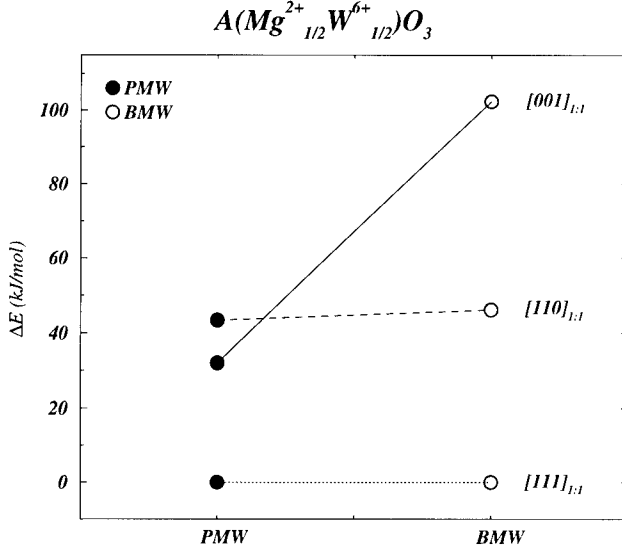


Figure 3. Total energies, relative to  $E_{[111]_{1:1}}$ , for  $A(Mg_{1/2}W_{1/2})O_3$  perovskite-based supercells.

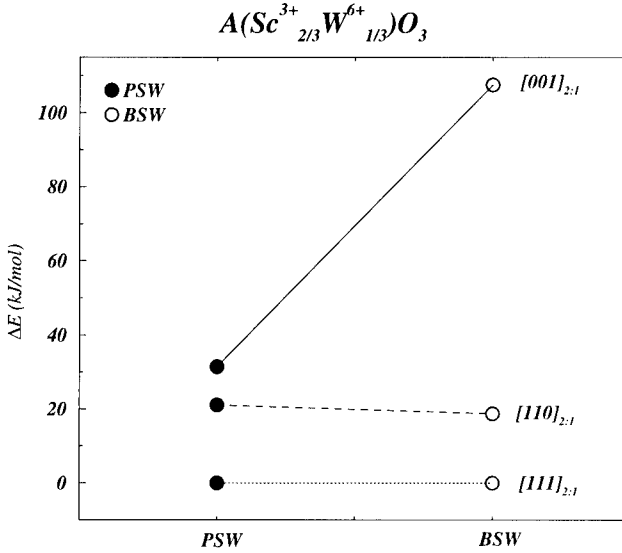
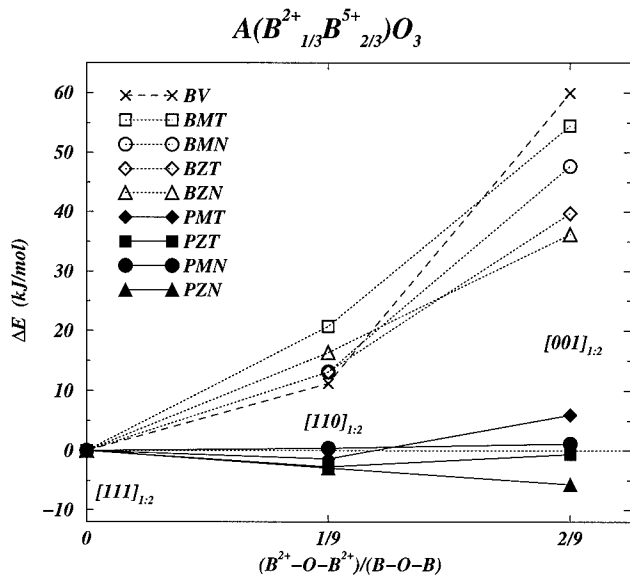


Figure 4. Total energies, relative to  $E_{[111]_{2:1}}$ , for  $A(Sc_{2/3}W_{1/3})O_3$  perovskite-based supercells.

$6 \times 6 \times 2$  for  $[111]_{1:2}$ ,  $[110]_{1:2}$  and  $[001]_{1:2}$  superstructures, respectively;  $4 \times 4 \times 4$ ,  $7 \times 7 \times 10$  and  $8 \times 8 \times 4$  for  $[111]_{1:1}$ ,  $[110]_{1:1}$  and  $[001]_{1:1}$ , respectively.

The total energies for  $A(B_{1/3}B'_{2/3})O_3$  supercells, relative to  $E_{[111]_{1:2}}$ , are plotted in figure 1 with the corresponding supercell energies calculated with the ionic model of Bellaiche and Vanderbilt (BV) [29], in which

$$E = \frac{e^2}{2\epsilon a} \sum_{l \neq l'} \frac{\Delta q_l \Delta q_{l'}}{|l - l'|} \quad (1)$$



**Figure 5.**  $\Delta E$  against the concentration of underbonded oxygens in the  $[111]_{1:2}$ ,  $[110]_{1:2}$  and  $[001]_{1:2}$  supercells.

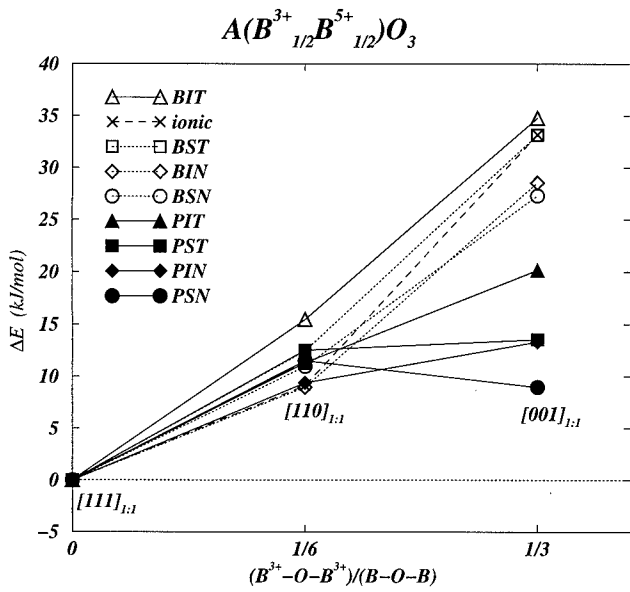


**Figure 6.**  $\Delta E$  against the concentration of underbonded oxygens in the  $[111]_{1:1}$ ,  $[110]_{1:1}$  and  $[001]_{1:1}$  supercells.

where  $E$  is the total energy;  $e$  is the electron charge;  $\epsilon$  is an electronic dielectric constant ( $\epsilon = 10$  for  $A(B_{1/3}B'_{2/3})O_3$  and  $\epsilon = 5$  for  $A(Sc_{1/2}B'_{1/2})O_3$ );  $a$  is the lattice constant ( $a = 4.07 \text{ \AA}$ )†;

† For  $A(B_{1/3}B'_{2/3})O_3$  systems  $a = 7.7 \text{ a.u.}$  and  $\epsilon = 10$  as in BV. For  $A(B_{1/3}B'_{2/3})O_3$  systems  $\epsilon = 5$  so that  $\Delta E_{[001]_{1:1}} \approx E(BSN)_{[001]_{1:1}} \approx E(BST)_{[001]_{1:1}}$ .

$\Delta q_l$  is the difference in charge between the ion at site  $l$  and the average  $B$ -site charge of +4, i.e.  $\Delta q_l = -2$  for  $Mg^{2+}$  and +1 for  $Nb^{5+}$ ; and  $a|l - l'|$  is the interionic separation. For the  $A(B_{1/3}B'_{2/3})O_3$  composition, this model predicts a 1:2 GS and a 1:2  $\Rightarrow$  disordered transition at high temperature, consistent with the experimental data for the  $Ba(B_{1/3}B'_{2/3})O_3$  systems.

In figures 1 and 2, the BV (ionic) model values and all the Ba systems, exhibit the same hierarchy:  $\Delta E_{[111]_{1:2}} < \Delta E_{[110]_{1:2}} < \Delta E_{[001]_{1:2}}$ . In the Pb systems, however, this hierarchy only occurs in PMN and PZT. Experimentally, the 1:2 structure ( $[111]_{1:2}$ ) is observed as the low-temperature (presumably GS) phase for all the Ba systems, and it is the predicted GS of the BV model. In the Pb systems, however, the 1:2 structure may not be the GS for any of them; in PMN for example, at least one 30-atom superstructure is predicted to have lower energy [30]. Energy ranges  $\Delta E_{[001]_{1:2}} - \Delta E_{[001]_{1:1}}$ , for the BV values and the Ba systems, are between 40 and 60 kJ mol<sup>-1</sup> (one mole is  $ABO_3$ ), but analogous ranges for the Pb systems,  $\Delta E_{\text{highest}} - \Delta E_{\text{lowest}}$  are between 1 and 8 kJ mol<sup>-1</sup>. In  $A(B_{1/2}B'_{1/2})O_3$  systems (figure 2),  $\Delta E$  ranges for the Pb systems are about half of those for the Ba systems, and similar results obtained for the  $A(Mg_{1/2}W_{1/2})O_3$  and  $A(Sc_{2/3}W_{1/3})O_3$  systems (figures 3 and 4). A second trend that occurs in both figures 1 and 2 is that  $\Delta E$ -ranges for  $A(B, Nb)O_3$  systems are typically a little smaller than those for the corresponding  $A(B, Ta)O_3$  systems; consistent with experimental data indicating higher transition temperatures for cation ordering in Ta systems (table 1).

### 3. Discussion

The configurational energy is apparently dominated by two contributions: long-range Coulomb interactions which favour configurations that maximize unlike charges on nearest-neighbour  $B$  sites; and short-range interactions that are primarily associated with the optimization of  $A$ -O bonds. Long-range electrostatic interactions dominate when the  $A$  cation is the larger, more regularly coordinated  $Ba^{2+}$ , and short-range interactions become competitive when it is the smaller, less regularly coordinated  $Pb^{2+}$ .

Concentrations of the underbonded oxygens in  $B^{2+}$ -O-B<sup>2+</sup> or  $B^{3+}$ -O-B<sup>3+</sup> environments increase monotonically in the sequences of structures  $[111]_{1:2}$ ,  $[110]_{1:2}$  and  $[001]_{1:2}$  (figure 5), and  $[111]_{1:1}$ ,  $[110]_{1:1}$  and  $[001]_{1:1}$  (figure 6); in both cases, the energies for BV (ionic) model calculations and Ba systems also increase monotonically. The Pb systems however, do not follow this trend and  $Pb(B_{1/3}, B'_{2/3})O_3$  systems depart from it more strongly than  $Pb(B_{1/2}B'_{1/2})O_3$ ,  $Pb(Mg_{1/2}W_{1/2})O_3$ , or  $Pb(Sc_{2/3}W_{1/3})O_3$  systems. Substitution of Pb for Ba drastically reduces the  $\Delta E$ -ranges, which implies that energetically favorable Pb-O interactions anticorrelate with electrostatically favourable  $B$ -site configurations. Thus, an increase in the concentration of electrostatically destabilizing configurations implies an increase in the concentration of stabilizing Pb-O bonds, leading to a reduced change in configurational energy for the  $Pb(B, B')O_3$  systems. This trend is much more pronounced in the  $A(B_{1/3}, B'_{2/3})O_3$  systems than in  $Pb(B_{1/2}B'_{1/2})O_3$  systems for two reasons: (1) oxygens in  $B^{2+}$ -O-B<sup>2+</sup> environments are more severely underbonded than those in  $B^{3+}$ -O-B<sup>3+</sup> environments, hence Pb-O bonds to the former are more stabilizing than those to the latter; and (2) the 1:1 stoichiometry of  $Pb(B_{1/2}B'_{1/2})O_3$  favours the ionic (1:1) GS. Point (1) above also explains why  $\Delta E$ -ranges are smaller in  $Pb(B_{1/3}, B'_{2/3})O_3$  systems than in  $Pb(Sc_{2/3}W_{1/3})O_3$  systems.

The importance of Pb 6s to O 2p hybridization in  $Pb(B)O_3$  perovskites is well established [31–35]. For example, Cohen [32] and Cohen and Krakauer [33] emphasized its role in the ferroelectricity of  $PbTiO_3$ . Bellaiche *et al* [34] and Wensell and Krakauer [35] compared the energetics of structural relaxations of PZN and BZN in the  $[111]_{1:2}$  (1:2) and  $[001]_{1:2}$  structures,

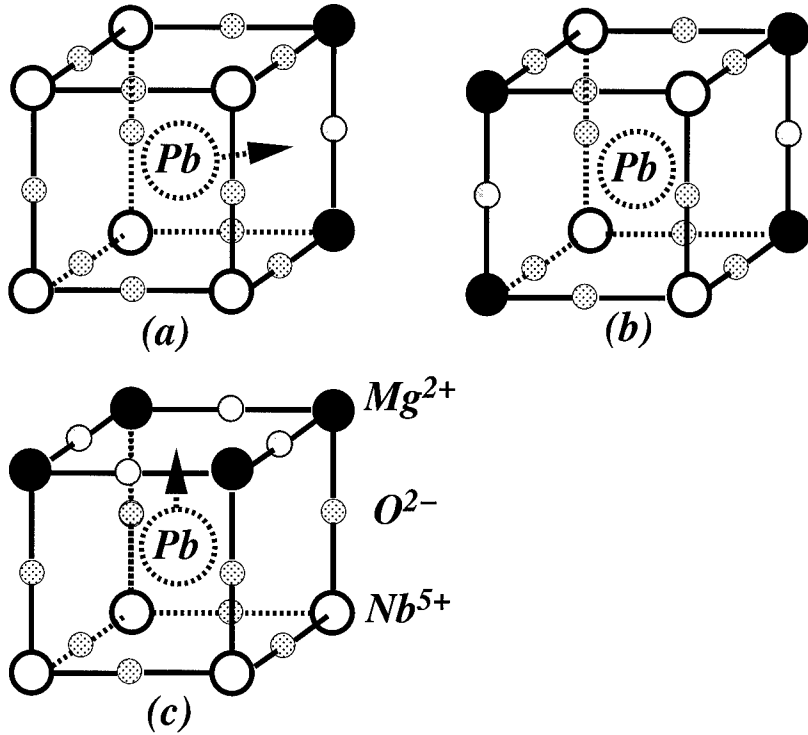


**Figure 7.** Three different lead environments in PMN supercells with arrows indicating how Pb relaxes towards underbonded oxygens (small grey circles): (a) environment with two-thirds of the Pb atoms in the  $[110]_{1:2}$  structure; (b) environment with the remaining one-third of the Pb atoms in  $[110]_{1:2}$ , and all the Pb atoms in  $[110]_{1:1}$ , symmetry prevents these Pb atoms from relaxing toward the underbonded oxygens; and (c) environment of two-thirds of the Pb atoms in the  $[001]_{1:2}$  structure, and all Pb atoms in  $[001]_{1:1}$ .

and emphasized the role of short Pb–O bonds in the  $[001]_{1:2}$  structure. Short Pb–O bonds also occur in the  $[110]_{1:2}$ ,  $[110]_{1:1}$  and  $[001]_{1:1}$  structures, but the most important point seems to be that the oxygens in these bonds are the otherwise underbonded oxygens in  $B^{2+}$ –O– $B^{2+}$  or  $B^{3+}$ –O– $B^{3+}$  triplets. Even if the ordered GS has no underbonded oxygens, as in  $[111]_{1:2}$  and  $[111]_{1:1}$ , thermal disordering will create them along with overbonded oxygens in  $B^{5+}$ –O– $B^{5+}$  or  $B^{6+}$ –O– $B^{6+}$  triplets. In the Ba systems the energetic costs of such configurations are not as strongly mitigated by short-range interactions, so ordered phases remain stable to higher temperatures and the  $\Delta E$ -hierarchies for Ba systems resemble those for the BV (ionic) model. In the Pb systems however, Pb–O bonds to underbonded oxygens typically contract, and those towards overbonded oxygens elongate if the configuration of the surrounding  $B$ -ions permits (figure 7).

In the PMN  $[110]_{1:2}$  supercell two-thirds of the Pb atoms occupy sites with a single  $Mg^{2+}$ –O– $Mg^{2+}$  triplet (figure 7(a)). The Pb–O bond to this oxygen is predicted to be only 2.38 Å, whereas bonds to oxygens in the other triplets are: 2.62 Å for  $Mg^{2+}$ –O– $Nb^{5+}$ , and 2.86, 3.09 and 3.36 Å for the  $Nb^{5+}$ –O– $Nb^{5+}$  triplets. The remaining one-third of Pb's in the  $[110]_{1:2}$  structure have two mirror-plane related  $Mg^{2+}$ –O– $Mg^{2+}$  triplets (figure 7(b)), which frustrate the formation of short Pb–O bonds, and leaves all the Pb–O distances about the same: 2.83 Å for  $Mg^{2+}$ –O– $Mg^{2+}$ ; 2.85 Å for  $Mg^{2+}$ –O– $Nb^{5+}$ ; 2.79 Å for  $Nb^{5+}$ –O– $Nb^{5+}$ . In the  $[110]_{1:1}$

structure all Pb's occupy sites with two mirror-related  $B^{3+}$ –O– $B^{3+}$  triplets (figure 7(b)), and  $\Delta E_{[110]_{1:1}} - E_{[111]_{1:1}}$  remains approximately constant when Pb is substituted for Ba (cf figures 1 and 2). Thus, Pb–O relaxation/stabilization effects are clearly present in the [001]₂₁, [110]₂₁ and [001]₁₁ structures, but absent from the [110]₁₁ structure, which has underbonded oxygens, for reasons of symmetry.

Qualitatively, the BV ionic model [29] captures the essence of cation ordering in the Ba systems, in which Coulomb interactions dominate, but it fails for the Pb systems because it ignores short-range interactions. BV suggested that the covalency of the short Pb–O bonds might provide a mechanism for stabilizing 1:1 order in place of 1:2, but no specific mechanism was described. Furthermore, they preferred the proposal that Pb<sup>4+</sup> on  $B$  sites might be responsible for ‘the weak 1:1 order in PMN and PMT’. Octahedral Pb<sup>4+</sup> is a possible contributing factor in real samples with excess lead, but it fails to explain why (in the absence of octahedral Pb<sup>4+</sup>) the  $\Delta E$ -ranges for Pb( $B$ ,  $B'$ )O<sub>3</sub> systems are so much smaller than those of the corresponding Ba systems. Evidently, Pb( $B_{1/3}B'_{2/3}$ )O<sub>3</sub> perovskites are more susceptible to  $B$ -site cation disorder than their Ba counterparts because of the near cancellation of long- and short-range contributions to the configurational energy.

#### 4. Conclusions

Comparing the first-principles calculations for Ba( $B$ ,  $B'$ )O<sub>3</sub> perovskites with those for Pb( $B$ ,  $B'$ )O<sub>3</sub> perovskites indicates that the long-range Coulomb interactions which drive  $B$ -site cation ordering in the Ba systems do not dominate in the Pb systems. Hybridization between the Pb 6s and O 2p states on otherwise *underbonded oxygens* in  $B^{2+}$ –O– $B^{2+}$  or  $B^{3+}$ –O– $B^{3+}$  environments leads to a near cancellation of long- and short-range contributions to the configurational energies in the Pb( $B_{1/3}$ ,  $B'_{2/3}$ )O<sub>3</sub> systems. Similar, but only partial cancellations occur in the Pb(Sc<sub>1/2</sub> $B'_{1/2}$ )O<sub>3</sub>, Pb(Mg<sub>1/2</sub>W<sub>1/2</sub>)O<sub>3</sub>, and Pb(Sc<sub>2/3</sub>W<sub>1/3</sub>)O<sub>3</sub> systems. Competition between long-range Coulomb interactions and short-range many-body interactions explains why Pb( $B$ ,  $B'$ )O<sub>3</sub> perovskites disorder at lower temperatures than Ba( $B$ ,  $B'$ )O<sub>3</sub> perovskites.

#### Acknowledgments

The author gratefully acknowledges the assistance of G Kresse with VASP calculations, and E Cockayne for useful discussions and some ionic model calculations.

#### References

- [1] Setter N and Cross L E 1980 *J. Appl. Phys.* **51** 4356
- [2] Cross L E 1987 *Ferroelectrics* **76** 241  
Cross L E 1994 *Ferroelectrics* **151** 305
- [3] Uchino K 1994 *Ferroelectrics* **151** 321
- [4] Akbas M A and Davies P K 1997 *Solid State Chemistry of Inorganic Materials* (Proc. 453) ed P K Davies *et al* p 483
- [5] Kawashima S, Nishida M, Ueda I and Ouchi H 1983 *J. Am. Ceram. Soc.* **66** 421
- [6] Lee C-C, Chou C-C and Tsai D-S 1998 *Ferroelectrics* **206/207** 293
- [7] Randall C A and Bhalla A S 1990 *Japan. J. Appl. Phys.* **29** 327
- [8] Krause H B, Cowley J M and Wheatley J 1979 *Acta Crystallogr. A* **35** 1015
- [9] Chen J, Chan H M and Harmer M 1989 *J. Am. Ceram. Soc.* **72** 593
- [10] Akbas M A and Davies P K 1997 *J. Am. Ceram. Soc.* **80** 2933
- [11] Kania A, Kugel G E, Roleder K and Pawelczyk M 1992 *Ferroelectrics* **125** 489  
Kania A, Roleder K, Kugel G E and Hafid M 1992 *Ferroelectrics* **135** 75

- [12] Yasuda N, Ohwa H, Oohashi J, Nomura K, Terauchi H, Iwata M and Ishibashi Y 1998 *J. Phys. Soc. Japan* **67** 3952
- [13] Kania A and Pawelczyk M 1991 *Ferroelectrics* **124** 261
- [14] Bokov A A, Rayevsky I P, Neprin V V and Smotrakov V G 1991 *Ferroelectrics* **124** 271
- [15] Treiber U and Kemmler-Sack S 1982 *J. Solid State Chem.* **43** 51
- [16] Hong K S, Kim I T and Kim C-D 1996 *J. Am Ceram. Soc.* **79** 3218
- [17] Guo R, Bhalla A S and Cross L E 1994 *J. Appl. Phys.* **75** 4704
- [18] The Columbite route is not successful in eliminating pyrochlore formation in  $\text{Pb}(\text{Zn}_{1/3}\text{Ta}_{2/3})\text{O}_3$ , see Chen J 1991 *PhD Thesis*
- [19] Stenger C G F and Burggraaf A J 1980 *Phys. Status Solidi a* **61** 275
- [20] Giniewicz J R, Bhalla A S and Cross L E 1998 *Ferroelectrics* **211** 281
- [21] Filip'ev V S and Fesenko E G 1966 *Sov. Phys.-Cryst.* **10** 532
- [22] Galasso F S and Darby W 1962 *J. Chem. Phys.* **66** 131  
Galasso F S 1969 *Structure, Properties and Preparation of Perovskite Type Compounds* (Oxford: Pergamon)
- [23] Brixner L 1960 *J. Chem. Phys.* **64** 165
- [24] Jones G G, Randall C A, Jang S J and Shrout T R 1990 *Ferroelectr. Lett.* **12** 55
- [25] Petric M, Suvorov D and Kolar D 1990 *J. Mater. Sci. Lett.* **9** 1117
- [26] Fresia E J, Katz L and Ward R 1959 *J. Am. Chem. Soc.* **81** 4783
- [27] Kresse G and Hafner J 1993 *Phys. Rev. B* **47** 558  
Kresse G 1993 *PhD Thesis* Technische Universität Wien  
Kresse G 1994 *Phys. Rev. B* **49** 14251  
Kresse G and Furthmüller J 1996 *Comput. Mater. Sci.* **6** 15  
Kresse G and Furthmüller J 1996 *Phys. Rev. B* **54** 11169  
<http://iph.tuwien.ac.at/vasp/guide/vasp.html>
- [28] Vanderbilt D 1990 *Phys. Rev. B* **41** 7892
- [29] Bellaiche L and Vanderbilt D 1998 *Phys. Rev. Lett.* **81** 1318
- [30] Burton B P 1999 *J. Phys. Chem. Solids* at press
- [31] Mattheiss L F 1972 *Phys. Rev. B* **6** 4718
- [32] Cohen R E 1992 *Nature* **358** 136
- [33] Cohen R E and Krakauer H 1992 *Ferroelectrics* **136** 65
- [34] Bellaiche L, Padilla J and Vanderbilt D 1999 *Phys. Rev. B* **59** 1834
- [35] Wensell M and Krakauer H 1998 First principles calculations for ferroelectrics *AIP Conf. Proc.* vol 436,  
ed R E Cohen p 165  
Wensell M and Krakauer H 1999 *J. Phys. Chem. Solids* at press

## Prediction of solution enthalpies of substitutional impurities in aluminium

Marcel H F Sluiter and Y Kawazoe

Institute for Materials Research, Tohoku University, Sendai, Japan, 980-8577

Received 16 September 1999, accepted for publication 23 November 1999

**Abstract.** A method for calculating the solution enthalpy of substitutional impurities in crystals is derived. A difficulty that arises in the *ab initio* calculation of the solution enthalpy is that the long-ranged elastic strain contribution cannot be computed within the rather small supercells that are computationally feasible. Here, we suggest combining atomistic *ab initio* methods with continuum elasticity theory to treat the problem of the long-ranged elastic strain. Additionally, it is shown that the solution enthalpy can be very useful for estimating the enthalpy of mixing.

### 1. Introduction

When an impurity is introduced in an otherwise perfect crystal, the surrounding atoms are displaced. Impurity shall refer to atoms of another species as well as the absence of an atom, that is, a vacancy. Far from the impurity, the displacement is both small and a smooth function of distance, so that the strain tensor is well defined. Therefore, at some distance from the impurity a continuum linear elastic description is applicable. In the immediate vicinity of the impurity, however, the displacements are not a smooth function of the distance. For example, in some cases atoms in the nearest neighbour shell move away from the impurity, while atoms in the second nearest neighbour shell move towards the impurity. Thus, near the impurity the displacements are irregular and cannot be described with a continuum theory. In an analogy with the dislocation theory, the energy of a single impurity can be considered as the sum of a linear elastic part applicable beyond some minimal distance from the impurity, and a core part that takes account of the irregular displacements as well as the usually short-ranged chemical effects.

The impurity core energy can be computed with local density approximation (LDA) electronic structure calculations by computing the total energies of supercells in which a single impurity has been, or has not been, introduced. However, such calculations are limited to a rather small number of atoms, whereas the elastic strain is not confined to such a small cell. Combining an atomic scale LDA electronic structure method with a continuum treatment using linear elasticity appears to be ideally suited to compute the energetics of impurities. Thus, the infinite crystal around the impurity is divided into two parts: a small cell around the impurity in which the relaxations are treated atomistically (atomistic region), and the rest of the crystal where the relaxations are treated with continuum elasticity (continuum region).

Here, we apply the method to the computation of the solution enthalpy of substitutional Mg and Sr impurities in Al, and of Al in Mg. The definition of the vacancy formation enthalpy is formally identical to that of the solution enthalpy, and the vacancy formation enthalpy in Al has

also been computed. Al was selected as the matrix material because of its practical applications and the fact that it is rather isotropic, which greatly simplifies the elasticity calculation. The case of a Mg impurity was chosen because Mg is one of the main alloying elements in Al. Alas, the atomic radius of Mg is only about 10% larger than that of Al, making the strain and relaxation effects rather small. Therefore, an element chemically similar to Mg, but with a much larger atomic size difference with Al was chosen. Sr has an atomic radius that is about 50% larger than that of Al, making for very significant relaxation and strain effects.

Knowledge of the solution enthalpy can be of use for estimating the enthalpy of mixing. The difference between the formation enthalpy of some ordered compound and the mixing enthalpy gives the ordering enthalpy. As the ordering enthalpy is roughly proportional to the order-disorder temperature, it follows that the enthalpy of mixing can be used to get an idea about the phase diagram of alloys. Below, the relationship between the various energetic properties will be derived.

## 2. Theory

### 2.1. Definition of solution energy

The solution energy  $\Delta E_{X(A)}$  of a substitutional atom  $X$  in a matrix of  $A$  atoms is the change in the energy produced by replacing a single  $A$  atom in an infinite crystal by an  $X$  atom and relaxing all atoms  $i$  to their new equilibrium positions  $R_i^0$

$$\Delta E_{X(A)} = \lim_{n \rightarrow \infty} [E_{A_n X}(R_i = R_i^0) - nE_A(a = a_A) - E_X(a = a_X)] \quad (1)$$

where  $a$  is the lattice parameter. It should be noted that the structure of pure  $A$  and pure  $X$  can differ, which means that a structural energy difference for the  $X$  phase may need to be considered. As all constituents are at their equilibrium lattice parameters, the pressure (or, more precisely the stress tensor) vanishes so that energies and enthalpies take the same numerical values. The definition indicates that there are two parts to  $\Delta E_{X(A)}$ , namely a chemical part  $\Delta E_{X(A)}^{\text{chem}}$ , caused by the change of the type of interatomic bonds, and a relaxation part  $\Delta E_{X(A)}^{\text{rlx}}$ , due to the repositioning of all atoms around the dissolved atom.

$\Delta E_{X(A)}^{\text{chem}}$  can be computed by subtracting the energies  $E$  of the pure elements  $A$  and  $X$  at their respective equilibrium lattice parameters from the energy of a large cell with  $A$  atoms and a single  $X$  atom where all atoms have positions corresponding to the pure  $A$  species:

$$\Delta E_{X(A)}^{\text{chem}} = \lim_{n \rightarrow \infty} [E_{A_n X}(a = a_A, R_i = R_i^A) - nE_A(a = a_A) - E_X(a = a_X)] \quad (2)$$

where  $R_i^A$  indicates the equilibrium positions in the pure  $A$  crystal, prior to the introduction of the impurity  $X$ . Chemical interactions in solids, especially in metals where strong electronic screening effects occur, have been shown to be relatively short-ranged. Typically, only the first few neighbour shells contribute to the chemical energy [1]. The relaxation part of the solution energy, given by

$$\Delta E_{X(A)}^{\text{rlx}} = \lim_{n \rightarrow \infty} E_{A_n X}(a = a_A, R_i = R_i^0) - E_{A_n X}(a = a_A, R_i = R_i^A) \quad (3)$$

is generally harder to compute because relaxations of atomic positions decay slowly with distance. In the first few neighbour shells around the defect the relaxation is irregular, but at greater distances the magnitudes of the relaxations become very regular and decay as the reciprocal of the distance squared [2]. Therefore, it is intuitive to divide  $\Delta E_{X(A)}^{\text{rlx}}$  into a part that is due to the irregular relaxation in the immediate vicinity of the defect, the ‘core’,  $\Delta E_{X(A)}^{\text{rlx-core}}$

and a part that is due to the long-ranged but regularly decaying relaxation elsewhere in the crystal  $\Delta E_{X(A)}^{\text{rlx-tail}}$

$$\Delta E_{X(A)}^{\text{rlx}} = \Delta E_{X(A)}^{\text{rlx-core}} + \Delta E_{X(A)}^{\text{rlx-tail}}. \quad (4)$$

For the purpose of practical calculations, it is convenient to compute  $\Delta E_{X(A)}^{\text{chem}}$  and  $\Delta E_{X(A)}^{\text{rlx-core}}$  together within some atomistic calculation, and to calculate  $\Delta E_{X(A)}^{\text{rlx-tail}}$  by means of linear elasticity in a continuum approximation,

$$\Delta E_{X(A)} = \Delta E_{X(A)}^{\text{core}} + \Delta E_{X(A)}^{\text{rlx-tail}} \quad (5)$$

where  $\Delta E_{X(A)}^{\text{core}} = \Delta E_{X(A)}^{\text{chem}} + \Delta E_{X(A)}^{\text{rlx-core}}$ . The solution enthalpy  $\Delta H_{X(A)}$  at zero pressure is obtained by minimizing  $\Delta E_{X(A)}$  with respect to volume or lattice parameter. It should be noted that the energies in an atomistic calculation have certain systematic and non-systematic errors. The accuracy of energy differences, such as the solution energy, is greatest when systematic errors are made to cancel, which is best achieved by computing all of the energies in the same cell, with the same Brillouin zone and the same  $k$ -points. The non-systematic (random) errors make that the ‘core’, or alternately  $n$ , should not be selected too large. Therefore, it is understood that in actual atomic calculations the limit over  $n$  in equations (1) and (2) should not be taken too literally.

The solution enthalpy can also be extracted from the enthalpy of mixing for solid solutions. In phase diagram assessments the enthalpy of mixing  $\Delta H_{\text{mix}}$  is fitted to a polynomial (Redlich–Kister formula) in the composition [3]

$$\Delta H_{\text{mix}}(x) = x(1-x)[L_{AX}^{(0)} + L_{AX}^{(1)}(1-2x) + L_{AX}^{(2)}(1-2x)^2] \quad (6)$$

where  $L_{AX}^{(n)}$  ( $n = 0, 1, 2$ ) are fitting parameters and  $x$  is the concentration of the solute  $X$ . The solution enthalpy is easily obtained from the mixing enthalpy

$$\Delta H_{X(A)} = \left( \frac{\partial \Delta H_{\text{mix}}}{\partial x} \right)_{x=0} \quad (7)$$

which gives

$$\Delta H_{X(A)} = L_{AX}^{(0)} + L_{AX}^{(1)} + L_{AX}^{(2)} \quad \Delta H_{A(X)} = L_{AX}^{(0)} - L_{AX}^{(1)} - L_{AX}^{(2)}. \quad (8)$$

Conversely, the enthalpy of mixing can be estimated from the solution enthalpies with cubic splines,

$$\Delta H_{\text{mix}}(x) \approx \Delta H_{X(A)}x(1-x)^2 + \Delta H_{A(X)}x^2(1-x). \quad (9)$$

Such an estimate is analogous to a derivation for the packing density of hard sphere mixtures [4].

## 2.2. Atomistic and continuum regions

The infinite crystal is divided into a spherical region around the impurity, the atomistic region, and the remainder of the crystal, the continuum region. The continuum region is characterized by a spherical cavity. The inclusion of a substitutional impurity in the atomistic region causes this spherical region to change volume. When the material is isotropic, as we shall assume here, the atomistic region will retain a spherical shape. The volume change of the atomistic region causes the cavity in the continuum region to change volume. Therefore, the volume change of the atomistic region is resisted by the continuum region. The equilibrium radius of the atomistic region after the impurity has been introduced can be computed by minimizing the sum of the energies of the atomistic region and the continuum region.

The energy associated with the volume change of the cavity in the continuum region can be computed analytically [2]. The elastic energy stored in the continuum region is a function of the elastic tensor, the strain at the ‘cavity wall’  $S$  and the size and shape of the ‘cavity’. There is spherical symmetry around the centre of the cavity, so that the usual spherical coordinates  $r, \phi$  and  $\theta$  are selected. The displacement vector  $u$  is radial, and a function of the radial coordinate  $r$  only, and following Landau and Lifshitz [5] its norm takes the form

$$u(r) = \alpha r + \beta r^{-2} \quad (10)$$

where  $\alpha$  and  $\beta$  are constants that are determined by boundary conditions. At an infinite distance from the impurity the displacement should vanish so that  $\alpha = 0$ . The constant  $\beta$  has a simple physical interpretation [2]: it is proportional to the volume change that the defect induces in the infinite matrix,  $\Delta V = 4\pi\beta$ .  $\beta$  is determined by the displacement at the cavity wall:

$$u(R) = \beta R^{-2} \quad (11)$$

where  $R$  is the radius of the cavity. The difference between the original (equilibrium) cavity radius  $R_0$  and the actual radius  $R$  gives the displacement at the cavity surface  $u(R) = R - R_0$ , so that  $\beta = R^2(R - R_0)$ . As the off-diagonal stress  $\sigma$  and strain  $\epsilon$  vanish, the elastic energy density is given by

$$\epsilon(r) = \sigma_{rr}\epsilon_{rr} + \sigma_{\phi\phi}\epsilon_{\phi\phi} + \sigma_{\theta\theta}\epsilon_{\theta\theta} \quad (12)$$

with

$$\begin{aligned} \epsilon_{rr} &= \frac{\partial u}{\partial r} & \epsilon_{\phi\phi} = \epsilon_{\theta\theta} &= \frac{u}{r} & \sigma_{rr} &= 2\lambda\frac{u}{r} + (\lambda + 2\mu)\frac{\partial u}{\partial r} \\ \sigma_{\phi\phi} = \sigma_{\theta\theta} &= 2(\lambda + \mu)\frac{u}{r} + \lambda\frac{\partial u}{\partial r} & & & & \end{aligned} \quad (13)$$

where  $\lambda$  and  $\mu$  are the usual Lamé coefficients. The elastic energy of the continuum  $\Delta E_{X(A)}^{\text{rlx-tail}}$  is obtained by integration of

$$\Delta E_{X(A)}^{\text{rlx-tail}} = \int_R^\infty dr 4\pi r^2 \epsilon(r) \quad (14)$$

which gives

$$\Delta E_{X(A)}^{\text{rlx-tail}} = 16\pi\mu R(R - R_0)^2. \quad (15)$$

Computing the energy of the spherical atomistic region requires some approximations. Embedding is required to avoid surface effects. The simplest embedding is to embed the region with itself, that is, to make a periodic arrangement of atomistic regions. Alas, spheres do not ‘tile’ three-dimensional space. However, certain approximately spherical polyhedrons, such as dodecahedrons, do tessellate in three-dimensional space. Thus, by selecting, say, a face centered cubic (fcc) arrangement of impurity atoms within the matrix (see figure 1), one obtains dodecahedral Wigner–Seitz cells that are close to a spherical shape. Moreover, the energy of such dodecahedral cells is easily computed as a function of their volume. In the terminology of Eshelby [2], we can note that impurities exert image forces on each other. However, the image forces can change the volume only to a limited extent because the matrix resists.

Using standard electronic structure methods, the total energy of such spheroid cells is computed as a function of the average lattice parameter of the underlying lattice. In other words for a cell with a fixed number of atoms, the total energy is computed as a function of the radius of the cell. The radius of the cell is defined by matching the cell volume  $\Omega$  with a corresponding sphere volume:

$$R = \left( \frac{3\Omega}{4\pi} \right)^{1/3}. \quad (16)$$

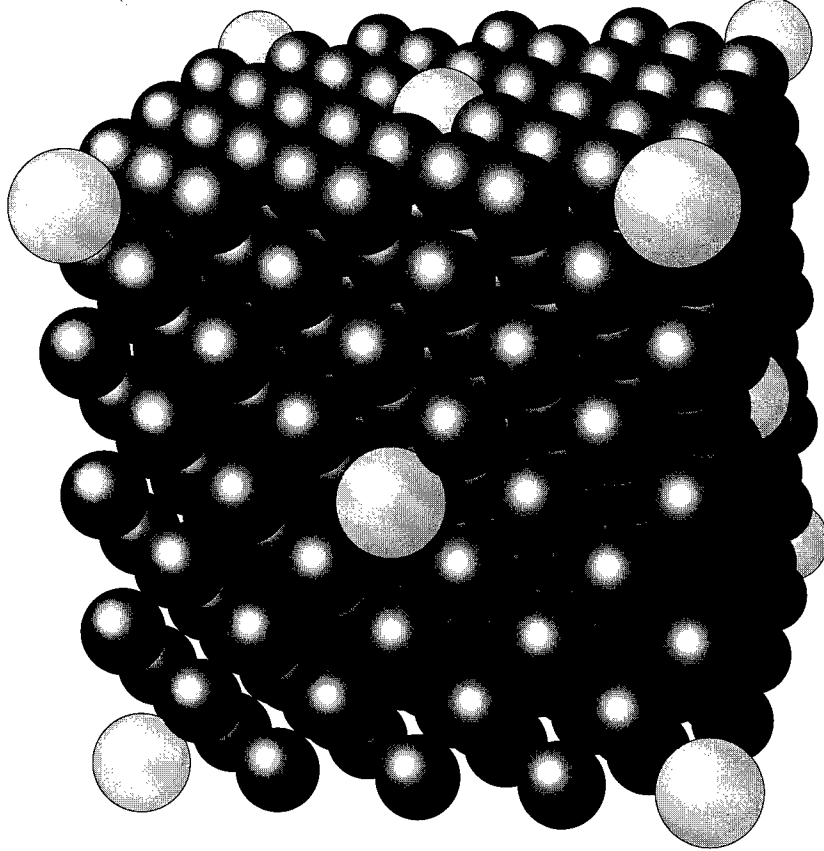


**Figure 1.** The fcc arrangement of impurity atoms (light) in an Al matrix (dark).

$R$  and the average fcc lattice constant  $\bar{a}$  in the core region are related through  $\Omega = (n/4)\bar{a}^3$ , where  $n$  is the number of atoms in the core region. Typically,  $\Delta E_{X(A)}^{\text{core}}(R)$  resembles a parabola centred around the relaxed equilibrium radius  $R_x$ ,

$$\Delta E_{X(A)}^{\text{core}}(R) \approx \Delta E_{X(A)}^{\text{core}}(R_x) + \frac{9}{2}BR_x(R - R_x)^2 \quad (17)$$

where  $B$  is the bulk modulus of the material in the core region. As mentioned above, generally,  $R_x$  will differ from the equilibrium radius of a cell without an impurity  $R_0$ .

The solution energy  $\Delta E_{X(A)}$  is found by inserting equation (15) into equation (5), and minimizing with respect to  $R$ ,

$$\Delta E_{X(A)} = \min_R [\Delta E_{X(A)}^{\text{core}}(R) + 16\pi\mu R(R - R_0)^2]. \quad (18)$$

The solution enthalpy  $\Delta H_{X(A)}$  at zero hydrostatic pressure is obtained by minimizing  $\Delta E_{X(A)}$  with respect to the lattice parameter.

### 2.3. Details of the methodology

The atomistic calculations for  $\Delta E_{X(A)}^{\text{core}}$  were performed with an *ab initio* electronic total energy method based on density functional theory in the LDA using ultra-soft pseudo potentials as implemented in the VASP software [6]. The cut-off energies for the pseudo potentials of Al,

Mg and Sr were 129, 106 and 86 eV. The Ceperly–Alder exchange-correlation function, as parameterized by Perdew and Zunger [7], was used. To achieve a nearly spherical region around each impurity, the impurities were arranged according to an fcc structure with [2 2 0] translation vectors, where  $[\frac{1}{2} \frac{1}{2} 0]$  are the translation vectors of the underlying fcc Al matrix. This geometry made for an atomistic region of 64 atoms, including the first to sixth and eighth neighbour shells around the central site. However, shells that lie on the cell boundary have displacement vectors that are restricted by symmetry considerations. The fourth to sixth and eighth neighbour shells are located at the cell boundary and therefore cannot relax away from fcc lattice positions. These shells can have non-zero displacements only as a result of changes of the average lattice parameter. The seventh neighbour does not occur in the 64 atom cell. The total energies of the pure elements, and for the Al<sub>63</sub>Mg and Al<sub>63</sub>Sr structures, with and without relaxations, were computed using this geometry. Reciprocal space integrations were carried out with 28 Monkhorst–Pack [8] special  $k$ -points in the irreducible wedge. Forces for relaxing the atomic positions were calculated using the Methfessel–Paxton method [9] for accounting for partial occupancies of electronic states.

In order to compute  $\Delta E_{X(A)}^{\text{rlx-tail}}$ , the Lamé elastic constant  $\mu$  for the Al matrix is needed. It was extracted from the theoretical elastic constants [10] at an fcc Al lattice parameter  $a_0 = 0.399$  nm:  $C_{11} = 121$  GPa,  $C_{12} = 63$  GPa,  $C_{44} = 33$  GPa. As the anisotropy ratio  $A = 2C_{44}/(C_{11} - C_{12})$  for Al is not precisely equal to unity, an average value of  $\mu$  has been defined as follows:

$$\mu = \frac{1}{2}(\mu_1 + \mu_2) \quad \mu_1 = C_{44} \quad \mu_2 = \frac{1}{2}(C_{11} - C_{12}). \quad (19)$$

The numerical values for  $\mu_1$  and  $\mu_2$  are close (33 and 29 GPa, respectively). In the continuum calculations  $\mu = 31$  GPa has been used.

### 3. Results and discussion

The properties computed for the pure elements (see table 1) are in good agreement with those reported in the literature and those obtained with all-electron methods. The lattice parameter and bulk modulus of Al agree completely with those obtained by FLAPW calculations [10]. For fcc Mg (Sr) good agreement is found with LMTO-ASA† calculations. This indicates that the ‘pseudization’ of the potential does not give significant errors other than those introduced by the LDA itself. A comparison of the fcc lattice parameters shows that Mg (Sr) is about 11% (46%) larger than the Al matrix. Both Mg and Sr are considerably ‘softer’ than Al. As was observed already by Hume Rothery and Raynor [11], one should not expect elements with a lattice mismatch beyond 15% to be very soluble. Therefore, these calculations suggest that Sr cannot dissolve in Al in appreciable amounts, which is borne out by the actual phase diagram [12].

Next, properties of the core-regions were computed, and some salient results are listed in table 2. The geometry of the 64 atom core region has been described above. For the accurate determination of the core contribution to the solution energy the pure elements were also computed in a 64 atom cell, and identical  $k$ -point grids were used. When all atoms are kept at the original fcc lattice positions (no relaxation) and when the original pure Al lattice parameter is maintained after introducing the impurity atom, naturally the energy cost is very high, as the high value of the core chemical solution energy indicates. Of course, Sr being still

† For the LMTO-ASA calculations spdf-like orbitals were included, 145  $k$ -points in the irreducible Brillouin zone were used for the tetrahedron-method reciprocal space integrations, and the so-called combined corrections were included.

**Table 1.** The computed equilibrium lattice parameter  $a$  and bulk modulus  $B$  of the pure elements as computed with VASP and all-electron methods.

Element	Method	$a$ (nm)	$B$ (GPa)	Reference
Al	VASP	0.398 11	82	This work
	LMTO-ASA	0.3979	86	This work
	FLAPW	0.399	82	[10]
Mg	VASP	0.443 32	42	This work
	LMTO-ASA	0.4420	41	This work
Sr	VASP	0.579 71	16	This work
	LMTO-ASA	0.5755	15	This work

**Table 2.** The results of the atomistic calculation of the 64 atom core region. ‘Vac’ refers to a vacancy,  $\bar{a}$  is the averaged fcc lattice parameter in the core region,  $B$  is the bulk modulus,  $E_{\text{tot}}$  is the total energy,  $\Delta E$  is the chemical or core solution energy with reference to fcc pure elements, without considering the effect of the tail relaxation energy  $\Delta E_{X(A)}^{\text{fix-tail}}$ .

Composition	Relaxed	$\bar{a}$ (nm)	$B$ (GPa)	$E_{\text{tot}}$ (eV)	$\Delta E$ (meV)
Al <sub>64</sub>	—	0.398 11	82	-267.149 09	—
Mg <sub>64</sub>	—	0.443 32	42	-112.615 80	—
Sr <sub>64</sub>	—	0.579 71	16	-122.152 52	—
Al <sub>63</sub> Mg	No	0.398 11	—	-264.659 80	$\Delta E_{\text{Mg(Al)}}^{\text{chem}} = 74.7$
Al <sub>63</sub> Mg	No	0.398 65	79	-264.664 91	$\Delta E_{\text{Mg(Al)}}^{\text{core}}(R_{\min}) = 69.6$
Al <sub>63</sub> Mg	Yes	0.398 68	80	-264.692 20	$\Delta E_{\text{Mg(Al)}}^{\text{core}}(R_x) = 42.3$
Al <sub>63</sub> Sr	No	0.398 11	—	-263.100 98	$\Delta E_{\text{Sr(Al)}}^{\text{chem}} = 1782.5$
Al <sub>63</sub> Sr	No	0.401 20	70	-263.237 31	$\Delta E_{\text{Sr(Al)}}^{\text{core}}(R_{\min}) = 1646.2$
Al <sub>63</sub> Sr	Yes	0.401 38	76	-263.901 96	$\Delta E_{\text{Sr(Al)}}^{\text{core}}(R_x) = 981.6$
Al <sub>63</sub> Vac	No	0.398 11	—	-262.254 33	$\Delta E_{\text{Vac(Al)}}^{\text{chem}} = 720.6$
Al <sub>63</sub> Vac	No	0.397 64	85	-262.257 86	$\Delta E_{\text{Vac(Al)}}^{\text{core}}(R_{\min}) = 717.0$
Al <sub>63</sub> Vac	Yes	0.397 52	86	-262.331 55	$\Delta E_{\text{Vac(Al)}}^{\text{core}}(R_x) = 643.3$

considerably larger than Mg, the Sr core chemical solution energy is much larger than that of Mg.

Next, when the atoms are kept at fcc lattice positions but the whole core region is allowed to expand from a radius  $R_0$  to a radius  $R_{\min}$  so as to accommodate the large impurity atom, the core solution energy drops a little. Percentage wise, the decrease is the same for Mg and Sr, about 7%. If one were to approximate the volume of the 64 atom core region by adding the atomic volumes of the pure elements, one would over-estimate the actual expansion by as much as 50%. The expansion is only about two-thirds of that expected on the basis of the pure element atomic volumes. Clearly, the rather ‘soft’ Mg and Sr atoms are getting squeezed in the Al matrix. In the case of a vacancy, only a slight contraction of the lattice results, in agreement with previous calculations [13]. This is due to the fact that the nearest neighbours surrounding the vacancy can move inward only a little before their mutual repulsion becomes too large. However, the small reduction in the lattice parameter causes an appreciable increase in the bulk modulus.

When the lattice parameter and atomic positions are fully relaxed, the core solution energy is considerably reduced, to about 55% of  $\Delta E_{X(A)}^{\text{chem}}$ . However, as the core radii  $R_{\min}$  and  $R_x$  are very close, the complete relaxation of the atomic positions changes the average lattice constant

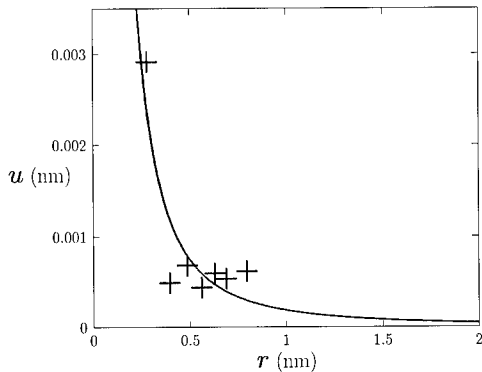
**Table 3.** Displacement vector  $\vec{u}$  in the 64 atom cell surrounding an impurity at the origin in terms of the average fcc lattice parameter. The average fcc lattice parameter is 0.4 nm. A displacement vector of  $\langle 000 \rangle$  means that a site moves in a homogeneous fashion as a function of the average lattice constant (or  $R$ ) only.

Shell	$\langle hkl \rangle$	$\vec{u}_{\text{Mg}} \times 10^5$	$\vec{u}_{\text{Sr}} \times 10^5$	$\vec{u}_{\text{Vac}} \times 10^5$
1	$\langle \frac{1}{2} \frac{1}{2} 0 \rangle$	$\langle 478 478 0 \rangle$	$\langle 2351 2351 0 \rangle$	$\langle -826 -826 0 \rangle$
2	$\langle 1 0 0 \rangle$	$\langle 45 0 0 \rangle$	$\langle -342 0 0 \rangle$	$\langle -108 0 0 \rangle$
3	$\langle 1 \frac{1}{2} \frac{1}{2} \rangle$	$\langle 73 20 20 \rangle$	$\langle 616 228 228 \rangle$	$\langle -35 -32 -32 \rangle$
4	$\langle 1 1 0 \rangle$	$\langle 0 0 0 \rangle$	$\langle 0 0 0 \rangle$	$\langle 0 0 0 \rangle$
5	$\langle \frac{3}{2} \frac{1}{2} 0 \rangle$	$\langle 42 -42 0 \rangle$	$\langle 188 -188 0 \rangle$	$\langle -10 10 0 \rangle$
6	$\langle 1 1 1 \rangle$	$\langle 0 0 0 \rangle$	$\langle 0 0 0 \rangle$	$\langle 0 0 0 \rangle$
7	$\langle \frac{3}{2} 1 \frac{1}{2} \rangle$	—	—	—
8	$\langle 2 0 0 \rangle$	$\langle 0 0 0 \rangle$	$\langle 0 0 0 \rangle$	$\langle 0 0 0 \rangle$

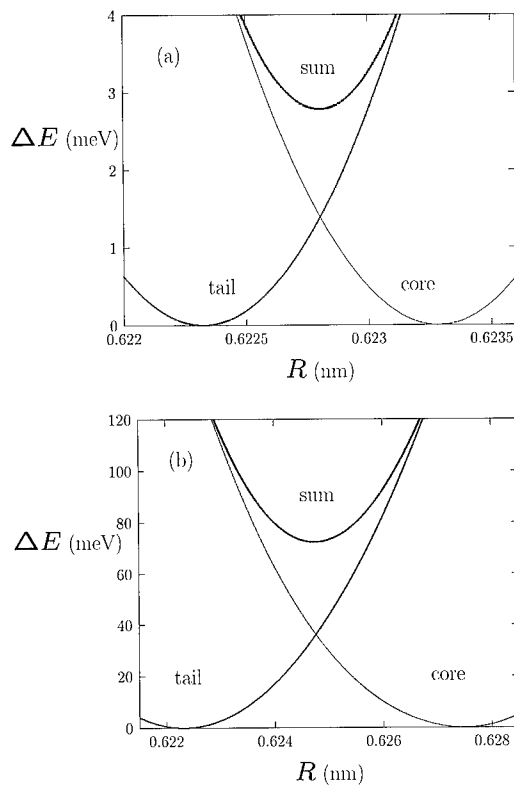
very little. Hence, the minimization with respect to the lattice parameter only, but with fixed fcc atomic positions, gives almost the correct lattice parameter, but misses a large part of the reduction of the solution energy, while the relaxation of the individual atoms does not change the average lattice parameter very much, but drastically reduces the solution energy. Clearly, individual atomic relaxations around an impurity are very important for computing solution energies. It is somewhat surprising that the relative change of the solution energy and of the average lattice parameter should be the same for Mg and Sr, especially considering that their bulk moduli differ considerably. For the vacancy, the effect of full relaxation is relatively minor. This is caused by the afore-mentioned limitation for inward movement of atoms in the nearest neighbour shell. The relaxation of the first and more distant neighbours is very small, as is also evident from table 3.

Table 3 shows the computed relaxations of Al atoms around a Mg and a Sr impurity and around a vacancy. The fourth to sixth and eighth neighbours can have non-zero displacements only as a result of changes of the average lattice parameter. As expected from the large size of the Sr atom, the relaxations around a Sr atom are much larger than those around a Mg atom. The relaxations around a Sr atom are not completely similar to that around a Mg atom. For example, in the second neighbour shell the relaxations have opposing signs. This is due to the fact that Sr is so large that the Al atoms in its nearest neighbour shell are widely separated from each other. This leaves gaps towards which the second neighbour Al atoms are drawn.

The Al atoms rather quickly approach the fcc lattice positions both around Mg and Sr. In the fifth shell, the largest distance that can freely relax in the 64 atom core region, the relaxation is one order of magnitude smaller than in the nearest neighbour shell for Mg and Sr, and is two orders of magnitude smaller for the vacancy. In figure 2 the relaxations as computed in the core region, and as given by the continuum approximation (equation (10)) are shown. The seven neighbour shells that are present in the 64 atom core region have been marked with plus signs. The relaxations in the core region at greater distances, in particular for the sixth and eighth nearest neighbour shells, show an upward trend, contrary to what would be expected from equation (10). The explanation for this is that those outer shells do not relax away from fcc lattice positions (see table 3). Thus, these shells move purely because the average lattice constant in the core region has been expanded by the impurity. Therefore, the more distant shells move strictly proportional to the expansion of the lattice, so that the eighth shell is found to move more than the sixth shell. This is an artefact of the geometrical constraints. However, the relaxation at as close a distance as the nearest neighbour shell is surprisingly well described by the continuum approximation.



**Figure 2.** Displacement  $u$  as a function of the distance to a Mg impurity  $r$ . The plus signs indicate the displacements as computed in the core region for the first to sixth and eighth neighbour shells, and the full curve is the relaxation according to equation (11). The radius of the core region  $R$  is 0.6228 nm.



**Figure 3.** Contributions to the solution energy of a single isolated substitutional impurity atom in an fcc Al matrix, (a) a Mg impurity and (b) a Sr impurity. The curve labelled ‘tail’ corresponds to  $\Delta E_{X(A)}^{\text{rlx-tail}}$ , the curve labelled ‘core’ represents  $\Delta E_{X(A)}^{\text{core}}(R) - \Delta E_{X(A)}^{\text{core}}(R_x)$ , and ‘sum’ is the sum of the ‘tail’ and ‘core’.  $R$  is the radius of the core region. Note, that the minimum of ‘tail’ occurs at  $R = R_0$  and the minimum of ‘core’ occurs at  $R = R_x$ .

The solution enthalpy has been determined with equation (18). The contributions of the core region and of the rest of the crystal are visualized in figure 3. The figure illustrates the

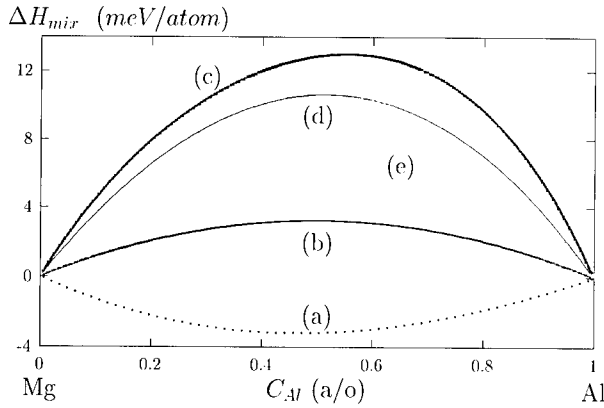


**Figure 4.** The enthalpy of mixing in fcc Al–Mg: as determined from phase diagram assessments (a) [16], (b) [15] and (c) [3]; (d) as estimated with equation (9) from computed solution enthalpies; and (e) as obtained from a cluster expansion using tetrahedron-octahedron clusters [18].

effect of the elastic tail. For the Mg and Sr impurities, the core region has its lowest energy ( $\Delta E_{X(A)}^{\text{core}}(R_x)$ ) at a core radius  $R_x$  that is larger than a pure Al core region would have ( $R_0$ ), so that the region outside the core is compressed, causing a high elastic tail energy. By slightly compressing the core region and diminishing the compression of the region outside the core the sum of the core and tail contributions can be minimized. For Mg (Sr) this occurs at a core radius of 0.6228 nm (0.6247 nm). This means that the atomic volume of a Mg (Sr) impurity in Al is just 15% (73%) larger than that of Al. This is to be compared with the atomic volume of pure fcc Mg (Sr) which is 38% (209%) larger. In the case of the vacancy, the contraction of the core is similarly diminished by the effect of the elastic tail. The vacancy reduces the volume by 0.0023 nm<sup>3</sup>, about 15% of the Al atomic volume, which is between the two existing experimental measurements of –5% and –38% [14].

The minimum of the curve labelled ‘sum’ indicates how much the solution energy is increased over the value of  $\Delta E_{X(A)}^{\text{core}}(R_x)$  by the effect of the elastic tail. As is to be expected on the basis of the atomic sizes, the elastic tail increases the solution energy of Sr more than that of Mg (72.4 meV versus 2.8 meV). These increases of the solution energy are both about 4% of the chemical solution energy ( $\Delta E_{X(A)}^{\text{chem}}$ ). Finally, the solution enthalpies for Mg and Sr are obtained by adding  $\Delta E_{X(A)}^{\text{core}}(R_x)$  to the minimum of the curve labelled ‘sum’ in figure 3. Thus, solution enthalpies of 45.1 meV (1054 meV) are calculated for Mg (Sr). The vacancy formation enthalpy is increased 2.7 meV by the elastic tail, giving a value of 646 meV.

Figure 3 also illustrates that the lower and upper bounds for the solution enthalpy can easily be obtained from a core-region atomistic calculation. The core solution energy computed in a relaxed cell at radius  $R_x$  clearly always provides a lower bound, whereas the core solution energy computed in a relaxed cell at radius  $R_0$  (corresponding to an average lattice parameter equal to that of the host material) provides an upper bound for  $\Delta H_{X(A)}$ .

The solution enthalpy  $\Delta H_{X(A)}$  as computed by equation (18) is about 60% of the solution energy  $\Delta E_{X(A)}^{\text{chem}}$ , where all atoms are kept at their original positions (no relaxations of any kind). As this ratio is the same for two impurities with very different atomic sizes and quite different elastic constants, it would be of some interest to see if a similar ratio exists for other impurities because  $\Delta E_{X(A)}^{\text{chem}}$  is much easier to compute than  $\Delta H_{X(A)}$ .

In the case of Mg it is possible to compare the computed solution enthalpy values based on experimental data. Phase diagrams assessments for the Al–Mg system [3, 15, 16] have given various values for the coefficients  $L_{AX}^{(n)}$  of equation (6) from which the solution enthalpies can

**Table 4.** Redlich–Kister coefficients for fcc Al–Mg alloys from various phase diagram assessments, and the solution enthalpies extracted from these coefficients according to equation (8), compared with *ab initio* solution enthalpies (the units are meV).

$L_{AX}^{(0)}$	$L_{AX}^{(1)}$	$L_{AX}^{(2)}$	$\Delta H_{\text{Al(Mg)}}$	$\Delta H_{\text{Mg(Al)}}$	Reference
13.0	0	0	13.0	13.0	[15]
-12.75	-1.86	0	-14.61	-10.89	[16]
51.5	9.3	9.8	70.6	32.4	[3]
—	—	—	45.1	40.8	This work

be computed with equation (8), see table 4. For completeness, we also computed the solution enthalpy of Al in fcc Mg. Clearly, the phase diagram assessments give contradictory results which do not compare well with each other. This indicates that the phase diagram assessment is a rather unreliable method to extract solution enthalpies. Nevertheless, our calculations suggest that the positive sign of  $L_{AX}^{(0)}$  found in [3, 15] is more reasonable than the negative signs of  $L_{AX}^{(0)}$  and  $L_{AX}^{(1)}$  found in [16]. Enthalpies of mixing can be estimated from the solution enthalpies with equation (9). Such an estimate compares rather well with that computed from a cluster expansion approach [17, 18] as is shown in figure 4.

The vacancy formation enthalpy in Al has been measured extensively with values ranging from 600 to 770 meV [14]. The most accurate experimental value is believed to be about 670 meV. A previous calculation [13] in which the elastic tail was ignored (which is insignificant) gave 660 meV. These values are in excellent agreement with the present result of 646 meV.

#### 4. Conclusion

A hybrid atomistic–continuum method has been presented to treat the elastic relaxation associated with impurities. It is shown that the long-ranged elastic tail associated with an impurity contributes to the solution enthalpy. In the particular case of an isolated substitutional Mg (Sr) impurity in an Al matrix, accounting for the long-ranged elastic tail changed the solution enthalpy by 2.8 meV (72.4 meV). The solution enthalpy of Mg (Sr) in fcc Al was found to be 45.1 meV (1054 meV). The solution enthalpy of Sr is so large that no significant solubility in Al can be expected, as is readily apparent from the phase diagram [12]. Only in the case of Mg was a comparison of the solution enthalpy with data from phase diagram assessments possible. Three such assessments existed, which contradicted each other on the sign of the mixing enthalpy and solution enthalpy. The present theoretical calculations of the solution enthalpy suggested that the assessments of [3, 15] appear more reasonable than that of [16].

In the case of a vacancy in Al, the effect of the elastic tail was found to be negligible, which could be explained on the basis of the very limited ability of the nearest neighbour atoms around a vacancy to relax inward. The vacancy formation enthalpy of 646 meV was in good agreement with other calculations and measurements. The volume change associated with vacancies was computed and was in the range of the experimental measurements. Our zero-temperature calculations show that vacancies slightly increase the bulk modulus. This surprising effect, which has a very limited extent due to the typically low concentration of vacancies, is associated with the decrease of the lattice parameter.

Solution enthalpies were shown to give a reasonable approximation to the mixing enthalpy. Additionally, it was shown that calculations for a relaxed core region can provide upper and lower bounds for the solution enthalpy.

## References

- [1] Sluiter M, Turchi P E A, Pinski F J and Stocks G M 1992 *J. Mater. Sci. Eng. A* **152** 1  
Sluiter M and Kawazoe Y 1995 *Phys. Rev. B* **51** 4062
- [2] Eshelby J D 1956 *Solid State Physics* vol 3, ed F Seitz and D Turnbull (New York: Academic) p 79
- [3] Ansara I 1994 *Thermochemical Database for Light Metal Alloys* (Luxembourg: European Commission) p 34
- [4] de Fontaine D 1986 private communication and lecture notes on Thermodynamics 201, Department of Materials Science and Engineering, University of California, Berkeley
- [5] Landau L D and Lifshitz E M 1970 *Theory of Elasticity, Course of Theoretical Physics* vol 7, 2nd edn (New York: Pergamon) ch 7, problem 2
- [6] Kresse G and Furthmüller J 1996 *Comput. Mat. Sci.* **6** 15  
Kresse G and Furthmüller J 1996 <http://tph.tuwien.ac.at/vasp/>
- [7] Perdew J P and Zunger A 1981 *Phys. Rev. B* **23** 5048
- [8] Monkhorst H J and Pack J D 1976 *Phys. Rev. B* **13** 5188
- [9] Methfessel M and Paxton A T 1989 *Phys. Rev. B* **40** 3616
- [10] Mehl M J, Klein B M and Papaconstantopoulos D A 1995 *Intermetallic Compounds, Principles and Practice* vol 1, ed J H Westbrook and R L Fleischer (New York: Wiley) p 195
- [11] Hume Rothery W and Raynor G V 1954 *The Structure of Metals and Alloys* (London: The Institute of Metals)
- [12] Alcock C B and Itkin V P 1989 *Bull. Alloy Phase Diagrams* **10** 624
- [13] Chetty N, Weinert M, Rahman T S and Davenport J W 1995 *Phys. Rev. B* **52** 6313
- [14] Ehrhart P, Jung P, Schulta H and Ullmaier H 1990 *Atomic Defects in Metals (Landolt-Börnstein, Numerical Data and Functional Relationships in Science and Technology New Series vol III 25)* (Berlin: Springer) p 213  
table 1.A1
- [15] Saboungi M L and Hsu C C 1977 *CALPHAD* **1** 237
- [16] Murray J L 1982 *Bull. Alloy Phase Diagrams* **3** 60
- [17] de Fontaine D 1994 *Solid State Physics* vol 47, ed H Ehrenreich and D Turnbull (New York: Academic) p 80
- [18] Sluiter M, Watanabe Y, de Fontaine D and Kawazoe Y 1996 *Phys. Rev. B* **53** 6137

## ***Ab initio* study of transitory metastable phases solidified by drop-tube processing**

C Berne<sup>†</sup>, A Pasturel<sup>‡</sup>, M Sluiter<sup>§</sup> and B Vinet<sup>†</sup>

<sup>†</sup> Commissariat à l'Energie Atomique, CEREM-Département d'Etudes des Matériaux,  
17 Rue des Martyrs, 38054 Grenoble Cedex 09, France

<sup>‡</sup> Laboratoire de Physique et Modélisation des Milieux Condensés, Maison des Magistères,  
BP 166 CNRS, 38042 Grenoble Cedex 09, France

<sup>§</sup> Institute for Materials Research, Tohoku University, Sendai 980-8577, Japan

Received 16 September 1999, accepted for publication 19 December 1999

**Abstract.** The solidification path of highly undercooled refractory metals and their alloys in an ultrahigh vacuum drop tube is shown to involve transitory metastable phases. First-principles calculations of the structural stability in these systems are developed to determine the possibility of obtaining metastable phases. We show that tetrahedrally close-packed (tcp) structures are good candidates to understand the origin of such metastable phases.

### **1. Introduction**

Under conditions of non-equilibrium thermodynamics, the solidification of metallic melts may lead to the formation of metastable crystal structures. The use of melt undercooling methods at moderate cooling rates is one experimental way of realizing a non-equilibrium solidification process. In particular, undercooling experiments on refractory metals and alloys can be performed by using the Grenoble drop-tube facility [1]. Unfortunately, the metastable phases recorded in these experimental studies are so ephemeral that they can hardly be frozen and subsequently analysed. Therefore, first-principles based total-energy calculations appear to be essential to evaluate the possibility of obtaining metastable phases and to get some insight into the physics of the nucleation path.

### **2. First-principles based calculations**

First-principles or *ab initio* methods allow total energy calculations without parameter fitting. The most widely used class of methods is based on the density functional theory (DFT) of Hohenberg and Kohn, in the formulation of Kohn and Sham [2], which reduces to the self-consistent solution of a single-particle Schrödinger equation. Two implementations of the DFT are classically used for studying the structural stability of elemental metals or alloys. First the FPLMTO [2] (full potential linearized muffin tin orbitals) and FLAPW (full potential linearized augmented plane wave) approaches display the advantage of being unified methods in that they can easily treat not only simple metals but also transition metals. Second, in the pseudopotential methods, the norm-conserving concept has played a central role in constructing modern pseudopotentials. The so-called ultra-soft new generation of pseudopotentials [3] allows the treatment of the transition metals by avoiding the expansion of the wavefunctions

in a huge set of plane waves. We have applied both FPLMTO and pseudopotential techniques when discussing the metastability of the transitory phases in pure refractory metals and in the Re–W and Re–Ta systems.

### 3. Pure refractory metals

As a first example, we discuss the transitory phases observed in Re and Ta droplets [2]. Temperature measurements of the solidification of highly undercooled Re and Ta droplets give evidence of two successive phase transformations with a transitory metastable equilibrium. Indeed the reproducibility of the temperature associated with the first recalescence peak is consistent with the melting temperature of a metastable phase. This quantity is the key point of our study because it is the only property that can be either experimentally determined or calculated. Thus, the theoretical strategy is as follows: (a) in the first step, for each metal, we calculate the cohesive properties for a set of candidate structures; (b) then the melting temperatures of these structures are calculated using a straightforward thermodynamic calculation which assumes that the entropy of melting of the metastable (MS) and stable (S) phases are similar:

$$T_m^{\text{MS}} \approx \frac{\Delta E_{\text{MS-S}} + \Delta H_{\text{S-liq}}(T_m^{\text{S}})}{\Delta S_{\text{S-liq}}(T_m^{\text{S}})} \quad (1)$$

where the difference in structural energies  $\Delta E_{\text{MS-S}}$  is derived from *ab initio* calculations; (c) finally, a comparison between measured and calculated melting temperatures allows us to identify the intervening metastable structure among the candidates. To choose the candidate structures, we assumed that the mechanism which favours undercooling-induced metastable phases is based on the idea of a polytetrahedral short-range order in the undercooled melt [4]. Our intuition is that both the undercooling-induced metastable phase and the undercooled melt present a similar short-range order. Since the tetrahedrally close-packed (tcp) structures are those which are built entirely out of tetrahedral packing units, they can be considered as the best candidates for the metastable phases. In contrast, the fcc structure consists of both tetrahedral and octahedral units, while the bcc structure is an intermediate case with the octahedra containing second-neighbour bonds. The tetrahedral packing in tcp phases leads to characteristic polyhedra which are labelled Z12, Z14, Z15 and Z16, where the numbers refer to the coordination number of the atom at the centre of the polyhedron. The simplest example of a tcp structure is the A15 structure, which has eight atoms per unit cell. Two of these are surrounded by Z12 polyhedra, which are icosahedra, and the remaining six by Z14 polyhedra. The three A15, sigma and chi tcp structures all together contain all the characteristic polyhedra of the tetrahedral packing, with percentages of icosahedral sites of 25%, 33% and 41% for A15, sigma and chi, respectively. Specifically, zero-temperature total energies  $E_0(V)$  were calculated for bcc, fcc, hcp, A15, sigma and chi structures and for Ta, W, Re and Os metals. The results are illustrated in figure 1 for both FPLMTO and pseudopotential techniques. The first spectacular result is the relative stability of the tcp phases for a range of electrons from 4.5 to 6.5. More particularly, the A15 structure is found to strongly compete with the bcc structure for Ta and W metals. Using the value of the lattice stability of Ta in the A15 structure,  $\Delta E = 2.8 \text{ mRyd atom}^{-1}$ , equation (1) gives a melting temperature of 2900 K (the enthalpy of melting of the bcc (Ta),  $\Delta H_{\text{S-liq}}(T_m^{\text{S}})$ , being taken as  $32 \text{ kJ mol}^{-1}$  and  $T_m^{\text{S}} = 3275 \text{ K}$  [2]), in unexpected good agreement with the measured temperature of  $2930 \pm 10 \text{ K}$ . The second important result of the present calculations is that all the lines in figure 1 intersect at one particular band filling, namely an electron-to-atom ratio of  $e/a = 6.7$ . As a consequence, the sequence A15–sigma–chi also depends on the band filling. As these three tcp phases display

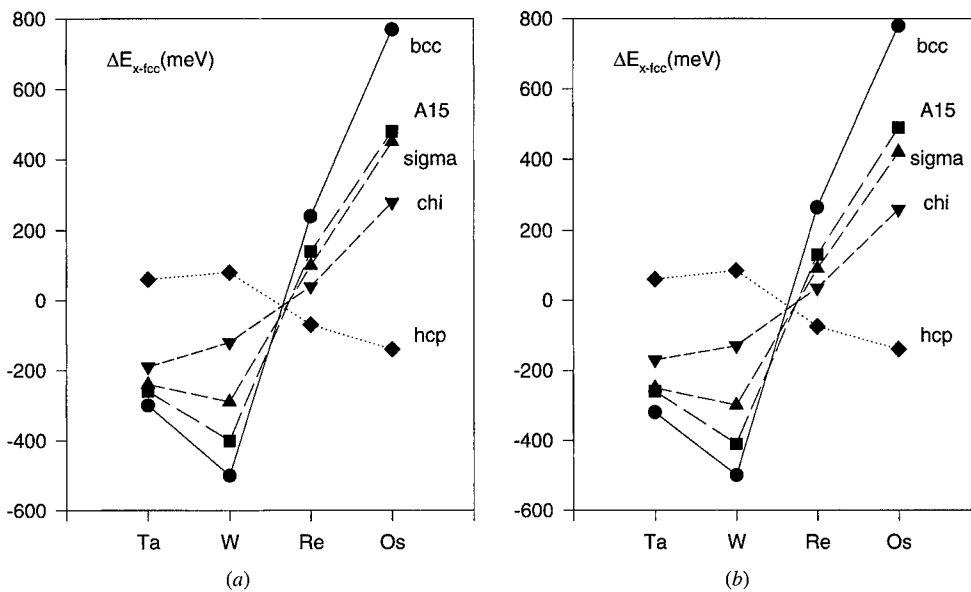
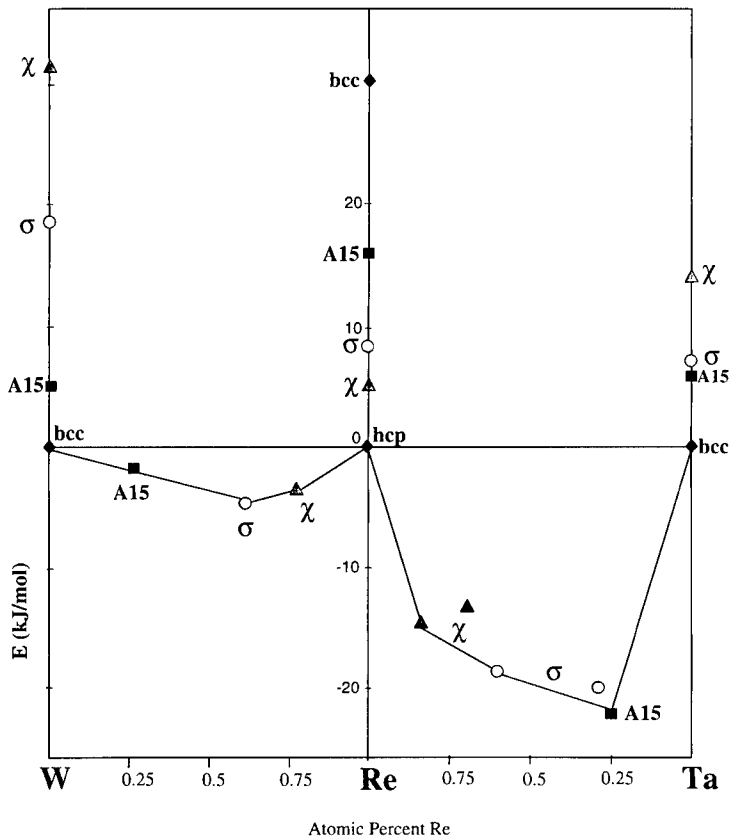


Figure 1. Structural energy differences for Ta, W, Re and Os. (a) FPLMTO; (b) pseudopotentials.

a different percentage of icosahedral sites, i.e. Z12 site, it is tempting to relate their relative structural stability with this percentage. Indeed we think that it is connected with the fact that perturbations conforming to the point group of the icosahedron do not affect the degeneracy of the d levels, but for all the other coordination symmetries the d-level degeneracy is partly broken. Thus, it appears that the icosahedral sites show a predominance for atoms with filled or nearly filled, or else empty d shells. Atoms with d shells close to half filled are mostly found in coordinations of lower symmetry, where the d orbitals may hybridize to form directed bonds.

#### 4. Re–W and Re–Ta systems

The experimental phase diagrams of binary systems based on refractory metals show that associating a hcp metal such as Re with a bcc metal such as W, Mo, Ta or Nb leads to complex phases. All these phases are tcp structures and, among them, the most frequent are the sigma, chi and A15 phases. The results of figure 1 can also be used to understand the sequence of tcp phases in these binary systems. For instance, if a chi phase exists at a given composition, by changing the composition which leads to a decrease in the  $e/a$  ratio, then it is possible to get a new phase which might be a sigma phase, a A15 phase, or a bcc solid solution, but not a hcp phase. Reciprocally, if the  $e/a$  ratio increases, then an hcp phase may occur. The sequence bcc–sigma–chi–hcp can be found in both Re–Ta and Re–W systems. In the Re–W system, the drop-tube experiments performed for different alloy compositions show that the double recalescence phenomenon occurs when undercooling the alloys between 18 and 35 at% Re: this reveals the existence of a metastable phase at high temperatures in a large domain of composition. In the Re–Ta system, double recalescence phenomena are observed in a narrow composition range between 14 and 17 at% Re and the corresponding droplets exhibit two kinds of morphologies: this may be consistent with two different nucleation paths with two different types of transitory phases. In order to understand the origin of these different metastabilities,



**Figure 2.** Calculated structural energies of sigma, chi, A15 and solid bcc solution in: (a) Re–W system; (b) Re–Ta system.

we have performed a theoretical analysis of the interatomic interactions in the Re–W and Re–Ta systems. In the first step, the energies of the ground state structures are calculated, as well as the formation energies of some metastable phases (see figure 2). The first observation is that the formation energies are markedly more negative in Re–Ta than in Re–W. The second result is that the A15 structure displays a metastable character at 25 at% Re for both systems. Therefore, in the Re–W system, the experimentally observed metastable phase is identified as the A15 phase. Moreover, Re–W develops weak heteroatomic interactions, so that entropic effects may become predominant at high temperatures. Such effects have been used to interpret the wide range of metastability of this A15 phase [5]. For the Re–Ta system, first-principles calculations show that the sigma phase competes with the A15 phase in the Ta-rich side. The metastable character of the sigma phase in this composition range can be related to the site occupation. Therefore, the second part of our study deals with the atom distribution in the sigma phase. The sigma phase displays five different sites, namely (a), (b), (c), (d) and (e). The (a) and (d) sites are 12-fold coordinated, the (c) and (e) sites are 14-fold coordinated, and the (b) sites have the largest coordination number, i.e. 15. CVM (cluster variation method) calculations using effective pair interactions extracted from first-principles calculations have been performed to study this site occupation [6]. Initial results show that for both systems, the (b) site has the strongest attraction to the Ta/W atoms, followed by the (c) and (e) sites. Let

us mention that in Re-Ta, this site preference is more pronounced than in the Re-W system. At 33 at% Re, when all (b), (c) and (e) sites are filled and when the Z12 sites become filled, Re-Ta and Re-W display a different behaviour. In the W-based system, the (a) and (d) sites are about equally attractive to the W atoms, while in the Ta-based system, the (a) sites are strongly attractive to Ta. This leads to a configuration which is as stable as the configuration at 60 at% Re, which is observed in the phase diagram and which is also as stable as the A15 phase. This peculiar configuration may explain the occurrence of the sigma phase as a metastable phase far from its well-known composition range.

## 5. Conclusion

High undercooling of refractory metal-based systems appears to be an exciting way to get metastable phases and to discuss competitive phase selection phenomena. First-principles calculations can be used as a guide to understand the origin of such metastability. Preliminary results suggest that the mechanism which stabilizes the metastable phases is related to the complex structure of the highly undercooled liquid. *Ab initio* molecular dynamics would be essential to analyse the structures of these undercooled liquids. Such work is in progress.

## References

- [1] Vinet B, Cortella L, Desré P and Favier J J 1991 *Appl. Phys. Lett.* **58** 97
- [2] Cortella L, Vinet B, Desré P, Pasturel A, Paxton A T and van Schilfgaarde M 1993 *Phys. Rev. Lett.* **70** 1469
- [3] Kresse G and Furthmüller J 1996 *Phys. Rev. B* **54** 11 169
- [4] Frank F C 1952 *Proc. R. Soc. A* **43** 215
- [5] Tournier S, Vinet B, Pasturel A, Ansara I and Desré P 1998 *Phys. Rev. B* **57** 3340
- [6] Sluiter M, Esfarjani K and Kawazoe Y 1995 *Phys. Rev. Lett.* **75** 3142

## Pseudo-critical slowing down within the cluster variation method and the path probability method

Tetsuo Mohri

Division of Materials Science and Engineering, Graduate School of Engineering,  
Hokkaido University 060-8628, Japan

Received 16 September 1999, accepted for publication 3 January 2000

**Abstract.** The pseudo critical slowing down phenomenon reported for an order-disorder transition of the first order is reproduced by the path probability method calculations on a  $L1_0$  ordered phase. The slowing down takes place towards the *instability temperature* of the metastable ordered phase rather than the *transition temperature*. In order to clarify the thermodynamic origin of the pseudo critical slowing down, the temperature dependency of generalized susceptibilities are calculated for the  $L1_0$  ordered phase as a function of  $v_{2,2}/v_{2,1}$ , where  $v_{2,n}$  is the  $n$ th nearest neighbour effective pair interaction energy. The diverging behaviour is observed towards the instability temperature through the transition temperature. This is pronounced, as the second-order character is emphasized. It is confirmed that the pseudo-critical slowing down phenomenon is caused by the flattening of the free energy surface, leading to the loss of the thermodynamic driving force for relaxation. The first-principles calculation of the susceptibility is attempted for Cu–Au system at a 1:1 stoichiometric composition. A sharp rise is confirmed near the transition temperature.

### 1. Introduction

Phase stability is a ‘static’ property of a given phase while phase transition involves more ‘dynamic’ phenomena originating from atomic diffusion and lattice dynamics. Although the first-principles studies have been put forward for various physical and thermodynamic properties of an alloy system, many of them have been centred around phase stability calculations.

The dynamic aspects associated with phase transition is manifested as approaching the transition temperature. These are mainly caused by fluctuations of concentration, degree of order, stiffness of a lattice etc and are termed pre-transition phenomena. Experimentally, one of the conventional ways of detecting pre-transition phenomena is the electric resistivity measurement at an isothermal ageing process following an up(down)-quenching operation. With increase (decrease) of the temperature, the relaxation time generally decreases (increases) due to the enhancement (suppression) of thermally-activated atomic diffusion. The temperature dependency, however, is not monotonic and it has been quite often observed that the relaxation time increases again near the transition temperature. For the second-order transition, this is a well known critical slowing down phenomenon, but even for the first-order transition, a similar phenomenon has been reported [1] for  $Ni_3Pt$  ordered phase and has been termed *pseudo-critical slowing down*.

Theoretically, a key quantity to analyse the pre-transition phenomenon is the generalized susceptibility, which is expressed as the second-order derivative of the free energy functional with respect to fluctuating variables. The second-order derivative provides the curvature of

the free energy surface, which is a driving force of the transition. Furthermore, the vanishing condition of the second-order derivative is a measure of the onset of the instability against the excitation and amplification of a particular fluctuation mode.

In order to grasp an essential feature of a pre-transition phenomenon, we start with a simple Landau-type free energy expansion. Following Sima's prescription [2], a free energy is expanded up to sixth order of a single-order parameter,  $\xi$ , in the following way:

$$F = F_0 + a(T - T^-) \frac{\xi^2}{2} + b \frac{\xi^4}{4} + c \frac{\xi^6}{6} \quad (1)$$

where  $F_0$  is the free energy for a random solid solution,  $a$ ,  $b$  and  $c$  are expansion coefficients and  $T^-$  is the *spinodal ordering* [3] temperature. Due to the symmetry of the 1:1 stoichiometric composition, all the terms with odd exponents vanish. The first-order transformation is characterized by the super-cooling and super-heating below and above the equilibrium transition temperature, respectively. These are ascribed to the existence of a free energy hump above (below) the transition temperature which leaves the ordered (disordered) phase in a metastable state. The assignment of positive values to  $a$  and  $c$  and a negative value to  $b$  in (1) satisfactorily reproduces such a temperature dependency of the free energy curve. In fact, the spinodal ordering temperature  $T^-$  is defined as that at which the free energy hump vanishes below the transition temperature and the onset of instability of the super-cooled disordered phase sets in. The counterpart corresponding to above the transformation temperature is *spinodal disordering* temperature denoted by  $T^+$ , for which the instability condition for a super-heated ordered phase is defined.

The second-order derivative of (1) yields the generalized susceptibility  $\chi$  given by

$$\chi^{-1} = \frac{\partial^2 F}{\partial \xi^2} = 4a \left[ \left( T_t + \frac{\Delta}{4} \right) - T \right]^{1/2} \left\{ \left[ \left( T_t + \frac{\Delta}{4} \right) - T \right]^{1/2} + \Delta^{1/2} \right\} \quad (2)$$

where  $T_t$  is the transition temperature and  $\Delta$  is defined as  $\Delta = T^+ - T^-$ . For the second-order transition for which  $T^+$  and  $T^-$  merge into  $T_t$  (more precisely  $T_c$ , where  $c$  stands for *critical*),  $\Delta$  vanishes. In fact, it is confirmed that in the limit of  $\Delta \rightarrow 0$ , (2) satisfactorily reproduces the classical value of the critical exponent of unity. This is the thermodynamic origin of the critical slowing down for the second-order transition.

Near the transition temperature, i.e.  $T \rightarrow T_t$  ( $T < T_t$ ) for the first-order transition, equation (2) can be further simplified as

$$\chi \rightarrow \frac{1}{a} \frac{1}{3\Delta + 8(T_t - T)}. \quad (3)$$

One realizes that the divergent behaviour towards the infinite value is suppressed due to the existence of the  $\Delta$  term. However, the value of  $\Delta$  for an actual alloy system is quite small compared with  $T_t$ , and the susceptibility is expected to grow, indicating the flattening of the free energy surface, which results in the loss of the thermodynamic restoring force against configurational fluctuation. Hence a phenomenological analysis based on Landau-type free energy expansion suggests an occurrence of a phenomenon similar to the critical slowing down of the second-order transition.

For the first-order transition, however, more complications arise, due to the spatially inhomogeneous, nucleation-growth events involving wetting phenomena. As the temperature approaches  $T_t$ , the free energies of the two competing phases become equivalent, leading to the loss of the driving force of the phase transition. Hence, two effects are mixed near the transition temperature and obscure each other. The present calculation only concerns the, former, effect originating from the flattening of free energy surface.

The accuracy of the theoretical analysis totally depends on the free energy to be employed. The key to the successful calculation is to incorporate a wide range of atomic correlation, which plays a significant role, in particular, near the transition temperature. Among various theoretical tools of statistical mechanics calculations for alloys, the cluster variation method (CVM) [4] has been recognized as one of the most powerful means to meet such a requirement. By combining with electronic structure total energy calculations, even first-principles studies have recently been put forward for thermodynamic properties at finite temperatures.

The path probability method (PPM) [5] is the natural extension of the CVM to the time domain and, therefore, inherits many advantageous features from the CVM. It is generally demonstrated that the steady-state quantities at an infinite time limit derived by the PPM calculation converge to the equilibrium values predicted by the CVM. Therefore, the combination of the CVM and PPM is best suited to perform synthetic study of non-equilibrium transient phenomenon towards the equilibrium state.

In the present study, we focus on  $L1_0$ -disorder transition at a 1:1 stoichiometric composition, and we calculate the temperature dependences of the relaxation time and the generalized susceptibility by the PPM and the CVM, respectively. The main emphasis is placed on the interpretation of the non-monotonic behaviour of the relaxation time in terms of the susceptibility in a consistent manner. Also, first-principles calculation of the susceptibility is attempted for the Cu–Au system. The organization of the present report is as follows. In the next section, the theoretical aspects of the CVM and the PPM are summarized. Since the technical aspects of the first-principles calculation have been amply demonstrated [6], we present merely a framework of the cluster expansion method [7], which plays a key role to combine the internal energy and entropy terms into a free energy formula. The final section is devoted to results and discussion.

## 2. Theoretical background

### 2.1. CVM and first-principles calculation

Theoretical aspects of the CVM and resultant thermodynamic quantities, including phase diagrams, have been amply demonstrated in the literature. Hence, in the present section, we simply reproduce only the necessary formulae employed in the present analyses.

For a fcc-based system, mainly due to the frustration effects, the pair approximation does not provide satisfactory results, and it is known that the minimum meaningful approximation is the tetrahedron approximation [8] for which the entropy term is written as

$$S_T = k_B \ln \frac{(\prod_{ij} (Ny_{ij})!)^6 (N!)^5}{(\prod_i (Nx_i)!)^5 (\prod_{ijkl} (Nw_{ijkl})!)^2} \quad (4)$$

where  $x_i$ ,  $y_{ij}$  and  $w_{ijkl}$  are the cluster probabilities for point, pair and tetrahedron clusters, respectively, and subscripts  $i$ ,  $j$ ,  $k$  and  $l$  designate an atomic species. Note that the expression above is for a disordered phase and one needs to distinguish sub-lattices in dealing with an ordered phase. In the case of the  $L1_0$  ordered phase, which is our main concern in the present study, degeneracy of the cluster probabilities for a disordered phase is lifted as  $x_i \rightarrow x_i^\alpha(1)$  and  $x_i^\beta(1)$ ,  $y_{ij} \rightarrow y_{ij}^{\alpha\alpha}(1)$ ,  $y_{ij}^{\alpha\beta}(4)$  and  $y_{ij}^{\beta\beta}(1)$  and the tetrahedron probability is rewritten as  $w_{ijkl}^{\alpha\alpha\beta\beta}$ . The number in the parenthesis indicates the multiplication factor for each cluster probability.

The one-step higher approximation beyond the tetrahedron approximation is tetrahedron–octahedron (T–O) approximation [9–11] for which the entropy term is written as

$$S_{\text{T-O}} = k_B \ln \frac{(\prod_{i,j,k} (Nz_{ijk})!)^8 (\prod_i (Nx_i)!)^6}{(\prod_{i,j,k,l,m,n} (Nv_{ijklmn})!) (\prod_{i,j,k,l} (Nw_{ijkl})!)^2 (\prod_{i,j} (Ny_{ij})!)^6} \quad (5)$$

where triangle ( $z_{ijk}$ ) and octahedron cluster probabilities ( $v_{ijklmn}$ ) are new participants.

The advantage of the T–O approximation is that the second-order pair is involved as a diagonal of the octahedron cluster and, therefore, the second nearest neighbour pair interaction energy can be explicitly incorporated in the free energy through the internal energy term.

Within the cluster expansion method [7, 12], the internal energy  $E^{(m)}$  of a phase specified by  $m$  is written as

$$E^{(m)}(\{\xi\}) = \sum_k v_k \xi_k^{(m)} \quad (6)$$

where  $v_k$  and  $\xi_k^{(m)}$  are effective cluster interaction energy and correlation function for a  $k$ -point(type) cluster, respectively. The formal definition of the correlation function is the ensemble average of the spin variable  $\sigma$  which takes either +1 or -1 depending upon the  $A$  or  $B$  atoms, respectively. It should be noted that the correlation function of  $k$  cluster depends on the phase of interest, but the effective cluster interaction energy is common once the alloy system is specified.

In actual practice, for a given alloy, the total energy  $E^{(m)}$  and the effective interaction energy  $v_k$  constitute a vector while the correlation function  $\xi_k^{(m)}$  is expressed by a matrix. The reader interested in more details of the correlation functions should consult the original literature [9, 10]. We simply provide the concrete form of the matrix for  $A(\text{fcc})$ ,  $A_3B(L1_2)$ ,  $AB(L1_0)$ ,  $AB_3(L1_2)$  and  $B(\text{fcc})$  with  $m = 1, 2, 3, 4$  and 5, respectively:

$$\begin{aligned} \begin{pmatrix} E^{(1)} \\ E^{(2)} \\ E^{(3)} \\ E^{(4)} \\ E^{(5)} \end{pmatrix} &= \begin{pmatrix} \xi_0^{(1)} & \xi_1^{(1)} & \xi_2^{(1)} & \xi_3^{(1)} & \xi_4^{(1)} \\ \xi_0^{(2)} & \xi_1^{(2)} & \xi_2^{(2)} & \xi_3^{(2)} & \xi_4^{(2)} \\ \xi_0^{(3)} & \xi_1^{(3)} & \xi_2^{(3)} & \xi_3^{(3)} & \xi_4^{(3)} \\ \xi_0^{(4)} & \xi_1^{(4)} & \xi_2^{(4)} & \xi_3^{(4)} & \xi_4^{(4)} \\ \xi_0^{(5)} & \xi_1^{(5)} & \xi_2^{(5)} & \xi_3^{(5)} & \xi_4^{(5)} \end{pmatrix} \begin{pmatrix} v_0 \\ v_1 \\ v_2 \\ v_3 \\ v_4 \end{pmatrix} \\ &= \begin{pmatrix} 1 & 1 & 1 & 1 & 1 \\ 1 & 1/2 & 0 & -1/2 & -1 \\ 1 & 0 & -1/3 & 0 & 1 \\ 1 & -1/2 & 0 & 1/2 & -1 \\ 1 & -1 & 1 & -1 & 1 \end{pmatrix} \begin{pmatrix} v_0 \\ v_1 \\ v_2 \\ v_3 \\ v_4 \end{pmatrix} \end{aligned} \quad (7)$$

or

$$\mathbf{E} = \boldsymbol{\xi} \cdot \mathbf{v}. \quad (8)$$

Note that cluster with  $k = 0$  is called a *null* cluster.

In general, the total energy  $E^{(m)}$  can be obtained by electronic structure calculations for a ground state. While the atomic arrangement at the ground state of a given phase is uniquely determined and, therefore, one can assign a value to each components of a correlation matrix such as equation (7). Hence, by knowing both  $\mathbf{E}$  and  $\boldsymbol{\xi}$ , one can obtain effective interaction energy  $\mathbf{v}$  by a matrix inversion:

$$\mathbf{v} = \{\boldsymbol{\xi}\}^{-1} \cdot \mathbf{E}. \quad (9)$$

The significance of the correlation function is that a set of correlation functions constitutes independent variables to describe atomic configurations at a given state, while the cluster

probabilities defined in the entropy expressions (equations (4) and (5)) are mutually dependent through normalization conditions and reduction relationships. It can easily be demonstrated that the cluster probability and correlation functions are linearly related through, for example,

$$x_i = \frac{1}{2}(1 + i\xi_1) \quad (10)$$

$$y_{ij} = \frac{1}{2^2}[1 + (1 + j)\xi_1 + ij\xi_2] \quad (11)$$

and

$$\begin{aligned} w_{ijkl} = \frac{1}{2^4}[1 + (i + j + k + l)\xi_1 + (ij + ik + il + \dots + kl)\xi_2 \\ + (ijk + ijl + \dots + jkl)\xi_3 + ijk\ell\xi_4]. \end{aligned} \quad (12)$$

Hence, by combining the internal energy given by (6) with entropy by equation (4) or (5), the free energy is symbolically expressed as

$$F = F(T, \{v_k\}; \xi_1, \xi_2, \dots, \xi_{E_{\max}}) = E(\{v_k\}; \xi_1, \xi_2, \dots, \xi_{E_{\max}}) - TS(\xi_1, \xi_2, \dots, \xi_{S_{\max}}) \quad (13)$$

where  $E_{\max}$  represents the tetrahedron and  $S_{\max}$  is either the tetrahedron (equation (4)) or T-O (equation (5)) clusters. The equilibrium state is determined by minimizing the free energy with respect to a set of correlation functions under a given temperature  $T$  and effective cluster interaction energies  $\{v_k\}$ . It is noted that, in the actual practice of the energy calculations, the total energy  $E^{(m)}$  of equation (6) is obtained as a function of the lattice parameter  $r$  (or equivalently volume for a cubic structure). Then, the resultant effective interaction energy is also a function of  $r$ , which imposes an additional optimization for a pressure,  $p$ . The conditions of the equilibrium state are finally given as

$$\left( \frac{\partial F}{\partial \xi_i} \right)_{T, \{\xi_m \neq i\}, r} = 0 \quad (14)$$

and

$$\left( \frac{\partial F}{\partial r} \right)_{T, \{\xi_m\}} = -p. \quad (15)$$

## 2.2. PPM

As was mentioned in the previous section, the PPM is the natural extension of the CVM to the time domain. One of the unique features of the PPM is that the PPM does not explicitly deal with state variables such as cluster probabilities (or correlation functions) or their time derivatives. Instead, *Path variable*,  $\Xi_{\psi, \phi}(t; t + \Delta t)$ , is defined to describe the transition of a state variable for a cluster  $\rho$  during an infinitesimal time  $\Delta t$  in the following way:

$$\rho_\phi(t + \Delta t) = \rho_\psi(t) + \sum C_{\lambda, \zeta} \Xi_{\mu, \zeta}(t : t + \Delta t) \quad (16)$$

where  $\psi, \phi, \lambda, \mu$  and  $\zeta$  represent an atomic configuration and  $C_{\lambda, \zeta}$  is a coefficient term, the form of which depends upon the kinetics.

One may readily grasp the arithmetic insight by exemplifying the point path variable  $\Xi_{\psi, \phi}(t; t + \Delta t) = X_{i,j}$  which describes the transition from  $i$  to  $j$  on a point cluster as follows:

$$x_1(t) = X_{1,1} + X_{\bar{1},1} \quad (17)$$

and

$$x_1(t + \Delta t) = X_{1,1} + X_{\bar{1},1} \quad (18)$$

where  $x_1$  is a point cluster probability representing a concentration of  $A$ . Hence, corresponding to (16), one may obtain

$$x_1(t + \Delta t) = x_1(t) - X_{1,\bar{1}} + X_{\bar{1},1} \quad (19)$$

with  $C_{1,\bar{1}} = -1$  and  $C_{\bar{1},1} = 1$ . In a similar manner, one can confirm the relationships given by equation (16) for a larger cluster.

Since the path variable characterizes the microscopic path of the transition of atomic configuration, the formulation of path variables totally depends on the kinetics adopted in the study. In fact, the present study deals with a simple spin kinetics (Glauber dynamics) [13], whereas exchange kinetics (Kawasaki dynamics) [14] and vacancy kinetics allow more freedom of the path and, therefore, the formulation based on (16) becomes further complicated. One major disadvantage of spin kinetics is the fact that the species is not conserved with time. However, when concentration-independent pair interaction energy is adopted, it has been demonstrated that the conservation of the species is assured at a 1:1 stoichiometric composition without imposing any additional constraints. In order to avoid numerical complications and to observe the conservative feature of an alloy system, the present calculation is limited at a 1:1 stoichiometric composition. The present study, based on spin kinetics, is, therefore, viewed as a precursor to the more complicated vacancy mediated diffusion mechanism.

A counterpart of the free energy of the CVM is the *path probability function*  $P(t; t + \Delta t)$  described as the product of three terms,  $P_1$ ,  $P_2$  and  $P_3$ . Each term is given as

$$P_1 = (\theta \Delta t)^{N(X_{1,2}+X_{2,1})} (1 - \theta \Delta t)^{N(X_{1,1}+X_{2,2})} \quad (20)$$

$$P_2 = \exp\left(-\frac{\Delta E}{2k_B T}\right) \quad (21)$$

and

$$P_3 = \frac{(\prod_{ij,kl} N Y_{ij,kl}!)^6 (N!)^5}{(\prod_{ikjl,mnop} N W_{ikjl,mnop}!)^2 (\prod_{i,j} N X_{i,j}!)^5} \quad (22)$$

where  $N$  is the total number of lattice points,  $\theta$  is the spin flip probability per unit time, which is further written as

$$\theta = v \exp\left(-\frac{\Delta G}{k_B T}\right) \quad (23)$$

where  $v$  is the attempt frequency,  $\Delta G$  the activation energy and  $k_B$  the Boltzmann constant. In (22)  $Y_{ij,kl}$  and  $W_{ikjl,mnop}$  are the path variables for the flipping from one spin configuration to another, designated by the subscript(s) (up spin and down spin) before (at time  $t$ ) and after (at time  $t + \Delta t$ ) the comma sign, on a pair and tetrahedron clusters, respectively. In (21)  $\Delta E$  is the change of the internal energy before and after the flipping events. Within the nearest-neighbour pair interaction model,  $\Delta E$  is further described as

$$\Delta E = \sum_{i=0}^2 \nu_i \Delta \xi_i(t) - \mu_1 \Delta \xi_1(t) \quad (24)$$

where  $\mu_1$  is the effective chemical potential.

One notices that the product of  $P_1$  and  $P_2$  corresponds to the Boltzmann factor in the free energy, while, as is implied by the close resemblance between  $P_3$  and  $S_T$  of equation (4),  $P_3$  is an entropy-like term describing the multiplicity of the microscopic path. The maximization of the path probability function  $P = P_1 P_2 P_3$  with respect to the path variables determines the optimized set of path variables:

$$\left( \frac{\partial P}{\partial \Xi_{\psi,\phi}} \right)_T = 0 \quad (25)$$

which corresponds to the minimization condition given by equation (14) for the CVM. Then, once path variables are optimized for each time  $t$ , a cluster probability at time  $t + \Delta t$  is determined through (16), and the repetition of this procedure traces the most probable path of time evolution.

### 3. Results and discussion

As was described in the previous section, the main concern of the present study is the  $L1_0$ -disorder transition rather than  $L1_2$ -disorder, for which pseudo-critical slowing down phenomenon through electrical resistivity measurements are reported [1]. This is because of the simplicity of the PPM calculations at a 1:1 stoichiometry with spin kinetics. However, we note that the first-order character of the transition was confirmed for  $L1_0$ -disorder and the essential feature of the analysis is not at all hampered [15].

Within the tetrahedron approximation of the CVM, the transition temperature determined at a 1:1 stoichiometric composition is  $k_B T_t/v_{2,1} = 1.89$  where  $v_{2,1}$  is the effective nearest-neighbour pair interaction energy. Hereafter, we simply describe the temperature by  $T$ , but authors should keep in mind that the temperature is hereafter always normalized with respect to  $v_{2,1}/k_B$ .

We up-quench the system from temperature  $T = 1.2$  to various temperatures below the transition temperature. From the time evolution behaviour of the long-range order parameter  $\eta$  defined as  $\eta(t) = x_1^\alpha(t) - x_1^\beta(t)$ , which is calculated by the PPM, the relaxation time  $\tau$  is obtained. In fact, the electrical resistivity often measured by the relaxation experiment is closely related to the long-range order parameter through Rossiter's formula [16]. It is noted that the relaxation time calculated in the present study is defined as follows:

$$\eta(t) = \eta(t = \infty) - \{\eta(t = \infty) - \eta(t = 0)\} \cdot \exp\left(-\frac{t}{\tau}\right) \quad (26)$$

where  $\eta_0$  and  $\eta_\infty$  are, respectively, the long-range order parameters at the initial state and at thermal equilibrium at a given temperature. A typical result of the temperature dependency is shown in figure 1 [17]. Note that the time is normalized with respect to the spin flip probability throughout this study. One confirms that the relaxation time once decreases with an increase

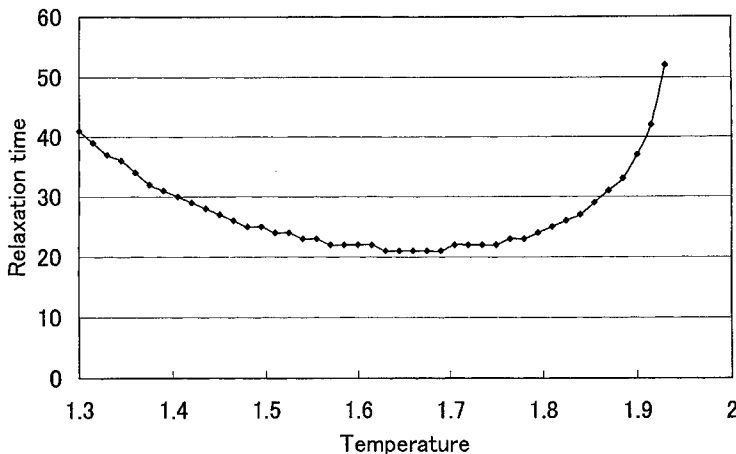
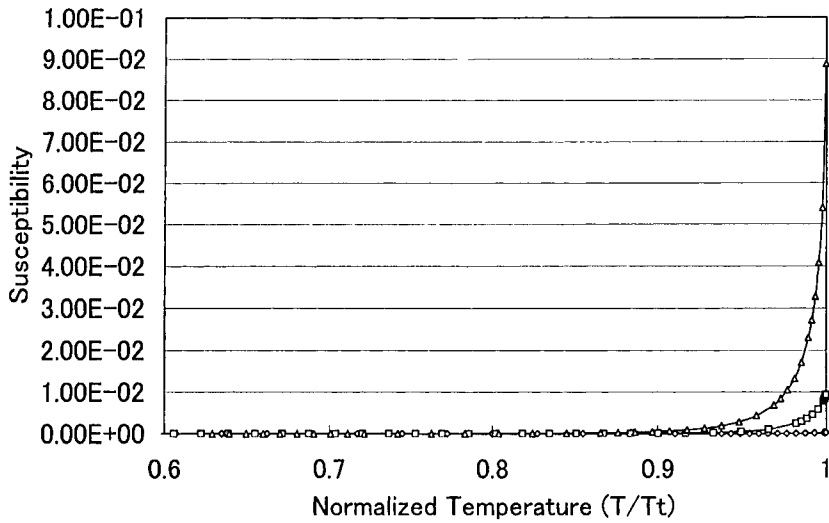


Figure 1. Temperature dependency of relaxation time at a 1:1 stoichiometry calculated by the PPM with  $v = 10$  and  $\Delta G = 12$  in (23).



**Figure 2.** Temperature dependency of susceptibilities calculated by T-O approximation of the CVM with  $\delta(v_{2,2}/v_{2,1}) = 0.0 (\diamond)$ ,  $-0.2 (\square)$  and  $-0.5 (\Delta)$  [18]. The temperature axis is normalized with respect to the transition temperature for each  $\delta$  value.

of temperature, then increases again through the transition temperature  $T_t = 1.89$  towards temperature  $T = 1.94$ . As is demonstrated for the susceptibility calculations below, this particular temperature,  $T = 1.94$ , is found to be the instability temperature  $T^+$  of metastable  $L1_0$  ordered phase up-quenched in the disordered-phase region.

In order to analyse the general aspects of the susceptibility, we first employ the T-O approximation which is able to incorporate both first and second nearest-neighbour pair interactions. The key parameter of the analysis is the ratio of the second to the first nearest-neighbour pair interaction energies,  $\delta = v_{2,2}/v_{2,1}$ . It is noted that 32 kinds of independent configurational variables are required to describe the  $L1_0$  ordered phase within the T-O approximation, which is in marked contrast with the Landau-type approach in which only a single order parameter  $\xi$  was introduced. The generalized susceptibility is calculated through

$$\chi = \left( \frac{\partial^2 F}{\partial \xi_1^\alpha} \right)^{-1} \quad (27)$$

where  $\xi_1^\alpha$  is the point correlation functions for the  $\alpha$  sub-lattice. When the  $\delta$  value is changed, the resultant transition temperature also changes. Hence, the temperature is normalized with respect to the transition temperature for each  $\delta$ . The results are shown in figure 2 [18]. One notices that the susceptibility increases approaching the transition temperature. This is more apparent with decreasing  $\delta$  values. In fact, with decreasing  $\delta$ , the original fcc lattice starts to decouple into cubic lattices formed by the second nearest-neighbour pairs, and the order-disorder transformation on a fcc lattice is reduced to a clustering reaction on the cubic lattice. Hence the second-order transition character comes in sight with decreasing  $\delta$  values. Although the critical exponent value is not explicitly estimated, it is expected that at an infinite (negative) value of  $\delta$ , the classical exponent of unity should be reproduced.

Shown in figure 3 is the temperature dependency of the susceptibility calculated within the tetrahedron approximation, which is of particular interest since the PPM calculations of relaxation time (figure 1) is carried out within the same tetrahedron approximation.

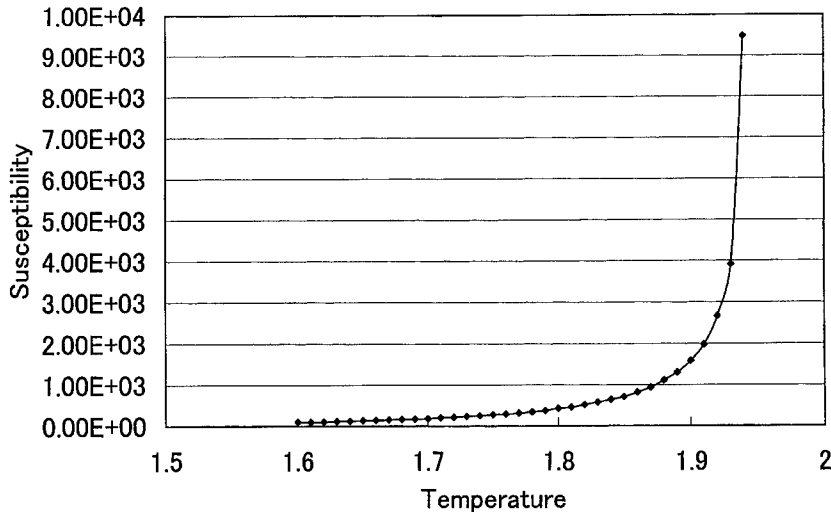


**Figure 3.** Temperature dependency of the susceptibility calculated within the tetrahedron approximation of the CVM. The transition temperature is  $T_t = 1.89$  and the instability temperature is  $T^+ = 1.94$ .

One certainly confirms that the susceptibility increases towards the temperature  $T = 1.94$  at which the relaxation time obtained by PPM increases exponentially. The PPM calculation of the pseudo-critical slowing down phenomenon shown in figure 1 is, therefore, interpreted as the flattening of the free energy surface. With an increase in the annealing temperature, the diffusion (spin flip) events are enhanced by a thermal-activation process, while the flattening of the free energy surface is manifested towards the instability temperature  $T^+ = 1.94$ , which leads to the loss of the thermodynamic driving force for the relaxation. Combination of these two effects yields the non-monotonic behaviour of the relaxation time. It should be noted, however, that the entire relaxation behaviour depends on the magnitudes of the attempt frequency  $\nu$  and the activation energy  $\Delta G$ . A more systematic PPM study on the dependency has been underway and will be reported elsewhere [17].

It is desirable to investigate temperature dependency of the relaxation time for a real alloy system. Unfortunately, however, the PPM calculations face serious difficulties when extended to a real alloy. As was described in the previous section, this is due to the proliferated microscopic paths for an exchange or vacancy-mediated diffusion mechanisms. Furthermore, although the saddle point energy  $\Delta G$  in (23) is a deterministic factor in controlling the alloy kinetics, the dependency of the saddle point energy on a local environment is too subtle to be estimated with a desired accuracy. Therefore, our attempt of applying the present analyses is limited to the calculation of the susceptibility. We focus on the Cu–Au  $L1_0$  ordered phase for which the increase of relaxation time estimated by electrical resistivity measurement has been determined at a 1:1 stoichiometric composition [19].

The effective interaction energies are evaluated through the cluster expansion method with total energy calculations via the augmented spherical wave method [6]. The entropy term is evaluated within the tetrahedron approximation. The derived transition temperature  $T_t$  is 908 K, which is overestimated as compared with the experimentally-determined transition temperature of  $\sim 650$  K. The overestimation has been ascribed to the neglect of local lattice relaxation effect [6], which is emphasized for a system consisting of elements with large difference in atomic size.

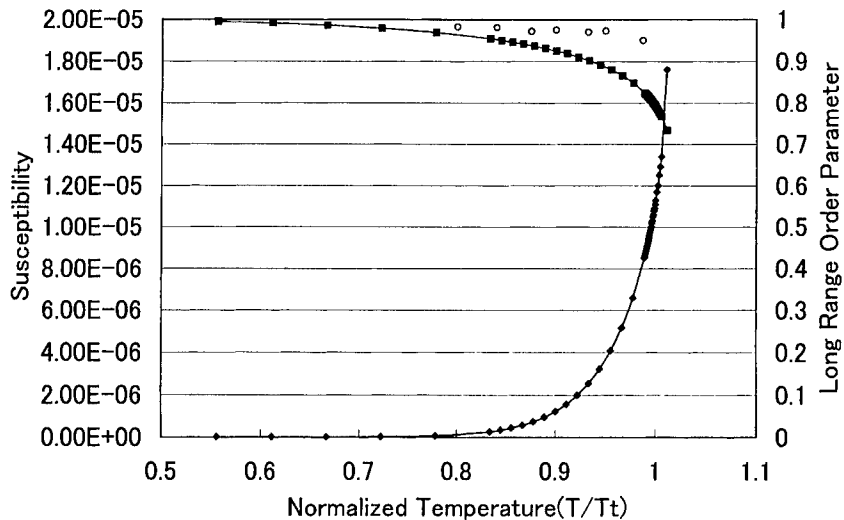


**Figure 4.** Temperature dependency of susceptibility (◆) and long-range order parameter (■) for Cu-Au at a 1:1 stoichiometric composition. The experimentally obtained long-range order parameter (○) is also plotted. The transition temperature  $T_i$  and instability temperature  $T^+$  obtained by this calculation are 908 K and 926 K, respectively. Note that the temperature axis is normalized with respect to the transition temperature.

The effect of the neglect of the local relaxation on the susceptibility is not fully elucidated. This should be the subject to be settled in the future calculations. In particular, more sophisticated first-principles calculations recently proposed by Ozolins *et al* [20, 21] incorporating local relaxation effects is expected to provide a satisfactory solution. In this study, however, we simply scaled the temperature axis by normalizing with respect to the transition temperature. The calculated temperature dependency of the susceptibility is shown in figure 4 together with a long-range order parameter. The calculated instability temperature  $T^+$  is nearly 1.020 (926 K) in the normalized (absolute) temperature scale. This value is close to that 1.026 (1.94/1.89), derived by the tetrahedron approximation.

One can confirm the sharp, rising behaviour near the transition temperature, indicating the flattening of the free energy surface. However, the comparison of the calculated long-range order parameters with experiment [22] plotted by open circles suggests that the first-order character is less emphasized in the present calculations. Hence, the sharpness of the susceptibility may be exaggerated. The cause of the underestimated long-range order may be attributed to the neglect of the local lattice relaxation or tetragonal distortion. These should be clarified in the future calculations. Finally, we emphasize, again, that the experimentally observed slowing down behaviour is a combined effect of the flattening of the free energy surface and the reduction of the difference of the free energies between the ordered and disordered phases. The experimental separation of these two effects is desirable with a well controlled rapid up-quenching operation.

## References

- [1] Dahmani C E, Cadeville M C and Pierron-Bohnes V 1985 *Acta Metall.* **33** 369
- [2] Sima V 1993 *J. Chem. Phys.* **90** 451
- [3] de Fontaine D 1975 *Acta Metall.* **23** 553

- [4] Kikuchi R 1951 *Phys. Rev.* **81** 998
- [5] Kikuchi R 1966 *Prog. Theor. Phys. Kyoto* **35** 1
- [6] Terakura K, Oguchi T, Mohri T and Watanabe K 1987 *Phys. Rev. B* **35** 2169  
Mohri T, Terakura K, Oguchi T and Watanabe K 1988 *Acta Metall.* **36** 547  
Mohri T, Terakura K, Takizawa S and Sanchez J M 1991 *Acta Metall.* **39** 493
- [7] Connolly J W D and Williams A R 1983 *Phys. Rev. B* **27** 5169
- [8] Kikuchi R 1974 *J. Chem. Phys.* **60** 1071
- [9] Sanchez J M and de Fontaine D 1978 *Phys. Rev. B* **17** 2926
- [10] Sanchez J M and de Fontaine D 1980 *Phys. Rev. B* **21** 216
- [11] Mohri T, Sanchez J M and de Fontaine D 1985 *Acta Metall.* **33** 1171
- [12] Sanchez J M, Ducastelle F and Gratias D 1984 *Physica A* **128** 334
- [13] Glauber R J 1953 *J. Math. Phys.* **4** 294
- [14] Kawasaki K 1966 *Phys. Rev.* **145** 224
- [15] Mohri T and Nagata F 1998 *Proc. 3rd Pacific Rim Int. Conf. on Advanced Materials and Processing* vol 1,  
ed M A Imami *et al* p 337
- [16] Rossiter P L 1987 *The Electrical Resistivity of Metals and Alloys* (Cambridge: Cambridge University Press)
- [17] Mohri T unpublished
- [18] Mohri T 1999 *Proc. Int. Conf. on Solid-Solid Phase Transformations '99 (JIMIC-3)* ed M Koiwa *et al* (The Japan  
Institute of Metals) pp 669–72
- [19] Pfeiler W 1999 private communications (Our interpretation is not exactly the same as the author's.)
- [20] Ozolins V, Wolverton C and Zunger A 1998 *Phys. Rev. B* **58** R598–900
- [21] Ozolins V, Wolverton C and Zunger A 1998 *Phys. Rev. B* **57** 6427–43
- [22] Roberts B W 1954 *Acta Metall.* **2** 597

## Infinitesimal lattice-constant treatment of liquid

Ryoichi Kikuchi<sup>†</sup> and C M van Baal<sup>‡</sup>

<sup>†</sup> Materials Science and Mineral Engineering, University of California, Berkeley,  
CA 94720-1760, USA

<sup>‡</sup> Technological University of Delft, Delft, The Netherlands

Received 16 September 1999, accepted for publication 3 February 2000

**Abstract.** The gas–liquid phase transition of a mono-atomic molecular fluid is studied by placing atoms and vacancies in cubic cells of a simple cubic lattice and by reducing the lattice constant to infinitesimal. The cluster variation method is used to formulate the entropy for three choices of the basic clusters: all shapes and orientations of cell pairs, all cell triplets and all cell quartets. The first two cases fail to derive a stable liquid phase. When we introduce certain approximations to the basic iterative equations of the quartet case, a stable liquid phase appears, although numerical results violate certain thermodynamic relations. The triplet formulation leads to the Persus–Yevick equation as a linearized form, and is also related to the hyper-netted chain equation through a slight modification.

### 1. Introduction

In statistical mechanics of cooperative phenomena [1], including the conventional cluster variation method (CVM) [2, 3], species are located on lattice points and their permutation is the main issue. In order to generalize the treatment to gas and liquid phases, the present paper makes the lattice constant decrease to the infinitesimally small limit. It is to be noted that the most of equations of the present paper can be derived by a different approach [4, 5] based on the CVM entropy and using the distribution functions. Since the cell-size reduction has its own merit and future, it is worthwhile to publish the present work

We consider a simple cubic lattice and distribute atoms over cubic cells, placing at most one atom in a cell. We assign  $j = 0$  and 1 to a vacant cell and an occupied cell, respectively. The probability of finding a  $j$  cell is written as  $[j]$ . In applying the CVM, we choose three cases for the basic cluster: all 2-cell (pair) clusters, all 3-cell (triplet or  $\Delta$ ) clusters and all 4-cell (quartet) clusters.

The entropy  $S$  for these cases can be derived using the correlation correction factor formulation [6] from a unified formulation.

$$\exp(S/k_B) = W_{\text{cell}} G_{2\text{-cell}} G_{3\text{-cell}} G_{4\text{-cell}} \quad (1.1)$$

where  $W_{\text{cell}}$  is the number of ways of distributing atoms over  $N$  cells, and  $G$ 's are the correlation correction factors. They are defined as

$$W_{\text{cell}} \equiv \frac{N!}{\{\text{Cell}\}_N}$$

$$G_{2\text{-cell}} \equiv \prod \left[ \frac{\{\text{Cell } j\}_N \{\text{Cell } k\}_N}{N! \{\text{Pair } ja k\}_N} \right]$$

$$\begin{aligned} G_{3\text{-cell}} &\equiv \prod \left[ \frac{N! \{\text{Pair } ja k\}_N \{\text{Pair } kb m\}_N \{\text{Pair } mc j\}_N}{\{\text{Cell } j\}_N \{\text{Cell } k\}_N \{\text{Cell } m\}_N \{3\text{-pts } ja kb mc\}_N} \right] \\ G_{4\text{-cell}} &\equiv \prod \left[ \frac{\{j\}\{k\}\{m\}\{n\}\{\Delta kmn\}\{\Delta jkm\}\{\Delta jmn\}\{\Delta jnk\}}{N!\{km\}\{kn\}\{kj\}\{mn\}\{nj\}\{jm\}\{\text{Quartet } jkmn\}} \right] \end{aligned} \quad (1.2)$$

The braces are for a product of factorials of probability variables [2], and  $j, k, m, n$  are the cell names. Details of the notation will be given in later sections.

## 2. 2-cell cluster (pair) treatment

The basic clusters are cell pairs of all distances and all orientations located anywhere in the system. In addition to the cell probability  $[j]$ , we define  $[ja k]$  as the probability of finding the configuration  $(ja k)$ , i.e.  $j$  cell at the base and  $k$  at the tip of a vector  $a$ . The reduction and the normalization relations are

$$[j] = \sum_k [ja k] \quad 1 = \sum_j [j]. \quad (2.1)$$

The entropy  $S$  is derived using the  $W_{\text{cell}}G_{2\text{-cell}}$  part of (1.2). In the product in  $G_{2\text{-cell}}$  we suppress translational symmetry and include all shapes and orientations of cell pairs. In the probability variables,  $S$  is written as

$$\frac{S_{\text{pair}}}{k_B N} = -1 - \sum_j L([j]) + \frac{1}{2} \sum_a \left( \sum_j L([j]) + \sum_k L([k]) - \sum_{jk} L([ja k]) \right) \quad (2.2)$$

where we use the function:

$$L[X] \equiv X \ln X - X. \quad (2.3)$$

The  $a$  summation includes both  $a$  and  $-a$ , and the factor  $\frac{1}{2}$  is to avoid double counting.

The pair-wise potential is written as  $\varepsilon(ja k)$ . This vanishes unless both  $j = 1$  and  $k = 1$ . The energy for a system is

$$\frac{E_{\text{pair}}}{N} = \frac{1}{2} \sum_{ja k} \varepsilon(ja k) [ja k]. \quad (2.4)$$

We write the chemical potential of a particle  $\mu_1$  as  $\mu$ , and define  $\mu_0 = 0$  for a vacant cell. Then the chemical potential term for a system of  $N_A = N[1]$  particles is

$$\mu N_A = N \sum_j [j] \mu_j. \quad (2.5)$$

In the subsequent minimization of the grand potential, we treat both  $[j]$  and  $[ja k]$  as independent. All pairs  $(ja k)$  sharing  $j$  satisfy the constraint relation:  $[j] = \sum_k [ja k]$ . We use Lagrange multipliers  $\alpha_{aj}$  and write the constraint term as

$$C_\alpha \equiv \sum_{ja} \alpha_{aj} \left\{ [j] - \sum_k [ja k] \right\} = \sum_{ja} \left\{ \alpha_{aj} [j] - \frac{1}{2} \sum_k (\alpha_{aj} + \alpha_{aj}) [ja k] \right\}. \quad (2.6)$$

Using these relations, we write the grand potential  $\Omega = F - \mu N_A = -pV$  as

$$\beta \Psi \equiv \beta \frac{\Omega}{N} = \beta \frac{E_{\text{pair}}}{N} - \frac{S_{\text{pair}}}{k_B N} - \beta \frac{\mu N_A}{N} + C_\alpha - \beta \lambda \left( 1 - \sum_j [j] \right) \quad (2.7)$$

where  $\beta \equiv 1/k_B T$ , and the last term is for the normalization of  $[j]$  in (2.1). The volume of the system is written as  $V$ .

When  $\Omega$  is minimized with respect to  $[j]$  and  $[ja k]$ , respectively, we obtain

$$[j] = \exp \left\{ -\beta\lambda + \beta\mu_j - \sum_a \alpha_{aj} \right\} \quad (2.8)$$

$$[ja k] = [j][k] \exp\{-\beta\varepsilon(ja k) + \alpha_{aj} + \alpha_{ak}\}. \quad (2.9)$$

When these are satisfied, (2.7) is simplified to lead to  $\lambda$

$$\lambda = -\Psi = -\Omega/N = pv \quad v \equiv V/N \quad (2.10)$$

where  $v$  is the volume of a cubic cell.

When we substitute (2.8) and (2.9) in the reduction relation (2.1), we obtain simultaneous equations for the Lagrange multipliers  $\exp(\alpha_{a0})$  and  $\exp(\alpha_{a1})$ . They reduce to a quadratic equation for their ratio and can be solved analytically. For the solution, it is convenient to write  $c \equiv [1]$  for the probability of finding an occupied cell, and hence  $[0] = 1 - c$ . Since  $c$  reduces to infinitesimal with the lattice constant, the solution can be written to the lowest power of  $c$ . Using the abbreviation  $\varepsilon(a) \equiv \varepsilon(1a1)$ , the solution is written as

$$\begin{aligned} \alpha_{a0} &= (e^{-\varepsilon(a)} - 1)c^2/2 + O(c^3) \\ \alpha_{a1} &= -(e^{-\varepsilon(a)} - 1)c + O(c^2). \end{aligned} \quad (2.11)$$

When we use (2.11) in (2.9) and when  $\varepsilon(1a1) \neq 0$ , we can derive the radial distribution function  $g(a)$  of the common use as

$$g(a) \equiv [1a1]/c^2 = e^{-\varepsilon(a)} \{1 - (e^{-\varepsilon(a)} - 1)c\}^2 + \dots \quad (2.12)$$

When  $\varepsilon(a) = 0$ , the two end cells of  $a$  are not correlated since  $[1a1] = c^2$ .

The equation of state can be derived by substituting  $\lambda = pv$  of (2.10) in the  $[j = 0]$  equation of (2.8) and using the solution of  $\alpha_{a0}$  in (2.11) as

$$\beta p v = c - (c^2/2) \sum_a \{e^{-\varepsilon(a)} - 1 + O(c)\}. \quad (2.13)$$

Defining the particle density  $\rho \equiv c/v = N_A/V$ , we can rewrite this for an infinitesimal  $c$  as

$$\frac{p}{k_B T} = \rho - \frac{1}{2} \rho^2 \int_* da (e^{-\varepsilon(a)} - 1) \quad (2.14)$$

where \* indicates to integrate  $a$  over all space. The ratio  $[1]/[0]$  from (2.8) leads to the chemical potential  $\mu$ , which can be transformed to the integration form as

$$\beta\mu = \ln v + \ln \rho - \rho \int_* da (e^{-\varepsilon(a)} - 1). \quad (2.15)$$

The diverging  $\ln v$  is irrelevant, because only differences of  $\mu$ 's are physically significant.

When we examine the pressure equation in (2.14), we see that this quadratic expression does not show the van der Waals-type phase transition. Therefore, the 2-point cluster treatment does not lead to a liquid state.

### 3. 3-cell cluster (triplet) treatment

In addition to  $[j]$  and  $[ja k]$  in (2.1), we introduce  $[ja kb mc]$  for the probability of a cell triangle made of three vectors  $a$ ,  $b$  and  $c = -(a + b)$  which connect three configurations  $j$ ,  $k$  and  $m$ . The following reduction relation is added to those in (2.1).

$$[ja k] = \sum_m [ja kb mc]. \quad (3.1)$$

Our notation is related to the conventional 3-body distribution function by

$$g(r_1, r_2, r_3) = [1r_2 - r_1 1r_3 - r_2 1r_1 - r_3]/[1]^3. \quad (3.2)$$

The entropy is the  $W_{\text{cell}} G_{2\text{-cell}} G_{3\text{-cell}}$  part of (1.1). The product for  $G_{3\text{-cell}}$  goes over the triplets of every shape and orientation with the translational symmetry suppressed. As for the energy,  $E_{\text{pair}}$  in (2.4) can be supplemented by the 3-body interactions:

$$\frac{E_{3\text{-pt}}}{N} = \frac{1}{3!} \sum_{j a k b m} \psi(j a k b m c) [j a k b m c]. \quad (3.3)$$

The grand potential is then written as

$$\beta\Psi = \beta \left( \frac{E_{\text{pair}}}{N} + \frac{E_{3\text{-pt}}}{N} \right) - \left( \frac{S_{\text{pair}}}{k_B N} + \frac{S_{3\text{-pt}}}{k_B N} \right) - \beta \frac{\mu N_A}{N} + \left( C_\alpha + \frac{1}{2} C_\gamma \right) - \beta \lambda \left( 1 - \sum_j [j] \right) \quad (3.4)$$

where  $C_\gamma$  is the constraint term for the reduction relations for triplets:

$$C_\gamma \equiv \sum_{j a k b} \left\{ \gamma_{c j a k b} [j a k] - \frac{1}{3} \sum_m (\gamma_{c j a k b} + \gamma_{a k b m c} + \gamma_{b m c j a}) [j a k b m c] \right\}. \quad (3.5)$$

The equilibrium is derived in two steps. The first is to minimize  $\beta\Psi$  with respect to  $[j]$ ,  $[j a k]$  and  $[j a k b m c]$ , and the second is to solve  $\alpha$ 's and  $\gamma$ 's to satisfy the reduction relations. The first step leads to three sets. The first two are from  $\delta\Omega/\delta[j]$  and  $\delta\Omega/\delta[j a k]$ :

$$[j] = \exp\{-\beta\lambda + \beta\mu_j - \sum_a \alpha_{aj}\} \quad (3.6)$$

$$[j a k] = [j][k] \exp \left\{ -\beta\varepsilon(j a k) + \alpha_{aj} + \alpha_{ak} - \sum_b \gamma_{c j a k b} \right\}. \quad (3.7)$$

In formulating the third set for  $\delta\Omega/\delta[j a k b m c]$ , we make use of the result of the second step that each of  $\alpha$ 's and  $\gamma$ 's is of the order of  $c$  or smaller. Then the third set leads to

$$[j a k b m c] = \frac{[j a k][k b m][m c j]}{[j][k][m]} \exp(-\beta\psi(j a k b m c)). \quad (3.8a)$$

We note that when  $\psi(1 a 1 b 1 c)$  vanishes,  $[1 a 1 b 1 c]$  reduces to Kirkwood's superposition approximation [7]. This is an indication that the CVM entropy expression is closely related to the superposition concept. The special case of (3.8a) for  $j = k = m = 1$  leads to the triplet distribution function:

$$g_3(a, b) \equiv [1 a 1 b 1 c]/c^3 = g(a)g(b)g(c) \exp(-\beta\psi(j a k b m c)). \quad (3.8b)$$

In (3.7), the sum of  $\gamma$ 's over the entire  $b$  changes into an integral, to result in

$$g(a) \equiv [1 a 1]/c^2 = \exp\{-\beta\varepsilon(a) - \rho I_{11}(a)\} \quad (3.9)$$

where

$$-\rho I_{11}(a) \equiv \rho \int db [(g(b) - 1)(g(c) - 1) + g(b)g(c)\{\exp(-\beta\psi(1 a 1 b 1 c)) - 1\}]. \quad (3.10)$$

This is an iterative equation to be solved for the distribution function  $g(a)$  for given  $T$  and  $\rho$ . The natural iteration method [8] can be used. Actually,  $g(a)$  is a function of  $a \equiv |a|$ .

The ratio  $[1]/[0]$  formed from (3.6) leads to  $\mu$  as

$$\begin{aligned} \beta\mu &= \ln v + \ln \rho - \rho \int da [g(a) - 1] + \frac{1}{3!} \rho^2 \int da \int db [3 - (g(a) + g(b) + g(c)) \\ &\quad - (g(a)g(b) + g(b)g(c) + g(c)g(a)) + 3g_3(a, b)]. \end{aligned} \quad (3.11)$$

The [ $j = 0$ ] equation of (3.6) leads to the equation of state as

$$\beta p = \rho - \frac{1}{2} \rho^2 \int da [g(a) - 1] + \frac{1}{3!} \rho^3 \int da \int db [2 - (g(a) + g(b) + g(c)) + g_3(a, b)]. \quad (3.12)$$

When  $\rho I_{11}(a)$  in  $g(a)$  and the  $\rho^3$  integral are missing, (3.12) reduced to the pair case (2.14). As for the van der Waals loop, it was found that the natural iteration method does not converge for the range of  $T$  and  $\rho$  corresponding to the liquid state, and it has been unsuccessful to derive the van der Waals loop. However, a liquid-like state is derived for a system confined inside a narrow slit [4] from a linearized equation of (3.12) [4, 9].

It can be shown [4] that the Persus-Yevick equation can be derived by linearizing (3.9) in  $\rho$ . When  $\psi(1a 1b 1c) = 0$ , we expand  $g(b) = e^{-\varepsilon(b)} + O(\rho)$  in the integrand of (3.10) to derive

$$g(a) e^{\varepsilon(a)} = 1 + \rho \int db (g(c) - 1) g(b) (1 - e^{\varepsilon(b)}). \quad (3.13)$$

This is the equation obtained by Persus and Yevick [10].

In  $g(a)$  of (3.9) and (3.10), we make  $\psi(1a 1b 1c) = 0$  and modify [4] (3.10) as

$$-\rho I_{11}(a) \equiv \rho \int db [(g(b) - 1 - \rho I_{11}(b))(g(c) - 1)]. \quad (3.14)$$

Then  $g(a)$  of (3.9) becomes the hyper-netted chain approximation.

We compare various approaches by expanding  $g(a) e^{\varepsilon(a)}$ , or  $g(r_{12}) \exp\{\varepsilon(r_{12})\}$  with  $r_{12} \equiv r_2 - r_1$ , in powers of  $\rho$  and compare coefficients of the  $\rho^2$  term:

$$g(r_{12}) \exp\{\varepsilon(r_{12})\} = 1 + A(r_{12})\rho + C(r_{12})\rho^2 + O(\rho^3). \quad (3.15a)$$

We note  $C(r_{12})$  is a sum of four integrals:

$$C(r_{12}) = q_1 H_1(r_{12}) + q_2 H_2(r_{12}) + q_3 H_3(r_{12}) + q_4 H_4(r_{12}) \quad (3.15b)$$

where the  $H$ 's are the following integrals and the  $q$ 's are numerical coefficients:

$$\begin{aligned} H_1(r_{12}) &\equiv \int dr_3 \int dr_4 h(r_{13})h(r_{14})h(r_{23})h(r_{24}) \\ H_2(r_{12}) &\equiv \int dr_3 \int dr_4 h(r_{13})h(r_{24})h(r_{34}) \\ H_3(r_{12}) &\equiv \int dr_3 \int dr_4 h(r_{13})h(r_{14})h(r_{24})h(r_{34}) \\ H_4(r_{12}) &\equiv \int dr_3 \int dr_4 h(r_{13})h(r_{14})h(r_{23})h(r_{24})h(r_{34}) \end{aligned} \quad (3.15c)$$

with

$$h(r_{34}) \equiv g(r_{34}) - 1. \quad (3.15d)$$

In these integrals  $r_1$  is at the origin,  $r_2 = r_{21}$  is fixed, and the integration is over  $r_3$  and  $r_4$ . Table 1 shows how the  $q$ 's depend on the approaches. The table is self-explanatory. The last line is the quartet result of the next section.

**Table 1.** The coefficients  $q_j$  in (3.15).

	$H_1$	$H_2$	$H_3$	$H_4$
Percus–Yevick	0	1	2	0
Hyper-netted chain	$\frac{1}{2}$	1	2	0
CVM triplet	$\frac{1}{2}$	2	2	0
CVM quartet and exact	$\frac{1}{2}$	1	2	$\frac{1}{2}$

#### 4. 4-cell cluster (quartet) treatment

In the quartet, four cells  $j, k, m$  and  $n$  are connected as six pairs  $(jak), (kbm), (mcn), (mdj), (nek)$  and  $(nfj)$ . The vectors satisfy the closure relations  $a + b + d = 0$ ,  $b + c + e = 0$  and  $a + b + c + f = 0$ . The probability of finding a quartet of this configuration can be written as  $[jakbmcn]$ , since  $d, e$  and  $f$  are derived from other vectors.

The entropy  $S_{\text{4-cell}}$  is the entire product of (1.1). Note  $G_{\text{4-cell}}$  in (1.2) is written using only the cell names. The energy is the sum of  $E_{\text{pair}}$  in (2.4),  $E_{\text{3-pt}}$  in (3.3) and the 4-body interaction:

$$\frac{E_{\text{4-pt}}}{N} = \frac{1}{4!} \sum_{jakbmcn} \chi(jakbmcn)[jakbmcn]. \quad (4.1)$$

The grand potential  $\Omega$  is written in the same way as in (2.7) and the triplet case. When we minimize  $\Omega$  with respect to  $[jakbmcn]$ , this function is written as an extension of (3.7). One of them is the quartet distribution function  $[1a1b1c1]/[1]^4 \equiv g_4(a, b, c)$ :

$$g_4(a, b, c) = \frac{g_3(a, b)g_3(a, b+c)g_3(a+b, c)g_3(b, c)}{g(a)g(a+b)g(b)g(a+b+c)g(b+c)g(c)} \exp(-\beta\chi(1a1b1c1)) \quad (4.2)$$

where we use

$$g(a) \equiv \frac{[1a1]}{[1]^2} \quad g_3(a, b) \equiv \frac{[1a1b1]}{[1]^3}. \quad (4.3)$$

When  $\chi(jakbmcn) = 0$ , (4.2) reduces to the superposition relation derived by Fisher and Kopeliovich [11].

Minimization of  $\Omega$  with respect to  $[1a1b1]$  leads to the triplet distribution function:

$$g_3(a, b) = g(a)g(b)g(a+b)\exp\{-\beta\psi(1a1b1) - \rho I_{111}(a, b)\} \quad (4.4)$$

where  $I_{111}(a, b)$  is an integral defined as

$$\begin{aligned} \rho I_{111}(a, b) &\equiv \rho \int dc \left[ 1 - g(c) - g(b+c) - g(a+b+c) + \frac{g_3(a, b+c)}{g(a)} + \frac{g_3(a, b+c)}{g(a+b)} \right. \\ &\quad \left. + \frac{g_3(b, c)}{g(a+b)} - \frac{g_4(a, b, c)}{g_3(a, b)} \right]. \end{aligned} \quad (4.5)$$

The pair distribution function is derived by minimizing  $\Omega$  with respect to  $[1a1]$  as

$$g(r_{12}) = \exp[-\beta\varepsilon(r_{12}) - \rho I_{12}(r_{12})] \quad (4.6a)$$

$$-\rho I_{12}(r_{12}) = \rho \sum_{j=1}^2 J_f(r_{12}) - \frac{1}{2}\rho^2 \sum_{j=3}^6 J_j(r_{12}) \quad (4.6b)$$

$$J_j(r_{12}) = \begin{cases} \int d\mathbf{r}_3 \gamma_j(r_{12}, \mathbf{r}_3) & j = 1, 2 \\ \int d\mathbf{r}_3 d\mathbf{r}_4 \gamma_j(r_{12}, \mathbf{r}_3, \mathbf{r}_4) & j = 3, \dots, 6. \end{cases} \quad (4.7a)$$

$$(4.7b)$$

With the abbreviation  $g_{23} \equiv g(r_{23})$  we write  $\gamma$ 's as

$$\begin{aligned}\gamma_1(\mathbf{r}_{12}, \mathbf{r}_3) &\equiv (g_{12} - 1)(g_{23} - 1) \\ \gamma_2(\mathbf{r}_{12}, \mathbf{r}_3) &\equiv g_{13}g_{23}(A_{123} - 1) \quad A_{123} \equiv \exp(\alpha_{\Delta 123})\end{aligned}\quad (4.8a)$$

$$\begin{aligned}\gamma_3(\mathbf{r}_{12}, \mathbf{r}_3, \mathbf{r}_4) &\equiv (g_{34} - 1)(g_{13}g_{14} - 1)(g_{23}g_{24} - 1) \\ \gamma_4(\mathbf{r}_{12}, \mathbf{r}_3, \mathbf{r}_4) &\equiv g_{34}g_{13}g_{14}(A_{134} - 1)(g_{23}g_{24}A_{234}A_{123}A_{124} - 1) \\ \gamma_5(\mathbf{r}_{12}, \mathbf{r}_3, \mathbf{r}_4) &\equiv g_{34}g_{23}g_{24}(A_{234} - 1)(g_{13}g_{14}A_{123}A_{124} - 1) \\ \gamma_6(\mathbf{r}_{12}, \mathbf{r}_3, \mathbf{r}_4) &\equiv g_{13}g_{14}g_{23}g_{24}(g_{34} - 1)(A_{123}A_{124} - 1).\end{aligned}\quad (4.8b)$$

$A_{123}$  or  $\alpha_{\Delta 123}$  for a triplet  $\Delta 123$  is written using  $\gamma_j(\Delta 123, \mathbf{r}_4)$  with  $j = 7-10$ , which are to be solved iteratively from the following equations:

$$\alpha_{\Delta 123} = \rho \sum_{j=7}^{10} \int d\mathbf{r}_r \gamma_j(\Delta 123, \mathbf{r}_4) \quad (4.9a)$$

$$\begin{aligned}\gamma_7(\Delta 123, \mathbf{r}_4) &\equiv (g_{14} - 1)(g_{24} - 1)(g_{34} - 1) \\ \gamma_8(\Delta 123, \mathbf{r}_4) &\equiv g_{14}g_{24}(A_{123} - 1)(g_{34}A_{234}A_{134} - 1) \\ \gamma_9(\Delta 123, \mathbf{r}_4) &\equiv g_{14}g_{34}(A_{134} - 1)(g_{24}A_{234} - 1) \\ \gamma_{10}(\Delta 123, \mathbf{r}_4) &\equiv g_{24}g_{34}(g_{14} - 1)(A_{234} - 1).\end{aligned}\quad (4.9b)$$

After  $\alpha_{\Delta jkm}$  are solved for all  $\Delta jkm$  from (4.9),  $g(\mathbf{r}_{12})$  is to be solved in a second set of iterations of (4.6)–(4.8).

Minimization of  $\Omega$  with respect to  $[j]$  leads to  $\mu$  and  $p$  equations, as was commented on in previous sections. The latter is

$$\begin{aligned}\beta p = \rho - \frac{1}{2}\rho^2[g(\mathbf{a}) - 1] + \frac{1}{3!}\rho^3 \int d\mathbf{a} \int d\mathbf{b} [2 - (g(\mathbf{a}) + g(\mathbf{b}) + g(\mathbf{a} + \mathbf{b})) + g_3(\mathbf{a}, \mathbf{b})] \\ + \frac{1}{4!}\rho^4 \int d\mathbf{a} \int d\mathbf{b} \int d\mathbf{c} Q\end{aligned}\quad (4.10a)$$

where  $Q \equiv 6 - 2P_1 + P_2 + T - g_4(\mathbf{a}, \mathbf{b}, \mathbf{c})$

$$\begin{aligned}P_1 &\equiv g(\mathbf{a}) + g(\mathbf{b}) + g(\mathbf{c}) + g(\mathbf{a}, \mathbf{b}) + g(\mathbf{b}, \mathbf{c}) + g(\mathbf{a}, \mathbf{b}, \mathbf{c}) \\ P_2 &\equiv g(\mathbf{a})g(\mathbf{c}) + g(\mathbf{b})g(\mathbf{a} + \mathbf{b} + \mathbf{c}) + g(\mathbf{a} + \mathbf{b})g(\mathbf{b} + \mathbf{c}) \\ T &\equiv g_3(\mathbf{a}, \mathbf{b}) + g_3(\mathbf{b}, \mathbf{c}) + g_3(\mathbf{a}, (\mathbf{b} + \mathbf{c})) + g_3((\mathbf{a} + \mathbf{b}), \mathbf{c}).\end{aligned}\quad (4.10b)$$

We note that the  $\rho$ ,  $\rho^2$  and  $\rho^3$  terms are the same as those in (3.12) for the triplet case. The effect of the  $\rho^4$  term on the  $p$  against  $\rho$  curve can be seen by numerical computation.

Since the two-stage iteration to solve all  $\gamma$ 's is time consuming, in order to obtain semi-quantitative information of the solution, we solve an approximated set of  $\gamma$ 's. First in the sum (4.9a) we keep only the  $\gamma_7$  integral to avoid iteration for  $A$ s so that

$$\alpha_{\Delta 123} \approx \rho \int d\mathbf{r}_4 (g_{14} - 1)(g_{24} - 1)(g_{34} - 1). \quad (4.11a)$$

The second approximation is to keep only the  $j = 3$  term in the second sum of (4.6b):

$$-\rho I_{12}(\mathbf{r}_{12}) \approx \rho[J_1(\mathbf{r}_{12}) + J_2(\mathbf{r}_{12})] - \rho^2 J_3(\mathbf{r}_{12})/2. \quad (4.11b)$$

For the numerical calculation of  $p$  and  $\mu$ , we use (3.12) and (3.11) for the triplet case without the 3-body interaction  $\psi$ , i.e. using the superposition relation in (3.8b). We use a 6–12 Lennard-Jones potential. The depth of the potential is written as  $-\varepsilon$ , and  $r_0$  is its position. Figure 1 is for the  $p$  against  $\rho$  curve at  $kT/\varepsilon = 1.5$ . This curve shows the van der Waals loop, and hence the stable liquid phase. The pair radial distribution function  $g(r)$  at  $\rho = 0.60/r_0^{-3}$  in the liquid phase is in figure 2.

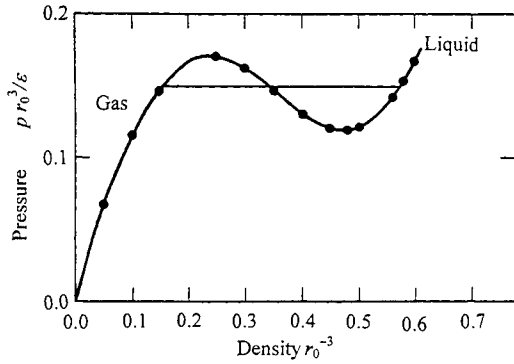


**Figure 1.** Equation of state based on the simplified quartet treatment using the Lennard-Jones potential and at  $kT/\epsilon = 1.5$ .

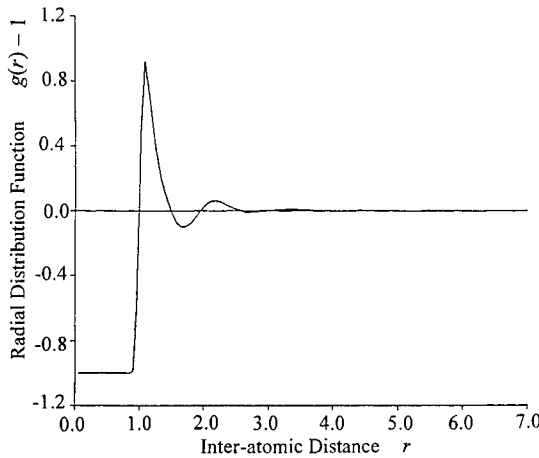


**Figure 2.** The radial distribution function  $g(r)$  corresponding to figure 1 at  $\rho = 0.60/r_0^3$  in the liquid phase. The ordinate is  $h(r) = g(r) - 1$ .

The critical temperature in this approximation is at about  $kT/\epsilon = 1.7$ . This is to be compared with the value 1.3, which is given in table VII of Hansen and McDonald [12] as the summary of experimental and calculation data for Ar. Although figure 2 establishes the liquid phase, we note a problem. Thermodynamics requires

$$\left( \frac{\partial \rho}{\partial \mu} \right)_T = \rho. \quad (4.12)$$

This relation holds nicely in the gas phase, but fails in the liquid phase, as shown in the  $p$  against  $\mu$  plot in figure 3. In all previous applications of the CVM, thermodynamic relations never failed to be satisfied, although numerical values are approximate, and this was counted as one of the advantages of the CVM. The failure in the present case, therefore, is due to the omission of some of the equations derived from the CVM.

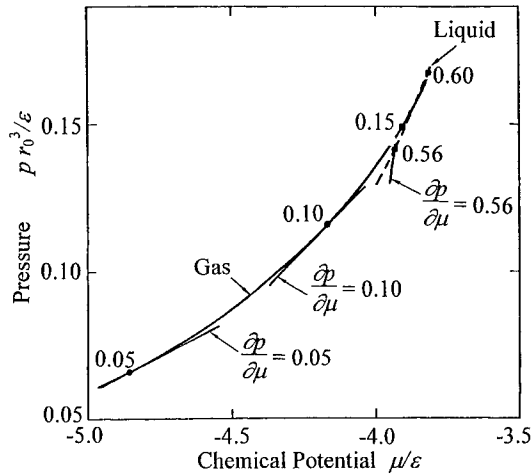


**Figure 3.** The  $p$  against  $\mu$  plot corresponding to figure 1. The full curve is for gas and broken curve for liquid. The numbers on the curves are the local  $\rho$  values from theory. A short full line shows  $\partial p / \partial \mu = 0.56$  for comparison.

## 5. Summary, comments and concluding remarks

We start with a simple cubic lattice as a reference frame in the space, distribute atoms and vacancies to cells, and then let the lattice constant decrease to zero, keeping the shape of the inter-atomic potential unchanged in real space. The correlation correction factors [6] in the CVM [2] are used to construct the entropy for three cases of the basic cluster: all cell pairs, all cell triplets and all cell quartets. The first two cases do not lead to a van der Waals-type equation of state. Using approximations to the set of basic equations, the quartet case does lead to a stable liquid phase.

We started with the simple cubic lattice, but the equations after  $c \rightarrow 0$  do not show any trace of the initial lattice. Therefore, it is judged that the results are independent of the choice of the initial lattice.

When we compare the present method with the Yvon–Born–Green (Y–B–G) approach [13], we notice close similarity in the closure procedure. In cutting off the hierarchy in the Y–B–G method, Kirkwood’s superposition approximation [7] is used. On the other hand, the entropy expression of the CVM is inherently based upon the superposition relations, and therefore it is understandable that in each section we can point out that the superposition approximation holds for the largest cluster of each approximation when there are no many-body interactions. The relation between the present and Y–B–G approaches may be understood more clearly in the Schlijper and Kikuchi paper [4], which is based on the CVM entropy but avoids the  $c \rightarrow 0$  procedure and is written using the distribution functions.

## Acknowledgments

Didier de Fontaine has helped to develop the CVM for many years, and it is a pleasure of the authors to dedicate this paper him. One of the authors (RK) expresses his thanks to S Radelaar for having invited him to Delft to work on this problem, and to A G Schlijper for his contribution to the liquid CVM work.

**References**

- [1] Onsager L 1944 *Phys. Rev.* **65** 117
- [2] Kikuchi R 1950 *Phys. Rev.* **79** 718
- [3] van Baal C M 1973 *Physica* **64** 571
- [4] Schijper A G and Kikuchi R 1990 *J. Stat. Phys.* **61** 143
- [5] Schijper A G and Harris C K 1991 *J. Chem. Phys.* **95** 7603
- [6] Kikuchi R 1994 *Prog. Theor. Phys. Suppl.* **115** 1
- [7] Kirkwood J G 1935 *J. Chem. Phys.* **3** 300
- [8] Kikuchi R 1974 *J. Chem. Phys.* **60** 1071
- [9] Schijper A G and Smit B 1992 *Fluid Phase Eq.* **67** 11
- [10] Percus J K and Yevick G J 1958 *Phys. Rev.* **110** 1
- [11] Fisher I Z and Kopeliovich B L 1960 *Sov. Phys. Dokl.* **5** 761
- [12] Hansen J P and McDonald I R 1976 *Theory of Simple Liquids* (New York: Academic)
- [13] See for example Temperley H N V, Rowlinson J S and Rushbrook G S (eds) 1968 *Physics of Simple Liquids* (Amsterdam: North-Holland)

## Electron and positron states in amorphous $\text{Ni}_{0.4}\text{Pd}_{0.4}\text{P}_{0.2}$

D M C Nicholson<sup>†</sup>, P A Sterne<sup>‡</sup>, J C Swihart<sup>§</sup>, Jeffry Tran<sup>||</sup> and Yang Wang<sup>¶</sup>

<sup>†</sup> Oak Ridge National Laboratory, Oak Ridge, TN 37831-6114, USA

<sup>‡</sup> Lawrence Livermore National Laboratory, Livermore, CA 94550, USA

<sup>§</sup> Physics Department, Indiana University, Bloomington, IN 47405, USA

<sup>||</sup> Physics Department, Luther College, Decorah, IA 52101, USA

<sup>¶</sup> Pittsburgh Supercomputing Center, Pittsburgh, PA 15213, USA

Received 16 September 1999, accepted for publication 10 February 2000

**Abstract.** We performed local density calculations of the electronic and positron states for a 300-atom model of bulk amorphous  $\text{Ni}_{0.4}\text{Pd}_{0.4}\text{P}_{0.2}$ . The procedure for constructing the model and the resulting distribution of bond angles and free volume are described. Comparisons are made to experiment and to models of amorphous  $\text{Ni}_{0.8}\text{P}_{0.2}$ .

### 0. Introduction

Bulk amorphous metals are an interesting class of new materials possessing unique properties that offer exciting possibilities for applications to a broad range of technologies. In contrast to the previous generation of amorphous metals, bulk amorphous metals can be produced in *bulk* form at cooling rates as low as  $\sim 1 \text{ K s}^{-1}$ . The understanding of their structure, is important to the explanation of their low cooling rate. One of the simplest and most studied bulk amorphous metal is  $\text{Ni}_{0.4}\text{Pd}_{0.4}\text{P}_{0.2}$  [1]. We can benefit from the earlier work of Weber and Stillinger [2] who developed interatomic potentials for the conventional metallic glass  $\text{Ni}_{0.8}\text{P}_{0.2}$  that were constructed specifically to reproduce the measured partial pair distribution functions (PDFs) [3]. Structures generated using these potentials have been used as the basis for density functional calculations of the electronic conductivity, density of electronic states, atomic density, and optical reflectivity [4]. The agreement of these calculations with experiment validates the atomic models and the interatomic potentials used in their construction. Recent measurements of the PDF and the Pd distribution function of  $\text{Ni}_{0.4}\text{Pd}_{0.4}\text{P}_{0.2}$  [5] provide a very useful guide for extending the potentials of Weber and Stillinger [2] to the ternary alloy  $\text{Ni}_{0.4}\text{Pd}_{0.4}\text{P}_{0.2}$ . We describe the use of these potentials to generate a 300-atom unit cell model of amorphous  $\text{Ni}_{0.4}\text{Pd}_{0.4}\text{P}_{0.2}$ . We have confidence in our model because it reproduces the measured partial distribution functions, and electronic and positron states calculated with this model agree with photo-emission and positron lifetime measurements. The calculations of the electron and positron states were performed using the first-principles, order- $N$ , locally self-consistent multiple scattering (LSMS) method [6]. We analysed the structure to determine the distribution of bonds, free volume, electronic states, and positron states. Comparisons were made to models of the conventional amorphous metal,  $\text{Ni}_{0.8}\text{P}_{0.2}$ . The most striking contrast is in the amount and distribution of free volume. Because free volume is so closely related to diffusion and the kinetics of glass stability it may be the key to the glass forming ability of  $\text{Ni}_{0.4}\text{Pd}_{0.4}\text{P}_{0.2}$ .

### 1. Computational technique: the LSMS method

The electronic structure of systems with a number of atoms,  $N$  in the unit cell as large as 300 cannot be obtained by conventional band structure methods. The LSMS method is an  $O(N)$  multiple scattering method that is specifically designed for massive parallel processors [6]. It relies on several stationary properties of density functional theory to ensure accurate free energy determination based on an electron density that is determined self-consistently at each site [7]. The LSMS method makes the simplifying assumption that, for the purpose of solving the Schrödinger equation, the effective potential beyond a cluster of neighbouring atoms (the local interaction zone (LIZ)) surrounding each atom can be approximated by a constant. Each atom is then taken to be at the centre of its own LIZ. In the calculations presented here the atomic potentials are taken to be spherical and are obtained self-consistently within the atomic-sphere-muffin-tin approximation [8]. The LIZ is taken to be a sphere of radius 10 Bohr radii.

### 2. Atomic model

The calculations were performed for a periodically reproduced cubic box containing an amorphous network consisting of 300 atoms for which the atomic positions had first been relaxed to a local energy minimum via two-body interactions [4].

The starting point for generating the amorphous configurations was a previously published [4] structure for amorphous  $\text{Ni}_{0.8}\text{P}_{0.2}$ . This configuration was generated by random packing, followed by interchanges to eliminate P–P neighbours, and finally relaxation via the pair potentials of Weber and Stillinger. The  $\text{Ni}_{0.8}\text{P}_{0.2}$  model structure has PDFs that agree well with experiment. We have considerable confidence in this structure because it has been used as the basis for many calculations that agree with experiment. However the algorithm that eliminated P–P nearest neighbours only frees the sample of P–P pairs that are closer than the smallest Ni–Ni distance. To remedy this weakness, without completely abandoning this model that has served us well, we scaled ‘ $r$ ’ by a factor of 0.5 in the P–P potential in order to force greater P–P separation. We also made a very small adjustment to the Ni–P potential. This left the model substantially intact, but pushed those few closely-spaced phosphorus pairs to positions clearly identifiable as second nearest neighbours. The Pd-containing structure was then generated by randomly replacing half of the Ni by Pd. We then relaxed the structure using Ni–Pd, Pd–Pd, and Pd–P potentials introduced to augment the already defined Ni–Ni, Ni–P, and P–P potentials. The newly-introduced potentials were adjusted to optimize agreement with the measured partial distribution functions. The potentials are of the form

$$V_{ij}(R) = C_{ij} e^{(\alpha_{ij} R - 1.652\ 194)^{-1}} [(\alpha_{ij} R)^{-12} - 1] \Theta(1.652\ 194 - \alpha_{ij} R) \quad (1)$$

with the parameters as given in table 1.  $\Theta(x)$  is the heaviside function. The PDFs from the model are compared to the measured values [5] in figure 1.

**Table 1.** Parameters for potentials. Units:  $\alpha$  is in units of inverse fcc Ni–Ni distance of 2.49 Å and  $C$  is in  $10^{-12}$  ergs.

	Ni–Ni	Ni–Pd	Ni–P	Pd–Pd	Pd–P	P–P
$C_{ij}$	1.134	1.172	1.701	1.211	1.7011	0.567
$\alpha_{ij}$	1.000	0.900	1.080	0.850	0.950	0.755

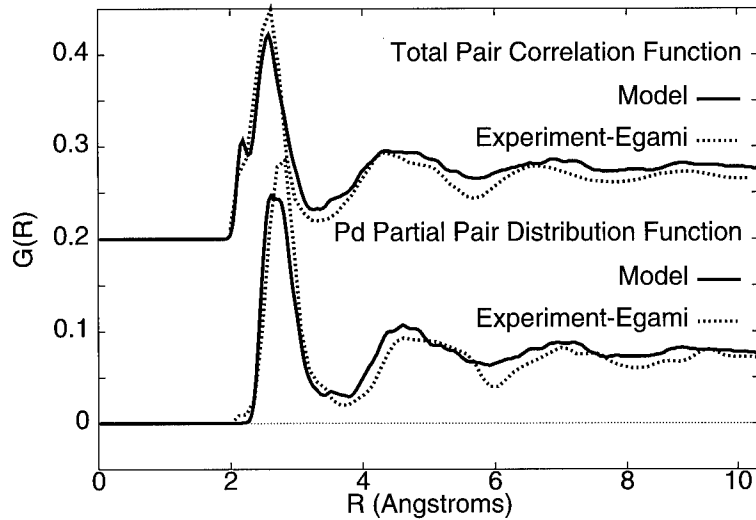


**Figure 1.** Comparison of model (full curves) amorphous pair distribution functions to measurements by Egami *et al* [5] (broken curves).

### 3. Stability and diffusion

Like many metallic glasses ( $Ni_xPd_{1-x})_{0.8}P_{0.2}$ ) alloys are associated with a deep eutectic. A reasonable assumption is that at compositions where the liquid state is stable at unusually low temperatures the amorphous phase, which is essentially a frozen liquid, has a free energy competitive with alternative crystalline phases. If long diffusion paths are required to reach energetically-favoured crystalline structures, or if diffusion barriers are high, the conditions for glass formation are enhanced.

In crystals, the diffusion rate is controlled by the density of vacancies and the hopping time. The hopping time depends on the height of the barrier to vacancy hopping. In glasses the definition of a vacancy is not clear cut. Sietsma and Thijssse [9] have made progress toward a workable definition of a vacancy in glass. They characterize the unoccupied regions in the glass system according to their volumes and number of surrounding atoms. They observe that annealing eliminates large, local, free-volume elements that have greater than nine surrounding atoms. These large volumes, which tend to anneal out, are considered to play the role of vacancies, while those that remain are thought to be similar to interstitial sites or constitutional vacancies in crystals. The large and small volumes are referred to as holes and voids, respectively. The distribution of free volume, because it dominates diffusion is likely to play an important role in the kinetic stability of the glass.

We attempt to extend the understanding of the free volume in two ways. First, because our model is based on matching the measured PDFs, there is the hope that it also reproduces characteristics of the distribution of free volume found in the experimental sample. Hence, we study the distribution of free volume in our model. Although the PDFs do not uniquely determine the atomic arrangement, they do constrain it considerably and the distribution of free volume in our model may be indicative of its distribution in a real sample. Second, we study positron wavefunctions. Because positrons are repelled by the nuclei, injected positrons spend most of their time meandering through the interstitial regions and vacancies until they annihilate. If defects that trap the positrons are plentiful, the majority of positrons

will diffuse through the system for only a short time before being trapped. Once trapped they find themselves in a region of low electron density and have an extended lifetime characteristic of the type of defect (i.e. in a crystal typical traps would be monovacancies and divacancies). We take the initial steps necessary for interpreting the information available in the annihilation photons; we calculate the positron density and lifetime.

#### 4. Atomic structure

We can further analyse the structure by tabulating distributions of bond angles. We find that the distribution of angles (figure 2) in  $\text{Ni}_{0.4}\text{Pd}_{0.4}\text{P}_{0.2}$  is very similar to the distribution in  $\text{Ni}_{0.8}\text{P}_{0.2}$ . They both peak near  $\theta = 60^\circ$  and  $108^\circ$  characteristic of icosahedral packing and differ only in small details. Fcc packing would have had peaks at  $60^\circ$ ,  $90^\circ$ , and  $120^\circ$ . The population of bond angle can be subdivided according to whether the vertex atom is phosphorus or transition metal and the number of phosphorus atoms among the remaining two atoms that form the angle. The angle populations involving only transition metal atoms at the two compositions are very similar and are very icosahedral in nature. The angles with a P vertex have very similar distributions at the two compositions; the angles are predominately around  $70^\circ$ , consistent with a lower coordination around P. The case of a transition metal vertex and a P and transition metal atom completing the angle shows the greatest change with composition. This change is because Pd and Ni sit at different distances from the phosphorus due to their different sizes. The angles formed by a transition metal atom at the vertex and two phosphorus atoms are distributed in a broad peak (not shown) centred at  $100^\circ$  with no angles below about  $80^\circ$  because there are no P-P nearest neighbours.

Another way of describing the bonds is to look at the atoms surrounding each bond. In a perfectly icosahedral system each bond would have five surrounding atoms that are common

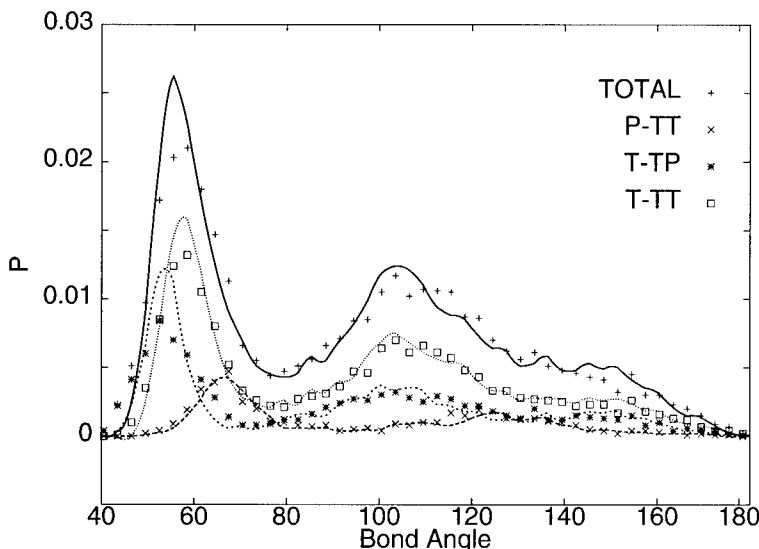


**Figure 2.** The distribution of bond angles: the curves denote results for  $\text{Ni}_{0.8}\text{P}_{0.2}$ ; the solid curve is for all bond angles, the long-dash curve is for the P-vertex bonding to two Ni, the short-dash curve is for the Ni-vertex bonding to a P and a Ni, the dotted curve is for all Ni. The symbols apply to  $\text{Ni}_{0.4}\text{Pd}_{0.4}\text{P}_{0.2}$  and are labelled in the key, *T* stands for Ni or Pd. For example, P-TT stands for a phosphorus-vertex bonding with two transition metal atoms.

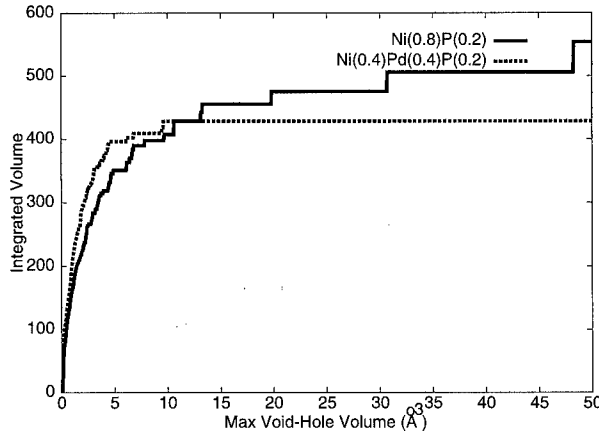


**Figure 3.** The integrated distribution of free volumes:  $\text{Ni}_{0.8}\text{P}_{0.2}$  is denoted by a full curve and  $\text{Ni}_{0.4}\text{Pd}_{0.4}\text{P}_{0.2}$  is denoted by a broken curve.

nearest neighbours to the two atoms that form the bond. Fcc would have four bond neighbours. In our models we find that the most commonly occurring number of bond neighbours is five. About half the bonds have five bond neighbours, with the remaining bonds having numbers of neighbours predominately in the range from four to seven. For transition metal bonds about four of the surrounding atoms are transition metal atoms and one is P. The bonds with more than five neighbours usually have an additional P. Again, there is no clear-cut distinction between the two systems. From the point of view of bonds the structure behaves substitutionally, with local dilation to account for the larger size of Pd, but on average preserving the bond angles. This is consistent with the observation made by Egami *et al* [5]: that the PDFs are roughly concentration independent; and the observation of Alamgir *et al* [10]: that the core levels are roughly concentration independent. It is doubtful that these small differences in bond statistics can be held accountable for the much greater glass forming ability of  $\text{Ni}_{0.4}\text{Pd}_{0.4}\text{P}_{0.2}$ .

Another way to characterize the atomic structure is to look where the atoms are not. We construct Voronoi polyhedra [11] according to the radical plane construction [12] using the radii 2.293, 2.66, and 1.963 au for Ni, Pd and P, respectively. We then shift our attention to the points farthest from the atoms, the vertices of the Voronoi polyhedra. These are the points associated with the free volume [9]. For each vertex we find the largest sphere that does not overlap any atomic sphere. We then group those vertex-centred spheres that overlap each other. The space defined by the overlapping, vertex-centred spheres defines a cell of free volume. The distribution of the volumes of these cells is shown in figure 3. The figure shows the integrated free volume (i.e. the sum of all free volume below a limiting void or hole size). There are two major differences between the two compositions. The Pd-containing composition has less free volume and less of the free volume is associated with large-volume cells. This could be a manifestation of the higher packing fraction possible with a distribution of atomic sizes.

In bulk amorphous alloys, as proposed by Sietsma and Thijssse, diffusion is probably controlled by the large free volumes, holes, that are smaller than vacancies but larger than the interstitial volumes in ordered materials. Reduction of the number of these holes may be the mechanism by which bulk amorphous alloys are prohibited from diffusive transformation to the crystalline ground state even when cooled slowly. It would be valuable to have measured values for the positron lifetimes at these two compositions. The validity of our model free-volume distributions would be supported if the lifetime was longer for  $\text{Ni}_{0.8}\text{P}_{0.2}$ , indicating that the more plentiful holes trapped the positrons.

## 5. Positron states

Positrons are trapped by defects, particularly vacancies. When they annihilate they provide information about the electron density at the defect as well as the atomic species of surrounding atoms. In a simple system, such as well annealed Cu with a few well dispersed monovacancies, two lifetimes are observed. One is a short lifetime associated with itinerant positrons in the bulk, and the other is a longer lifetime associated with positrons trapped at the vacancies. The density of vacancies and the electron density at the vacancy site can be determined. In more complex systems there may be one lifetime, or several lifetimes. For example, amorphous metals typically have one broadened lifetime, the interpretation of which is not clear. It is still debatable whether all annihilation is of the bulk type or from defects. In these more complex systems models are needed to extract useful information from the positron experiments.

The two photons created when a positron annihilates with an electron carry away the momentum and energy of the pair. Because the positrons have (shortly after injection) only thermal energies, a high-momentum photon pair indicates annihilation with a high-momentum core electron, rather than a low-momentum valence electron. The high momentum part of the core annihilation profile as a function of momentum is characteristic of the element and can be obtained by experiments on the pure element and by calculation [13]. In multicomponent systems, the high momentum profile of positrons trapped in vacancies can be compared to profiles from the pure elements to indicate the atomic number of the atom whose core electron participated in the annihilation [13]. The simplest assumption is that the atoms participating in the annihilation are nearest neighbours of the trapping defect.

At this stage we can calculate the positron wavefunctions and determine which nuclei have the greatest overlap with the positron density. We did this by calculating the electrostatic potential of our self-consistent electron density. The local approximation to the electron–positron correlation potential [14] was added to the electrostatic part to provide a one-particle Schrödinger equation for the positrons. We used the LSMS to solve for the positron wavefunctions. The site decomposed density of states shows that the low-energy positrons are predominately on P sites. The product of the electron and positron densities adjusted for correlation and multiplied by the annihilation cross section gives the positron annihilation rate [14]. We have not yet incorporated the matrix elements that couple the positron wavefunctions to the electronic core levels. Therefore, we cannot predict the characteristic patterns that will be seen in high-momentum positron annihilation experiments on  $\text{Ni}_{0.4}\text{Pd}_{0.4}\text{P}_{0.2}$  when they are carried out. We have observed that the positrons have their greatest overlap with the phosphorus core so we can anticipate that the high-momentum annihilation will indicate annihilation at phosphorus cores.

We can compare our calculated positron lifetime to some interesting preliminary measurements by Somieski [15] of the positron lifetime in  $\text{Ni}_{0.4}\text{Pd}_{0.4}\text{P}_{0.2}$ . Their measurements give lifetimes in an as-quenched specimen distributed in the range 140–180 ps [15]. After annealing for 24 h at 200 °C a second group of lifetimes appears in the range 100–120 ps. Our calculated average lifetime for the lowest eight positron states is 114 ps. One possible explanation of these results is that the as-quenched sample has large defects similar to quenched-in thermal vacancies in rapidly-cooled crystals. These defects in the amorphous structure may have long lifetimes in the 140–180 ps range. These defects could have large trapping cross sections that could account for nearly all annihilation events. In the computer-generated model these large vacancies are probably precluded by the model construction procedure. When the experimental sample is annealed, the number of large vacancies is reduced and eventually the smaller-free-volume cells similar to those seen in the model begin to trap positrons with sufficient probability to be observed in the experiments in the range 100–120 ps.

## 6. Electronic states

The electronic density of states is modified considerably by the addition of Pd (figure 4). Substitution of Pd for Ni greatly increases the overall d-band width of  $\text{Ni}_{0.4}\text{Pd}_{0.4}\text{P}_{0.2}$  relative to  $\text{Ni}_{0.8}\text{P}_{0.2}$  [4]. This occurs because of the broader d-band width of elemental Pd and because the centres of the Ni and Pd d-bands are displaced from each other. The Ni states occupy the upper part of the band and the Pd states dominate in the lower part of the band. This separation is seen in the behaviour of the x-ray photo-emission spectrum (XPS) as a function of Pd concentration [10].

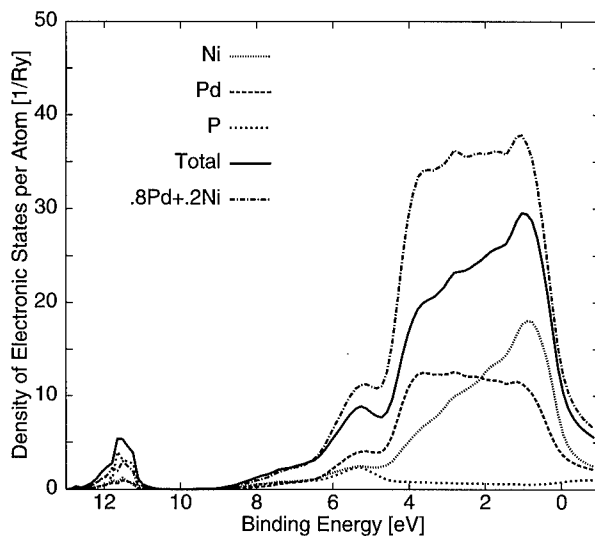


**Figure 4.** Density of states as function of electron energy for amorphous  $\text{Ni}_{0.4}\text{Pd}_{0.4}\text{P}_{0.2}$ ; the zero of the energy scale is the Fermi energy. The dash-dot curve is the XPS calculated using a rough approximation to the inclusion of matrix elements (arbitrary units).

There is a long tail of states below the d-band that are contributed equally from Ni, Pd, and P states. From our experience with Ni-P we speculate that these tail states are somewhat localized due to the disorder. The fact that all species contribute equally to these tails would tend to make them independent of composition. This can be seen in the lack of composition dependence of the XPS data between 5 and 8 eV.

We find low-lying phosphorus states split-off from the d-bands. These states may be responsible for the barely perceptible bulge in the XPS data at a binding energy of 12.5 eV.

Our calculated density of states at the Fermi energy is higher than that seen in the XPS. Furthermore, we did not see a minimum in the density of states near the Fermi energy that, if present, would have indicated the effects of the stabilizing mechanism suggested by Nagel and Tauc [16]. Our density of states has a dip at 4.5 eV that is not seen in the XPS. A further difference between the density of states and the XPS is that the XPS d-band is almost symmetric about the band centre, while the calculation shows a strong Ni peak at the upper d-band edge. In order to show how inclusion of matrix elements affect the agreement, we plotted the weighted sum of the Ni and Pd densities of states. We weighted the Pd states by a factor of four relative to the Ni states. This is based on the statement of Almagir *et al* [10] that the  $P$  matrix element is very small and the matrix element for Pd is four times as large as for

Ni. This rough approximation to a true calculation [17] of the XPS gives excellent agreement with the measured spectrum.

## 7. Conclusions

We have used the PDFs recently measured by Egami *et al* [5] to develop interatomic potentials suitable for Ni–Pd–P amorphous alloys. We do not make any claim for the usefulness of the energy comparisons based on these potentials. Combined with the procedure of randomly packing hard spheres they should be viewed as part of an interpolation or extrapolation procedure that can use the PDFs of  $\text{Ni}_{0.8}\text{P}_{0.2}$  and  $\text{Ni}_{0.4}\text{Pd}_{0.4}\text{P}_{0.2}$  to construct models at other compositions. The geometric properties of the model are discussed along with the resulting electron and positron states. The comparisons of the electronic density of states and positron lifetimes with measurements are promising. These comparisons are not straight forward and there are additional questions to be addressed; still, it is fair to say at this stage that there are no contradictions that discredit the validity of our model structure.

## Acknowledgments

Electronic and positron state calculations were performed at the Center for Computational Science at ORNL and the Pittsburgh Supercomputing Center. Work sponsored by ORNL Laboratory Directed Research and Development Fund, BES–DMS, and OCTR–MICS US Department of Energy under subcontract DEAC05-96OR22464 with Lockheed-Martin Energy Research Corporation. This work was also performed under the auspices of the US Department of Energy by the Lawrence Livermore National Laboratory under contract W-7405-ENG-48.

## References

- [1] He Y, Schwarz R B and Archuleta J I 1996 *Appl. Phys. Lett.* **69** 1861  
Schwarz R B and He Y 1997 *Proc. Int. Symp. on Metastable, Mechanically Alloyed and Nanocrystalline Materials* (Los Alamos, NM: Los Alamos National Laboratory) Publication LA-UR-96-1703
- [2] Weber T W and Stillinger F H 1985 *Phys. Rev. B* **31** 1954–63
- [3] Lamarter P and Steeb S 1985 *Rapidly Quenched Metals* ed S Steeb and H Warlimont (Amsterdam: Elsevier) pp 459–68
- [4] Yang H, Swihart J C, Nicholson D M and Brown R H 1993 *Phys. Rev. B* **47** 107–14  
Yang H, Swihart J C, Nicholson D M and Brown R H 1993 *Materials Theory and Modeling (Mater. Res. Soc. Symp. Proc. vol 291)* ed J Broughton, P D Bristowe and J M Newsam, pp 419–24
- [5] Egami T, Dmowski W, He Y and Schwarz R B 1998 *Met. Mater. Trans. A* **29** 1805
- [6] Wang Y, Stocks G M, Shelton W A, Nicholson D M C, Szotek Z and Temmermann W M 1995 *Phys. Rev. Lett.* **75** 2867–70
- [7] Nicholson D M C, Stocks G M, Wang Y, Shelton W A, Szotek Z and Temmerman W M 1994 *Phys. Rev. B* **50** 14686–9
- [8] Zhang X-G and Nicholson D M C 1999 *Phys. Rev. B* **60** 4551
- [9] Sietsma J and Thijssse B J 1995 *Phys. Rev. B* **52** 3248
- [10] Alamgir F M, Jain H, Miller A C, Williams D B and Schwarz R B 1999 *Phil. Mag. B* **79** 239
- [11] Yang Wang and Stocks G M 1994 *Phys. Rev. B* **49** 5028
- [12] Watson R E and Bennett L H 1991 *Phys. Rev. B* **43** 11642
- [13] Asokakumar P *et al* 1996 *Phys. Rev. Lett.* **77** 2097
- [14] Sterne P A and Kaiser J A 1991 *Phys. Rev. B* **43** 13892
- [15] Bertram Somieski 1998 Oak Ridge National Laboratory, unpublished results
- [16] Nagel S R and Tauc J 1975 *Phys. Rev. Lett.* **35** 380
- [17] Winter H, Durham P J, Temmerman W M and Stocks G M 1986 *Phys. Rev. B* **33** 2370

## Change from a bulk discontinuous phase transition in V<sub>2</sub>H to a continuous transition in a defective near-surface skin layer

J Trenkler<sup>†¶</sup>, H Abe<sup>†+</sup>, P Wochner<sup>‡</sup>, D Haeffner<sup>§</sup>, J Bai<sup>||</sup>, H D Carstanjen<sup>‡</sup> and S C Moss<sup>†</sup>

<sup>†</sup> Department of Physics, University of Houston, Houston, TX 77204-5506, USA

<sup>‡</sup> Max-Planck-Institut für Metallforschung, D-70569 Stuttgart, Germany

<sup>§</sup> Advanced Photon Source, Argonne National Laboratory, Argonne, IL 60439-4815, USA

<sup>||</sup> Oak Ridge Associated Universities, Oak Ridge, TN 37831, USA

Received 27 October 1999, accepted for publication 13 April 2000

**Abstract.** Using high- and low-energy x-ray scattering techniques, we have studied the effect of defects on the  $\beta_1$ – $\beta_2$  phase transition in V<sub>2</sub>H. Since we earlier observed two length scales in this crystal, we focus here exclusively on either the pure bulk or the defective skin layer, which is several micrometres thick. While we found a strong and narrow discontinuous transition in the bulk, there is a continuous transition in this defective skin layer in which the mosaic spread decreases with depth. We suggest that the strain field associated with the change of the mosaic spread most likely prompts the conversion of the order of the phase transition.

We present here a study of the effect of defects on the order-disorder  $\beta_1$ – $\beta_2$  phase transition in the interstitial alloy V<sub>2</sub>H, which is believed to be a system analogous to a metamagnet [1, 2]. Recent theoretical efforts have shown that a temperature-driven discontinuous transition of a pure system may be converted to a continuous transition if quenched i.e. static, bond randomness is added [3–8]. Very recently, it was shown that random fields convert a first-order transition to a second-order transition even more effectively [9, 10]. In this paper, we report an experimental study of V<sub>2</sub>H through the  $\beta_1$ – $\beta_2$  phase transition either exclusively in the pure bulk, which displays a discontinuous phase transition, or in a defective ‘skin’ layer of the same crystal, which exhibits a continuous transition; the skin layer may be understood as a defective layer of several micrometres thickness below the surface.

The  $\beta_1$ – $\beta_2$  phase transition is from an ordered monoclinic  $\beta_1$  phase to a disordered body-centred tetragonal (bct)  $\beta_2$  phase in which the  $c$ -axis is along  $z$  (for the phase diagram see [11]). While in the  $\beta_1$  phase, mostly one sublattice, namely the  $z$ -axis octahedral  $O_{z1}$  sublattice, is occupied by hydrogen (H) atoms, both the  $O_{z1}$  and  $O_{z2}$  sublattices are occupied in the  $\beta_2$  phase (for a review see [12–14]). The  $\beta_1$ – $\beta_2$  transition is particularly interesting as it appears to be analogous to the transition of a metamagnet for which tricritical model calculations can be found (for a review see [15]). The ferromagnetic sites of a metamagnet can thereby be compared to occupied  $O_{z1}$  sites and the antiferromagnetic coupling between the layers to the alternating occupation of  $O_z$  sites [1]. The occupation of mainly  $O_{z1}$  sites in every other  $(0\ k/2\ \bar{k}/2)$  plane leads to a periodic distortion of the vanadium (V) host lattice and thus to  $\{0\ k/2\ \bar{k}/2\}$  superstructure peaks (pseudo bct notation) [14, 16, 17]. In this ordering process,

¶ Present address: Max-Planck-Institut für Metallforschung, D-70569 Stuttgart, Germany.

† Present address: National Defense Academy, Hashirimizu, Yokosuka 239-8686, Japan.

the structure factor can be expressed in terms of the modulated distortion of the V lattice planes [18] ( $h, k, l$  are the conventional Miller indices).

Our crystal was loaded by R Hempelmann and subsequently polished and etched (for the sample preparation see [2, 19, 20]). A residual pressure and a hydrogen extraction measurement yielded a (bulk) concentration ratio of  $c_H/c_V = 0.525 \pm 0.005$ .

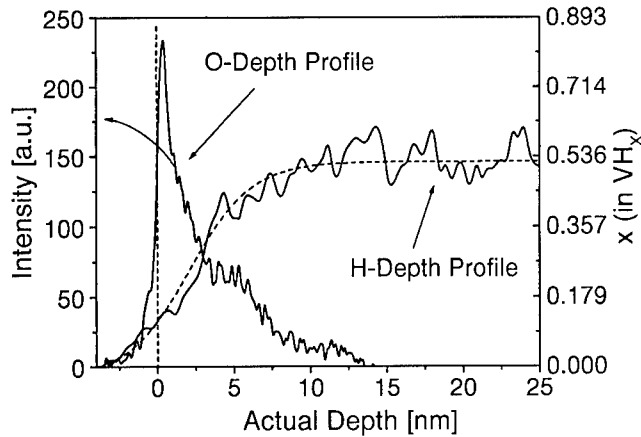


**Figure 1.** Corrected H and O depth profiles at the near-surface of our  $VH_{0.525}$  crystal, measured by HERDA. The vertical broken line indicates the position of the free surface.

A high-resolution elastic recoil detection analysis (HERDA) measurement [20], a secondary neutral mass spectroscopy (SNMS) measurement [2], a larger  $d$  spacing in the defective near-surface layer than in the bulk [2] and the decay of the mosaic spread with penetration depth [21] all provide evidence for the presence of a *defective* near-surface layer in our sample. Since the ‘penetration depth’ is the effective absorption-corrected vertical depth in an x-ray experiment, we shall call it the ‘effective depth’ in what follows. While the oxygen (O) content decays drastically with increasing depth in the first 150 Å, the hydrogen (H) content increases to an equilibrium concentration of  $c_H/c_V = 0.525$  for depths larger than 150 Å, revealed from the HERDA and SNMS measurements. The O and H gradients obtained from HERDA measurements are shown in figure 1 (for the SNMS measurement see figure 2 in [2]). We emphasize that the levelling off of the H concentration for depths larger than 150 Å corresponds exactly to the bulk concentration, which was independently determined as described above. Moreover, a protective oxide cap layer forms naturally and is essential in  $V_2H$  to prevent loss of hydrogen. Using  $E = 9.0$  keV x-ray photons and low momentum transfers in our most surface-sensitive experiment, the influence in the scattering contribution arising from the upper 150 Å, which is the region of the H and O gradient, is about 0.2%, deduced from the fraction  $R$  of the diffracted intensity down to an effective depth  $d$  in the sample, calculated by  $R = 1 - \exp[-2(\mu d / \sin \Theta)]$  for a symmetric scattering geometry, where  $\mu$  is the linear absorption coefficient of x-rays, and  $\Theta$  is the Bragg angle [22]. The only ‘defect’ penetrating up to several micrometres is the decaying mosaic spread in our sample, as shown in figure 2. We note that there must be a depth-dependent stress field associated with the strong change in the mosaic spread with effective depth [23]. This identification of the active defects in the skin layer is at variance with our earlier suggestion [2] that defect-decorated oxide clusters are responsible for the unusual crossover behaviour of the critical scattering in the skin layer at larger reduced temperatures. In a later treatment following this paper [21] we note the similarity in the decay of the mosaic spread in figure 2 with the decay of the

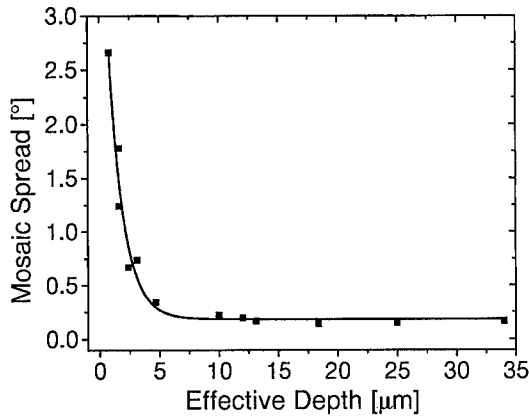


**Figure 2.** Mosaic spread of our crystal against effective depth, obtained from five different experiments at different reflection angles and different x-ray energies, namely  $E = 5.9, 9.0, 10.5, 11.95$  and  $17.5$  keV.

correlation length and ‘actual’  $T_C$ . We are thus drawn to consider the dislocation network and its associated strain field as the active agent in generating the putative random bonds/random fields in the skin layer.

We performed several x-ray diffraction experiments both with high-energy photons in transmission geometry to probe the pure bulk, and with low-energy photons in reflection geometry to measure the defective near-surface skin layer. The high-energy transmission x-ray experiment was performed at the undulator beamline SRI-CAT, 1-ID beamline, at the Advanced Photon Source (APS) at the Argonne National Laboratory with an optimal x-ray energy of  $E = 44.1$  keV from a Si-311 monochromator, together with a Si-111 analyser crystal and a Ge solid-state detector. We verified that there was no contamination from higher harmonics throughout the experiment. The reflection experiments were performed with Mo  $K\alpha 1$  x-rays at a RU-200 in-house rotating anode source, and with  $E = 5.9$  and  $9.0$  keV x-rays at the beamline X14A at the National Synchrotron Light Source (NSLS) at the Brookhaven National Laboratory. In the reflection experiments, we used a focussing Si-111 monochromator, and for the NSLS experiments additionally a Ge-111 analyser crystal. We note that the effective penetration of the x-rays was tuned by choosing appropriate x-ray energies and incident angles, which then yielded a depth sensitivity on a micrometre scale. The high-energy experiment in the transmission mode and the low-energy experiments in the reflection mode allowed us to detect separately the influence arising from the defective skin layer and from the bulk since we earlier observed two length scales in this crystal [2], i.e. a broad ‘bulk’ peak and a diverging sharp peak from the defective surface skin. In all experiments, the sample was mounted in a strain-free manner under a vacuum of approximately  $10^{-4}$  Torr. The temperature fluctuations of the entire set-up were less than  $0.05$  K at  $T > 445$  K. Sufficient time, determined by quenching the sample and detecting the recovery of the superstructure reflection, was taken to reach equilibrium at each temperature.

The radial intensity distribution around the higher-order fundamental reflection ( $0\ 4\ \bar{4}$ ) clearly revealed a  $0.6$  K broad two-phase region in the defective skin layer. A second fundamental reflection appears for  $T = T_C - 0.3$  K, which is associated with the high-temperature  $\beta_2$  phase, as shown in figure 2 of [20]. While the second fundamental reflection is the only remaining reflection for  $T > T_C + 0.3$  K, the fundamental reflection associated with the  $\beta_1$  phase disappeared for  $T > T_C + 0.3$  K, yielding a  $0.6$  K narrow two-phase region.

According to Krivoglaz [24], however, the composition and the concentration  $c_H/c_V$  of the sample is still considered close enough to the critical point to observe critical behaviour. We note, as above, that  $T_C$  was determined using the extrapolated FWHM of a superstructure intensity line profile, which is constant below  $T_C$  and increases above  $T_C$ ; the intersection yields an extrapolated or ‘effective’  $T_C$ .

We now turn to the defective skin layer. Using x-rays in the reflection geometry to tune the effective penetration as described above, the long-range order parameter exponent in the defective skin layer can be determined from the integrated Bragg intensities,  $I$ , of superstructure reflections, where  $I \propto \Phi^2 = -B(T/T_C - 1)^{2\beta}$  and  $\Phi$  is the Bragg–Williams order parameter [25],  $B$  is a constant, and  $\beta$  is the critical exponent (for the data corrections see [20]). From the corrected integrated Bragg intensities of the  $(0 \frac{5}{2} \frac{5}{2})$  and  $(0 \frac{7}{2} \frac{7}{2})$  superstructure reflections, we obtained a value of  $\beta = 0.13 \pm 0.02$  by including the narrow two-phase region (broken curve) as shown in figure 3 (reproduced from [20]). Omitting the data point associated with the two-phase region within 0.6 K by treating, in this case  $T_C$  as a fit parameter as, for example in [1],  $\beta = 0.18 \pm 0.02$  is obtained (full curve), when both reflections were considered. If we neglect the influence of the two-phase region, our experimental value of  $\beta$  indicates that we observe tricritical behaviour in the defective skin layer although it is smaller than the theoretically expected value ( $\beta = 0.25$ ). Our value is comparable with an earlier measurement [1] and with other tricritical systems. For example,  $\beta = 0.15$  in  $\text{CsCoCl}_3 \cdot 2\text{D}_2\text{O}$  by Bongaarts and de Jonge [26],  $\beta = 0.18$  in  $\text{ND}_4\text{Cl}$  by Yelon *et al* [27] and, more recently, by Seec *et al* [28] where  $\beta = 0.16$  was obtained from lattice parameter data in  $\text{ND}_4\text{Cl}$  before applying lattice compressibility corrections, while  $\beta = 0.22$  was found after the corrections.

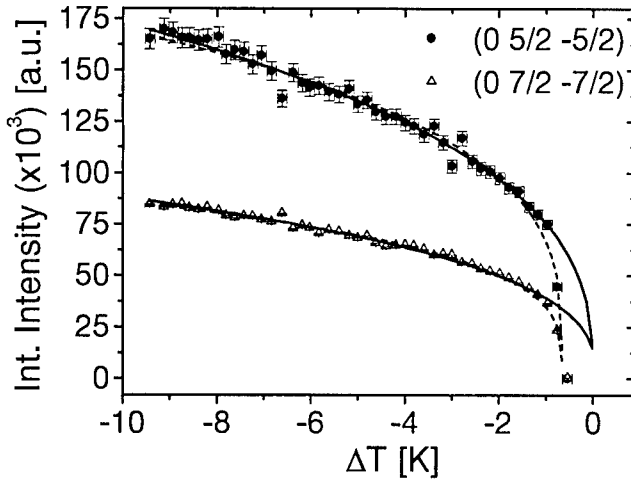


**Figure 3.** Corrected integrated intensities of the  $(0 \frac{5}{2} \frac{5}{2})$  and  $(0 \frac{7}{2} \frac{7}{2})$  superstructure reflections in a heating run against  $\Delta T = T - T_C$ , measured with Mo  $\text{K}\alpha$  x-rays to probe the defective near-surface skin layer (for the determination of  $T_C$ ; see text). This leads to the critical exponent  $\beta = 0.13 \pm 0.02$  by including the small (0.6 K) two-phase region (broken curve). Neglecting the data point associated with the two-phase region and letting  $T_C$  vary as a fit parameter, we obtain  $\beta = 0.18 \pm 0.02$  (full curve). (Reproduced from [20].)

On the other hand, the high-energy experiment in the transmission geometry yielded a strong discontinuous (first-order) phase transition in the bulk, as shown in figure 4. This can be seen by the strong drop of the  $(0 \frac{5}{2} \frac{5}{2})$  superstructure intensity by a factor of more than 400 at  $T_C$ . The sharp transition width of about 0.3 K, together with the abrupt broadening of

the superstructure intensity profiles, as shown in the inset of figure 4, supports strongly the presence of a discontinuous transition in the bulk.

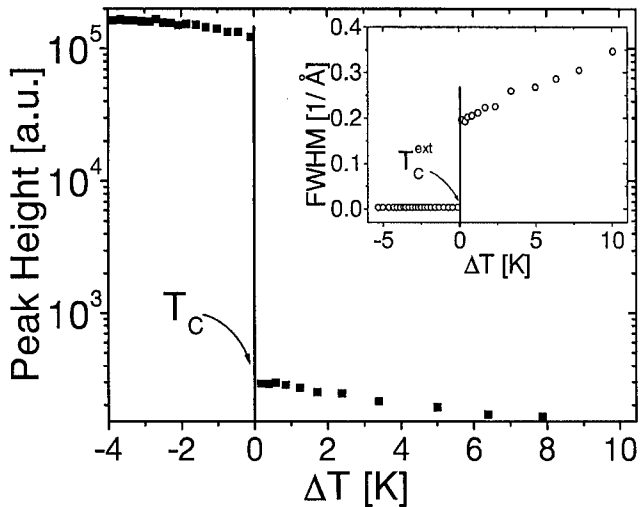


**Figure 4.** Peak height of the  $(0 \frac{5}{2} \frac{5}{2})$  superstructure reflection against  $\Delta T = T - T_C$  in a heating run, measured by high-energy x-ray diffraction in transmission geometry to probe the (pure) bulk. A strong discontinuous phase transition in the bulk is displayed with an intensity drop by a factor of more than 400. The inset shows the FWHM of the  $(0 \frac{5}{2} \frac{5}{2})$  superstructure reflection against  $\Delta T = T - T_C$  in a heating run, confirming a strong discontinuous phase transition in the bulk.

The change in the order of the transition from the bulk-discontinuous to the defective skin layer-continuous (tricritical) transition is not associated with a change in the concentration ratio of  $c_H/c_V$ . Since we measured  $c_H/c_V = 0.525 \pm 0.005$  in the bulk by residual pressure and hydrogen extraction measurements, and since the levelling-off in the concentration of H shown in figure 1 is the same after the first 150 Å, being 99.8% of the scattering contribution for our most surface-sensitive measurement (see also above), the conversion of the order of the transition is certainly not due to a change in the position of the phase diagram due to a concentration change (no evidence for phase separation in the vicinity of the Bragg peaks was found outside the narrow 0.6 K region). The change in the order of the transition is also not due to the presence of dissolved oxygen in the first 150 Å since the fraction  $R$  of the diffracted intensity arising from the upper 150 Å is less than 0.2% as stated above. Furthermore, the strong first-order transition in the bulk with a transition width of less than 0.3 K is not accompanied by a crossing of a two-phase coexistence region since two Bragg peaks associated with either the low- or the high-temperature phase were not observed in the bulk. We therefore propose, as discussed earlier, that the observed change in the order of the phase transition, as the bulk grades into the skin layer, may be due to the presence of random bonds [3–8], or random fields [9, 10], and is most likely prompted by the increase in the mosaic spread (dislocation walls) with decreasing effective depth, since the change of the mosaic spread is the only ‘defect’ penetrating up to several micrometres. We also note that the fitted  $T_C$  for the long-range order parameter measured in reflection was 443.5 K [20]; the  $T_C$  of the bulk is substantially lower, or the bulk-order would overwhelm the surface order in a reflection experiment that probes both i.e. with Mo K $\alpha$  radiation, or at 11.96 keV at the NSLS.

In summary, we have observed a change in the order of the phase transition in a V<sub>2</sub>H crystal, namely a discontinuous transition in the pure bulk and a continuous transition in the

presence of defects in a near-surface skin layer. Since we earlier observed two length scales in this crystal [2], we have focused here on the separate influence of the pure bulk and the defective skin layer. We may exclude the possibility that the change in the order of the phase transition is due to a change of the position of the phase diagram between the defective skin layer and the pure bulk, due to an oxygen gradient in the upper 150 Å, or due to phase separation and a crossing of a two-phase region within this sharp transition width of less than 0.3 K. We thus propose that the change in the order of the transition is due to the presence of random bonds or random fields, most likely prompted by the change in the mosaic spread within the defective skin layer. This suggestion may be modelled theoretically once we have a realistic picture of the dislocation substructure [23]. The simulation will incorporate the presumed strain fields in order to probe their effect on the critical behaviour. It is our belief that a continuous change in defect density can produce a discontinuous change in the nature of the phase transition as postulated in the literature [3–10]. In addition, a strong uniaxial strain field, associated with the depth-dependent mosaic spread in the skin layer [23], may, by itself, promote the observed conversion in the order of the phase transition [29].

### Acknowledgments

We thank R Hempelmann for loading the crystal used in these experiments and U Gebhard, D Lott, P Chow, K E Bassler and G Reiter for help in the experiment and/or fruitful discussions. We further thank the beamline personnel at the SRI-CAT at the Advanced Photon Source (APS) at the Argonne National Laboratory for assistance during the high-energy experiment. This work was supported by the NSF on DMR 92-08450 and 97-29297. The APS is supported by the US Department of Energy, BES-DMS, under contract W-31-109-ENG-38. JT thanks the Deutscher Akademischer Austauschdienst Doktorandenstipendium im Rahmen des gemeinsamen Hochschulprogramms III von Bund und Länder. We also wish to thank Professor de Fontaine on this special occasion for many years of interesting and critical discussions.

### References

- [1] Schönfeld B *et al* 1987 *Phys. Rev. B* **36** 5466
- [2] Trenkler J *et al* 1998 *Phys. Rev. Lett.* **82** 2276
- [3] Hui K and Berker A N 1989 *Phys. Rev. Lett.* **62** 2507
- [4] Berker A N 1990 *Phys. Rev. B* **42** 8640
- [5] Aizenman M and Wehr J 1989 *Phys. Rev. Lett.* **62** 2503
- [6] Cardy J and Jacobsen J L 1997 *Phys. Rev. Lett.* **79** 4063
- [7] Berker A N and Migliorini G 1998 *Phys. Rev. B* **57** 426
- [8] Cardy J 1999 *Physica A* **263** 215
- [9] Branco N S 1999 *Phys. Rev. B* **60** 1033
- [10] Kabakcioglu A and Berker A N 1999 *Phys. Rev. Lett.* **82** 2572
- [11] Schober T and Pesch W 1979 *Z. Phys. Chem.* **114** 21
- [12] Moss S C 1983 *Electronic Structure and Properties of Hydrogen in Metals* (New York: Plenum)
- [13] Fukai Y 1993 *The Metal–Hydrogen System* vol 21 (Berlin: Springer)
- [14] Trenkler J 1999 *PhD Thesis* University of Houston
- [15] Lawrie D and Sarbach S 1984 *Phase Transitions and Critical Phenomena* 2nd edn, vol 9, ed C Domb and J L Lebowitz (London: Academic)
- [16] Jo H S U *et al* 1980 *J. Appl. Cryst.* **13** 486
- [17] Noda Y *et al* 1985 *Acta Cryst. C* **41** 1566
- [18] Jo H S U *et al* 1979 *AIP Conf. Proc.* No 53
- [19] Hempelmann R 1986 Jü1-2096, ISSN 0366-0885
- [20] Trenkler J *et al* 1999 *Proc. Monterey Conf.* at press
- [21] Trenkler J *et al* 2000 *Phys. Rev. Lett.* submitted

- [22] Schwartz L H and Cohen J B 1987 *Diffraction from Materials* (Berlin: Springer)
- [23] Barabash R 1999 private communication, to be published
- [24] Krivoglaz M A 1996 *Diffuse Scattering of X-rays and Neutrons by Fluctuations* (Berlin: Springer)
- [25] Warren B E 1990 *X-ray Diffraction* (New York: Dover)
- [26] Bongaarts A L M and de Jonge W J M 1977 *Phys. Rev. B* **15** 3424
- [27] Yelon W B *et al* 1974 *Phys. Rev. B* **9** 4843
- [28] Seecq O H *et al* 1998 *Phys. Rev. B* **58** 623
- [29] Fähnle M 2000 private communication

## The Ni–Ni<sub>3</sub>Al phase diagram: thermodynamic modelling and the requirements of coherent equilibrium

A J Ardell

Department of Materials Science and Engineering, University of California, Los Angeles,  
CA 90095-1595, USA

Received 16 September 1999, accepted for publication 20 March 2000

**Abstract.** The Ni-rich portion of the Ni–Al phase diagram is examined in light of data on coherent equilibrium between the  $\gamma$  (Ni–Al solid solution) and  $\gamma'$  (Ni<sub>3</sub>Al) phases, as well as on the thermodynamic requirements of coherent equilibrium. The model of Ardell and Maheshwari was used to calculate the difference between the incoherent and coherent solubility limits over the temperature range of 400–800 °C. New data on the elastic constants of Ni<sub>3</sub>Al as a function of temperature and composition, as well as the Gibbs free energy functions of the most recent thermodynamic model of the Ni–Al alloy system, were used in the calculations. With these input parameters the predicted differences between the incoherent and coherent solubility limits are very small, and inconsistent with recent experimental data on the variation of the coherent solubility with the  $\gamma'$  volume fraction. The inconsistency is a consequence of the large curvature of the Gibbs free energy function for the  $\gamma$  phase obtained from the thermodynamic model. These findings are discussed in the context of the accuracy of thermodynamic modelling of phase diagrams.

### 1. Introduction

The Ni-rich portion of the Ni–Al phase diagram, which describes equilibrium between the Ni–Al solid solution ( $\gamma$ ) and Ni<sub>3</sub>Al ( $\gamma'$ ) phases, is quite important for technical reasons, serving as the basis for many Ni base superalloys. It is well established, theoretically, that coherent phases in thermodynamic equilibrium have solubility limits that differ from the solubility limits in incoherent, unstressed, equilibrium [1–3]. It was first realized by Williams [4, 5] that the coherent solubility limits can depend on the initial alloy composition,  $X_0$ . A consequence of this highly unusual aspect of coherent equilibrium is that the lever rule cannot necessarily be used for the precise calculation of the volume fraction,  $f$ , of a dispersed coherent phase. This is because the phase boundaries in nearly all conventional phase diagrams represent incoherent equilibrium solubility limits, but the solubility limits for these same phases differ when they are in coherent contact.

Coherency strains arise when the lattice constants of the phases in coherent equilibrium are unequal. For the  $\gamma$  and  $\gamma'$  phases in Ni–Al alloys, the relative mismatch in the lattice parameters,  $\varepsilon$ , is 0.0047 at room temperature;  $\varepsilon$  decreases slightly as the temperature increases [6]. Even though  $\varepsilon$  is not very large compared with the values in some other binary Ni base alloys [6], it is still of sufficient magnitude to produce an appreciable difference between the incoherent and coherent solubilities,  $X_{I\alpha}$  and  $X_{C\alpha}$ , respectively, of the  $\gamma'$  phase at low temperatures. Ardell and Maheshwari [7] concluded from an examination of data of Gentry and Fine [8] that  $X_{C\alpha}$  in a Ni–Al alloy containing 13.8 at% Al was greater than in an alloy containing 11.1 at% Al at two ageing temperatures, 425 and 450 °C. The difference between

the values of  $X_{C\alpha}$  in the two alloys is quite large, about 1.34 at% at 425 °C and 1.52 at% at 450 °C. Li and Ardell [9] recently conducted ageing experiments at 500 °C on Ni-Al alloys with three different compositions and showed that the difference between the values of  $X_{C\alpha}$  for alloys containing 11.4 and 15.9 at% Al is approximately 0.7 at%.

Ardell and Maheshwari [7] developed a model for coherent equilibrium in alloys containing spherical precipitates (the AM model). The AM model predicts the dependence of  $X_{C\alpha}$  on a variety of thermodynamic and physical parameters, and is consistent with experimental results which show that  $X_{C\alpha}$  increases as  $X_o$  (or equivalently  $f$ ) increases. These predictions were recently tested quantitatively by Li and Ardell [10], who used the best estimates of all the physical parameters for the  $\gamma$  and  $\gamma'$  phases, and employed an important thermodynamic parameter derived from a model for  $\gamma-\gamma'$  equilibrium published by Calderon *et al* [11].

Subsequent to the publication of Li and Ardell [10], new values of the elastic constants of the  $\gamma$  and  $\gamma'$  phases have been measured as functions of temperature and composition [12, 13]. Also, a more recent and presumably more accurate model of the thermodynamics of this alloy system has been published [14]. One of the objectives of this work is to re-examine the predictions of the AM model in light of the most recent values of these important parameters. This re-examination also serves the purpose of providing a, perhaps, more stringent evaluation of the available thermodynamic models of the Gibbs free energy functions than can be obtained just by comparing the predicted and experimentally determined phase diagram. The reason for this is that coherent equilibrium involves the second derivatives of the Gibbs free energy, whereas fitting the phase boundaries involves only the first derivatives via the common tangent rule in the absence of data on the activities of the components in solid solution. The accuracy of the thermodynamic modelling is, therefore, also addressed in this work.

There are two other issues considered in this paper. The Ni-rich portion of the Ni-Al phase diagram has been investigated on numerous occasions, and there is considerable scatter in the data. One issue is whether the scatter can be explained by the fact that some investigators might have measured incoherent equilibrium while others measured coherent equilibrium. The other issue involves the fact that Li and Ardell [9] measured coherent solubility limits at the relatively low temperature of 500 °C. Since the quantitative impact of coherent equilibrium is expected to decrease with increasing temperature [7], it is important to determine whether there are any real, practical consequences associated with the concept of coherent solubility in Ni-Al alloys at higher temperatures (600–800 °C), where the ageing kinetics are much faster.

## 2. Ni-Ni<sub>3</sub>Al phase diagram

The Ni-Ni<sub>3</sub>Al phase diagram is shown in figure 1. It includes nearly all the extant data on equilibrium between the  $\gamma$  and  $\gamma'$  phases over the temperature range of 400–1300 °C (the oldest data of Alexander and Vaughan [15], Schramm [16] and Taylor and Floyd [17], which are in reasonably good agreement with the data shown, are excluded for the sake of clarity). The entire Ni-Al phase diagram has recently been evaluated thermodynamically by Ansara *et al* [14], but the most recent data on the phase boundaries relevant to  $\gamma-\gamma'$  equilibrium were provided by Dupin [18]. These are presented in figure 1, as is the  $\gamma'$  solvus calculated by Calderon *et al* [11]. The  $\gamma'$  solvus of Calderon *et al* [11] is displaced to lower Al concentrations with respect of that of Ansara *et al*, but both are in equally good agreement with the data at temperatures below 1200 °C.

It is quite reasonable to conclude that nearly all of the previous investigations of the  $\gamma/\gamma'$  equilibrium in Ni-Al alloys have measured *coherent solubility limits* because incoherent

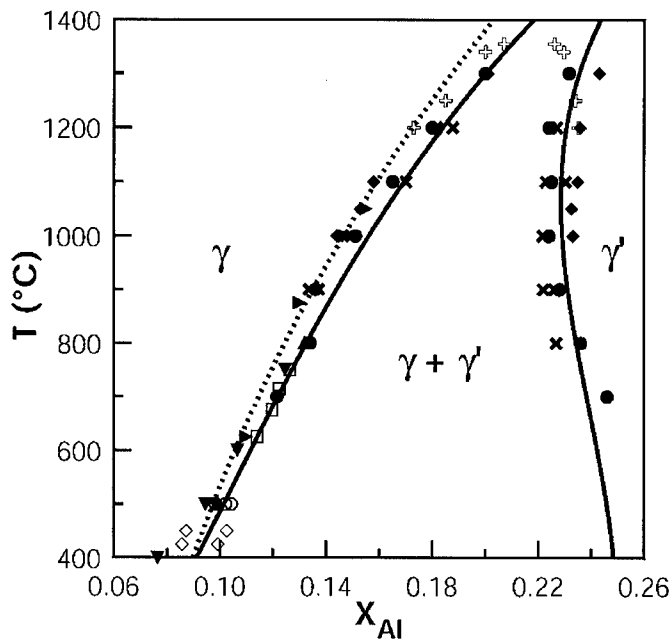


**Figure 1.** The Ni-rich region of the Ni–Al phase diagram. The data shown are from:  $\diamond$ , Gentry and Fine [8];  $\circ$ , Li and Ardell [9];  $\blacktriangleright$ , Williams [19];  $\blacktriangledown$ , Hornbogen and Kreye [20];  $\square$ , Rastogi and Ardell [21];  $\blacklozenge$ , Janssen [22];  $\triangle$ , Chellman and Ardell [23];  $+$ , Verhoeven *et al* [24];  $\bullet$ , Jia via Okamoto [25]; and  $\times$ , Watanabe *et al* [26]. The full curves are the phase boundaries from the model of Ansara *et al* [14], updated by Dupin [18], and the broken curve is the solvus calculated by Calderon *et al* [11].

equilibrium between the  $\gamma$  and  $\gamma'$  phases is rarely observed as a consequence of normal heat-treatment, for example solution treatment and ageing or very slow cooling from high temperatures. An example of the persistence of coherent equilibrium between the  $\gamma$  and  $\gamma'$  phases is shown in figure 2, which is an electron micrograph of plate-shaped  $\gamma'$  particles in a well aged Ni–Al alloy. The particles in figure 2 are nearly  $1\ \mu m$  in length, but are nevertheless fully coherent, as evidenced by the absence of dislocations at the interfaces and the very strong  $\delta$ -fringe contrast that arises because the matrix becomes tetragonally distorted near the  $\gamma$ – $\gamma'$  interface [27]. Another example of the persistence of coherent equilibrium is demonstrated in the experiments of Watanabe *et al* [26], who determined the solubility limits from chemical analysis of diffusion couples. They found that the  $\gamma$  and  $\gamma'$  phases even became coherent during diffusion anneals at high temperatures, and remained so throughout the course of the experiments.

The coherent solubility limits measured by Li and Ardell [9] vary from 0.098 to 0.105 at  $500\ ^\circ C$ . This range of solubilities is undoubtedly due to the influence of coherency strains, but it is, nevertheless, small compared to the uncertainties in the solubility limits evident in figure 1. Since the incoherent solvus is unknown, it is useful to determine whether it lies within the range of the scatter in the  $\gamma'$  solvus seen in figure 1. At present, this can only be determined by calculation. Such calculations have already been carried out by Li and Ardell [10], and these calculations are repeated here using the most recent data on the elastic constants of the  $\gamma$  and  $\gamma'$  phases, and the Gibbs free energies of mixing of the model of Ansara *et al* [14] and Dupin [18].



**Figure 2.** High-voltage transmission electron micrograph ( $\sim 500$  keV) showing large coherent precipitates of  $\text{Ni}_3\text{Al}$  in a Ni-13.53 at% Al alloy aged for 450 h at 700 °C.

### 3. Theoretical background

#### 3.1. Equations of the AM model

According to the AM model the incremental increases in the coherent solubilities of the  $\alpha$  and  $\beta$  phases,  $\Delta X_\alpha$  and  $\Delta X_\beta$ , respectively, as a function of the volume fraction,  $f$ , are given by the equations

$$\frac{\Delta X_\alpha}{\Delta X_I} = \frac{\Lambda \{-\delta(\eta f)^2 + 2\eta f + 1\}}{2(1 - \delta\eta f)} \quad (1)$$

and

$$\Delta X_\beta = \frac{\chi_\alpha}{\chi_\beta} \Delta X_\alpha \quad (2)$$

where

$$\Delta X_\alpha = X_{C\alpha} - X_{I\alpha} \quad (3)$$

$$\Delta X_\beta = X_{C\beta} - X_{I\beta} \quad (4)$$

and

$$\Delta X_I = X_{I\beta} - X_{I\alpha}. \quad (5)$$

In equations (3)-(5) the subscripts C and I refer to the coherent and incoherent states, respectively, and the subscripts  $\alpha$  and  $\beta$  to the majority and minority (dispersed) phases, respectively.  $X_{I\alpha}$  is the equilibrium incoherent solubility of B in  $\alpha$ ,  $X_{I\beta}$  is the equilibrium

incoherent solubility of B in  $\beta$ , and the parameters  $\eta$ ,  $\delta$  and  $\Lambda$  are defined by the equations:

$$\eta = \frac{3K_\alpha}{4\mu_\alpha} \quad (6)$$

$$\delta = \frac{K_\beta - K_\alpha}{K_\alpha \Gamma_\beta} \quad (7)$$

and

$$\Lambda = \frac{9\varepsilon^2 K_\beta}{\chi_\alpha \Gamma_\beta \Delta X_I^2}. \quad (8)$$

In equations (6)–(8) the parameter  $\varepsilon$  is the stress-free lattice misfit, defined as

$$\varepsilon = \frac{a_\beta - a_\alpha}{a_\alpha} \quad (9)$$

where  $a_\alpha$  and  $a_\beta$  are the lattice constants of the stress-free  $\alpha$  and  $\beta$  phases,  $K_\alpha$  and  $K_\beta$  are the bulk moduli of the  $\alpha$  and  $\beta$  phases,  $\mu_\alpha$  is the shear modulus of the  $\alpha$  phase,  $\Gamma_\beta$  is defined as

$$\Gamma_\beta = 1 + \frac{3K_\beta}{4\mu_\alpha} \quad (10)$$

and the parameters  $\chi_\alpha$  and  $\chi_\beta$  are given by the equations

$$\chi_\alpha = \frac{n_o}{N_A} \left. \frac{\partial^2 G_\alpha}{\partial X^2} \right|_{X=X_{I\alpha}} = \frac{n_o}{N_A} G''_{I\alpha} \quad (11)$$

and

$$\chi_\beta = \frac{n_o}{N_A} \left. \frac{\partial^2 G_\beta}{\partial X^2} \right|_{X=X_{I\beta}} = \frac{n_o}{N_A} G''_{I\beta} \quad (12)$$

where  $n_o$  is the number of atomic sites per unit volume (essentially the reciprocal of the atomic volume) which is assumed to be equal in the  $\alpha$  and  $\beta$  phases,  $N_A$  is Avogadro's number and  $G_\alpha$  and  $G_\beta$  are the Gibbs free energies of mixing in the  $\alpha$  and  $\beta$  phases, respectively. Owing to the inverse relationship between  $\Lambda$  and  $\chi$  in equation (8), and the proportionality between  $\Delta X_\alpha$  and  $\Lambda$ , the curvature of the Gibbs free energy plays an extremely important role in determining the magnitude of  $\Delta X_\alpha$  via equation (1). In equations (1)–(12)  $\alpha$  is the majority phase and  $\beta$  the dispersed phase; it is perhaps worth stating that  $\alpha$  corresponds to  $\gamma$  and  $\beta$  to  $\gamma'$ .

### 3.2. Parameters

The recent results of Kamara *et al* [6] provide reliable values of  $\varepsilon$  from room temperature to 700 °C. The empirical equation describing the temperature dependence of  $\varepsilon$  with temperature,  $T$  (in kelvin) is

$$\varepsilon = 4.2426 \times 10^{-3} + (2.6664 \times 10^{-6})T - (2.8752 \times 10^{-9})T^2. \quad (13)$$

The single-crystal elastic constants,  $c_{ij}$ , for both phases have recently been measured [12, 13], and are described as functions of  $T$  (in kelvin) and concentration of Al,  $X_{\text{Al}}$ , by the empirical equation

$$c_{ij} = k_1 + k_2 T + k_3 X_{\text{Al}} + k_4 X_{\text{Al}} T + k_5 T^2 + k_6 X_{\text{Al}}^2 \quad (14)$$

where the  $k_i$  are empirical constants that differ for the two phases. Since the AM theory is based on the use of isotropic elasticity, the  $c_{ij}$  must be converted to  $K_\alpha$ ,  $K_\beta$  and  $\mu_\alpha$  for use

in the calculations. The bulk moduli pose no difficulty, and can be calculated from the  $c_{ij}$  for both phases using the formula

$$K = \frac{c_{11} + 2c_{12}}{3}. \quad (15)$$

Estimating  $\mu_\alpha$  is more problematic, since the choices are numerous. We have chosen to calculate an isotropic value of  $\mu_\alpha$  using the mean of the upper ( $\mu_u$ ) and lower ( $\mu_l$ ) bounds of the Hashin–Shtrikman (HS) [28] values. The upper and lower bounds are given by the equations:

$$\mu_l = \mu_{110} + 3\left(\frac{5}{\mu_{100} - \mu_{110}} - 4\beta_1\right)^{-1} \quad (16)$$

and

$$\mu_u = \mu_{100} + 2\left(\frac{5}{\mu_{110} - \mu_{100}} - 6\beta_2\right)^{-1} \quad (17)$$

where

$$\mu_{110} = \frac{c_{11} - c_{12}}{2} \quad (18)$$

$$\mu_{100} = c_{44} \quad (19)$$

$$\beta_1 = \frac{-3(K + 2\mu_{110})}{5\mu_{110}(3K + 4\mu_{110})} \quad (20)$$

and

$$\beta_2 = \frac{-3(K + 2\mu_{100})}{5\mu_{100}(3K + 4\mu_{100})}. \quad (21)$$

The values of  $\mu_\alpha$  vary from about 55 to 66 GPa over the temperature range of 400–800 °C, which are smaller than handbook values of the shear modulus of pure Ni by 20–30 GPa. The reduction of the shear modulus of Ni on alloying with Al and increasing the temperature is consistent with expected behaviour [12].

Evaluation of the parameters  $\chi_\alpha$  and  $\chi_\beta$  requires thermodynamic models of the  $\gamma$  and  $\gamma'$  phases. The model of Calderon *et al* [11] was used in the previous calculation by Li and Ardell [10]. In this work  $G''_{I\alpha}$  was obtained from model of Ansara *et al* [14] and Dupin [18].

$X_{I\alpha}$  was calculated by evaluating the left- and right-hand sides of (1) and (2) independently, making use of the mass balance equation

$$f = \frac{X_0 - X_{C\alpha}}{X_{C\beta} - X_{C\alpha}}. \quad (22)$$

Since  $X_{I\beta}$  is also unknown, additional assumptions are needed for a complete analysis. To simplify the process the experimentally measured values of  $X_\beta$  were taken to represent  $X_{C\beta}$ , and the differences between  $X_{C\beta}$  and  $X_{I\beta}$  were assumed to be relatively small at all temperatures. To expedite the calculations the empirical equation

$$X_{C\beta} = 0.171\ 9088 + (3.251\ 375 \times 10^{-4})T - (4.569\ 817 \times 10^{-7})T^2 + (2.340\ 7391 \times 10^{-10})T^3 - (3.724\ 450 \times 10^{-14})T^4 \quad (23)$$

where  $T$  is in kelvin, was fitted to the data on the  $(\gamma + \gamma')/\gamma'$  phase boundary provided by Dupin [18].

Taking into account the dependence of the parameters in equations (6)–(12) on composition and temperature, equations (1) and (2) were solved iteratively, utilizing (22). The assumption that  $X_{C\beta}$  is known fixes the value of  $\chi_\beta$  and simplifies the calculations considerably.

The iterative procedure began by assuming a trial value of  $X_{I\alpha}$ , which was then used to calculate all the parameters depending on  $X_{I\alpha}$  that appear in (1). Both sides of (1) were calculated iteratively using new trial values of  $X_{I\alpha}$  until the difference between the left- and right-hand sides of (1) resulted in a difference of  $X_{I\alpha}$  amounting to less than 0.000 01.

#### 4. Results and discussion

The incoherent solubilities calculated using the thermodynamic model of Ansara *et al* [14] and Dupin [18], as well as the experimental data on which they are based, are shown in figure 3(a). It is evident that the differences between the coherent and incoherent solubility limits are very small and would probably be undetectable experimentally. This is a far different result from that reported by Li and Ardell [10], and stems mainly from the large values of the curvature of the Gibbs free energy function used in the present calculations compared to those used previously. In the model of Calderon *et al* [11] the curvature is given by the equation

$$G''_{I\alpha} = \frac{RT}{X_{I\alpha}(1 - X_{I\alpha})} - 2A - 6B(1 - 2X_{I\alpha}) \quad (24)$$

where  $A = 3.29574T - 104361 \text{ J mol}^{-1}$  and  $B = 41291.4 \text{ J mol}^{-1}$ . A comparison of the magnitudes of  $G''_{I\alpha,A}$  and  $G''_{I\alpha,C}$  from the models of Ansara *et al* and Calderon *et al*, respectively, is presented in figure 4; the values of  $X_{I\alpha}$  provided by Dupin [18] were used in this comparison. It is evident that  $G''_{I\alpha,A}$  is significantly larger than  $G''_{I\alpha,C}$ , especially at lower temperatures. The values of  $X_{I\alpha}$  calculated using (24) are shown in figure 3(b); the differences between  $X_{I\alpha}$  and  $X_{C\alpha}$  are much larger than those in figure 3(a) and do not differ significantly from those calculated by Li and Ardell [10].

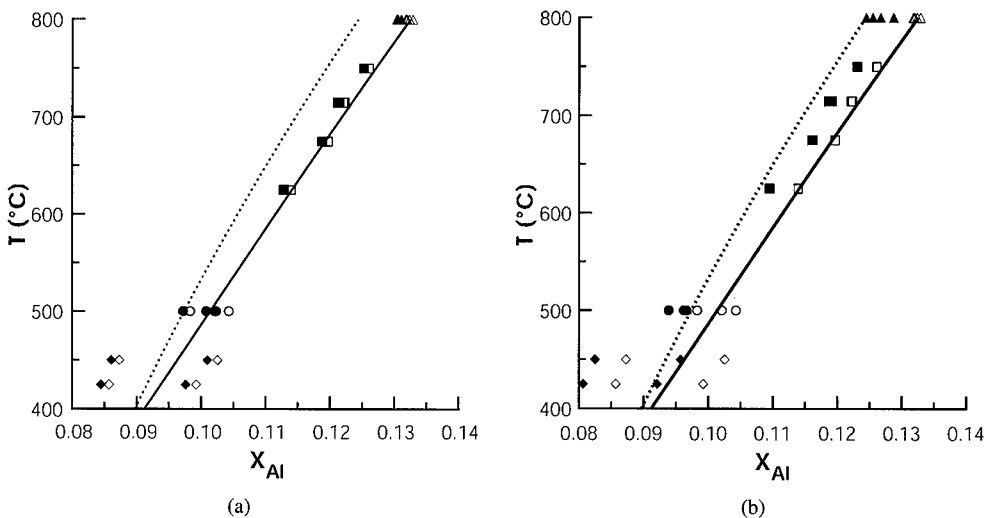


**Figure 3.** The incoherent solubilities of Ni<sub>3</sub>Al predicted by the AM model using: (a) the thermodynamic model of Ansara *et al* [14] and (b) the model of Calderon *et al* [11]. The open symbols represent the coherent solubilities measured experimentally from data on the depletion of solute kinetics during coarsening, the corresponding full symbols represent the calculated incoherent solubilities. Data of:  $\diamond$ , Gentry and Fine [8];  $\circ$ , Li and Ardell [9];  $\square$ , Rastogi and Ardell [21];  $\triangle$ , Chellman and Ardell [23]. The full curve in each figure is the solvus from the model of Ansara *et al* [14] and Dupin [18], and the broken curve is the solvus of Calderon *et al* [11].

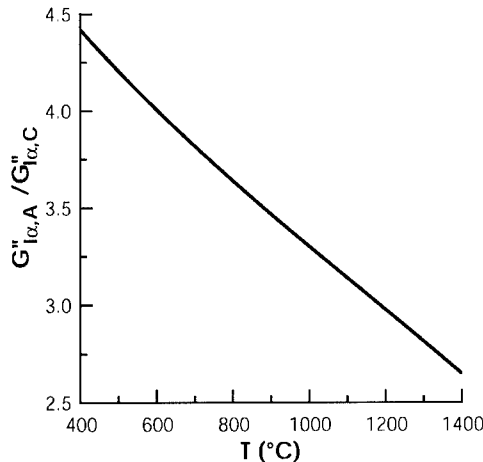


**Figure 4.** The ratio of the curvatures of the Gibbs free energy of mixing,  $G''_{l\alpha}$ , against temperature,  $T$ , calculated using the models of Ansara *et al* [14] and Dupin [18] (subscript A) and Calderon *et al* [11] (subscript C).

There can, of course, be only one value of  $X_{l\alpha}$  at any temperature. The values of  $X_{l\alpha}$  calculated from the experimentally measured values of  $X_{C\alpha}$  should therefore coincide. They do not even come close to doing so using the model of Ansara *et al*, which implies either that there is something wrong with the data analysed, that the AM model is quantitatively incorrect, or that there is something wrong with the parameters used in the AM model. Regarding the first possibility, we know from the experiments of Li and Ardell [9] that the increase in  $X_{C\alpha}$  with increasing  $X_0$  in Ni-Al alloys was also observed in the coarsening experiments on Ni-Ga and Ni-Ti alloys. There is little doubt that the data are meaningful and that the expected changes in  $X_{C\alpha}$  are measurable.

Regarding the AM model, it is important to recognize that coherent equilibrium always involves the curvatures of the Gibbs free energy functions of the phases involved. This is independent of the geometry of the phases. Examples are Cahn's theory of spinodal decomposition [1], the general model of Cahn and Larché [29], the models considered by Johnson and Chiang [30] and Johnson and Müller [31], which involve equilibrium between phases in the form of parallel plates, and the models of Johnson and Voorhees [32] and Pfeiffer and Voorhees [33], which are similar to the AM model but involve different boundary conditions for the elastic strains. In all these models a quantity similar to  $\Lambda$  in equation (8), i.e. one that includes the ratio of the square of a misfit parameter multiplied by an elastic constant divided by  $G''_{l\alpha}$  (or a closely related quantity), emerges naturally. It thus appears that a parameter similar to  $\Lambda$  is a ubiquitous feature of any theory of coherent equilibrium and is independent of the precise details of the model.

Regarding the parameters involved in the AM model, the most poorly constrained one is  $G''_{l\alpha}$ . It is obvious that the Ni-rich portion of the Ni-Al phase diagram is described very well by the thermodynamic model of Ansara *et al* [14] and Dupin [18]. Moreover, their free energy functions are clearly consistent with the rather limited data on the chemical potentials of Al and Ni in the Ni-rich solid solution at temperatures greater than 1273 K (see figure 7 of their paper). The first derivatives of their free energy functions are therefore reasonably accurate at these higher temperatures, but additional data on the chemical potentials are required to ensure that the curvatures of the high-temperature free energy functions are also reasonably

accurate, and such data are currently unavailable. Also, there are no data on the activities of Al and Ni at lower temperatures, for example 750–1000 K, which is the regime of temperatures in which the coherent solubility limits have been measured. In this range of temperatures the free energy functions can only be estimated by fitting the phase diagram, i.e. by invoking the common tangent criterion for equilibrium. The values of  $G''_{\text{I}\alpha}$  from the model of Ansara *et al* are therefore far less reliable at lower temperatures than at higher temperatures, which is unfortunate because the impact of coherent equilibrium is much greater at low temperatures.

The  $\gamma'$  solvus from the model of Calderon *et al* [11] also agrees quite well with the experimental data in figure 1, so there is little to choose between the two models insofar as fitting this part of the phase diagram is concerned. However, the prediction of the  $\gamma'$  solvus must be fortuitous to some extent because their thermodynamic functions make use of the data of Kaufman and Nesor [34], who treat the  $\gamma'$  phase as a line compound. The model of Calderon *et al* thus involves equilibrium between the  $\gamma$  solid solution and a  $\gamma'$  phase of fixed composition, and it is well known that the composition of the  $\gamma'$  phase deviates considerably from stoichiometry (see figure 1, for example). This is completely different from the model of Ansara *et al* [14], who regard the  $\gamma'$  phase as a continuous solid solution varying in composition from 0 to 100% Al.

It is fair to state that the  $\gamma'$  solvus has been calculated with comparable accuracy by two different thermodynamic models that utilize very different functions for the Gibbs free energy of mixing. Both models succeed equally well, partly because the phase boundaries themselves play an important role in fitting the free energy functions. The curvatures of these functions are not critical in fulfilling the common tangent construction for equilibrium, and in the absence of data on the activities of the components their curvatures are not easy to estimate, especially at lower temperatures. Moreover, the curvatures are essential in assessing the magnitude of the effect of elastic strains on coherent equilibrium. The function for  $G''_{\text{I}\alpha}$  of Calderon *et al*, equation (24), in conjunction with the AM model, predicts a dependence of  $X_{\text{C}\alpha}$  on  $X_0$  that is easily measured experimentally. The corresponding dependence predicted by the model of Ansara *et al* is significantly smaller and would be rather difficult to detect. As is apparent in figure 3, the data of Li and Ardell [9] are consistent to a far greater extent with the predictions of the AM model provided that  $G''_{\text{I}\alpha}$  is calculated using the model of Calderon *et al*.

Regarding the other two issues alluded to in the introduction, it is quite apparent that the practical consequences of coherent equilibrium are small in the Ni–Al system. For example, if it were necessary to know the equilibrium volume fraction of the  $\gamma'$  phase at low temperatures, say 600 °C or lower, with high precision, then the influence of the coherent equilibrium might come into play. However, the differences between  $X_{\text{C}\alpha}$  and  $X_{\text{I}\alpha}$  are expected to become smaller and smaller as  $T$  increases, and the consequences of coherent equilibrium at  $T > 600$  °C can be safely ignored. It also appears as if the scatter in the data, plainly visible in figure 1, cannot be accounted for by invoking coherent equilibrium, since the scatter generally exceeds the differences in the experimentally measured values of  $X_{\text{C}\alpha}$  [9].

## 5. Summary

The incoherent solvus describing the equilibrium between the  $\gamma$  and  $\gamma'$  phases in Ni–Al alloys has been calculated using the AM model of coherent equilibrium. The calculations reported in this work utilize the most up-to-date values of the thermodynamic and physical parameters for Ni–Al alloys. These include experimentally measured lattice constants and elastic constants as functions of composition and temperature, and the most recent thermodynamic model of the Ni–Al phase diagram. The calculations suggest that the differences between the incoherent and coherent solubility limits as a function of temperature are very small, and of essentially no consequence. This conclusion is belied, however, by experimental measurements which

indicate that  $X_{C\alpha}$  increases as  $X_o$  increases, as predicted theoretically, with increases that are relatively easy to detect. The crux of this apparent dilemma is tied to the behaviour of  $G''_{l\alpha}$ . The large values of predicted by the thermodynamic model of Ansara *et al* [14] are responsible for the very small differences between  $X_{C\alpha}$  and  $X_{l\alpha}$  calculated using the AM theory and cannot account for the much larger differences measured experimentally.

### Acknowledgments

The author is grateful to the National Science Foundation for financial support under Grant DMR-9900714. He also thanks Dr Nathalie Dupin for providing new thermodynamic data on the Ni-Al alloy system and stimulating discussions and insight on the thermodynamic modelling of alloys.

### References

- [1] Cahn J W 1961 *Acta Metall.* **10** 795–801
- [2] Larché F and Cahn J W 1973 *Acta Metall.* **21** 1051–63
- [3] Robin P Y 1974 *Am. Mineral.* **59** 1299–318
- [4] Williams R O 1980 *Metall. Trans. A* **11** 247–53
- [5] Williams R O 1984 *Calphad* **8** 1–14
- [6] Kamara A B, Ardell A J and Wagner C N J 1996 *Metall. Trans. A* **27** 2888–96
- [7] Ardell A J and Maheshwari A 1995 *Acta Metall. Mater.* **43** 1825–35
- [8] Gentry W O and Fine M E 1972 *Acta Metall.* **20** 181–90
- [9] Li F and Ardell A J 1997 *Scr. Mater.* **37** 1123–8
- [10] Li F and Ardell A J 1998 *J. Phase Equil.* **19** 334–9
- [11] Calderon H A, Voorhees P W, Murray J L and Kostorz G 1994 *Acta Metall. Mater.* **42** 991–1000
- [12] Prikhodko S V, Carnes J D, Isaak D G and Ardell A J 1998 *Scr. Mater.* **38** 67–72
- [13] Prikhodko S V, Carnes J D, Isaak D G, Yang H and Ardell A J 1999 *Metall. Trans. A* **30** 2403–8
- [14] Ansara I, Dupin N, Lukas H L and Sundman B 1997 *J. Alloys Compound.* **247** 20–30
- [15] Alexander W O and Vaughan N B 1937 *J. Inst. Metals* **61** 247–60
- [16] Schramm J 1941 *Z. Metallkde* **33** 347–55
- [17] Taylor A and Floyd R W 1952–53 *J. Inst. Metals* **81** 25–32
- [18] Dupin N 1999 personal communication
- [19] Williams R O 1959 *Trans. AIME* **215** 1026–32
- [20] Hornbogen E and Kreye H 1966 *Z. Metallk.* **57** 122–9
- [21] Rastogi P K and Ardell A J 1969 *Acta Metall.* **17** 595–602
- [22] Janssen M M P 1973 *Metall. Trans.* **4** 1623–33
- [23] Chellman D J and Ardell A J 1974 *Acta Metall.* **22** 577–88
- [24] Verhoeven J D, Lee J H, Laabs F C and Jones L L 1991 *J. Phase Equil.* **12** 15–23
- [25] Jia C C 1990 *Thesis* Tohoku, cited by Okamoto H 1993 *J. Phase Equil.* **14** 257–9
- [26] Watanabe M, Horita Z, Smith D J, McCartney M R, Sano T and Nemoto M 1994 *Acta Metall. Mater.* **42** 3381–7
- [27] Ardell A J 1967 *Phil. Mag.* **16** 147–58
- [28] Hashin Z and Shtrikman S 1962 *J. Mech. Phys. Solids* **10** 335–42
- [29] Cahn J W and Larché F 1984 *Acta Metall.* **32** 1915–23
- [30] Johnson W C and Chiang C S 1988 *J. Appl. Phys.* **64** 1155–65
- [31] Johnson W C and Müller W H 1991 *Acta Metall. Mater.* **39** 89–103
- [32] Johnson W C and Voorhees P W 1987 *Metall. Trans. A* **18** 1213–28
- [33] Pfeifer M J and Voorhees P W 1991 *Metall. Trans. A* **39** 1921–35
- [34] Kaufman L and Nesor H 1974 *Metall. Trans.* **5** 1623–9

## The energetics of surface-alloy formation: an embedded-atom-method, second-order-expansion study

M Asta<sup>†</sup>, V Ozoliņš and J J Hoyt

Sandia National Laboratories, MS 9161, PO Box 969, Livermore, CA 94551-0969, USA

Received 16 September 1999, accepted for publication 21 December 1999

**Abstract.** Chemical ordering and clustering instabilities in alloys are governed by the Fourier transform of the effective pair interactions,  $V(\mathbf{k})$ . We make use of a second-order-expansion formalism, based upon embedded-atom-method interatomic potentials, to calculate chemical and elastic contributions to  $V(\mathbf{k})$  for monolayer surface alloys on single-crystal substrates. It is demonstrated that the elastic contribution to  $V(\mathbf{k})$  is characterized by a finite slope at the origin, consistent with continuum models which predict that  $V(\mathbf{k}) \propto -|\mathbf{k}|$  for small wavevectors. As a consequence, the global minimum in  $V(\mathbf{k})$  always occurs at finite  $\mathbf{k}$ , and therefore compositional instabilities in ultrathin surface-alloy films are generally of an ordering (as opposed to clustering,  $\mathbf{k} = \mathbf{0}$ ) type.

### 1. Introduction

In the article ‘Configurational thermodynamics of solid solutions’ [1], de Fontaine reviews how the stability of a disordered alloy solid solution with respect to chemical ordering or clustering can be analysed in terms of the Fourier transform of the Hessian of the free energy:

$$\phi(\mathbf{R} - \mathbf{R}') = \left[ \frac{\partial^2 F}{\partial \langle \delta c(\mathbf{R}) \rangle \partial \langle \delta c(\mathbf{R}') \rangle} \right]_0$$

where  $\langle \delta c(\mathbf{R}) \rangle$  is the ensemble-averaged concentration deviation at site  $\mathbf{R}$ , and the subscript 0 indicates that the Hessian is evaluated in the homogeneous solid solution phase (where  $\langle \delta c(\mathbf{R}) \rangle = 0 \forall \mathbf{R}$ ). At high temperatures, where the solid solution is thermodynamically stable,  $\phi(\mathbf{R} - \mathbf{R}')$  is positive definite, i.e., all of its eigenvalues are positive. As the temperature is lowered, a critical point is reached below which one or more of the eigenvalues of the Hessian becomes negative, indicating an instability with respect to composition modulation. Within mean-field theory, the critical wavevector  $\mathbf{k}^*$  characterizing this instability is determined by the global minimum of the Fourier transform of the effective-pair interactions (EPIs) [2],  $V(\mathbf{k})$ . In bulk solid solutions it has long been recognized (see, e.g., the 1969 work of Cook and de Fontaine [3]) that  $\mathbf{k}^*$  is determined by a balance between ‘chemical’ and ‘elastic’ contributions to  $V(\mathbf{k})$ , which describe the energetics of atomic swaps on a rigid lattice, and the relaxation energy associated with static atomic displacements, respectively.

Recently, the semi-empirical, embedded-atom-method approach was used to calculate  $V(\mathbf{k})$  for bulk late-transition-metal alloys within the formalism of a second-order expansion of the alloy energy [4]. Below we generalize this treatment to study the ordering energetics of

<sup>†</sup> Present address: Department of Materials Science and Engineering, Northwestern University, Evanston, IL 60208-3108, USA.

monolayer alloy films on elemental single-crystal substrates. The present study is motivated by the commonly observed phenomenon of surface alloying in metal heteroepitaxial growth [5–7]. When one type of metal is deposited onto another, thin alloy layers typically form which are localized near the film–substrate interface. This trend has proven to be remarkably general, with surface alloying observed even in cases where the atomic constituents do not mix appreciably in the bulk [8, 9]. From an analysis of the chemical and elastic contributions to  $V(\mathbf{k})$  we will demonstrate below that ordering (as opposed to clustering) is generally energetically favoured in ultrathin surface alloys.

## 2. Method

In order to study the energetics of atomic ordering in surface alloys we will make use of slab geometries (see figure 1), embedded-atom-method (EAM) [10, 11] interatomic potentials, and a second-order-expansion (SOE) formalism [4]. The slab geometries used in this work are illustrated in cross section in figure 1(a). They consist of a total of  $2T + 1$  layers, with a monolayer of surface alloy (red and blue circles in figure 1(a)) on the top and bottom, capping  $2T - 1$  layers of substrate (green circles in figure 1(a)) atoms. The regions above and below the slabs are vacuum.

The positions of the atoms in the slab are given as  $\mathbf{R} + \mathbf{u}(\mathbf{R})$ , in terms of ‘ideal’ lattice postions  $\mathbf{R}$ , defined below, and displacements  $\mathbf{u}(\mathbf{R})$ . The atomic configurations in the surface-alloy layers are specified by site-composition variables  $c(\mathbf{R})$  equal to one or zero, depending upon which atom type is associated with site  $\mathbf{R}$ . In the SOE approach the energy is expanded to second order in the displacement and composition variables. The expansion is carried out with respect to a reference state, illustrated in figure 1(b), in which the individual (red and blue) surface-alloy atoms are replaced by ‘virtual’ (grey) atoms. Associated with these virtual atoms are interatomic potentials which are concentration-weighted averages of those corresponding to the two different atom types in the alloy, as described in detail in [4]. The ideal lattice sites  $\mathbf{R}$  are defined as the equilibrium atomic positions in the reference slab.

Formally, the second-order expansion of the energy can be written as follows:

$$\begin{aligned} E(\mathbf{u}(\mathbf{R}), c(\mathbf{R})) = E_0 + \frac{1}{2} \sum_{l,l'} \sum_{\mathbf{r}_l, \mathbf{r}'_{l'}} [\theta_{l,l'}(\mathbf{r}_l - \mathbf{r}'_{l'}) \delta c_l(\mathbf{r}_l) \delta c_{l'}(\mathbf{r}'_{l'}) \\ + 2\psi_{\alpha,l,l'}(\mathbf{r}_l - \mathbf{r}'_{l'}) \delta c_l(\mathbf{r}_l) \mathbf{u}_{\alpha,l'}(\mathbf{r}'_{l'}) + \phi_{\alpha,\beta,l,l'}(\mathbf{r}_l - \mathbf{r}'_{l'}) \mathbf{u}_{\alpha,l}(\mathbf{r}_l) \mathbf{u}_{\beta,l'}(\mathbf{r}'_{l'})] \quad (1) \end{aligned}$$

where  $E_0$  represents the energy of the ‘virtual-atom’ reference state, summation over repeated Cartesian indices  $\alpha$  and  $\beta$  is implied, and the ideal lattice positions ( $\mathbf{R}$ ) have been labelled by a layer index ( $l$ ) and a position vector ( $\mathbf{r}_l$ ) within the layer. In equation (1)  $\delta c_l(\mathbf{r}_l) = c_l(\mathbf{r}_l) - \bar{c}$  is the deviation of the composition variable at a given site from the average concentration  $\bar{c}$  within the surface-alloy layer.  $\delta c_l(\mathbf{r}_l)$  is defined as zero for substrate atoms (we do not consider atom exchanges between the surface alloy and substrate layers). The second expression on the right-hand side of equation (1) represents the leading-order term in the Taylor-series expansion of the energy of the slab (figure 1(a)) with respect to that of the reference state (figure 1(b)).

$$\theta_{l,l'}(\mathbf{r}_l - \mathbf{r}'_{l'}) = \left[ \frac{\partial^2 E}{\partial \delta c_l(\mathbf{r}_l) \partial \delta c_{l'}(\mathbf{r}'_{l'})} \right]_0$$

is the second derivative of the energy with respect to the local composition variables, and the subscript 0 indicates that derivatives are evaluated in the reference state. If either  $l$  or  $l'$  are substrate layers  $\theta$  is defined to be zero, and provided  $T$  is large (thick slabs)  $\theta$  also vanishes

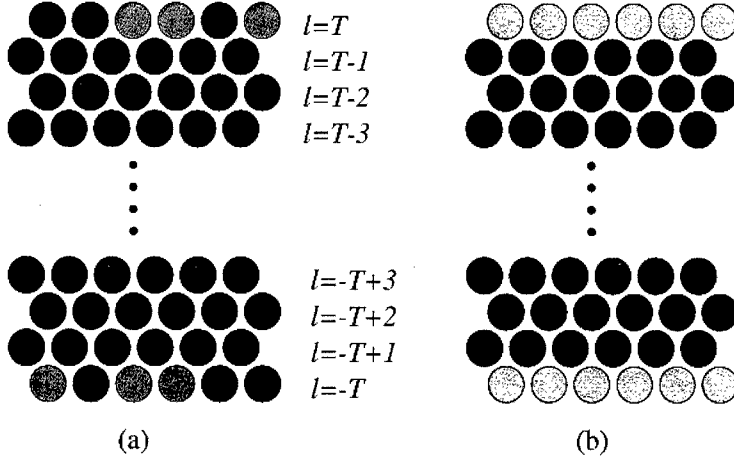


**Figure 1.** Schematic diagram illustrating the cross section geometry of the slabs used in the EAM-SOE calculations. Red and blue circles represent the surface-alloy atoms, while green circles are the substrate atoms. Grey atoms represent ‘virtual’ surface-alloy atoms, as discussed in the text.

unless  $l$  and  $l'$  are equal to the same surface-alloy layer.

$$\psi_{\alpha,l,l'}(\mathbf{r}_l - \mathbf{r}'_{l'}) = \left[ \frac{\partial^2 E}{\partial \delta c_l(\mathbf{r}_l) \partial u_{\alpha,l'}(\mathbf{r}'_{l'})} \right]_0$$

and  $\psi_{\alpha,l,l'}(\mathbf{r}_l - \mathbf{r}'_{l'})\delta c_l(\mathbf{r}_l)$  is the  $\alpha$ -component of the force on an atom in layer  $l'$ , at  $\mathbf{r}'_{l'}$  which arises from a deviation of the concentration from its average value at site  $\mathbf{r}_l$  in the surface-alloy layer  $l$  ( $\psi_{\alpha,l,l'}(\mathbf{r}_l - \mathbf{r}'_{l'})$  is again defined to be zero unless  $l$  is a surface-alloy layer).  $\phi_{\alpha,\beta,l,l'}(\mathbf{r}_l - \mathbf{r}'_{l'})$  is the force-constant matrix of the reference-state slab illustrated in figure 1(b).

From equation (1), the equilibrium energy corresponding to a given surface-alloy configuration can be determined by minimizing with respect to the atomic displacements. Specifically, by imposing the condition of mechanical equilibrium [ $\partial E / \partial u_l(\mathbf{r}_l) = \mathbf{0} \forall l, \mathbf{r}_l$ ], the energy can be rewritten as follows:

$$E = E_0 + \frac{1}{2} \sum_{l=-T,T} \sum_{\mathbf{r}_l, \mathbf{r}'_l} \delta c_l(\mathbf{r}_l) \delta c_l(\mathbf{r}'_l) \left[ \theta_{l,l}(\mathbf{r}_l - \mathbf{r}'_l) - \sum_{l',l''} \sum_{\mathbf{r}_l, \mathbf{r}'_{l'}} \psi_{\alpha,l,l'}(\mathbf{r}_l - \mathbf{r}'_{l'}) \phi_{\alpha,\beta,l',l''}^{-1}(\mathbf{r}'_{l'} - \mathbf{r}''_{l''}) \psi_{\beta,l,l''}(\mathbf{r}'_{l'} - \mathbf{r}''_{l''}) \right] \quad (2)$$

where the first sum on the right-hand side is over the two surface-alloy layers, and  $\phi^{-1}$  is the inverse of the force-constant matrix. By making use of a *two-dimensional* Fourier transformation, equation (2) can be simplified further:

$$E = E_0 + \frac{n}{2} \sum_{l=-T,T} V_{l,l}(\mathbf{k}) |\delta c_l(\mathbf{k})|^2 \quad (3)$$

where  $n$  is the number of unit cells per layer, and  $V_{T,T}(\mathbf{k}) = V_{-T,-T}(\mathbf{k})$  is defined as follows:

$$V_{T,T}(\mathbf{k}) = \theta_{T,T}(\mathbf{k}) - \sum_{l,l'} \psi_{\alpha,T,l}(\mathbf{k}) \phi_{\alpha,\beta,l,l'}^{-1}(\mathbf{k}) \psi_{\beta,T,l'}^*(\mathbf{k}). \quad (4)$$

From equations (1) and (2) it can be seen that the first and second terms on the right-hand side of equation (4) are the ‘chemical’ and elastic (relaxation) contributions to the Fourier transform of the EPs.

Below we present results for the energetics of bulk and surface Cu–Ag alloys, computed using the formalism described above. In the application of this formalism, we have used the EAM potentials of Foiles *et al* [11]. The details concerning the calculation of the terms  $E_0$ ,  $\theta$ ,  $\psi$  and  $\phi$  within the EAM are given in [4]. The results presented below for surface alloys were obtained with 101-layer slabs ( $T = 50$  in figure 1).

### 3. Results and discussion

In figure 2 we show calculated values of  $V(\mathbf{k})$  for surface (figure 2(a)) and bulk (figure 2(b)) equiatomic Cu–Ag alloys. Results are plotted for values of  $|\mathbf{k}|$  varying between zero and the Brillouin-zone boundary along the high-symmetry direction of a primitive reciprocal-lattice vector ( $G_1$ ); for both surface and bulk Cu–Ag alloys these directions contain the global minimum in  $V(\mathbf{k})$ . The surface-alloy results were obtained for Cu–Ag on a Pd(111) substrate. This choice of substrate was motivated by the experimental studies of Cu–Ag/Ru(0001) performed by Stevens and Hwang [9]; similar to the (0001) surface of Ru, Pd(111) is close-packed and is characterized by a nearest-neighbour spacing intermediate between that of pure Cu and Ag.

The results for *bulk* Cu–Ag in (figure 2(b)) are qualitatively similar to those previously discussed for other size-mismatched bulk systems (e.g. [4]). The chemical contribution to  $V(\mathbf{k})$  (red line) is analytic everywhere, and the limiting value of the relaxation contribution to  $V(\mathbf{k})$  attains a minimum as  $|\mathbf{k}| \rightarrow \mathbf{0}$  along a given direction. From a comparison between the red lines in figures 2(a) and (b) it is clear that the EAM predicts only small differences between the chemical interactions for Cu–Ag in the bulk and on a Pd(111) surface. A similar comparison of the results plotted with blue lines shows that the nature of the  $\mathbf{k} = \mathbf{0}$  singularity in the elastic contribution to  $V(\mathbf{k})$  is qualitatively different for surface alloys as compared to their bulk counterparts. In particular, the elastic contribution to  $V(\mathbf{k})$  for the surface alloy is characterized by a finite slope at the origin. Since  $V(\mathbf{k}) = V(-\mathbf{k})$  for finite  $|\mathbf{k}|$ , this implies a slope discontinuity for  $V(\mathbf{k})$  at the origin.

The main features characterizing the elastic contribution to  $V(\mathbf{k})$  in figure 2(a) can be understood by considering the energetics of laterally ‘striped’ surface-alloy structures  $A_p B_p$ , consisting of  $p$  layers of atom type  $A$  followed by  $p$  layers of  $B$  along a particular direction on the substrate  $C$ . Associated with such a striped phase is a fundamental Fourier component of the composition modulation with wavevector  $|\tilde{\mathbf{k}}| = 2\pi/2dp$ , where  $d$  is the interlayer separation. By making use of the continuum elasticity model of Marchenko [12], the formation energy  $\Delta E(p)$  of an  $A_p B_p$  striped structure on an isotropic substrate  $C$  can be written for large  $p$  (small  $|\tilde{\mathbf{k}}|$ ) as follows [13, 14]:

$$p\Delta E(p) = I_C - (\sigma_{A/C} - \sigma_{B/C})^2 \frac{1 - \nu^2}{\pi \mu} \log(2pd/\pi b) \quad (5)$$

where  $I_C$  is a chemical interfacial energy (which may be either positive or negative), and the second term on the right-hand side is the elastic relaxation energy associated with the array of interfaces between regions of pure  $A$  and  $B$ . In the expression for the elastic relaxation energy,  $(\sigma_{A/C} - \sigma_{B/C})$  is the difference between the surface stresses associated with films of pure  $A$  and  $B$  on  $C$ ,  $\nu$  and  $\mu$  are the Young’s modulus and Poisson ratio associated with the isotropic substrate, respectively, and  $b$  is the cutoff distance smaller than which elastic continuum theory no longer applies (analogous to a core radius in dislocation theory). The second term on the right-hand side of equation (5) corresponds to an elastic contribution to  $V(\mathbf{k})$  which decreases linearly with  $|\mathbf{k}|$  near the origin [13, 14], consistent with the results plotted in figure 2(a).

Equation (5) holds only for striped phases with large  $p$ . As  $p$  decreases (increasing  $|\tilde{\mathbf{k}}|$ ), overlapping strain fields lead to a short-ranged elastic repulsion between  $A/B$  and  $B/A$

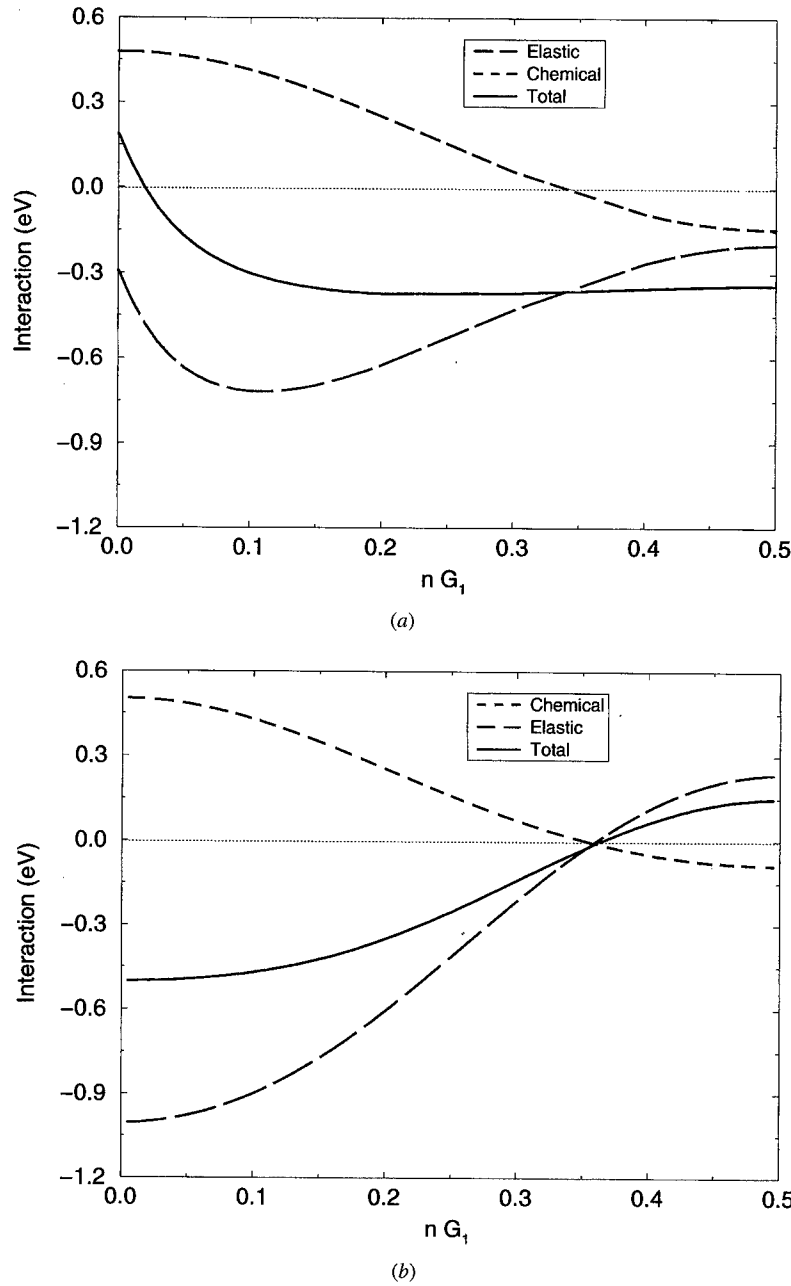


**Figure 2.** EAM-SOE-calculated values of the reciprocal space interactions ( $V(k)$ ) for surface (a) and bulk (b) Cu–Ag alloys, plotted along a high-symmetry direction. The red and blue curves represent the chemical and elastic contributions to  $V(k)$ , and the sum is plotted by a black curve. The results for surface alloys were obtained using 101-layer slabs and a Pd(111) substrate†.

interfaces, analogous to the case of surface steps [15]. The competition between the short-ranged elastic repulsion of interfaces and the relaxation energy associated with individual

† For an anisotropic substrate, such as Pd(111), the linear relationship between  $V(K)$  and  $[k]$  still holds, although the slope depends upon the direction  $\hat{k}$ .

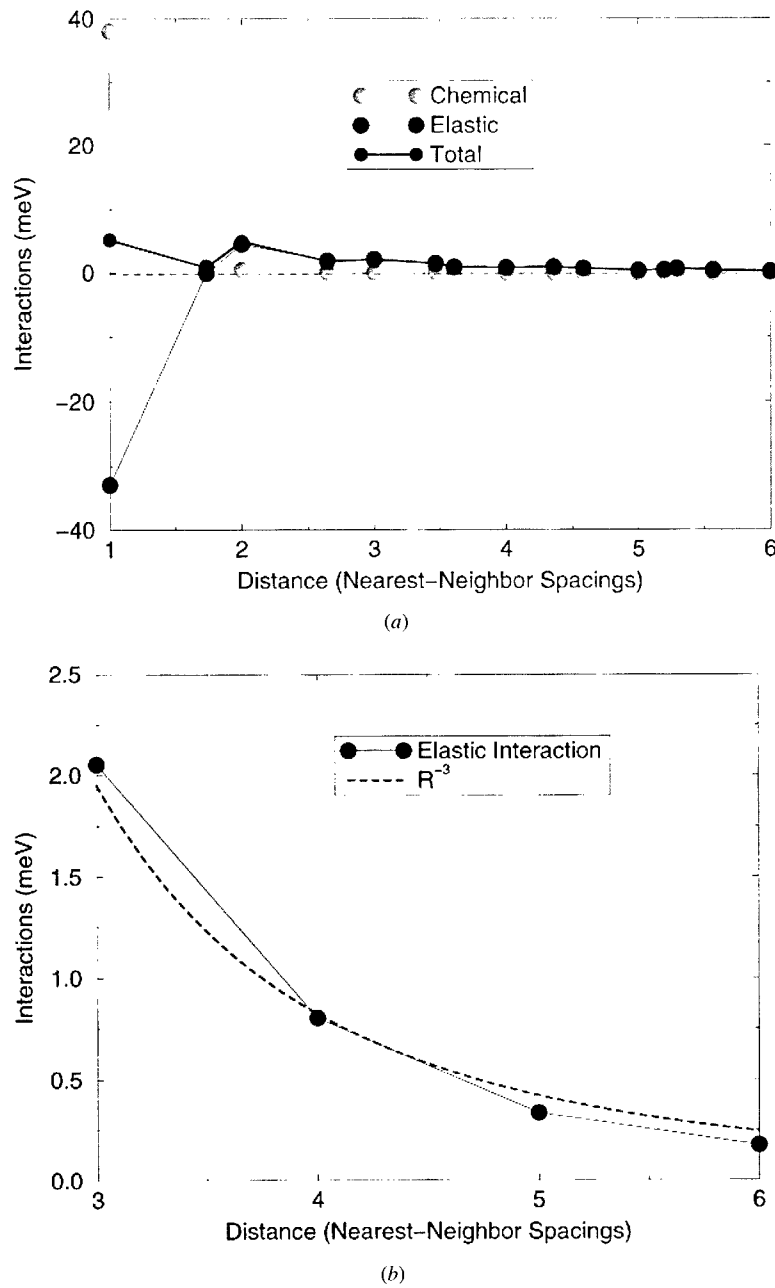


**Figure 3.** Chemical, elastic and total values of the calculated EPIs for Cu–Ag on Pd(111) are plotted as a function of distance in real space in (a). The elastic contributions are plotted on a different scale in (b), where the dashed line illustrates a  $R^{-3}$  dependence characteristic of a continuum model of interacting elastic dipoles.

interfaces gives rise to a finite  $p$  minimum in the elastic contribution to  $\Delta E(p)$ , and a finite  $|k|$  minimum in the elastic contribution to  $V(k)$ , as shown in figure 2(a). We have performed EAM calculations for a number of surface-alloy systems and in each case we have found that the minimum elastic contribution to  $V(k)$  occurs for values of  $|k|$  equal to roughly 0.1 in units

of  $2\pi/a$ , with  $a$  the surface lattice constant. In cases where the chemical interactions favour phase separation (i.e. a minimum at  $\mathbf{k} = \mathbf{0}$ ), this implies that the global minimum of the total  $V(\mathbf{k})$  will be for  $|\mathbf{k}|$  intermediate between 0 and 0.1, implying the stability of long-period striped superstructures with unit cells spanning roughly 10 or more lattice constants.

In figure 3(a) the calculated elastic and chemical contributions to the EPIs for Cu–Ag/Pd(111) are plotted as a function of distance in real space. The total interactions (black circles) are predicted to be rather weak by the EAM. The small value of the nearest-neighbour EPI results from a near cancellation of the much larger chemical and elastic contributions, plotted with red and blue circles, respectively. While the chemical EPIs decay very rapidly in real space, the elastic pair interactions are characterized by a long-ranged tail, which is plotted on a different scale in figure 3(b). The dashed line in figure 3(b) is consistent with a  $R^{-3}$  dependence characteristic of interacting elastic dipoles. The EAM-SOE results for the elastic interactions are found to be consistent with this asymptotic behaviour at large distances.

To summarize, we have presented the results of an EAM-SOE analysis of the effective pair interactions characterizing the mixing energetics of monolayer surface alloys on single-crystal substrates. It is demonstrated that the minimum of the Fourier-transformed EPIs is governed by a competition between elastic and chemical contributions to  $V(\mathbf{k})$ . For the Cu–Ag/Pd(111) system considered here these contributions are of comparable magnitude. It is demonstrated that the elastic contribution to  $V(\mathbf{k})$  is qualitatively different for surface alloys as compared to their bulk counterparts. In particular, for surface alloys this contribution is characterized by a finite slope at the origin, ensuring that the minimum in the total  $V(\mathbf{k})$  is always displaced from the origin. As a consequence, chemical instabilities and short-range order in surface alloys should generally be of ordering (i.e. finite  $|\mathbf{k}|$ ) type.

## Acknowledgments

This research was supported by the Office of Basic Energy Science, Division of Materials Science, of the US Department of Energy under Contract No DE-AC04-94AL85000. We thank N C Bartelt for many helpful discussions.

## References

- [1] de Fontaine D 1979 *Solid State Phys.* **34** 73
- [2] Sanchez J M, Ducastelle F and Gratias D 1984 *Physica* **128A** 334
- [3] Cook H E and de Fontaine D 1969 *Acta Metall.* **17** 915
- [4] Asta M and Foiles S M 1996 *Phys. Rev. B* **53** 2389
- [5] Hwang R Q and Bartelt M C 1997 *Chem. Rev.* **97** 1063
- [6] Bardi U 1994 *Rep. Prog. Phys.* **57** 939
- [7] Christensen A, Ruban A V, Stoltze P, Jacobsen K W, Skriver H L, Nørskov J K and Besenbacher F 1997 *Phys. Rev. B* **56** 5822  
Pleth Nielsen L, Besenbacher F, Stensgaard I, Lægsgaard E, Engdahl C, Stoltze P, Jacobsen K W and Nørskov J K 1993 *Phys. Rev. Lett.* **71** 754
- [8] Stevens J L and Hwang R Q 1995 *Phys. Rev. Lett.* **74** 2078
- [9] Daw M S and Baskes M I 1983 *Phys. Rev. Lett.* **50** 1285  
Daw M S and Baskes M I 1984 *Phys. Rev. B* **29** 6443
- [10] Foiles S M, Baskes M I and Daw M S 1986 *Phys. Rev. B* **33** 7983
- [11] Marchenko V I 1981 *JETP Lett.* **33** 382
- [12] Vanderbilt D 1992 *Surf. Sci.* **268** L300  
Ng K-O and Vanderbilt D 1995 *Phys. Rev. B* **52** 2177
- [13] Ozoliņš V, Asta M and Hoyt J J, to be published
- [14] Srolovitz D J and Hirth J P 1991 *Surf. Sci.* **255** 111

## Vibrational thermodynamics: coupling of chemical order and size effects

Dane Morgan<sup>†</sup>, Axel van de Walle<sup>†</sup>, Gerbrand Ceder<sup>†</sup>, Jeffrey D Althoff<sup>‡</sup> and Didier de Fontaine<sup>‡</sup>

<sup>†</sup> Department of Materials Science and Engineering, Massachusetts Institute of Technology, Cambridge, MA 02139, USA

<sup>‡</sup> Department of Materials Science and Mineral Engineering, University of California, Berkeley, CA 94720, USA

Received 16 September 1999, accepted for publication 1 March 2000

**Abstract.** The effects of chemical order on the vibrational entropy have been studied using first-principles and semi-empirical potential methods. Pseudopotential calculations on the  $Pd_3V$  system show that the vibrational entropy decreases by  $0.07k_B$  upon disordering in the high-temperature limit. The decrease in entropy contradicts what would be expected from simple bonding arguments, but can be explained by the influence of size effects on the vibrations. In addition, the embedded-atom method is used to study the effects of local environments on the entropic contributions of individual Ni and Al atoms in  $Ni_3Al$ . It is found that increasing numbers of Al nearest neighbours decreases the vibrational entropy of an atom when relaxations are not included. When the system is relaxed, this effect disappears, and the local entropy is approximately uniform with increasing number of Al neighbours. These results are explained in terms of the large size mismatch between Ni and Al. In addition, a local cluster expansion is used to show how the relaxations increase the importance of long-range and multisite interactions.

### 1. Introduction

The role of vibrational thermodynamics in phase stability is still poorly understood. Traditionally, the effects of vibrations have not even been considered in theoretical phase stability studies, which focused primarily on substitutional influences [1–4]. There is growing evidence, both experimental [5–12] and theoretical [13–24] that vibrational thermodynamics can have a significant influence on phase diagrams.

Unfortunately, at present there are only the beginnings of a qualitative understanding of how differences in vibrational thermodynamics arise. In real systems, various mechanisms such as volume differences, bond type differences, internal strain effects, and defect structures (impurities, grain boundaries, etc) can all contribute to the vibrational thermodynamics, making it difficult to separate out the contributions of each. An advantage of computational approaches is that it is possible to manipulate the system being studied so as to isolate different mechanisms, for example, by removing thermal expansion or restricting internal relaxations. In this paper we will use computational approaches to study how relaxations and bonding changes between different chemical orderings influence vibrational entropies.

The key results can be summarized as follows. First-principles pseudopotential calculations for the vibrational entropy of  $Pd_3V$  indicate that upon disordering the  $DO_{22}$  phase the vibrational entropy *decreases* by  $0.07k_B$  [25]. This is somewhat surprising since the  $DO_{22}$  phase is expected to have stiffer bonds, and therefore a lower vibrational entropy,

than the disordered phase. More detailed analysis shows that despite the small size mismatch between Pd and V there is significant relaxation allowed in the disordered phase that is not possible in the  $DO_{22}$  structure. The different relaxations occur because any given disordered configuration has much lower symmetry than the  $DO_{22}$  phase (although, when the occupations are thermodynamically averaged, the averaged disordered phase has higher symmetry than  $DO_{22}$ ). It is shown that the greater relaxation allows a stiffening of the Pd–V bonds, which leads to the lowering of the entropy with disordering.

When the embedded-atom method is used to calculate a local vibrational entropy for each atom in  $Ni_3Al$ , it is found that for an unrelaxed crystal the local entropy increases with increasing numbers of Al nearest neighbours, but that this trend disappears when the proper relaxations are included [26]. The effects of the relaxations are understood in terms of the large size mismatch between the Ni and Al atoms. When no relaxations are allowed, the large Al crowd the atoms they surround, reducing the vibrational entropy. When relaxations are allowed, the large Al push each other away, which reduces crowding and does not change the vibrational properties of a surrounded atom very strongly. A local cluster expansion is used to analyse the relaxation effects in more detail, and the results show that the relaxations increase the importance of long-range and multisite interactions.

This paper is arranged as follows. Section 1 contains the introduction. Section 2 contains the qualitative framework in which we will analyse the calculations. A Lennard-Jones potential is used to demonstrate how the qualitative picture is realized in a simple system. Section 3 discusses first-principles calculations of the vibrational entropy difference between  $DO_{22}$  and disordered  $Pd_3V$ . Section 4 discusses embedded-atom method calculations of the influence of local environments on the local vibrational entropy in  $Ni_3Al$ . Finally, section 5 gives a summary and conclusions.

## 2. Qualitative framework

First we will discuss a simple qualitative picture of the effects of changing chemical order on the vibrational thermodynamics. We will restrict the discussion to various lattice decorations of a fixed parent lattice at a fixed composition. In the harmonic approximation [27], the vibrational thermodynamics of a given structure are determined by its dynamical matrix, which in turn is given by the force constant matrix and the masses. At a fixed composition and high temperatures the masses contribute a constant term to the vibrational thermodynamics and can therefore be ignored when considering differences [2]. Changes in the vibrational thermodynamics between different lattice decorations must therefore come from changes in the proportions of different force constants, or changes in their actual values.

A sensible starting model for how the force constants are affected by chemical order is what we will call the ‘bond-proportion model’. This model assumes that each type of bond carries with it an approximately fixed force constant, and that changes in the force constants with chemical order are due primarily to changes in the proportions of different types of bonds. This sort of model is often used to give a simple starting Hamiltonian from which more elaborate theoretical calculations are tractable [14, 28].

If this bond-proportion model is accurate, even qualitatively, there are certain implications for the behaviour of vibrational entropies. For example, consider an ordered compound, and compare it to the pure elements from which it is made. As a first approximation the force constants between unlike species are given by the harmonic mean of the force constants between like species. For bonding of this type the bond-proportion model predicts very little change in the vibrational thermodynamics upon disordering [14]. For a strongly ordering material it is to be expected that bonds between unlike species are more stable, and therefore have somewhat

stiffer force constants than the harmonic mean of the bonds between like species. The stiffer average force constants would generally cause the ordered phase to have a lower vibrational entropy than the average of the pure elements (which have only like neighbour bonds). Define the vibrational formation entropy of a binary compound  $A_{1-c}B_c$  by

$$\Delta S_{\text{form}} = S_{\text{ord}} - (1 - c)S_A - cS_B \quad (1)$$

where  $S_{\text{ord}}$ ,  $S_A$ , and  $S_B$  are the vibrational entropies of the ordered, pure A, and pure B materials, respectively. The above arguments show that the bond-proportion model predicts that for an ordering alloy the vibrational formation entropy would be negative. Another implication of the bond-proportion model is that for an ordering alloy, the disordered phase will have a larger vibrational entropy than an ordered phase of the same composition. This follows from the fact that the disordered phase has fewer unlike neighbour bonds associated with stiff force constants than the ordered phase.

Unfortunately, neither experiments nor direct first-principles calculations support the predictions of the bond-proportion model in general. Calculations of the high-temperature limit of  $\Delta S_{\text{form}}$  based on experimentally measured force constants and densities of states show that many ordered compounds have positive values of  $\Delta S_{\text{form}}$  [12]. Furthermore, first-principles calculations on the Cu–Au system found positive values of  $\Delta S_{\text{form}}$  for all the ordered structures studied [23]. These results are not consistent with the bond-proportion model.

Experimental measurements for a number of systems [6–9, 11] have consistently found that the vibrational entropy increases with disordering, which matches the predictions of the bond-proportion model. On the other hand, first-principles results for Ni<sub>3</sub>Al, which is a very strongly ordered compound, essentially show no change in entropy between the ordered and disordered phases [22].

We propose that to explain, even qualitatively, the changes in vibrational entropy, one must go beyond a simple bond-proportion model and incorporate size effects. By size effects we mean the effects on the force constants that are associated with compression and stretching of the bonds. Size effects are not included in the simple bond-proportion model, where all bonds are considered fixed in their strength. For example, if elements A and B have very different sizes, there is no reason to expect A–A bonds to have similar force constants in A and B rich environments, since the A–A bonds will be of very different lengths in the two cases.

An intuitive understanding of the interplay between size and bond-type effects can be obtained by considering a simple nearest-neighbour Lennard-Jones potential. This potential has been used to calculate the change in the value of the vibrational thermodynamics between ordered L1<sub>0</sub> and a fcc disordered phase in the harmonic approximation. In the high-temperature limit the relevant thermodynamics can be calculated from the logarithmic average of the density of states ( $\langle \ln \omega \rangle$ ), which is defined by

$$\langle \ln \omega \rangle = \int_0^\infty \ln(\omega)g(\omega) d\omega \quad (2)$$

where  $g(\omega)$  is the vibrational density of states and  $\omega$  is the frequency. Define the change in  $\langle \ln \omega \rangle$  by  $\Delta \langle \ln \omega \rangle = \langle \ln \omega \rangle_{\text{disordered}} - \langle \ln \omega \rangle_{\text{ordered}}$ . The change in vibrational free energy ( $\Delta F$ ) and entropy ( $\Delta S$ ) with disordering can then be written simply as

$$\Delta F = k_B T \Delta \langle \ln \omega \rangle \quad (3)$$

$$\Delta S = -k_B \Delta \langle \ln \omega \rangle. \quad (4)$$

The disordered phase was modelled by randomly distributing A and B type atoms on a cube-shaped 256-atom supercell of fcc, where the concentration was constrained to remain at A–50 at% B. Calculations were converged to within  $\pm 0.01$  in  $\langle \ln \omega \rangle$  with respect to  $k$ -points. The L1<sub>0</sub> structure was completely relaxed whereas the corresponding disordered phase was

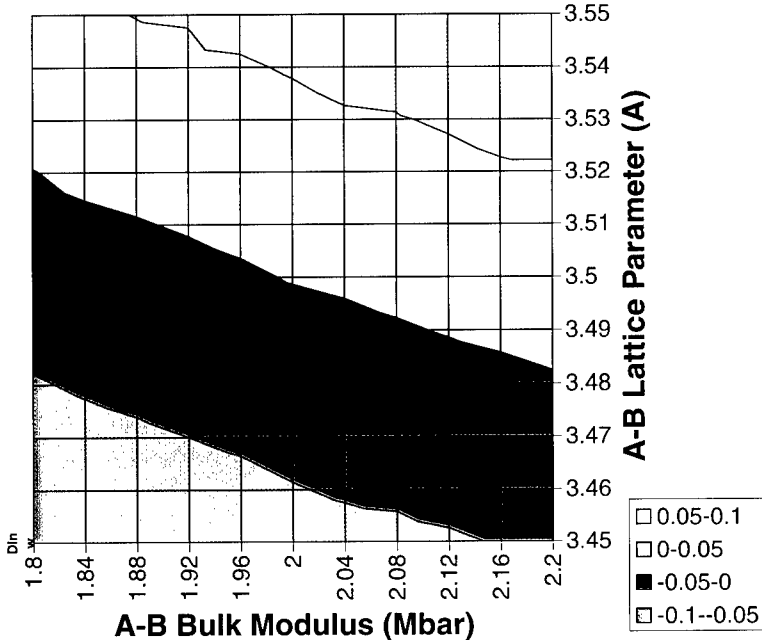


**Figure 1.**  $\Delta\langle\ln\omega\rangle$  as a function of the effective bulk modulus and lattice parameter of the A–B bonds. A–A and B–B bonds are fixed to an effective bulk modulus of 2 Mb and lattice parameter of 3.5 Å. The calculations are all performed with a nearest-neighbour Lennard-Jones potential.

only relaxed internally, keeping the overall volume per atom fixed  $L1_0$  and the three supercell lattice parameters equal to each other. This removed any complications that might occur due to volume changes between the two phases. No thermal expansion effects were included. All calculations were performed using the GULP program [29].

In figure 1 the values of  $\Delta\langle\ln\omega\rangle$  are plotted as a function of the bulk modulus and lattice parameter that would be obtained for an fcc structure made of A–B bonds only (this is not physically realizable but characterizes the A–B bond properties in a transparent manner). The A–A and B–B bonds are all fixed to give a bulk modulus of 2 Mb and a lattice parameter of 3.5 Å for pure A and B lattices.

Consider first the values along the horizontal line for which the A–B lattice parameter is equal to 3.5. Here all the bonds are the same length and there are no size effects, so it is expected that the bond-proportion arguments should be valid. This is seen to be the case by the fact that for softer A–B bonds one obtains  $\Delta\langle\ln\omega\rangle < 0$ , but for stiffer A–B bonds one obtains  $\Delta\langle\ln\omega\rangle > 0$ . Now consider the values along the vertical line for which the A–B bulk modulus is equal to two. Here all the bonds have the same strength, so any changes in the thermodynamics between ordered and disordered phases are due to size effects. For smaller A–B bonds the unlike bonds are stretched by the larger A–A and B–B bonds and therefore the A–B bonds are actually weaker than they would be at their equilibrium length. This causes an effect similar to what is seen for the weak A–B bonds with no size effects, and one obtains  $\Delta\langle\ln\omega\rangle < 0$ . Similar arguments show why larger A–B bonds yield  $\Delta\langle\ln\omega\rangle > 0$ . For the intermediate cases the bond-proportion and size effects both contribute. Although the nearest-neighbour Lennard-Jones potential demonstrates how vibrational thermodynamics are influenced by both size and bond effects, their complex interplay cannot be reliably investigated with such a simple model. Therefore, we now turn to more accurate potential and first-principles models.

### 3. First-principles study of Pd<sub>3</sub>V

Pd<sub>3</sub>V is a system for which one might expect the bond-proportion model to be accurate. Pd and V have a very small size mismatch [30]

$$\frac{(V_{\text{Pd}} - V_{\text{V}})}{(V_{\text{Pd}} + V_{\text{V}})/2} = 0.06$$

so size effects should not be too large. Pd<sub>3</sub>V forms in an ordered *DO*<sub>22</sub> structure for temperatures below 1090 K [31], so it is to be expected that Pd–V bonds will be stronger than the harmonic mean of Pd–Pd and V–V bonds. In addition, Pd and V are on either side of the transition metals in the periodic table. In general, bulk moduli tend to reach a maximum near the middle of the transition metals series. To the extent that a Pd–V bond resembles one between two elements of the middle of the transition metals series, it is to be expected that the Pd–V bonds will be stiffer than Pd–Pd or V–V bonds. Given these arguments, the bond-proportion model predicts that the vibrational entropy should increase upon disordering Pd–V, since fewer Pd–V bonds are present in the disordered phase.

First-principles methods have been used to calculate the vibrational thermodynamics of a few different structures of the Pd<sub>3</sub>V system. Calculations have been performed with the quasiharmonic method [27], which extends the harmonic method to approximately include anharmonic terms by allowing volume dependent frequencies. All the entropy values quoted for Pd<sub>3</sub>V were calculated in the high-temperature limit at the zero-temperature equilibrium volumes of the structures. The effects of thermal expansion are not reported for simplicity as they are very small, contributing less than 0.01k<sub>B</sub> to the entropy difference between the *DO*<sub>22</sub> and disordered phases at a temperature of 1000 K. The required force constants were fit to *ab initio* calculations of forces in supercells with slightly displaced atoms [32].

The calculations were made computationally feasible by restricting displacements to consist of whole planes of atoms, thereby maintaining as much symmetry as possible. Planar force constants were obtained from the displacements and forces according to the relation

$$-\mathbf{F}^{\alpha}(n) = \sum_{m,\beta} \lambda^{\alpha\beta}(n-m) \mathbf{u}^{\beta}(m) \quad (5)$$

where  $\mathbf{F}^{\alpha}(n)$  is the force on atom  $\alpha$  in layer  $n$ ,  $\mathbf{u}^{\beta}(m)$  is the displacement of atom  $\beta$  in layer  $m$ , and  $\lambda^{\alpha\beta}(n-m)$  is the  $(n-m)$ th layer planar force constant in the direction normal to the planes. The planar force constants can be related to the more usual force constant matrix between atoms  $\alpha$  and  $\beta$  by the formula

$$-\lambda^{\alpha\beta}(n) = \sum_{(\mathbf{R}|\hat{\mathbf{e}} \cdot (\mathbf{R} + \tau_{\alpha\beta}) = d_n)} \mathbf{D}^{\alpha\beta}(\mathbf{R}) \quad (6)$$

where  $d_n$  is the distance between the planes being considered,  $\hat{\mathbf{e}}$  is the normal vector to the planes,  $\tau_{\alpha\beta}$  is the basis vector connecting atoms  $\alpha$  and  $\beta$  in a unit cell, and  $\mathbf{R}$  is a lattice translation vector.  $\mathbf{D}^{\alpha\beta}(\mathbf{R})$  is the usual force constant matrix between atoms  $\alpha$  and  $\beta$ , separated by basis vector  $\tau_{\alpha\beta}$  and lattice vector  $\mathbf{R}$ , which is calculated by second derivatives of the energy with respect to displacements of those atoms. Equation (6) shows that the planar force constants are obtained by collecting the usual force constants for all atoms in the appropriate plane, projecting these force constants along the plane normal, and then summing the resulting terms. By performing calculations along a number of directions and applying symmetry relations it is possible to determine all the desired force constants from equations (5) and (6).

Our *ab initio* calculations were performed within the local density approximation (LDA) using the VASP [33, 34] package, which implements ultra-soft [35] pseudopotentials [36]. To ensure that the errors in the calculated forces did not introduce errors in the vibrational

**Table 1.** Correlations of the structures used.  $p_n$  denotes the  $n$ th nearest-neighbour correlation while  $t_{lmn}$  denotes a triplet made of overlapping  $p_l$ ,  $p_m$  and  $p_n$  pairs.

Structure	$p_1$	$p_2$	$t_{111}$	$t_{112}$	$t_{113}$	$t_{114}$
$L1_2$	0	1	1/2	-1/2	1/2	-1/2
$DO_{22}$	0	2/3	1/2	-1/6	1/6	1/6
SQS-8	1/4	1/3	-1/4	0	-1/12	-1/6
Random	1/4	1/4	-1/8	-1/8	-1/8	-1/8

entropies that exceed  $0.02k_B$ , the following parameters were used. The number of  $k$ -points in the first Brillouin zone was chosen to be approximately  $(14)^3$  divided by the number of atoms in the unit cell. A high energy cutoff of 365 eV was used to accurately determine the equilibrium cell shapes, while a cutoff of 211 eV was sufficient to obtain accurate forces.

Since we were interested in the change in vibrational thermodynamics upon disordering it was necessary to be able to calculate vibrational properties of the disordered phase. The disordered state was modelled by a special quasirandom structure (SQS) [37]. The SQSs are small unit cell structures that are constructed to mimic the short-range correlations of a truly random structure as much as possible. They have been shown to give good estimates of disordered values for a number of electronic [38] and vibrational [26] properties. For this study an eight-atom SQS (SQS-8) is used, which we believe is large enough to accurately represent the vibrational thermodynamics of the disordered lattice, but is small enough to be computationally tractable. A useful way to represent the SQS-8 is in terms of correlations. These are defined as follows. Assign to each lattice site the pseudospin value of -1 or +1, depending on whether the site is occupied by a Pd or V, respectively. Any cluster of sites can then be assigned a cluster function, which is simply the product of the pseudo-spin values on all the sites in the cluster. A correlation is a cluster function averaged over all symmetry equivalent clusters in the parent lattice. Structures with similar correlations tend to have atoms in similar environments. The correlations for the SQS-8 used in this work, as well as the  $L1_2$ ,  $DO_{22}$ , and a truly random structure, are given in table 1. Note that the correlations for the SQS-8 and random structures are quite similar, showing that the SQS-8 has similar local environments to the disordered phase.

In calculating the force constants some choice must be made about how many to include. Table 2 shows the convergence of the entropy as a function of the number of neighbours included in the force constant matrix. Unfortunately, computational limitations restrict us to including only first-neighbour force constants in the SQS-8 structure. It can be seen that over the first three neighbour shells the total entropy of the  $L1_2$  and  $DO_{22}$  structures change by about  $0.1k_B$ , but that the entropy difference between them is converged to within about  $0.02k_B$  by the first-neighbour shell. This suggests that the entropy difference between the SQS-8 and  $DO_{22}$  structures is probably also well converged after the first-neighbour force constants.

Table 2 shows that the entropy of the disordered phase is  $0.07k_B$  below that of  $DO_{22}$ . The major sources of error in this result are likely to be the use of the SQS-8 to approximate the disordered phase and the limiting of the force constants to the nearest-neighbour shell. The error due to the SQS-8 can be estimated by considering differences between  $L1_2$  and  $DO_{22}$ . These two structures have an entropy difference of  $0.08k_B$  and correlations that are identical for the first-neighbour shell and fairly close after that. For comparison, the SQS-8 and totally random structures also have identical first-neighbour correlations and farther range correlations that are much more similar than those of  $L1_2$  and  $DO_{22}$ . It is therefore to be expected that the entropy difference between the SQS-8 and random structure would be significantly less

**Table 2.** Vibrational entropy in units of  $k_B$  as a function of the interaction range included in the spring model. Range is expressed as the number of nearest neighbour shells. Only stretching and bending terms are included for the column labelled 1(sb) (see text).

Structure	1(sb)	1	2	3
$L1_2$	-4.40	-4.39	-4.44	-4.48
$DO_{22}$	-4.48	-4.47	-4.53	-4.58
SQS-8	-4.53	-4.54		
$L1_2-DO_{22}$	0.08	0.08	0.08	0.10
SQS-8- $DO_{22}$	-0.05	-0.07		

than the  $0.08k_B$  entropy difference between  $L1_2$  and  $DO_{22}$ . Based on the correlations shown in table 1 we estimate the error associated with using the SQS-8 at less than  $0.04k_B$ . The error due to the use of only nearest-neighbour force constants we believe to be about  $0.02k_B$ , again based on comparison to the entropy difference between the  $L1_2$  and  $DO_{22}$  structures. Even if we make a very pessimistic error estimate and base the rate of convergence on the absolute vibrational entropies, rather than their differences, we still get an error less than about  $0.1k_B$ . Even in the presence of these errors, we can still exclude the possibility that the change in entropy upon disordering is large and positive, which is the most important feature of our calculations.

Indeed, the decrease in vibrational entropy upon disordering is in the opposite direction from what would be expected based on the bond-proportion model discussed above. The reason is that size effects, even in this system with almost no apparent size mismatch, contribute significantly to the vibrational thermodynamics. We argued earlier that a Pd–V bond might behave similarly to a bond between two elements of the middle of the transition metal series, which typically have a larger stiffness. However, elements of the middle of the transition metal series are also characterized by smaller lattice constants. One would then expect Pd–V bonds to be shorter than V–V or Pd–Pd bonds. As we will see, the short Pd–V bond length is indeed at the source of the important relaxations observed in Pd–V. The importance of size effects in this system will be demonstrated by analysing bond strengths and lengths.

Unfortunately, there is no single parameter which represents the strength of the force constants between two atoms, since this is, in general, a nine-element matrix. A great simplification is to represent the force constant matrix in terms of two parameters, a stretching and a bending term. This determination of the stretching and bending terms is done in the following manner. Start by considering a  $3 \times 3$  force constant matrix between two atoms, represented in cartesian coordinates with one axis along the bond between the atoms. The diagonal terms of the force constant matrix then represent a stretching and two bending terms, which can be reduced to one by requiring the bending terms to be orientation independent. The remaining off-diagonal terms are assumed to be zero.

The ‘reduced’ force constant matrix is thus fully defined by the elements of its diagonal: an element  $S$  (stretching), corresponding to the bond direction and two elements  $B$  (bending) corresponding to the other two directions. By a simple rotation, the reduced matrix can then be transformed back into the usual cartesian coordinate system. It will no longer be diagonal, but all the elements will still be given by linear functions of  $S$  and  $B$ . The values of  $S$  and  $B$  are then determined by fitting (by a least-squares method) the reduced force constant matrices to the forces obtained from *ab initio* calculations, as described at the beginning of section 3.

It is very interesting to note that the entropies calculated with only stretching and bending terms differ by less than  $0.01k_B$  from the entropies calculated with the exact nearest-neighbour force constant matrix for all the cases considered (see column 1(sb) in table 2).

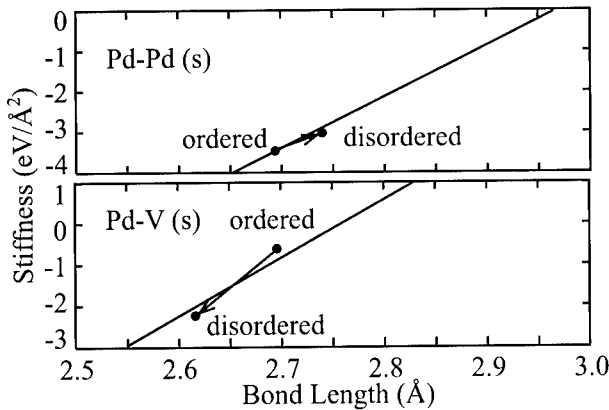


**Figure 2.** Shift in average stiffness (defined as the spring constant along the stretching direction) and bond length upon disordering. The fitted line of stiffness versus length is shown for reference.

Figure 2 shows the average stiffness of Pd–Pd and Pd–V first-neighbour bonds as a function of their average distance in both the ordered  $DO_{22}$  and  $L1_2$  structures and the SQS-8. The stiffness here is taken to be the stretching term defined above. No V–V bond results are included as there are very few of those (none in the ordered phases). Figure 2 shows that in disordering there is a significant change in both the Pd–Pd and Pd–V bond lengths. The change in bond lengths occurs because in the ordered phase all the bonds are constrained by symmetry to be the same length, but in the disordered structure the naturally shorter Pd–V bonds can contract and the naturally longer Pd–Pd bonds can expand. As would be expected, when bonds contract (expand) their stiffness increases (decreases). The contraction of the Pd–V bonds is much greater than the expansion of the Pd–Pd bonds and it is this imbalance which leads to an overall stiffening of the disordered phase and the lowering of the entropy with disorder.

The importance of the relaxations can be seen more quantitatively by removing them in an approximate manner. To do this, we use the stretching and bending model discussed above. We take the stretching and bending parameters for each nearest-neighbour bond in the SQS-8 structure and compute an average for each bond type (Pd–Pd, Pd–V and V–V). This averaging is needed because a given type of bond (e.g. Pd–Pd) may have slightly different values of  $S$  and  $B$ , depending on the bond's local environment. These average Pd–Pd, Pd–V and V–V force constants matrices are an approximation to the ‘true’ force constants we would expect with no symmetry constraints. These force constants are then used to calculate the entropy for both the ordered  $DO_{22}$  and SQS-8 structures and the increase in entropy with disordering is found to be  $0.26k_B$ . This calculation uses a single set of bond length independent force constants for both the ordered and disordered phases and therefore does not include the relaxation differences between the two phases. Without the relaxation effects involved the bond-proportion model applies and the expected entropy increase is seen to occur. Therefore, we conclude that the relaxations are what cause the bond-proportion model to give an incorrect prediction and the vibrational entropy to decrease with disordering.

It can be shown that the stretching and bending force constants are approximately independent of the chemical environment, provided that the proper bond length is used. By this it is meant that a given bond, say Pd–Pd, will have similar values for  $S$  and  $B$  for a given bond length, whether the Pd–Pd bond is in a  $L1_2$ ,  $DO_{22}$ , or SQS structure. This raises the possibility of using the values of  $S$  and  $B$  determined from simple cases to obtain force constants for a variety of complex chemical environments.

This idea is similar to that explored by Sluiter *et al* [39], where an attempt was made to develop transferable force constants by averaging over configurations. Sluiter *et al* found that the averaged force constants were not able to accurately represent the vibrational free energy of different chemical orderings. They attribute at least part of this problem to violation of invariances that the force constants must satisfy. We believe the approach chosen here may be more accurate than the averaged force constants of Sluiter *et al* for two reasons. Most importantly, the stretching and bending model allows the force constants to depend on bond length, which the work presented in this paper proves to be very important. In addition, by using only the diagonal  $S$  and  $B$  terms, the force constant matrices automatically satisfy all the invariances associated with crystal symmetry. This should alleviate some of the problems associated with violations of the invariances. Further testing of the stretching and bending model is necessary before its accuracy can be established.

A more detailed discussion of this work on Pd<sub>3</sub>V can be found in [25].

#### 4. Embedded-atom method study of Ni<sub>3</sub>Al

Ni<sub>3</sub>Al is ordered in the  $L1_2$  structure essentially up to its melting point at about 1670 K [31], although it is possible to create a metastable disordered phase. There have been a number of experimental [6, 40] and theoretical [19–22, 26] studies of the vibrational thermodynamics of ordered and disordered Ni<sub>3</sub>Al. The experiments and calculations have given a range of results for the change in entropy with disordering, probably due to variations in potentials used and differences between the perfect crystals modelled in calculations and those actually obtained in experiment (for further discussion of this, see [12, 22, 41]). In this section we will not focus on the overall change in vibrational thermodynamics between phases, but instead on how the local environment of a given atom affects its vibrational behaviour.

The advantage of a local approach is that it allows one to directly identify how each atom is being influenced by its surroundings. The local vibrational thermodynamics of an atom can be calculated by the following approach. The total density of states,  $g(\omega)$ , can be written

$$g(\omega) = \sum_{\alpha\kappa} \left[ \frac{\Omega}{(2\pi)^3} \right] \sum_j \int dk |e_\alpha(\kappa; jk)|^2 \delta(\omega - \omega_j(k)) = \sum_{\alpha\kappa} g_{\alpha\kappa}(\omega) \quad (7)$$

where  $\Omega$  is the volume per atom,  $\alpha$  and  $\kappa$  denote a Cartesian direction and atom in the unit cell, and  $k$  and  $j$  are the wavevector and branch of each phonon mode.  $e_\alpha(\kappa; jk)$  is the value of the eigenvector for mode  $jk$  associate with direction  $\alpha$  and atom  $\kappa$ , and  $\omega_j(k)$  is the frequency of mode  $jk$ . The  $g_{\alpha\kappa}(\omega)$  are projected densities of states, and represent how much of the total density of states can be attributed to motion of atom  $\kappa$  in direction  $\alpha$ . In this study we will calculate the projected densities of states onto an atom,  $g_\kappa(\omega)$ , which simply involves summing  $g_{\alpha\kappa}(\omega)$  over the possible values of  $\alpha$ . Once the projected density of states onto an atom has been calculated the local vibrational thermodynamics can be found in the harmonic approximation by integrating against the appropriate function [42].

All the calculations shown here for Ni<sub>3</sub>Al were performed using the embedded-atom method [43–45] with the Foiles and Daw Ni<sub>3</sub>Al potential [46]. Calculations are converged to within less than 0.01  $k_B$  with respect to density of states integration and  $k$ -point sampling.

In order to investigate the effects of various local environments the local entropy was calculated for every atom in a randomly decorated 256-atom supercell of Ni<sub>3</sub>Al. The entropies were calculated at a temperature of 600 K, which is near the Debye temperature for this material [40]. The local entropies are plotted in figure 3 as a function of the number of Al nearest neighbours for two cases: one where the atoms were forced to remain on their ideal

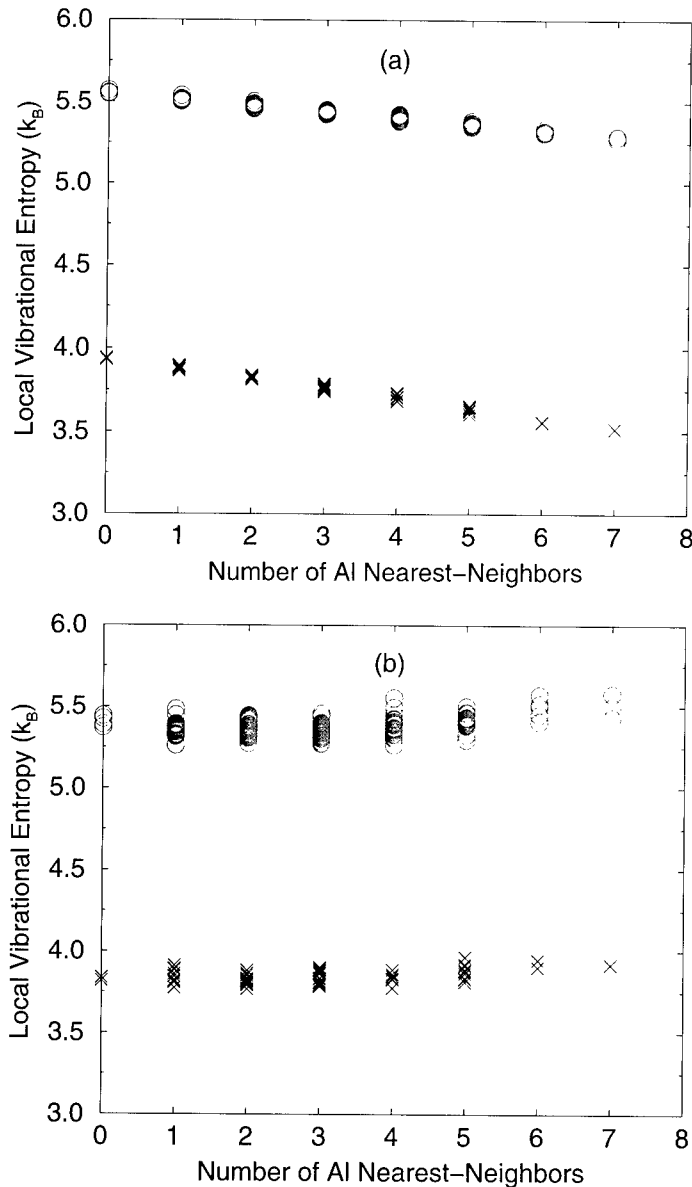


**Figure 3.** The local entropy for Ni (open circles) and Al (crosses) atoms as a function of the number of Al nearest neighbours, as determined from a disordered configuration. Results are given for the unrelaxed (a) and relaxed (b) structures.

lattice sites and one where the atoms were allowed to relax to their equilibrium positions. All these calculations were done at the equilibrium volume of the unrelaxed disordered phase.

There are two important things to notice about these results. The first is that the Ni atoms have consistently higher local entropies than the Al atoms. There are two contributions to this difference. First, the Al generally have stiffer force constants than the Ni, which tend to decrease the Al entropy relative to the Ni. A somewhat larger effect is that Ni is about 2.2 times as heavy as Al, which again causes it to have a larger vibrational entropy than Al.

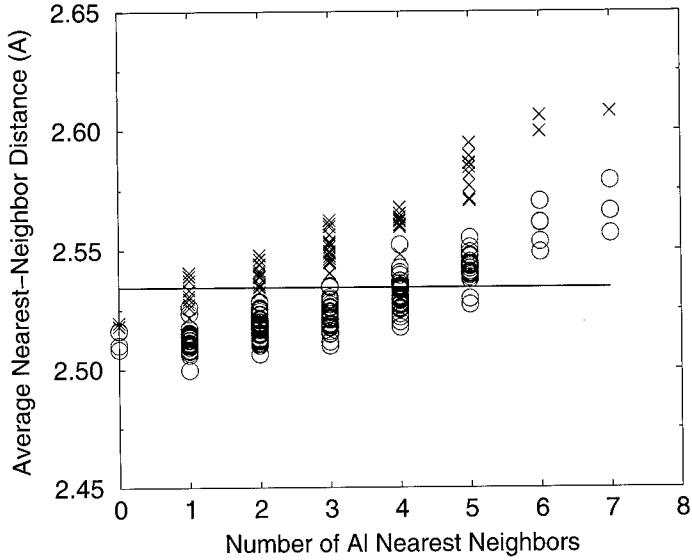


**Figure 4.** The average nearest-neighbour distance for Ni (open circles) and Al (crosses) atoms as a function of the number of Al nearest neighbours, as determined from a relaxed disordered configuration. The average nearest-neighbour distances for the unrelaxed configuration are given by the solid line.

The other important thing to notice is that the overall behaviour of the entropy as a function of local environment changes dramatically when relaxations are included. When no relaxations are allowed the entropy decreases for both types of atoms as more Al neighbours are included. When relaxations are allowed the entropy becomes much noisier, and seems fairly flat, or even slightly increasing, as a function of the number of Al neighbours. To make sense of these results we need to consider size effects.

The size mismatch between Ni and Al is very large [30]

$$\frac{(V_{\text{Al}} - V_{\text{Ni}})}{(V_{\text{Al}} + V_{\text{Ni}})/2} = 0.41$$

which means that relaxation effects are likely to be very important. Figure 4 shows the average distance to the nearest-neighbour shell for all the atoms as a function of the number of Al nearest-neighbour pairs. For the unrelaxed case the neighbours are always the same distance, but the relaxation allows the neighbours to spread apart more and more as they become predominately made up of large Al atoms. The behaviour of the local entropy can now be understood. When there is no relaxation, replacing Ni neighbours with Al neighbours creates progressively more crowding of the central atom. This leads to compressed bonds, which are stiffer, and the vibrational entropy of the central atom decreases. When relaxation is allowed to take place the large Al atoms can move apart to make more space, the bonds of the central atom are no longer compressed, and the atom's entropy does not decrease with increasing numbers of Al neighbours.

It is interesting to consider the predictions of the bond-proportion model for the local entropy of the unrelaxed case. Ni has a bulk modulus that is more than twice as large as that for Al (the potentials fit the experimental bulk moduli exactly) [46], so based on the pure elements one would expect that the Ni–Ni bonds would be much stiffer than the Al–Al bonds. As more Al atoms are added to the environment of a Ni or an Al one would expect a decrease in the average bond stiffness (because of fewer bonds to Ni) and an increase in vibrational

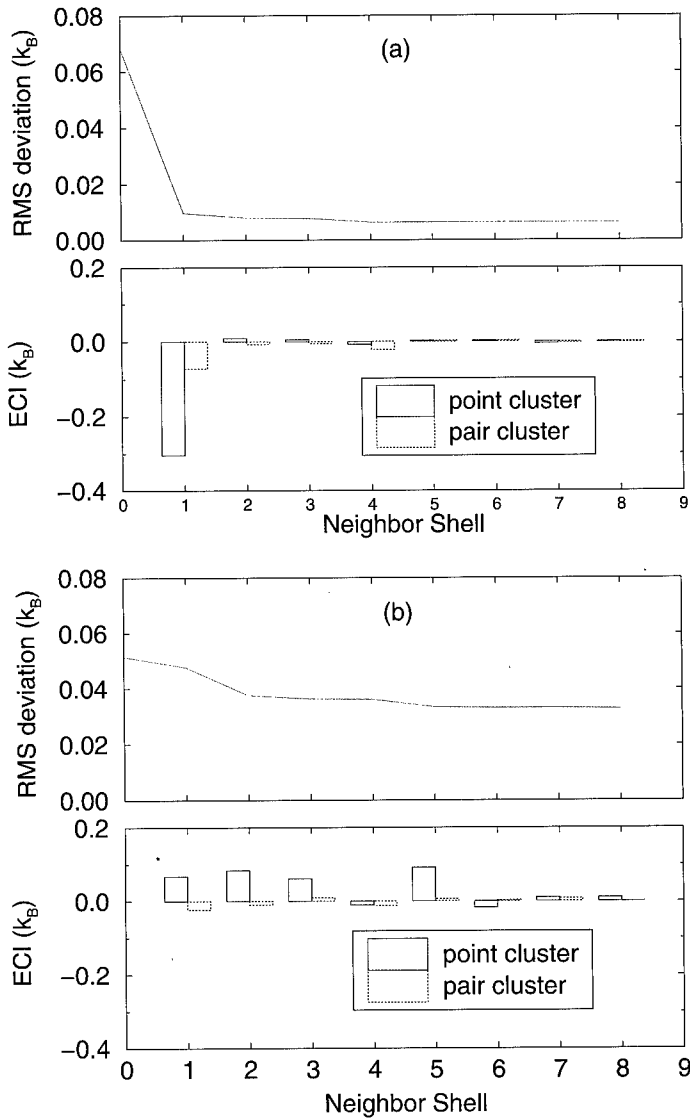
entropy. These predictions are the opposite of what is seen for the unrelaxed case. The failure of the bond-proportion model is again due to the influence of size effects.  $\text{Ni}_3\text{Al}$  is between pure Ni and pure Al in average lattice parameter, so the Al–Al bonds are compressed and the Ni–Ni bonds are expanded in the unrelaxed lattice. This strain effectively brings the bond stiffness of Al–Al bonds above that of Ni–Ni bonds. If one takes this size induced reversal of bond stiffnesses into account, then the bond-proportion model predicts the correct qualitative behaviour. The change in behaviour that is seen when the system relaxes is due in part to the release of some of the strain in the bonds, making Ni–Ni bonds stiffer and Al–Al bonds less stiff.

Figure 3 shows that the nearest-neighbour environment determines the local entropy quite precisely when there are no relaxations, but relaxations introduce other significant influences on the local thermodynamics. This can be made more quantitative by constructing a local cluster expansion. The cluster expansion formalism [3, 4, 37] is used to represent the dependence of functions of lattice decoration in terms of real-space interactions. In section 3 we defined cluster functions. It can be shown that these form a complete orthonormal basis for functions of lattice decoration. The cluster expansion is just an expansion in the basis of cluster functions. The coefficients for each cluster function are called effective cluster interactions (ECI). Because we are studying local quantities we will make use of a local cluster expansion [26, 41], in which there are somewhat different independent ECI than in the traditional cluster expansion. We make a local cluster expansion by fitting the local entropies for all the 256 atoms in a large disordered cell to ECI for the first eight neighbour shells (there is a point and pair ECI for each shell). The results of this fit, both the ECI and the root-mean-square (RMS) error between the true and fitted entropy values, are shown for both the relaxed and unrelaxed case in figure 5.

The local cluster expansion clearly shows the dramatic influence of relaxations. When no relaxations are present the expansion is dominated by the first-neighbour shell, which can be seen by the large first-neighbour ECI and the very low RMS error obtained with only the first shell. When relaxations are included the ECI become much longer range (the largest ECI is in fact in the fifth-neighbour shell). The introduction of longer-range interactions when relaxations are included has also been found in cluster expansions of the total energy [4, 48–51]. In addition, in the relaxed case the RMS error is almost constant after the fifth-neighbour shell, even though it is about five times as large as the corresponding error in the unrelaxed case. The failure of longer-range pairs to improve the RMS error shows that multisite interactions are contributing to the local entropy in the relaxed case. Furthermore, the ECI go from being primarily negative to primarily positive when the relaxations are included. This is the manifestation in the cluster expansion of the above discussed release of strained bonds with relaxation. Finally, note that the point ECI are generally more important than the pair ECI. Point ECI contribute the same amount to a given atom's local entropy independent of the type of the atom. This means that the vibrations of both Ni and Al are influenced similarly by their environment. This is not consistent with the bond-proportion model where one would expect, for example, a very different influence of an Al neighbour on a Ni than an Al. The dominance of the point ECI is just one more way in which the size effects show their importance.

In this section we have shown that for  $\text{Ni}_3\text{Al}$  the local entropy of an atom is primarily determined by the area in which it is free to move. Without relaxation, large Al neighbours crowd a central atom, inhibiting its vibrations, but when relaxation is allowed the Al spread out and the crowding effect essentially disappears. Without relaxation, the compressed Al–Al and Al–Ni bonds are effectively stiffer than the expanded Ni–Ni bonds, despite the much larger bulk modulus of pure Ni than pure Al. It is clear that the local vibrational thermodynamics of  $\text{Ni}_3\text{Al}$  cannot be understood in terms of a simple bond-proportion model and that the behaviour is dominated by the large size effects.

A more detailed discussion of this work on  $\text{Ni}_3\text{Al}$  can be found in [26].



**Figure 5.** The results of a cluster expansion of the local entropy for an unrelaxed (a) and relaxed (b) disordered configuration. The upper panels show the RMS error in the local entropy values predicted by the ECI compared to the exact calculated values, as a function of the number of neighbour shells in the cluster expansion. The lower panels show the point (full) and pair (broken) ECI for each neighbour shell.

## 5. Conclusions

This work discusses the importance of size effects in the behaviour of vibrational thermodynamics. We have shown that a simple bond-proportion model, in which each bond type is assumed to have a fixed stiffness, cannot reliably explain the configurational dependence of the vibrational thermodynamics, even for systems with small size mismatch.

First-principles calculations on the Pd<sub>3</sub>V system predict that the vibrational entropy decreases by  $0.07k_B$  upon disordering the  $DO_{22}$  phase. This decrease is explained by the

stiffening of the disordered phase that occurs as the broken symmetry allows the Pd–V bonds to contract.

We have also performed embedded-atom method calculations of the local vibrational entropy for all the individual atoms in a large Ni<sub>3</sub>Al supercell. The local entropy, as a function of the number of Al nearest neighbours, decreases when no relaxation is included, but remains fairly flat on average when relaxation is included. This can be explained by the fact that the larger Al atoms crowd a central atom when relaxations are not allowed, but push apart and allow for more vibrations when relaxations are included. A local cluster expansion is performed and shows the increased contributions of long-range and multisite ECI due to the relaxations.

This work highlights the importance of relaxation effects in vibrational studies. Ignoring or treating inaccurately the relaxation effects can lead to errors of a qualitative nature, even for systems with very small size mismatch. This problem is particularly challenging for those involved in first-principles research, where accounting for the dependence of the force constants on the magnitude of the local relaxations can come at a high computational cost. This work does suggest some methods by which relaxation effects can be included in a computationally tractable manner. The use of the stretching and bending model, with the force constants parametrized as a function of bond length, seems to give very accurate results and could effectively provide transferable force constants to allow calculations for very complex unit cells. This approach is presently under further development.

## Acknowledgments

This work was supported by the Department of Energy, Office of Basic Energy Sciences under Contract Nos DE-FG02-96ER45571, DE-AC03-76SF00098 and DE-AC04-94AL85000. This work was also supported by NSF cooperative agreement ACI-9619020 through computing resources provided by the National Partnership for Advanced Computational Infrastructure (NPACI) at the San Diego Supercomputing Centre. Axel van de Walle acknowledges support from a ‘1967’ scholarship from the Natural Sciences and Engineering Research Council of Canada. The authors wish to thank G Garbulsky and S M Foiles for providing computer programs which made this work possible. The authors would also like to thank M D Asta for stimulating discussions.

## References

- [1] de Fontaine D 1979 *Solid State Phys.* **34** 73
- [2] Ducastelle F 1991 Order and phase stability in alloys *Cohesion and Structure* vol 3 (The Netherlands: North-Holland)
- [3] de Fontaine D 1994 *Solid State Phys.* **47** 33
- [4] Zunger A 1994 Statics and dynamics of alloy phase transformations *NATO ASI Series. Series B. Physics* vol 319, ed P E A Turchi and A Gonis (New York: Plenum) p 361
- [5] Nagel L J 1996 *PhD Thesis* California Institute of Technology
- [6] Fultz B *et al* 1995 *Phys. Rev. B* **52** 3315
- [7] Anthony L, Nagel L J, Okamoto J K and Fultz B 1994 *Phys. Rev. Lett.* **73** 3034
- [8] Nagel L J, Anthony L and Fultz B 1995 *Phil. Mag. Lett.* **72** 421
- [9] Nagel L J, Fultz B, Robertson L J and Spooner S 1997 *Phys. Rev. B* **55** 2903
- [10] Fultz B *et al* 1995 *Phys. Rev. B* **52** 3280
- [11] Nagel L J, Fultz B and Robertson J L 1997 *Phil. Mag. B* **75** 681
- [12] Bogdanoff P D and Fultz B 1999 *Phil. Mag. B* **79** 753
- [13] Garbulsky G D 1996 *PhD Thesis* Massachusetts Institute of Technology
- [14] Garbulsky G D and Ceder G 1994 *Phys. Rev. B* **49** 6327
- [15] Garbulsky G D and Ceder G 1994 *Phys. Rev. B* **53** 8993

- [16] Tepesch P D *et al* 1996 *J. Am. Ceram. Soc.* **49** 2033
- [17] Tseng W T and Stark J P 1994 *Phil. Mag. B* **70** 919
- [18] Cleri F and Rosato V 1993 *Phil. Mag. Lett.* **67** 369
- [19] Ackland G J 1994 *Alloy Modelling and Design* ed G Stocks and P Turchi (Pittsburgh, PA: Minerals, Metals and Materials Society) pp 149–53
- [20] Althoff J D *et al* 1997 *Phys. Rev. B* **56** R5705
- [21] Ravelo R *et al* 1998 *Phys. Rev. B* **57** 862
- [22] van de Walle A, Ceder G and Waghmare U V 1998 *Phys. Rev. Lett.* **80** 4911
- [23] Ozoliņš V, Wolverton C and Zunger A 1998 *Phys. Rev. B* **58** R5897
- [24] Shaojun L, Suqing D and Benkun M 1998 *Phys. Rev. B* **58** 9705
- [25] van de Walle A and Ceder G 2000 First-principles computation of the vibrational entropy of ordered and disordered  $Pd_3V$  *Phys. Rev. B* **61**
- [26] Morgan D, Althoff J D and de Fontaine D 1998 *J. Phase Equilibria* **19** 559
- [27] Maradudin A A, Montroll E W and Weiss G H 1971 *Theory of Lattice Dynamics in the Harmonic Approximation* 2nd edn (New York: Academic)
- [28] Wojtowicz P J and Kirkwood J G 1960 *J. Chem. Phys.* **33** 1299
- [29] Gale J D 1991–8 *GULP (General Utility Lattice Program)* version 1.2 (London: Royal Institution of Great Britain and Imperial College)
- [30] Pearson W B, Villars P and Calvert L 1985 *Pearson's Handbook of Crystallographic Data for Intermetallic Phases* (Metals Park, OH: American Society for Metals)
- [31] 1990 *Binary Alloy Phase Diagrams* ed B Massalski *et al* (New York: ASM International) 2nd edn
- [32] Wei S and Chou M Y 1992 *Phys. Rev. Lett.* **69** 2799
- [33] Kresse G and Furthmüller J 1996 *Phys. Rev. B* **54** 11 169
- [34] Kresse G and Furthmüller J 1996 *Comp. Mat. Sci.* **6** 15
- [35] Vanderbilt D 1990 *Phys. Rev. B* **41** 7892
- [36] Phillips J C and Kleinman L 1959 *Phys. Rev.* **116** 287
- [37] Zunger A, Wei S-H, Ferreira L and Bernard J E 1990 *Phys. Rev. Lett.* **65** 353
- [38] Hass K C, Davis L C and Zunger A 1990 *Phys. Rev. B* **42** 375
- [39] Sluiter M H, Weinert M and Kawazoe Y 1999 *Phys. Rev. B* **59** 4100
- [40] Anthony L, Okamoto J K and Fultz B 1993 *Phys. Rev. Lett.* **70** 1128
- [41] Morgan D 1998 *PhD Thesis* University of California Berkeley
- [42] Callaway J 1974 *Quantum Theory of the Solid State* student edn (San Diego, CA: Academic)
- [43] Daw M S and Baskes M I 1984 *Phys. Rev. B* **29** 6443
- [44] Foiles S M, Baskes M I and Daw M S 1986 *Phys. Rev. B* **33** 7983
- [45] Daw M S, Foiles S M and Baskes M I 1993 *Mater. Sci. Rep.* **9** 251
- [46] Foiles S M and Daw M S 1987 *J. Mater. Res.* **2** 5
- [47] Sanchez J M, Ducastelle F and Gratias D 1984 *Physica A* **128** 334
- [48] Laks D B, Ferreira L G, Froyen S and Zunger A 1992 *Phys. Rev. B* **46** 12 587
- [49] Wolverton C and Zunger A 1997 *Comp. Math. Sci.* **8** 107
- [50] Wolverton C, Ozolins V and Zunger A 1998 *Phys. Rev. B* **57** 4332
- [51] Ozolins V, Wolverton C and Zunger A 1998 *Phys. Rev. B* **57** 6427

## First-principles alloy theory in oxides

G Ceder<sup>†‡</sup>, A Van der Ven<sup>†</sup>, C Marianetti<sup>†</sup> and D Morgan<sup>†</sup>

<sup>†</sup> Department of Materials Science and Engineering, 77 Massachusetts Ave, Rm 13-5056, Cambridge, MA 02139, USA

<sup>‡</sup> Center for Materials Science and Engineering, 77 Massachusetts Ave, Rm 13-5056, Cambridge, MA 02139, USA

Received 16 September 1999, accepted for publication 16 February 2000

**Abstract.** The physical mechanisms which may contribute to the energy and entropy of mixing in oxide systems are identified and discussed. Ionic size, magnetism and electrostatics can all contribute to the configurational energy dependence of transition-metal oxides. While the many sources of substitutional disorder make configurational entropy an essential contribution to the free energy of oxides, electronic and magnetic entropy may be of the same order of magnitude. This is illustrated with some first-principles results on  $\text{LiCoO}_2$  and  $\text{LiMnO}_2$ .

### 1. Introduction

First-principles thermodynamics of crystalline materials is often referred to by the more general name of alloy theory, reflecting its historical focus on metallic mixtures. Accordingly, first-principles calculations have been applied to study a large number of binary metals [1–11], and even some ternaries [8, 12, 13]. An excellent overview of all the metallic systems investigated up to 1994 can be found in the review article by de Fontaine [14]. In the more recent decade much of the alloy theory formalism has been transferred to semiconductor alloys, with significant success [15].

Applications to oxides have been considerably more scarce, although the stimulus of high-temperature superconductivity led to some *ab initio* alloy work on the phase diagram of  $\text{Y}_2\text{Ba}_2\text{Cu}_3\text{O}_{7-\delta}$  [16, 17] in the early 1990s. Perovskites with mixed B sites have also received attention because of their technological importance as ferroelectrics and dielectrics [18–22].

In this paper we identify the differences and similarities between alloy theory in oxides and metals. The varying degrees of electron localization possible in oxides poses significant challenges to a proper description of the entropy and energy as will be illustrated with examples from  $\text{Li}_x\text{CoO}_2$  and  $\text{LiMnO}_2$ .

### 2. Sources of configurational entropy in oxides

In metallic systems, configurational entropy is the key to reproducing the correct phase diagram topology of alloys. Similarly, it is an essential part of a correct description of oxide thermodynamics. There are several sources of substitutional disorder in oxides which may contribute to the configurational entropy. As in metals, multiple cations or anions can share a common sublattice. This is, for example, the case in  $\text{Ba}(\text{Zn}_{1/3}\text{Nb}_{2/3})\text{O}_3$  where Zn and Nb ions are distributed over the cubic lattice of B-sites in the perovskite structure (figure 1(a)) [21].

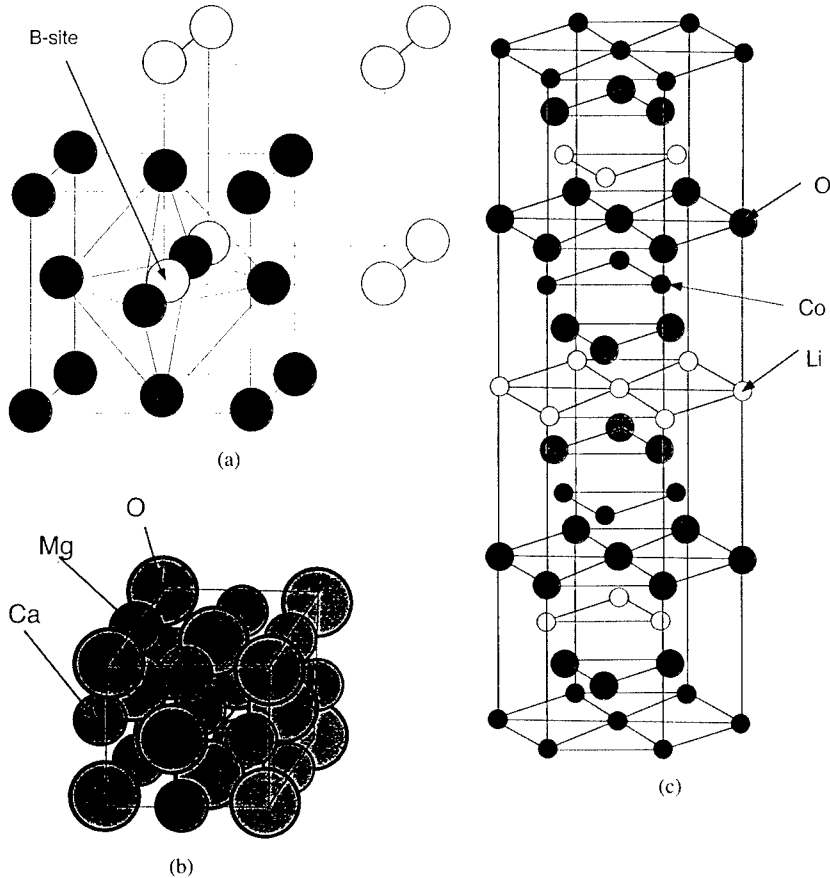


**Figure 1.** (a) Cubic perovskite unit cell. The B sites (white circles) form a simple cubic lattice. (b) In  $\text{Ca}_x\text{Mg}_{1-x}\text{O}$  rocksalts the Ca and Mg ions mix on the fcc lattice of octahedral interstitials (c)  $\text{LiCoO}_2$  is a rocksalt with Li and Co ions ordered in alternating planes of octahedral sites along the rocksalt (111) direction. Lithium can be removed electrochemically leading to order-disorder transitions between lithium and vacancies.

In  $\text{Ca}_x\text{Mg}_{1-x}\text{O}$  the cations share a common fcc lattice, formed by the octahedral interstices of the close-packed oxygen framework (figure 1(b)) [23]. While this type of cationic disorder is quite similar to that in binary metals, the filled anion array in oxides plays a key role in the interaction between the cation sites.

Because many oxides can be seen as close-packed anion arrays with metal interstitials, many structures are at least mechanically stable against removal of a substantial fraction of metal ions. This can lead to configurational disorder between filled and vacant sites.  $\text{Li}_x\text{CoO}_2$  (figure 1(c)) is an extreme example of this type of substitutional disorder as  $x$  (the amount of Li per formula unit) can be varied between 0 and 1 with little or no variation of the host structure. Over this composition range the Li ions go through several order-disorder reactions with the vacancies [24–27].

Due to their structural role the concentration of anion vacancies is usually not as large as for cations and often requires the presence of large cations such as  $\text{Ba}^{2+}$  or  $\text{Pb}^{2+}$  that reside in the oxygen framework. Hence,  $\text{YBa}_2\text{Cu}_3\text{O}_{7-\delta}$  can have oxygen-vacancy order-disorder transitions [16, 17] as does  $\text{Ba}_2\text{In}_2\text{O}_{6-\delta}$  [28, 29].

One should keep in mind that the types of disorder mentioned above can occur simultaneously on different sublattices in one system. For example, in pyrochlores of composition  $A_2B_2O_7$  the A and B cations order on the sites of an fcc-like sublattice while oxygen-vacancy ordering takes place on the tetrahedral interstitials of this lattice [30–32]. Partial disorder on these sublattices is intricately linked [33]. Similarly, disorder on the transition metal cation sublattice of materials such as  $Li_x(Ni, Co)O_2$  is found to depress the ordering tendency of Li and vacancies [34]. Such coupled order-disorder problems are common in oxides as they often arise from the charge compensation mechanism that couples the off-stoichiometry on different sublattices. For example, when  $ZrO_2$  is alloyed with  $CaO$ , the mixing of Ca onto the Zr sublattice is accompanied by the creation of oxygen vacancies on the anion sublattice. The configurational state of each of these sublattices can be strongly coupled, even in a fully-disordered state.

Coupling between disorder on various sublattices can be dominated by symmetry, coupling interactions or correlated fluctuations [33].

### 3. Configurational expansions

The methods to describe configurational disorder and its effect on a free energy are now well developed. We review them here only briefly, with some attention paid to the coupling of disorder between various sublattices. The approach consists of coarse graining the faster degrees of freedom (such as vibrational and electronic) [35] until only substitutional degrees of freedom remain in the partition function. The free energy corresponding to such a partition function can then be calculated by standard methods for lattice models. The Hamiltonian of the effective lattice model is obtained with a cluster expansion [36]. The cluster expansion method is described in several excellent reviews [14, 15]. Basically, it characterizes the configurational state with occupation variables  $\sigma_i$  for each lattice site  $i$  (e.g.  $\sigma_i$  is  $\pm 1$  depending on occupation of site  $i$  by species A or B, where one of these can be a vacancy). The energy is then expanded in polynomials of the occupation variables. The polynomials  $\varphi_\alpha$  correspond to products of occupation variables within a cluster of lattice sites  $\alpha$ ,

$$\varphi_\alpha = \prod_{i \in \alpha} \sigma_i \quad (1)$$

and are referred to as cluster functions. These clusters are, for example, pairs, triplets, quadruplets of sites, etc. Their corresponding functions form a complete and orthonormal basis. Any property of a configuration, such as the energy, volume, etc can, therefore, be expressed as a linear combination of the polynomials  $\varphi_\alpha$ . A cluster expansion of the configurational energy, for example, takes the form

$$E = V_0 + \sum_\alpha V_\alpha \cdot \varphi_\alpha \quad (2)$$

where the summation extends over all clusters  $\alpha$ , and  $V_0$  and the  $V_\alpha$  are constant expansion coefficients. The expansion coefficients for the energy are generally called effective cluster interactions (ECIs).

Typically, the values of the ECIs are calculated from first principles energy models by fitting the expansion to the energy of a series of ordered configurations described by small supercells. The fit to the first-principles energies can be performed with either a least-squares procedure or a more elaborate method based on linear programming techniques [1].

The cluster expansion can be extended to systems in which multiple sublattices contain substitutional disorder [33]. An appropriate basis for the system as a whole can be constructed from the cluster functions describing the disorder on each individual sublattice. If  $\varphi_\alpha$  and  $\theta_\beta$

are respectively the cluster functions describing the binary disorder on two separate sublattices, the new basis function

$$\psi_{\alpha\beta} = \varphi_{\alpha}\theta_{\beta} \quad (3)$$

can describe the state of the total system. This basis offers an unbiased description of the configuration of all ions and does not rely on any simplifying assumptions often used in modelling defects in oxides (such as the association between vacancies and dopant cations, etc).

#### **4. Factors that contribute to the effective cluster interactions**

In metallic systems, the ECIs are largely defined by direct metal–metal orbital overlap. We discuss below the physical phenomena that determine the ECI in oxides as they can be considerably different from those in metals.

*Ionic size* effects are often the most dominant contribution to the effective interactions in oxides. Insertion of a large cation into the interstitial of a close-packed oxygen framework will displace the oxygen ions around it, thereby changing the energy required to insert an ion at a neighbouring site. Note that the relaxation of oxygen ions around an inserted cation is not necessarily outwards, since it is a competition between an inward relaxation (due to the electrostatic attraction between the oxygen and cation) and the outward relaxation due to steric effects. In closed-shell oxides, such as MgO or CaO, indirect interaction through oxygen displacements is practically the only contribution to the ECIs, and empirical energy models with no direct cation–cation interaction can qualitatively reproduce the experimental phase diagram [23]. Many cation ordered structures can be explained on the basis of size alone.

*Covalent interaction* through direct overlap of atomic wavefunctions, one of the main factors which determines the ordering or phase separation in metals [37, 38], has often a small effect in oxides. This is due to the rather contracted nature of orbitals (e.g. in 3d transition-metal oxides) or the complete absence of any valence electrons (e.g. closed-shell oxides such as MgO).

*Electrostatic interactions* are obviously a key contribution to the effective interactions between differently charged cations. In some cases, the electrostatic interactions dominate over all others and the stable structure can be obtained by simply minimizing the Madelung energy of a distribution of ions over fixed lattice sites. Examples include the perovskites Ba(Mg<sub>1/3</sub>Ta<sub>2/3</sub>)O<sub>3</sub> and Ba(Zn<sub>1/3</sub>Ta<sub>2/3</sub>)O<sub>3</sub> [20, 21, 39–41] in which the B cations are ordered in a 1:2 repeat period along the ⟨111⟩ cubic perovskite direction. Several studies [20, 42] have indicated that this configuration is the one with the lowest electrostatic energy for a system with composition (1/3, 2/3) on a cubic lattice.

In other systems relaxation effects and electrostatics compete for different ground states [43]. ABO<sub>2</sub> ordered rocksalt form the LiScO<sub>2</sub> structure which is the electrostatic ground state, when the A and B cations are similar in size, while the α-NaFeO<sub>2</sub> structure is formed for equiatomic mixtures of large and small cations (e.g. LiCoO<sub>2</sub> or LiAlO<sub>2</sub> [43]). The latter structure is preferred for systems with very different cation size because its symmetry allows for independent anion relaxations around each type of cation.

Electrostatic interactions can be screened considerably by the high polarizability of the oxygen atoms or by the presence of transition metal ions with variable valence. Figure 2 shows the change in electron density in Li<sub>x</sub>CoO<sub>2</sub> when two Li ions are inserted into CoO<sub>2</sub>. The plane shown is defined by the oxygen, cobalt and lithium positions in the unit cell. Although Li is ionized to +1, a large screening electron accumulation is present on the oxygen orbitals

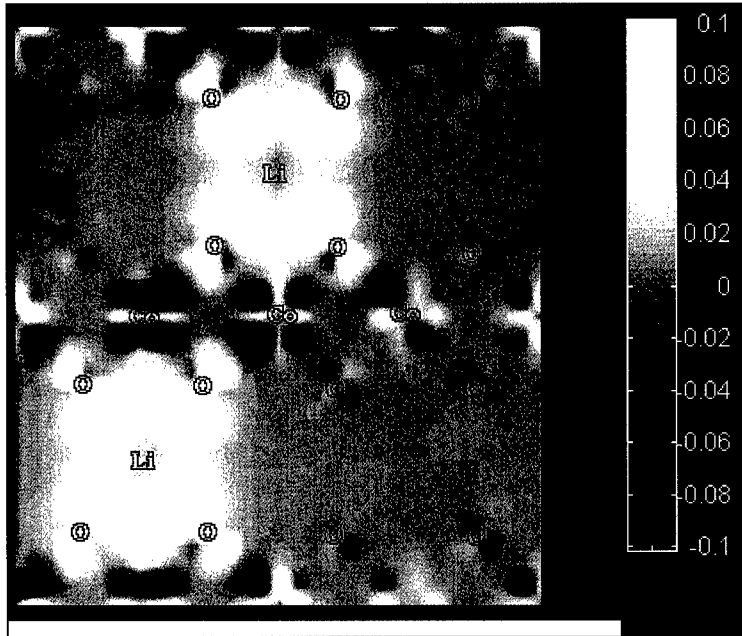


**Figure 2.** Electron density change when two Li ions are inserted into  $\text{CoO}_2$ . Yellow means electron gain while black indicates a decrease in electron density.

surrounding the Li ions. This effect can reduce the bare Coulombic interaction between neighbouring Li ions by a factor of 40<sup>†</sup>. As a result Li ordering barely persists above room temperature.

Besides size, electrostatic and covalent effects, *electron-lattice coupling* and *magnetism* can play a significant role in oxides. Because of the localized nature of electron orbitals in many oxides, partially-filled degenerate states can easily lead to spontaneous symmetry breaking of the environment around the cation. Peierls or Jahn-Teller distortions are therefore quite prevalent in transition metal oxides [44]. For example, in  $\text{LiMnO}_2$ , oxygen octahedra around  $\text{Mn}^{3+}$  are significantly Jahn-Teller distorted in order to break the degeneracy of the two  $e_g$  orbitals (figure 3). The degeneracy is broken by lengthening one of the octahedral axes, lowering the energy of the  $d_{z^2}$  orbital which lies along this axis. The energy is lowered because the  $e_g$  ( $d_{z^2}$ ) orbital is antibonding and therefore becomes lower in energy with increasing ion separation. In  $\text{LiMnO}_2$  the difference between the short and long bonds of the  $\text{MnO}_6$  octahedron can be as much as 20%, making effectively for an ‘elliptical’ Mn ion [45].

Such local environment changes can make for ‘hidden’ configurational problems. For example, when Li is partially removed from  $\text{LiMnO}_2$ , configurational disorder not only occurs on the Li-vacancy sublattice but also on the Mn sublattice due to the creation of Jahn-Teller ( $\text{Mn}^{3+}$ ) and non-Jahn-Teller ( $\text{Mn}^{4+}$ ) ions. Such electronically coupled configurational problems pose an interesting challenge to *ab initio* alloy theory.

Magnetism is expected to be more important in oxides than it is in metals due to the large magnetic moments that are often found on transition metal cations in an oxide. In addition, the localized nature and valence dependence of the moments can couple them directly to

<sup>†</sup> This can be seen from comparing the effective interaction, calculated in [25] with the bare electrostatic potential.

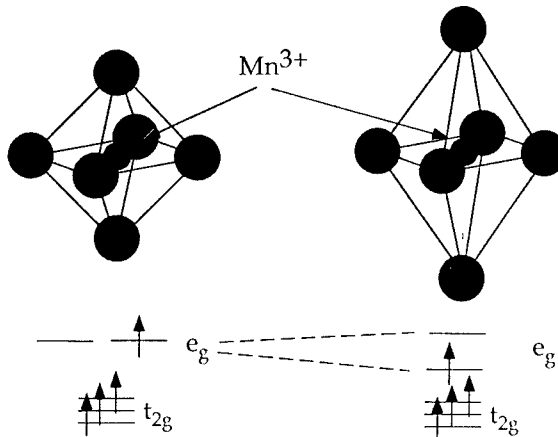


**Figure 3.** The Jahn–Teller distortion of an octahedron around  $\text{Mn}^{3+}$  splits the degenerate  $e_g$  levels.

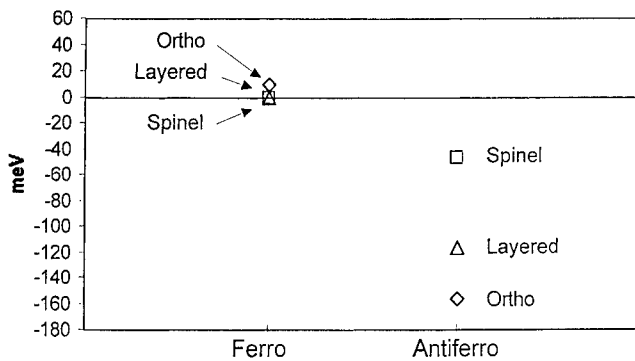


**Figure 4.** Energy of three different lithium manganese orderings in rocksalts with ferromagnetic and antiferromagnetic spin polarization.

ionic configuration changes on other sublattices. Figure 4 shows the relative stability of three different orderings of Li and Mn over the octahedral sites of the rocksalt lattice in  $\text{LiMnO}_2$  as calculated with an ultra-soft pseudopotential method [45]. Note that magnetism has a substantial effect on the energy differences between these structures. Ferromagnetic and antiferromagnetic spin ordering even leads to a different ground state. Such interplay between magnetism and structural stability can be used to tailor the relative stability of these structures with compositional changes [46].

Magnetism can also cause several metastable configurations to appear for a particular ionic arrangement [47]. Figure 5 shows the energy versus volume for a lithiated  $\text{Li}_2\text{Mn}_2\text{O}_4$  spinel for different spin and symmetry states. The lowest energy is obtained for a Jahn–Teller distorted structure (triangles in figure 5) in which Mn is high spin ( $t_{2g}^3 e_g^1$  electronic configuration). The Jahn–Teller distortion makes the otherwise cubic spinel unit cell tetragonal and splits the  $e_g$  levels. At significantly lower volume the same structure, but with partially low-spin Mn, has another local minimum (diamond symbols). This minimum corresponds to  $\text{Mn}^{3+}$  in configuration  $t_{2g}^4 e_g^0$  with an electron-only moment of  $2\mu_B$ . Because of the reduced spin on the Mn ion, the symmetry of this spinel is cubic. Also shown (circles) is the energy versus volume for a spinel with cubic symmetry (thereby not allowing for the Jahn–Teller

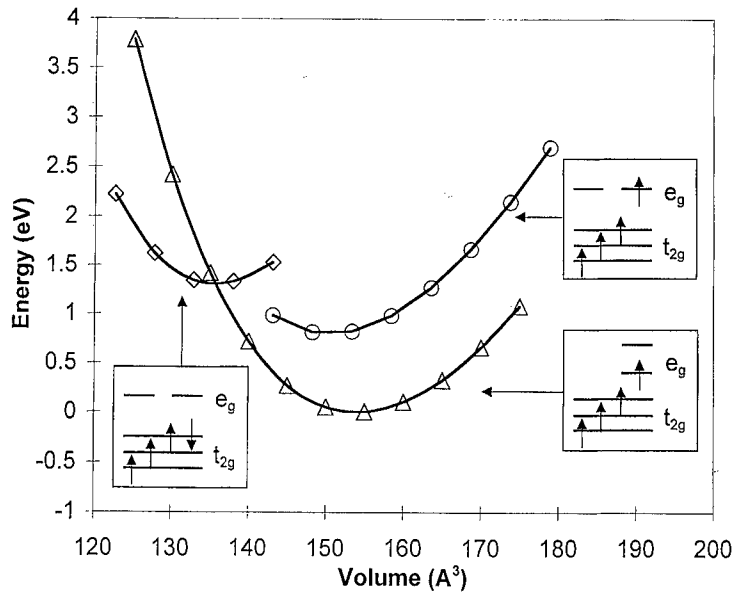


Figure 5. Energy versus volume for different electronic states of  $\text{LiMnO}_2$ .

distortion) and high-spin  $\text{Mn}^{3+}$ . All three structures are local minima in the density functional theory equation of state. Care should therefore be exercised to obtain the correct electronic and magnetic ground states when calculating energy differences or phase diagrams for these materials. To our knowledge, such magnetism-induced metastability has never been observed before in density functional theory calculations.

## 5. Non-configurational entropy

While application of lattice model statistical mechanics, such as the cluster variation method [48] or Monte Carlo simulation, to the cluster expansion can determine the configurational entropy explicitly, the entropy arising from other excitations has to be implicitly included in the values of ECIs. These additional entropy contributions make the ECIs temperature dependent [35]. In metallic alloys both vibrational [49–51] and electronic entropy [52] have been included in this way. Oxides may produce additional sources of entropy which cannot easily be dealt with. When identical ions with different valence are present (such as  $\text{Mn}^{3+}$  and  $\text{Mn}^{4+}$  or  $\text{Cu}^{1+}$  and  $\text{Cu}^{2+}$ ) a configurational-like electronic entropy term should be considered [53, 54]. While an ideal-solution term can be easily added to account for the configurational disorder of different valence states, problems arise when this distribution is coupled to the configurations of ions on another sublattice (e.g. Li vacancy and  $\text{Mn}^{3+}/\text{Mn}^{4+}$  ordering in  $\text{Li}_x\text{MnO}_2$ ). Since the concentration of  $\text{Mn}^{3+}$  is equal to the lithium concentration, total decoupling of the Mn and Li sublattice would generate an entropy of  $-2k_B[x \ln x + (1-x) \ln(1-x)]$  (assuming fully disordered states on both sublattices). However, localization of the  $\text{Mn}^{3+}$  ions near Li (as opposed to vacancies) would strongly reduce this entropy, and in the limit of fully-coupled configurational states the entropy would be only  $-k_B[x \ln x + (1-x) \ln(1-x)]$ . The uncertainty in the configurational entropy associated with the electronic coupling between the two sublattices is therefore of the same order of magnitude

as the total entropy. The localized-charge entropy can further be reduced by *delocalization* (bringing the entropy towards the metallic limit) or by charge *ordering* (bringing it towards zero) [55, 56]. Calculation of the electronic entropy between the localized and delocalized limit will require the development of electronic structure methods that go beyond the local density approximation.

Besides entropy associated with the ‘localization’ of electrons, entropy can arise from the different orientations of symmetry breaking transitions, such as Jahn–Teller distortions, or ordering of the magnetic moments.

## 6. The $\text{Li}_x\text{CoO}_2$ phase diagram: failure of density functional theory around a metal–insulator transition

$\text{Li}_x\text{CoO}_2$  is an important material for applications in rechargeable lithium batteries as it reversibly intercalates lithium ions with little change to the  $\text{CoO}_2$  host framework. In the discharge cycle of a Li battery, Li is absorbed by the host material. Upon charging this process is reversed. While laboratory experiments have shown reversible lithium intercalation between  $x = 0$  and  $x = 1$  on  $\text{Li}_x\text{CoO}_2$  [57], cycling in commercial batteries is limited to the range  $0 < x < 0.5$ .

Figure 1(c) shows the  $\text{LiCoO}_2$  structure which consists of close-packed oxygen layers stacked in ABC sequence with Li and Co occupying alternating planes of octahedral interstices. Since the octahedral interstices of an ABC stacked oxygen framework form an fcc lattice, a one-to-one correspondence exists between the possible Li–Co distributions and the ground states of fcc lattice models. The specific ordering of  $\text{LiCoO}_2$  is L1<sub>1</sub> (or CuPt prototype in alloys). As Li is extracted from  $\text{LiCoO}_2$ , Li-vacancy ordering can occur. Figure 6(a) shows the calculated phase diagram for this material as a function of lithium content. An experimental compilation of results is shown in figure 6(b). For  $x > 0.25$  the host material shown in figure 1(c) is stable. For  $x < 0.25$  minor modifications in the oxygen framework are predicted to occur, necessitating the use of cluster expansions on different lattices. One should keep in mind that the phase diagram of figure 6(a) indicates the most stable states in the layered structures or variants thereof, and it cannot be excluded that other host structures are more stable. Finding the most stable host structures among the infinite number of possibilities is still an unsolved problem in first-principles materials theory. More details on this specific calculation can be found in [25]. In general, there is quite good agreement between the calculated and experimental results. The ordered Li-vacancy configuration predicted to occur at  $x = 0.5$  is the same as the one put forward on the basis of XRD data [26]. In addition, the H1-3 phase, a structure in which Li ions occupy only every other possible plane, is consistent with the observed changes in XRD patterns around that composition [58]. However, one significant discrepancy exists between the calculated and experimental information. Experimentally, two phases with distinct Li composition but identical symmetry are predicted to occur between  $x = 0.75$  and  $x = 0.95$ . In the calculation no such two-phase region can be observed. This failure of *ab initio* alloy theory to reproduce this phase transition is consistent with the recent understanding that it cloaks a metal–insulator transition [25, 59]. While  $\text{LiCoO}_2$  is a semiconductor, removal of Li introduces localized holes in the Co t<sub>2g</sub> valence band. It is expected that at a critical concentration these holes overlap and the material becomes metallic. The view of this transition as a metal–insulator transition has recently been reinforced by conductivity and NMR measurements as a function of Li content [59]. Density functional theory, which was the basis for the calculated diagram of figure 6(a), cannot be expected to capture the subtle energetic and entropic effects associated with such an electronic transition.

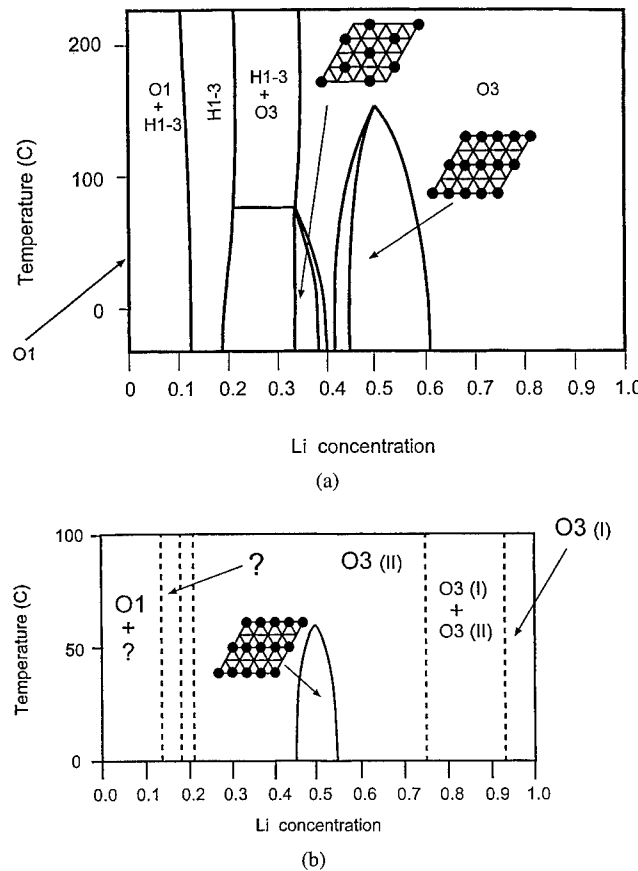


**Figure 6.** (a) Calculated  $\text{Li}_x\text{CoO}_2$  phase diagram. (b) Experimentally compiled  $\text{Li}_x\text{CoO}_2$  phase diagram.

The calculated phase diagram in figure 6(a) shows the strong screening effect of the Li–Li interaction. The phase diagram is highly asymmetric with respect to lithium concentration. This can be understood from the charge compensation mechanism in these structures. The electrostatic interaction between the positively charged  $\text{Li}^+$  ions in  $\text{LiCoO}_2$  is strongly screened by the large and polarizable electron density on the oxygen ions. As Li is removed from  $\text{LiCoO}_2$ , charge neutrality requires the removal of electron density from the  $\text{CoO}_2$  framework. Since this electron density is largely taken from the oxygen ions [60, 61], Li removal reduces the screening power of the oxygens, thereby increasing the effective Li–Li interaction.

## 7. Conclusion

Although alloy theory has been successful in predicting and explaining the phase diagrams of binary metals, oxides present a new series of challenges for this field. The strong coupling between electronic, magnetic, positional and configurational degrees of freedom may necessitate the development of a temperature-dependent electronic theory which can describe the continuous transition between the localized and delocalized states that can occur in oxides.

### Acknowledgments

This work was supported by the Department of Energy, Office of Basic Energy Sciences under contract No DE-FG02-96ER45571. We thank the San Diego Supercomputing Center for access to their T90. One of the authors (AVdV) gratefully acknowledges support from the DOE Computational Science Graduate Fellowship Program.

### References

- [1] Garbulsky G D and Ceder G 1995 *Phys. Rev. B* **51** 67–72
- [2] Ceder G, de Fontaine D, Dreysse H, Nicholson D M, Stocks G M and Gyorffy B L 1990 *Acta Metall. Mater.* **38** 2299–308
- [3] Asta M, de Fontaine D, Van Schilfgaarde M and Sluiter M 1992 *Phys. Rev. B* **46** 5055–72
- [4] Asta M, McCormack R and de Fontaine D 1993 *Phys. Rev. B* **48** 748–66
- [5] Sluiter M, Turchi P E A, Pinski F J and Stocks G M 1992 *J. Phase Equilibria* **13** 605–11
- [6] Sluiter M, Turchi P, Zezhong F and de Fontaine D 1988 *Phys. Rev. Lett.* **60** 716
- [7] Turchi P E A, Sluiter M, Pinski F J, Johnson D D, Nicholson D M, Stocks G M and Staunton J B 1991 *Phys. Rev. Lett.* **67** 1779–82
- [8] Wolverton C M 1993 *PhD Thesis* University of California at Berkeley
- [9] Wolverton C, Ceder G, de Fontaine D and Dreyssé H 1993 *Phys. Rev. B* **48** 726–47
- [10] Burton B P, Osburn J E and Pasturel A 1992 *Phys. Rev. B* **45** 7677–83
- [11] Sanchez J M, Stark J P and Moruzzi V L 1991 *Phys. Rev. B* **44** 5411
- [12] McCormack R, de Fontaine D, Wolverton C and Ceder G 1995 *Phys. Rev. B* **51** 15 808–22
- [13] de Rooy A, Van Royen E W, Bronsveld P M and de Hosson J T M 1980 *Acta Metall.* **28** 1339–47
- [14] de Fontaine D 1994 *Solid State Physics* vol 47, ed H Ehrenreich and D Turnbull (New York: Academic) pp 33–176
- [15] Zunger A 1994 *Statics and Dynamics of Alloy Phase Transformations* ed P E A Turchi and A Gonis (New York: Plenum) pp 361–419
- [16] Ceder G, Asta M, Carter W C, Sluiter M, Mann M E, Kraitchman M and de Fontaine D 1990 *Phys. Rev. B* **41** 8698–701
- [17] Ceder G 1994 *Molec. Simul.* **12** 141–53
- [18] Burton B P and Cohen R E 1995 *Phys. Rev. B* **52** 792–7
- [19] Burton B P 1999 *Phys. Rev. B* **59** 6087–91
- [20] Takahashi T, Wu E, Van der Ven A and Ceder G 1999 *Japan. J. Appl. Phys.* at press
- [21] Takahashi T, Wu E and Ceder G 1999 *J. Mater. Res.* submitted
- [22] Bellaiche L, Padila J and Vanderbilt D 1999 *Phys. Rev. B* **59** 1834–9
- [23] Tepesch P D, Kohan A F, Garbulsky G D, Ceder G, Coley C, Stokes H T, Boyer L L, Mehl M J, Burton B, Cho K and Joannopoulos J 1996 *J. Am. Ceram. Soc.* **79** 2033–40
- [24] Ceder G and Van der Ven A 1999 *Electrochimica Acta* **45** 131–50
- [25] Van der Ven A, Aydinol M K, Ceder G, Kresse G and Hafner J 1998 *Phys. Rev. B* **58** 2975–87
- [26] Reimers J N and Dahm J R 1992 *J. Electrochem. Soc.* **139** 2091–7
- [27] Wolverton C and Zunger A 1998 *Phys. Rev. Lett.* **81** 606–9
- [28] Goodenough J B, Ruiz-Diaz J E and Zhen Y S 1990 *Solid State Ion.* **44** 21–31
- [29] Prasanna T R S and Navrotsky A 1993 *J. Mater. Res.* **8** 1484–6
- [30] Haile S M and Wuensch B J P E 1990 *Neutron Scattering for Materials Science (Mater. Res. Soc. Symp. Proc., vol 166)* ed S M Shapiro, S C Moss and J D Jorgensens pp 81–6
- [31] Tepesch P D and Ceder G 1997 *Computational Modeling of Materials and Processing (Ceramic Transactions, vol. 69)* ed J H Simmons, E R Fuller, A L Dragoo and E J Garboczi pp 123–8
- [32] Ceder G, Kohan A F, Aydinol M K, Tepesch P D and Van der Ven A 1998 *J. Am. Ceram. Soc.* **81** 517–25
- [33] Tepesch P D, Garbulsky G D and Ceder G 1995 *Phys. Rev. Lett.* **74** 2272–5
- [34] Reimers J N, Dahm J R and Von Sacken U 1993 *J. Electrochem. Soc.* **140** 2752–4
- [35] Ceder G 1993 *Comput. Mater. Sci.* **1** 144–50
- [36] Sanchez J M, Ducastelle F and Gratias D 1984 *Physica A* **128** 334–50
- [37] Ducastelle F 1991 *Cohesion and structure Order and Phase Stability in Alloys* vol 3, ed F R de Boer and D G Pettifor (Amsterdam: North-Holland)
- [38] Pettifor D G 1978 *Solid State Commun.* **28** 621–3

- [39] Burton B P and Cohen R E 1994 *Third Williamsburg Workshop on First Principles Calculations for Ferroelectrics* vol 164, pp 201–12
- [40] McCormack R and Burton B P 1996 *Symp. on Solid-State Chemistry of Inorganic Materials* ed P K Davies, A J Jacobson, C C Torardi and T A Vanderahs pp 449–54
- [41] Burton B P, McCormack R P, Toby B H and Goo E K 1996 *Fourth Williamsburg Workshop on First Principles Calculations for Ferroelectrics* vol 194, pp 187–206
- [42] Bellaiche L V 1998 *Phys. Rev. Lett.* **81** 1318–21
- [43] Wu E J, Tepesch P D and Ceder G 1998 *Phil. Mag. B* **77** 1039–47
- [44] Burdett J K 1995 *Chemical Bonding in Solids* (New York: Oxford University Press)
- [45] Mishra S K and Ceder G 1999 *Phys. Rev. B* **59** 6120–30
- [46] Ceder G and Mishra S K 1999 *Electrochem. Solid State Lett.* **2** 550–2
- [47] Van der Ven A, Marianetti C, Morgan D and Ceder G 1999 *Solid State Ion.* at press
- [48] Kikuchi R 1951 *Phys. Rev.* **81** 988–1003
- [49] Van de Walle A and Ceder G 2000 *Phys. Rev. B* **61** 5972–8
- [50] Van de Walle A, Ceder G and Waghmar U 1998 *Phys. Rev. Lett.* **80** 4911–14
- [51] Ozolins V, Wolverton C and Zunger A 1998 *Phys. Rev. B* **58** R5897–900
- [52] Wolverton C and Zunger A 1995 *Phys. Rev. B* **52** 8813–28
- [53] Schleger P, Hardy W N and Casalta H 1994 *Phys. Rev. B* **49** 514–23
- [54] Tetot R, Pagot V and Picard C 1999 *Phys. Rev. B* **59** 14 748–52
- [55] Ahn K H and Millis A J 1998 *Phys. Rev. B* **58** 3697–703
- [56] Rodríguez-Carvajal J, Rousse G, Masquelier C and Hervieu M 1998 *Phys. Rev. Lett.* **81** 4660–3
- [57] Amatucci G G, Tarascon J M and Klein L C 1996 *J. Electrochem. Soc.* **143** 1114–23
- [58] Van der Ven A, Aydinol M K and Ceder G 1998 *J. Electrochem. Soc.* **145** 2149–55
- [59] Menetrier M, Saadoune I, Levasseur S and Delmas C 1999 *J. Mater. Chem.* **9** 1135–40
- [60] Ceder G, Aydinol M K and Kohan A F 1997 *Comput. Mater. Sci.* **8** 161–9
- [61] Ceder G, Chiang Y-M, Sadoway D R, Aydinol M K, Jang Y-I and Huang B 1998 *Nature* **392** 694–6

## First-principles theory of 250 000-atom coherent alloy microstructure

C Wolverton

Ford Research Laboratory, MD3028/SRL, Dearborn, MI 48121-2053, USA

Received 16 September 1999, accepted for publication 28 February 2000

**Abstract.** Microstructural issues in alloys such as precipitation have largely been outside the realm of first-principles electronic structure calculations due to the length scales involved in precipitation microstructure (typically nanometres to micrometres) and the inherent thermodynamic/statistical nature of the problem. Here, we show that modern, first-principles total energy calculations can be combined with a mixed-space cluster expansion approach (a generalized real/reciprocal space Ising model) and Monte Carlo simulations to yield a method capable of describing equilibrium coherent precipitate shapes in alloys with system sizes up to 250 000 atoms. Both the (anisotropic) interfacial free energies and the coherency strain between precipitate and matrix are accounted for in this method as well as the short-range atomic-scale ordering of the solid solution. Illustrations of the technique are given for several famous examples of coherent precipitation in aluminium alloys: Al–Mg, Al–Cu and Al–Ni.

### 1. Introduction

Understanding the precipitation microstructure and its evolution with heat treatment is important when optimizing the hardness or yield strength of many alloy systems. The precipitation of solute atoms out of a solid solution increases the hardness of alloys because the precipitate and its surrounding strain field interfere with dislocation motion through the crystal: the dislocation must either pass through the precipitate and shear it or avoid the precipitate by bowing around it. (See, e.g., the review articles [1, 2] and references therein.) *Coherent* precipitates are those which possess the same underlying lattice structure as the solid solution matrix and all crystallographic planes are perfectly continuous through precipitate and matrix. These precipitates often appear at the early stages of precipitation, may produce significant strain fields surrounding the precipitate, and are often quite effective at increasing hardness in alloys. The size and shape (e.g., plates, spheres, rods) of the precipitate morphology dictates the energetic penalty for dislocation motion through or around it, and hence knowledge of the precipitate shapes is an important step towards understanding the strengthening mechanism in alloys. Therefore, the study of the shape of coherent precipitates has been an active field of both theoretical and experimental research [3–11].

First-principles calculations have not typically been used to study problems of precipitation due to the fact that the precipitate alone is often a few nanometres to a few micrometres in size, and hence can be composed of anywhere from hundreds to billions of atoms or more. Additionally, the problem of predicting a precipitate shape of solute atoms in a disordered solid solution matrix requires that one perform a statistical sampling of the configuration space involved. In other words, one might need to evaluate the energy of hundreds of thousands of atoms in hundreds of thousands of configurations to accurately account for the thermodynamic

nature of this microstructural problem. We show here a method which combines a set of *small-unit-cell* (averaging about five to six atoms per cell), first-principles total energy calculations with a generalized Ising-like model to extend the length scales of first-principles calculations to that of coherent precipitate microstructure. This generalized Ising-like model, which accounts for both the interfacial and strain energies between the precipitate and matrix, is called the *mixed-space cluster expansion* (CE) [12–14]. The CE may be combined with Monte Carlo simulations to efficiently sample configuration space and treat the thermodynamic aspects of the problem. Examples of this technique are shown for the aluminium alloy systems: Al–Mg, Al–Cu and Al–Ni.

## 2. Methodology

The mixed-space cluster expansion method and the construction of the expansion from first-principles have previously been described in detail [12–14, 18]. We only give the salient points here, and for a detailed discussion of the method we refer the interested reader to the above references. The mixed-space cluster expansion expression for the formation enthalpy (the energy with respect to the compositional average of the alloy constituents, all at zero pressure) of any configuration  $\sigma$  is given by

$$\Delta H(\sigma) = \sum_k J(k)|S(k, \sigma)|^2 + \sum_f D_f J_f \bar{\Pi}_f(\sigma) + \frac{1}{4x(1-x)} \sum_k \Delta E_{\text{CS}}^{\text{eq}}(\hat{k}, x)|S(k, \sigma)|^2. \quad (1)$$

$J_f$  and  $J(k)$  are the Ising-like interaction energies,  $f$  is a symmetry-distinct figure comprised of several lattice sites,  $D_f$  is the number of figures per lattice site, and  $\bar{\Pi}_f$  is a product of the variables  $\hat{S}_i$ , over all sites of the figure  $f$  averaged over all symmetry equivalent figures of lattice sites. Each of the  $N$  sites of the lattice (in this paper, fcc) is associated with either an A atom ( $\hat{S}_i = -1$ ) or a B atom ( $\hat{S}_i = +1$ ). (Note, however, that the atoms are not required to sit *at* the lattice positions, and that atomic relaxation is accurately treated within this expansion [13].)

The first summation of equation (1) includes all pair figures, summed using the reciprocal-space concentration-wave formalism [6, 15, 16].  $J(k)$  and  $S(k, \sigma)$  are the lattice Fourier transforms of the real-space pair interactions and spin-occupation variables. The second summation of equation (1) includes only non-pair figures,  $f$  (e.g., three- and four-body interactions). The third summation involves  $\Delta E_{\text{CS}}(\hat{k}, x)$ , the *coherency strain energy*, defined as the strain energy of bulk A and B required to maintain coherency along an interface with orientation  $\hat{k}$ . In practice, this may be calculated from the energy change when the bulk solids A and B are deformed biaxially from their equilibrium cubic lattice constants  $a_A$  and  $a_B$  to a common lattice constant  $a_{\perp}$  in the plane perpendicular to  $\hat{k}$ , and relaxed in the third direction,

$$\Delta E_{\text{CS}}(\hat{k}, x) = \min_{a_{\perp}} [(1-x)\Delta E_A^{\text{epi}}(\hat{k}, a_{\perp}) + x\Delta E_B^{\text{epi}}(\hat{k}, a_{\perp})] \quad (2)$$

where  $\Delta E_A^{\text{epi}}(\hat{k}, a_{\perp})$  is the energy required to deform A biaxially to  $a_{\perp}$  (see, e.g., [17]).

One should note several points about the calculation of coherency strain and its incorporation into the CE.

- (1) Composition-dependent, anisotropic, and anharmonic elastic response are incorporated into the calculation of equation (2).
- (2) In terms of superlattice structures,  $A_nB_m$ , the strain energy of equation (2) corresponds to the long-period limit ( $n, m \rightarrow \infty$ ), where interfacial energies (which scale with the area of the interface) are negligible compared to the strain energy (which scales with the

volume of the system). Thus, the coherency strain of equation (2) is formulated in terms of the elastic response of the pure constituents, A and B, and this energy has been referred to previously as the *constituent* strain energy [12].

- (3) For short-period superlattices both interfacial and strain energies can be important: Interfacial energies are incorporated into the CE via first-principles calculations of short-period superlattice energies, which are used to construct the Ising-like interactions of equation (1). The coherency strain energy in (1) must treat both long-period superlattices and short-period superlattices (as well as random alloys and other configurations). This form is constructed in such a way as to give not only the correct long-period superlattice limit (equation (2)), but also the energetics of fully-relaxed short-period superlattices as directly calculated from first principles. The construction of the coherency strain has recently been discussed in [18].

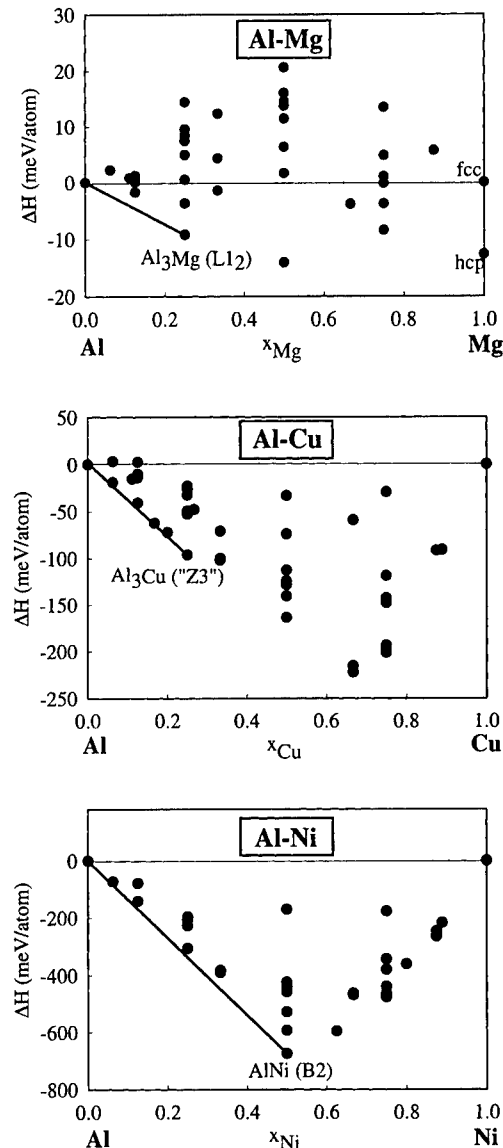
Mixed-space CE Hamiltonians have been constructed for the following fcc alloy systems: Al–Mg, Al–Cu and Al–Ni. First-principles total energies were computed in all cases using fully-relaxed, full-potential, linearized augmented plane wave (LAPW) [19] calculations. Total energies of 30–40 ordered compounds for each alloy system were used to fit the values of the interaction energies of equation (1),  $J(\mathbf{k})$  and  $J_f$ . All compounds were relaxed to their energy-minimizing geometry with respect to volume, unit cell vector lengths, and cell-internal coordinates; however, vibrational effects were neglected. The ordered compounds included short-period superlattices for a variety of orientations (e.g., [100], [111], [110], etc), special quasi-random structures (ordered structures which mimic the random alloy), and other structures. LAPW epitaxial energies of the alloy constituents for five orientations ([100], [111], [110], [201], and [311]) were used to compute  $\Delta E_{\text{CS}}^{\text{eq}}(\hat{\mathbf{k}}, \mathbf{x})$ . The mixed-space CE Hamiltonian of equation (1) thus contains both interfacial and strain energies, determined from a first-principles quantum-mechanical approach.

To compute thermodynamic properties and efficiently search configuration space for equilibrium precipitate shapes, we used the mixed-space CE Hamiltonian in a dual real/reciprocal space Monte Carlo code in the canonical ensemble (fixed composition), as described in [20]. System sizes of  $N = 20^3\text{--}64^3 = 8000\text{--}262\,144$  sites were used with 100–1000 Monte Carlo steps (per site) used for thermal equilibration and statistical averages. We used periodic boundary conditions, but for the precipitation calculations, atoms at the boundary of the Monte Carlo cell were fixed (i.e. they were never involved in any exchanges) to prohibit precipitates from ‘joining’ with their periodically repeated images. For several different CE Hamiltonians, tests were performed by varying the size of the simulation cell while maintaining a constant number of solute atoms. No qualitative differences in precipitate shapes were found, thus suggesting that our simulation cells are large enough to deduce equilibrium precipitate shapes. One should note that the method described here is a strictly thermodynamic approach, with the constraint that the system is required to remain coherent (i.e. fcc based). Kinetic aspects of this problem, such as coarsening, nucleation, quenched-in vacancies, etc, are not directly simulated here.

### 3. Results

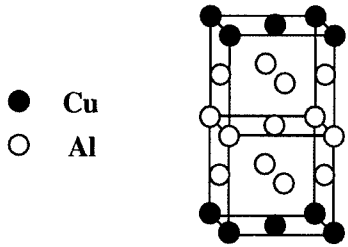
#### 3.1. Formation enthalpies

Figure 1 shows the LAPW-calculated formation enthalpies of 30–40 fcc-based ordered compounds for the Al–Mg, Al–Cu and Al–Ni systems. These energies were used to fit the Ising-like interactions of equation (1). Also shown is the predicted Al-rich coherent ground state for each system. These ground states were predicted by performing Monte Carlo simulated



**Figure 1.** First-principles (LAPW) calculated formation enthalpies for ordered compounds in the Al–Mg, Al–Cu and Al–Ni systems, relative to the fcc constituents. For each system, 30–40 ordered compound energies were used to fit the Ising-like interactions of the cluster expansion. Tie-lines are drawn to the Al-rich predicted coherent (fcc-based) ground states which are the phases predicted to appear in the later stages of the coherent precipitation sequences of these alloys. (In Al–Ni, B2 is listed as a coherent fcc-based phase because the fcc-based  $\text{L}1_0$   $\text{AlNi}$  compound relaxes directly (without an energy barrier) into the B2 structure.)

annealing calculations of the mixed-space cluster expansions, starting from high temperatures and cooling down slowly to find the lowest-energy state. Thus, these are not merely the lowest-energy structures out of the 30–40 calculated, but actually involve an efficient search of the configurational space of  $2^N$  possibilities, where  $N$  can be as large as 262 144. From figure 1, we note several points.



**Figure 2.** The predicted  $\text{Al}_3\text{Cu}$  coherent ground state, referred to as ‘Z3’. This compound is an (001) superlattice with  $\text{Al}_3\text{Cu}_1$  stacking.

(This figure is in colour only in the electronic version, see [www.iop.org](http://www.iop.org))

- (i) All three systems possess ordered compounds with negative formation enthalpies, and therefore possess stable ordered compounds. The Al–Mg system, however, has a variety of compounds with both positive and negative  $\Delta H$ .
- (ii) Formation energies generally increase in magnitude as one goes from Al–Mg to Al–Cu to Al–Ni. Interestingly, the general trend of observed solubilities of these three elements in Al also follows this order: Mg has the highest solubility in Al ( $\sim 19\%$ ), followed by Cu ( $\sim 2.5\%$ ) and then Ni ( $\sim 0.02\%$ ). (The formation enthalpies in Al–Mg are extremely small; hence a very fine  $k$ -point mesh was necessary to obtain numerically converged results in this system.)
- (iii) For the Al–Mg system, the Al-rich coherent ground state is predicted to be  $\text{Al}_3\text{Mg}$  ( $L1_2$ ). The  $L1_2$  structure is a ground state of the nearest-neighbour (ordering-type) Ising model, but the structure is cubic and possesses no crystallographic degrees of freedom to provide strain relief. The fact that it is nevertheless the lowest energy state suggests that chemical ordering of Al and Mg (as opposed to atomic relaxation) is the dominant mechanism for compound formation in Al–Mg. The calculated lattice mismatch of fcc Al and fcc Mg is 11%, however, and so atomic relaxation also plays an important (though somewhat smaller) role.
- (iv) In contrast, the Al–Cu and Al–Ni system both show very low energy (001)-type superlattices for Al-rich compositions. For Al–Cu, the predicted coherent ground state is an  $\text{Al}_3\text{Cu}$  compound (‘Z3’) which is a stacking of  $\text{Al}_3\text{Cu}_1$  planes along (001), shown in figure 2. For Al–Ni, the ground state is the familiar  $\text{AlNi}$  ( $B2$ ) compound which is a bcc stacking of  $\text{Al}_1\text{Ni}_1$  planes along (001). Although the  $B2$  structure is a bcc superlattice, we have listed it as a coherent fcc-based phase because the fcc-based  $L1_0$   $\text{AlNi}$  compound ( $\text{Al}_1\text{Ni}_1$  fcc stacking along (001)) relaxes directly (without an energy barrier) into the  $B2$  structure. This  $L1_0 \rightarrow B2$  relaxation tendency has previously been shown for FeAl, CoAl, and NiAl [21].
- (v) Calculations of a 16-atom  $\text{Al}_3\text{Mg}$  special quasi-random structure (SQS) gives a direct estimate of the enthalpy of mixing of the disordered solid solution (i.e. directly from first-principles, with no need for a cluster expansion). Relative to fcc Al and hcp Mg, the formation enthalpy of the  $\text{Al}_3\text{Mg}$  SQS is  $+1.2 \text{ kJ mol}^{-1}$ , which is in good agreement with measured and assessed values of the mixing enthalpy [22] which are approximately +1 to  $+1.5 \text{ kJ mol}^{-1}$  for a 20% Mg alloy.

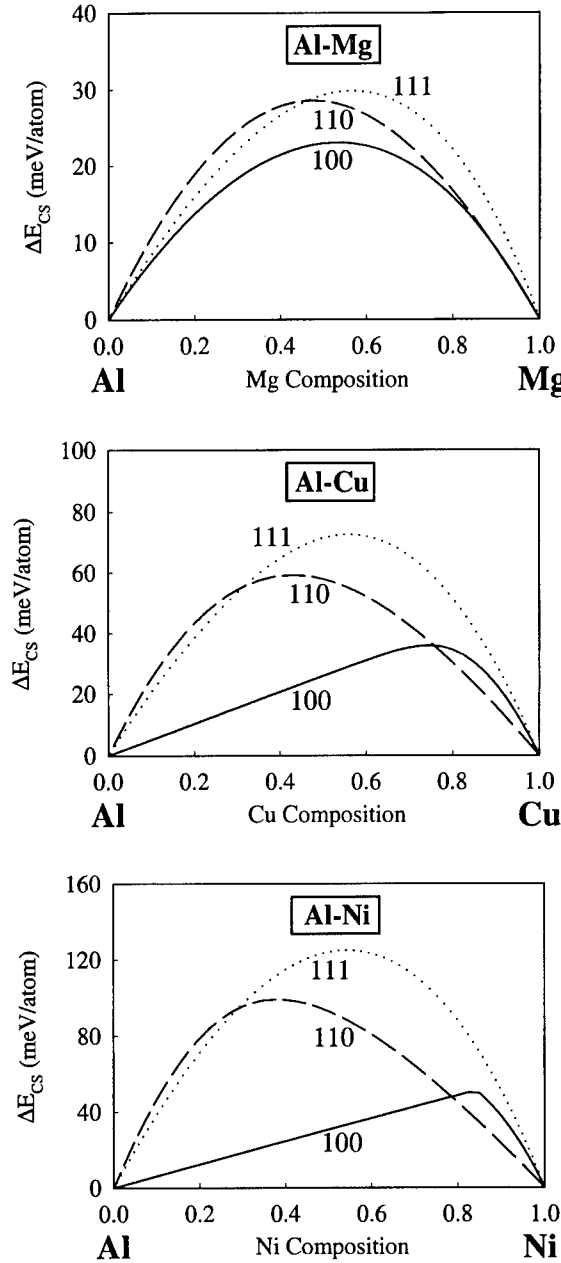


Figure 3. Calculated (100), (111), and (110) coherency strains for Al–Mg, Al–Cu and Al–Ni.

### 3.2. Coherency strain

Figure 3 shows the calculated coherency strain for the three alloy systems. For visual clarity, only the calculated results for the (100), (111), and (110) directions are shown. Several points concerning the strain of these systems can be seen from the comparisons in figure 3.

- (i) The relative size of the coherency strain in these three systems follows the magnitudes of  $\Delta H$  values in figure 1: Al–Mg has the smallest strain energy, followed by Al–Cu, and

then Al–Ni. The fact that the strain in Al–Cu is smaller than in Al–Ni is simply due to the size mismatch of Al–Cu being smaller than that of Al–Ni. The fact that both Al–Cu and Al–Ni have larger strain than Al–Mg is a reflection of two facts: (a) Mg is elastically much softer than Cu or Ni, and (b) Cu and Ni are smaller than Al whereas Mg is larger. For Al–Cu and Al–Ni, one is either expanding a hard material (Cu and Ni) or compressing a soft one (Al). Compressing Al (in Al–Cu and Al–Ni) is energetically much more costly than expanding it (in Al–Mg) due to the anharmonic equation of state, leading to larger strain energies in alloys of Al with a smaller metal.

- (ii) The strain of Al–Mg is nearly isotropic compared to that of Al–Cu or Al–Ni. Additionally, although Mg is stable in the hcp structure, we find that it is metastable in the fcc structure (i.e. all the epitaxial distortions considered raise the energy of fcc Mg). This is interesting because a contrasting case has recently been found for another hcp metal: Zn is unstable in the fcc structure [23], with this instability strongly influencing properties of Al–Zn alloys.
- (iii) For Al-rich compositions, Al–Cu and Al–Ni are extremely soft for (100) deformations due to elastic response of Cu and Ni [17]. This elastic softness causes (001) superlattices to be low in energy in these systems (and ultimately gives rise to the (001) planar Guinier–Preston zones in Al–Cu).
- (iv) In all systems considered, anharmonic elastic effects are important: harmonic continuum elasticity dictates that the energy of distortions along (110) must always be intermediate between that of (100) and (111). In each of the three cases in figure 3, the energy of (110) becomes the hardest elastic direction for Al-rich compositions, a clear manifestation of anharmonic elasticity (which is inherently included in the first-principles calculations).
- (v) Although Al and Au have similar sizes, they have different elastic properties. Nevertheless, the calculated coherency strains of Al–Cu and Al–Ni are similar to those of Au–Cu and Au–Ni, respectively [14]. This fact demonstrates that strain in these alloys (particularly for Al-rich compositions) is dominated by the elastic response of pure Cu and pure Ni.

### 3.3. Precipitate shapes

By mapping the first-principles results of figures 1 and 3 onto the mixed-space cluster expansion of equation (1) and using this expansion in Monte Carlo simulations, one can study coherent alloy precipitate shapes. Before presenting first-principle results, we start with a ‘prototype’ calculation (figure 4), and simply choose the terms of equation (1) to reveal generic behaviour: the first term in equation (1) is modelled via a clustering nearest-neighbour pair interaction  $J_{NN} < 0$ . Multibody terms (second term of equation (1)) are neglected. Coherency strain is modelled by a low-order expansion ( $K_0$  and  $K_4$ ) of Kubic harmonics, similar in functional form to that of continuum harmonic elasticity [17]. A negative value of the elastic anisotropy,  $\Delta = C_{44} - (C_{11} - C_{12})/2$ , is used, leading to elastically soft (111) directions. (Prototype calculations were also performed with positive values of  $\Delta$  yielding similar results for an elastically soft (100) direction.) Each equilibrium shape is the result of a simulation begun at high temperature and slowly cooled down through the miscibility gap to low temperatures. In the limit of pair energy only (i.e. zero strain energy, left-hand side of figure 4), the precipitation problem has a solution given by the Wulff-shape construction. The Wulff-shape for a simple nearest-neighbour pair interaction (with the  $T = 0$  interfacial energies as constraints) is the cuboctohedron, and our Monte Carlo simulations give the atomistic analogue of this solution. However, as coherency strain is slowly ‘turned on’, the facets of the precipitate along the elastically soft directions grow, the precipitate elongates, and eventually when the strain energy dominates, the equilibrium precipitate shape becomes planar [6] with the normal to the precipitate plane being the soft elastic direction. This planar shape of the strain-only

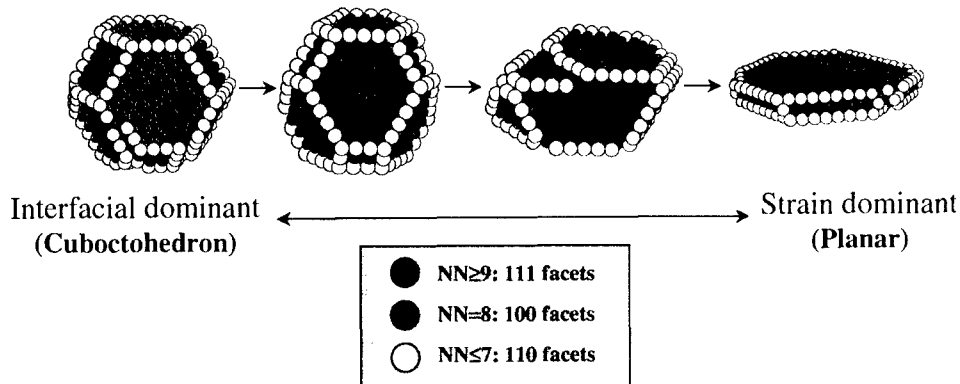


**Figure 4.** See caption opposite.

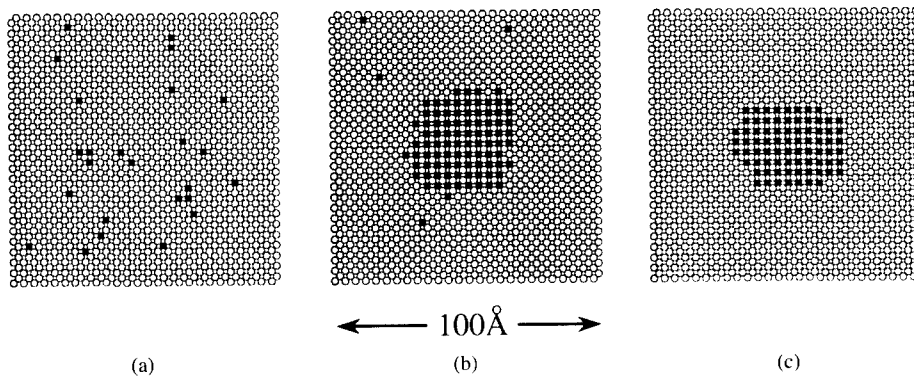


**Figure 5.** See caption opposite.

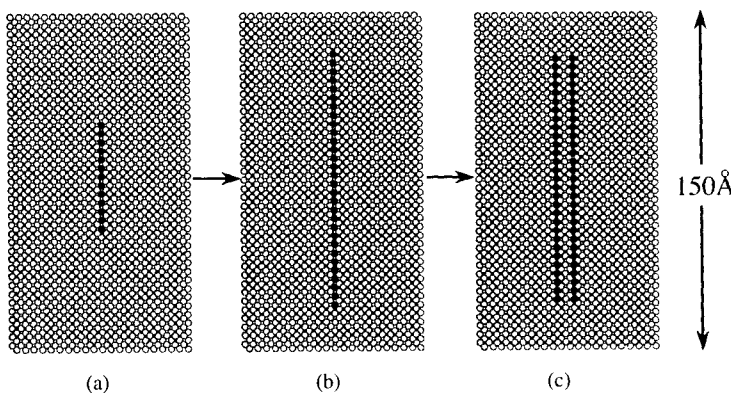


**Figure 6.** See caption opposite.

precipitation problem can be seen from the form of the coherency strain in equation (1), where a planar precipitate with normal  $\hat{G}$  is composed solely of composition waves along the direction  $\hat{G}$ . Thus, a planar precipitate with normal along the elastically softest direction is the lowest-energy shape [6].

We next turn to the calculation of precipitate shapes in actual alloy systems with the terms in equation (1) given by the first-principles energetics of figures 1 and 3. We show in

**Figure 4.** Calculated equilibrium precipitate shapes with both strain and interfacial energy contributions. Interfacial energy is included via a (clustering) nearest-neighbour pair interaction in equation (1) and strain is included via harmonic continuum elasticity in which the (111) direction is the soft elastic direction. Simulations were performed for a 27 000-atom cell with 1350 minority atoms (only the minority atoms are shown, colour-coded by the number of the 12 nearest neighbours which are also minority atoms). Each equilibrium shape is the result of a Monte Carlo simulation begun at high temperature and slowly cooled down through the miscibility gap to low temperatures. As strain becomes progressively larger, one can see the (111) facets (red) become predominant.

**Figure 5.** Predicted coherent precipitate shapes for  $\text{Al}_{0.98}\text{Mg}_{0.02}$ . Shown are results of a simulation with 64 000 atoms and 2% Mg for various temperatures: (a)  $T = 1.05T_{\text{coh}}$ , above the coherent phase boundary (in the solid solution), (b)  $T = 0.95T_{\text{coh}}$ , below the coherent phase boundary (where the precipitate forms), and (c) a low temperature where very few Monte Carlo swaps are accepted. In each case, only a portion of the Monte Carlo cell is shown, cut along the (001) direction. Al atoms are yellow and Mg atoms are blue.

**Figure 6.** Predicted coherent precipitate shapes for Al–Cu. Shown are results of three simulations with progressively larger precipitate sizes with  $\sim 1\%$  Cu: (a)  $30^3 = 27\,000$  total atoms (270 Cu atoms), (b)  $56^3 = 175\,616$  total atoms (1404 Cu atoms), and (c)  $64^3 = 262\,144$  total atoms (2898 Cu atoms). Al atoms are yellow and Cu atoms are red. In each case, only a portion of the Monte Carlo cell is shown, cut along the (001) direction. The equilibrium precipitate shapes show the evolution with size of the precipitates from Cu monolayers (GP1) to a Cu/Al/Al/Al/Cu structure (GP2), based on the ‘Z3’  $\text{Al}_3\text{Cu}$  ground state of figure 2.

figure 5 the thermal evolution of the equilibrium coherent precipitate shapes for the Al–Mg system. For high temperature (above the coherent phase boundary temperature,  $T_{\text{coh}}$ ), the solid solution is stable, as one can see from the disordered arrangement of Al and Mg atoms in figure 5(a). Although this is simply a ‘snapshot’ of the actual simulation (which is thermally averaged), it shows the qualitative behaviour of the solid solution. One can see some aspects of the short-range order (SRO) in Al–Mg from this figure: nearest-neighbour Mg–Mg pairs are absent, and hence Al–Mg pairs are enhanced relative to random statistics, leading to a negative Warren–Cowley SRO parameter for the nearest-neighbour shell. On the other hand, several next-nearest-neighbour Mg–Mg pairs are seen in figure 5(a), showing that the SRO parameter for this shell is positive. (For a calculation of a 15% Mg alloy at 350 K, the SRO parameters for the first two shells are  $\alpha_1 = -0.05$  and  $\alpha_2 = +0.08$ .) As one lowers the temperature below  $T_{\text{coh}}$ , Mg precipitates out of the solid solution as the  $\text{Al}_3\text{Mg}$  ( $L1_2$ ) phase shown in figure 1. In the  $\text{Al}_3\text{Mg}$  ordered phase, Mg atoms sit at the corners of the conventional fcc cube and Al atoms sit in the faces. Thus, this structure has no Mg–Mg *nearest* neighbours, but every Mg atom is surrounded completely by Mg atoms on the *next-nearest*-neighbour shell, leading to  $\alpha_1 = -0.333$  and  $\alpha_2 = +1.00$  for the completely ordered structure. Thus, the SRO in the high-temperature solid solution represents small fluctuations of the low-temperature *coherent* phase. As one can see from figure 5, the precipitate forms a perfectly ordered  $L1_2$  structure, with no ‘mistakes’ in the structure (i.e. no Mg–Mg *nearest* neighbours, and within the interior of the precipitate, no Al–Mg *next-nearest*-neighbour bonds)<sup>†</sup>. The shape of this precipitate is roughly spherical. The observed precipitation sequence in Al–Mg goes through an initial period of coherent Guinier–Preston zones followed by the formation of a coherent ordered

<sup>†</sup> One might expect the  $\text{Al}_3\text{Mg}$  precipitate to be partially ordered. The perfectly ordered structure seen in the simulations is due to the following. The composition was kept quite dilute (2% Mg) to avoid having too large a precipitate which would interact with its periodically repeated images. Because of the dilute composition, the coherent phase boundary is quite low in temperature, and thus the  $\text{Al}_3\text{Mg}$  ordered compound at this temperature is quite well ordered. At compositions commonly used in age hardening experiments in Al–Mg (10–15% Mg), the coherent phase boundary is much higher, and the observed  $\text{Al}_3\text{Mg}$  precipitate is more likely to be partially ordered.

phase (usually labelled  $\beta''$ ), followed by subsequent semicoherent and incoherent precipitates [24]. Although there was initially some debate about the structure of  $\beta''$ , it is now generally accepted that it has an  $L1_2$  structure and forms roughly spherical precipitates [25, 26]. Our predicted precipitate shapes support this interpretation of both the structure ( $\text{Al}_3\text{Mg}$   $L1_2$ ) and shape (roughly spherical) for the  $\beta''$  phase in Al–Mg. As one continues to lower the temperature (figure 5), the precipitate begins to show some (001) facets corresponding to both the slightly lower strain and interfacial energies in this orientation. Calculations of  $L1_2/\text{fcc}$  interfacial energies [27] have shown that even a strong anisotropy which exists in  $T = 0$  interfacial energies can be eliminated at very modest temperatures where the interfacial free energies become isotropic. This temperature-induced isotropy of the interfacial free energies is a possible reason for the more spherical form of the precipitates at higher temperatures, although this hypothesis has not been investigated in detail.

Next, we turn to the coherent precipitates in Al–Cu. Al–Cu is possibly the most famous example of coherent precipitation, in which Cu atoms precipitate out of the solid solution as coherent plates along (001). Two types of these plates, or Guinier–Preston (GP) zones, have been proposed, although there has been significant controversy concerning the nature and ordering of these GP zones [7]. The first-principles mixed-space cluster expansion approach described here has recently been applied to the problem of GP zone formation in Al–Cu [28], and figure 6 shows the calculated zone shapes. ‘Slices’ of three Monte Carlo simulation cells are shown for  $\sim 1\%$  Cu with progressively larger cell sizes. (The largest of these cells contained 262 144 atoms.) For small precipitate sizes, we find disc-shaped Cu monolayers (figure 6(a)), while for larger precipitate sizes, the equilibrium precipitate shape is two Cu monolayers separated by three Al layers (figure 6(c)). Remarkably, these two theoretically-predicted structures correspond to the ‘traditional model’ of GP1 and GP2 zones, respectively. The stacking sequence we have found for the GP2 structure has previously been shown to result from minimization of elastic energy alone [4]. We have recently [28] explained this size-dependent transition in the precipitate shape as a competition between the interfacial energy penalty around the perimeter of the disc (favouring GP1 at small sizes) and the thermodynamic driving force for the  $\text{Al}_3\text{Cu}$  coherent ground state of figure 2 (favouring GP2 at large sizes). This transition is in excellent agreement with HREM measurements of Sato and Takahashi [29] who aged Al–1.7 at% Cu at 423 K and observed single-layer GP1 zones for sizes up to  $\sim 150$  Å (but not larger) and GP2 zones (with structure corresponding to the ‘traditional model’) with sizes down to  $\sim 100$  Å (but not smaller). Thus, as observed in age hardening experiments, we predict that GP2 zones will form only for longer ageing times or higher temperatures (where kinetics will lead to larger precipitate sizes).

#### 4. Conclusions

We have shown that modern, first-principles total energy calculations can be combined with a mixed-space cluster expansion approach (a generalized real/reciprocal space Ising model), and Monte Carlo simulations to yield a method capable of describing equilibrium coherent precipitate shapes in alloys with system sizes up to 250 000 atoms. Both the interfacial free energies and the coherency strain between precipitate and matrix are accounted for in this method, as well as the short-range atomic-scale ordering of the solid solution.

First-principles calculations of ordered compound formation enthalpies and coherency strain energies (the necessary ingredients for constructing the cluster expansions) were shown for Al–Mg, Al–Cu and Al–Ni. Both the formation enthalpies and coherency strains increase in magnitude as one goes from Al–Mg to Al–Cu to Al–Ni. Additionally, although Al–Cu and Al–Ni showed elastically soft (001) directions for Al-rich compositions (due to the elastic

response of pure Cu and pure Ni), Al–Mg is much more isotropic. The coherent ground states for Al-rich compositions were predicted to be  $\text{Al}_3\text{Mg}$  ( $L1_2$ ),  $\text{Al}_3\text{Cu}$  ('Z3'), and  $\text{AlNi}$  ( $B2$ ), with the former two observed as  $\beta''$  and 'GP2' in precipitation experiments.

We have shown illustrations of generic precipitation behaviour of 'prototype' systems, which demonstrate that compact precipitate shapes are favoured for systems which are dominated by interfacial energies, whereas planar shapes are favoured for strain-dominated cases. First-principles calculations of the equilibrium precipitate shapes were presented for Al–Mg and Al–Cu. The calculated Al–Mg equilibrium coherent precipitate shapes were roughly spherical  $\text{Al}_3\text{Mg}$  ( $L1_2$ ) particles, in agreement with observations of  $\beta''$  precipitates. In Al–Cu, platelets along (001) were found, with a size-dependent transition between isolated monolayers and two Cu layers separated by three Al layers, corresponding to the traditional model of GP1/GP2 structures.

### Acknowledgment

The portions of this work performed at the National Renewable Energy Laboratory were supported by the Office of Energy Research (OER) (Division of Materials Science of the Office of Basic Energy Sciences (BES)), US Department of Energy, under contract No DE-AC36-98-GO10337.

### References

- [1] Kelly A and Nicholson R B 1963 *Prog. Mater. Sci.* **10** 149
- [2] Ardell A 1985 *Metall. Trans A* **16** 2131
- [3] Guinier A 1959 *Solid State Phys.* **9** 293
- [4] Seitz E and de Fontaine D 1978 *Acta Metall.* **26** 1671
- [5] Cohen J B 1986 *Solid State Phys.* **39** 131
- [6] Khachaturyan A G 1983 *Theory of Structural Transformations in Solids* (New York: Wiley)
- [7] For a review of the controversial results on coherent precipitation in Al–Cu, see the *Scripta Metallurgica* Viewpoint Set: Gerold V (ed) 1988 *Scripta Metall.* **22** 927–62
- [8] Thompson M E, Su C S and Voorhees P W 1994 *Acta Metall. Mater.* **42** 2107
- [9] Doi M 1996 *Prog. Mater. Sci.* **40** 79
- [10] Zandbergen H, Andersen S J and Jansen J 1997 *Science* **277** 1221
- [11] Lee J K 1998 *Mater. Trans. JIM* **39** 114
- [12] Laks D B, Ferreira L G, Froyen S and Zunger A 1992 *Phys. Rev. B* **46** 12 587
- [13] Wolverton C and Zunger A 1995 *Phys. Rev. Lett.* **75** 3162
- [14] Ozoliņš V, Wolverton C and Zunger A 1998 *Phys. Rev. B* **57** 6427
- [15] Cook H E and de Fontaine D 1969 *Acta Metall.* **17** 915  
Cook H E and de Fontaine D 1970 *Acta Metall.* **18** 189
- [16] de Fontaine D 1979 *Solid State Phys.* **34** 73
- [17] Ozoliņš V, Wolverton C and Zunger A 1998 *Appl. Phys. Lett.* **72** 427  
Ozoliņš V, Wolverton C and Zunger A 1998 *Phys. Rev. B* **57** 4816
- [18] Wolverton C, Ozoliņš V and Zunger A 2000 *J. Phys.: Condens. Matter* **12** 2749
- [19] Wei S-H and Krakauer H 1985 *Phys. Rev. Lett.* **55** 1200  
Singh D J 1994 *Planewaves, Pseudopotentials and the LAPW Method* (Boston: Kluwer)
- [20] Lu Z W, Laks D B, Wei S-H and Zunger A 1994 *Phys. Rev. B* **50** 6642
- [21] Zou J and Fu C L 1995 *Phys. Rev. B* **51** 2115
- [22] Zuo Y and Chang Y A 1993 *Computer Coupling of Phase Diagrams and Thermochemistry* **17** 161
- [23] Müller S, Wang L-W, Zunger A and Wolverton C 1999 *Phys. Rev. B* **60** 16 448
- [24] Starink M J and Zahra A-M 1997 *Phil. Mag. A* **76** 701
- [25] Sato T, Kojima Y and Takahashi T 1982 *Metal. Trans. A* **13** 1373
- [26] Osamura K and Ogura T 1984 *Metal. Trans. A* **15** 835
- [27] Asta M 1996 *Theory and Applications of the Cluster Variation and Path Probability Methods* (New York: Plenum) p 237
- [28] Wolverton C 1999 *Phil. Mag. Lett.* **79** 683
- [29] Sato T and Takahashi T 1988 *Scr. Metall.* **22** 941

## Morphology and dynamics of 2D Sn–Cu alloys on (100) and (111) Cu surfaces

Jose F Aguilar<sup>†</sup>, R Ravelo<sup>†</sup> and M I Baskes<sup>‡§</sup>

<sup>†</sup> Physics Department and Materials Research Institute, University of Texas, El Paso, TX 79968, USA

<sup>‡</sup> Materials Reliability Department, Sandia National Laboratories, Livermore, CA 94551, USA

Received 28 September 1999, accepted for publication 31 January 2000

**Abstract.** We have performed calculations of Sn deposition on Cu(111) and Cu(100) surfaces. The atomic interactions are described by modified embedded atom method (MEAM) potentials. This is a modification of the embedded atom method (EAM) to include higher moments in the electron density. We find that at low coverages Sn deposited on Cu(111) leads to the formation of a two-dimensional (2D) alloy phase with a  $p(\sqrt{3} \times \sqrt{3})\text{-R } 30^\circ$  structure which is stable up to temperatures of 1200 K. For deposition of Sn on Cu(100), a coverage of one-quarter of a monolayer results in the formation of a stable 2D alloy phase with a  $p(2 \times 2)$  structure. These results are in agreement with ion-scattering experiments. It is found that on both Cu(100) and Cu(111) surfaces, the resulting alloy phases are rippled with the Sn atoms displaced outward from the surfaces.

### 1. Introduction

Experimental studies of ultrathin Sn films evaporated onto Cu substrates show that when the overlayer is annealed, the Sn atoms incorporate into the substrate surface instead of forming an overlayer [1, 2]. This is expected due to the high solubility of Sn in Cu. A more unexpected result is that for both low-index surfaces, (100) and (111), the incorporation of the Sn atoms lead to the formation of truly two-dimensional (2D) alloy phases for Sn coverages of one-third of a monolayer for Sn/Cu(111) [1] and one-quarter of a monolayer for Sn/Cu(100) structure [2].

The deposition and subsequent annealing of ultrathin layers of Sn on a Cu(111) substrate have resulted in the formation of a stable 2D Cu–Sn alloy phase with a  $p(\sqrt{3} \times \sqrt{3})\text{-R } 30^\circ$  structure that is a single monolayer thick [1]. This ordered structure is stable against changes in coverage and temperature up to about 900 K. Above this temperature, Overbury and Ku [1] report a reduction of Sn at the surface due to diffusion of Sn into the bulk, whereas the  $p(\sqrt{3} \times \sqrt{3})\text{-R } 30^\circ$  reconstruction is maintained. The 2D alloy structure is characterized by a surface ripple with the Sn atoms located above the Cu atoms by about 0.39 Å [1]. This same structure has been observed in experiments of Sn segregation to a Cu(111) surface [3–6]. Erlewein and Hofmann using a single crystal of Cu(111) doped with 0–0.5% Sn, found that the maximum surface concentration is 33% and corresponds to a  $p(\sqrt{3} \times \sqrt{3})\text{-R } 30^\circ$  ordered structure [3]. Above 1000 K, a decrease in Sn coverage was observed. Similar results were obtained by Viljoen and du Plessis [4–6] for surface segregation of Sn in a single crystal Cu(111) in the temperature range 660–840 K. Investigations of segregation using Auger electron spectroscopy (AES) and low-energy electron diffraction (LEED) patterns showed the same

§ Present address: MST-8, MS G755 Los Alamos National Laboratory, Los Alamos, NM 87545, USA.

overlayer structure obtained by Erlewein and Hoffmann [3], namely a  $p(\sqrt{3} \times \sqrt{3})\text{-R } 30^\circ$  structure at a maximum concentration of 33%. These findings were more recently confirmed by Contini *et al* [7], on studying the segregation of Sn in Cu(111) by AES and reflection high-energy electron diffraction (RHEED). Using scanning tunnelling microscopy (STM) they identified a single-layer  $\text{Sn}_{0.33}\text{Cu}_{0.66}$  alloy phase with a  $p(\sqrt{3} \times \sqrt{3})\text{-R } 30^\circ$  reconstruction. They also reported a decrease in the Sn concentration at the surface when the temperature is raised above 1100 K. However, no rippling effect was observed. The lack of rippling was attributed to the reduction of surface strain by the existence of surface defects and steps. In short, the ordered  $p(\sqrt{3} \times \sqrt{3})\text{-R } 30^\circ$  Cu-Sn alloy structure observed on the (111) surface is obtained either via deposition of Sn on Cu or migration of Sn to the surface from a bulk alloy.

Experimental results of deposition of Sn on Cu(100) are less clear in regard to the resulting surface structure(s) than those for the Sn/Cu(111) system. Low-temperature deposition studies of thin films of Sn on Cu(100) using a combination of Rutherford backscattering/channelling (RBS), LEED and AES found evidence of formation of a commensurable 2D phase with a  $p(2 \times 2)$  structure [2]. This phase was reported to be strongly dependent on annealing temperature and Sn concentration [2, 8]. Equilibrium surface segregation studies of Sn to the low-index surfaces of Cu(100) single crystals by means of AES and LEED, showed the formation of a  $p(2 \times 2)$  ordered structure at the maximum Sn surface concentration of 25% [3, 5]. This structure appears to be more sensitive to temperature changes, with the Cu composition of the alloy phase increasing with temperature.

We carried out computer simulations using modified embedded atom method (MEAM) potentials [9, 10] which support the results of the experimental studies of the Cu(111) and Cu(100) surfaces. This work was motivated by a previous work on the initial stages of Cu/Sn alloy formation [11]. We will present results of calculations of surface segregation energies of Sn to the (111) and (100) surfaces of Cu that agree well with experimental results. The comparison of the energetics of the Sn atoms on the surface with the energetics of the Sn atoms incorporated into the surface layer demonstrates that the formation of an ordered surface layer is favoured at submonolayer coverages in both the (100) and (111) surfaces of Cu. The stability and concentration changes with temperature were investigated with molecular dynamics (MD) simulations at various temperatures. It was found that both surfaces are rippled with the Sn atoms displaced outward from the surfaces at low temperatures. At elevated temperatures (above 800 K), Cu atoms from layers below the surface migrate to the topmost layer in the Sn/Cu(111) system. This is also consistent with experimental observations of the reduction of the Sn concentration at the surface with temperature. In the next section, we discuss the methodology and geometries of the systems employed in the simulations. This will be followed by our main results and concluding remarks.

## 2. Potentials

In this work the Sn–Sn, Cu–Sn and Sn–Sn interactions are described by the MEAM potentials [9, 10]. The MEAM formalism is a modification of the well known embedded atom method (EAM) [12, 13] that reproduces the physical properties of many metals quite well. In MEAM, as in the EAM, the energy of an atom consists of two parts: the energy to embed an atom in the background electron density coming from the rest of the atoms and a classical pairwise interaction. In the EAM, the background electron density is given as a linear superposition of spherically-symmetric contributions from all of the other atoms, while in the MEAM it is augmented to include angularly-dependent terms, using a multipole expansion. This expansion of the electron density has been shown to be equivalent to an angular dependence in the bonding [10]. The MEAM has been used to successfully reproduce the mechanical and thermodynamic

properties of  $\alpha$ ,  $\beta$  and liquid Sn [14]. The Sn–Sn interaction parameters were chosen from [14], while the Cu–Cu and Cu–Sn parameters were those published in [11, 15]. Angular screening was implemented using the method detailed in [16] with some modifications as outlined in [15].

A detailed discussion of the potential has been fully given in [10, 16] and we only briefly review the method here. The general energy expression is written as

$$E = \sum_i \left( F(\bar{\rho}_i) + \frac{1}{2} \sum_{j \neq i} \phi(r_{ij}) \right) \quad (1)$$

where  $\phi(r_{ij})$  is a pair potential and  $r_{ij}$  the distance between atoms  $i$  and  $j$ . The embedding function  $F(\bar{\rho})$  is taken as  $F(\bar{\rho}) = AE_c\bar{\rho} \ln(\bar{\rho})$ .  $A$  is an adjustable parameter,  $E_c$  is the cohesive energy and  $\bar{\rho}$  is the background electron density. Unlike EAM, where the electron density is assumed to be spherically symmetric, MEAM assumes that the background electron density at a specific site  $\bar{\rho}_i$ , is a function of angle-dependent ‘partial electron densities’  $\rho^{(h)}$ :

$$\rho_i^{(0)} = \sum_{j \neq i} \rho_j^{a(0)} \quad (2)$$

$$[\rho_i^{(1)}]^2 = \sum_{\alpha} \left[ \sum_{j \neq i} \rho_j^{a(1)} x_{ij}^{\alpha} \right]^2 \quad (3)$$

$$[\rho_i^{(2)}]^2 = \sum_{\alpha\beta} \left[ \sum_{j \neq i} \rho_j^{a(2)} x_{ij}^{\alpha} x_{ij}^{\beta} \right]^2 - \frac{1}{3} \left[ \sum_{j \neq i} \rho_j^{a(2)} \right]^2 \quad (4)$$

$$[\rho_i^{(3)}]^2 = \sum_{\alpha\beta\gamma} \left[ \sum_{j \neq i} \rho_j^{a(3)} x_{ij}^{\alpha} x_{ij}^{\beta} x_{ij}^{\gamma} \right]^2 \quad (5)$$

where  $x_{ij}^{\alpha} = r_{ij}^{\alpha}/r_{ij}$  ( $\alpha = x, y, z$ ). The  $\rho_i^{a(h)}$  represent the atomic electron densities with decay constants  $\beta^{(h)}$  and are of the form

$$\rho_i^{a(h)}(r) = \rho_i^0 \exp[-\beta^{(h)}(r/r_0 - 1)] \quad (6)$$

where  $h = 0, 1, 2$  and  $3$  and  $r_0$  is the equilibrium nearest distance in the reference lattice for Cu and Sn.

The angular dependence is captured by a single scalar  $\Gamma$ :

$$\Gamma_i = \sum_{h=1,3} t_{av}^{(h)} (\rho_i^{(h)} / \rho_i^{(0)})^2 \quad (7)$$

where  $\rho_i^{(0)}$  is the spherically-symmetric electron density defined above and  $t_{av}^{(h)}$  are weights depending on the atomic environment:

$$t_{av}^{(h)} = \frac{\sum_{j \neq i} t_j^{(h)} \rho_j^{a(0)}}{\sum_{j \neq i} \rho_j^{a(0)}} \quad (8)$$

where  $t_j^{(h)}$  are constants. The host electron density is given by

$$\bar{\rho}_i = \rho_i^{(0)} \sqrt{1 + \Gamma_i} \quad \text{for Cu} \quad (9)$$

$$\bar{\rho} = \frac{2\rho_i^{(0)}}{[1 + \exp(-\Gamma_i)]} \quad \text{for Sn.} \quad (10)$$

The mixed pair potential  $\phi_{\text{Cu–Sn}}$  is derived using the L1<sub>2</sub> Cu<sub>3</sub>Sn reference state [16]

$$\phi_{\text{Cu–Sn}} = \frac{1}{3} E_{\text{u}} - \frac{1}{4} F_{\text{Cu}} \left( \frac{\bar{\rho}_{\text{Cu}}}{12} \right) - \frac{1}{12} F_{\text{Sn}} \left( \frac{\bar{\rho}_{\text{Sn}}}{4} \right) - \phi_{\text{Cu–Cu}} \quad (11)$$

where

$$\bar{\rho}_{\text{Cu}} = \frac{\sqrt{[8\rho_{\text{Cu}}^{\text{a}(0)} + 4\rho_{\text{Sn}}^{\text{a}(0)}]^2 + \frac{8}{3}t^{(2)}_{\text{Cu}}(\rho_{\text{Cu}}^{\text{a}(2)} - \rho_{\text{Sn}}^{\text{a}(2)})^2}}{12\rho_{\text{Cu}}^0} \quad (12)$$

$$\bar{\rho}_{\text{Sn}} = \frac{3\rho_{\text{Cu}}^{\text{a}(0)}}{\rho_{\text{Sn}}^0}. \quad (13)$$

In (11)  $E_u$  is the universal equation of state [17] for the Cu<sub>3</sub>Sn intermetallic and  $\phi_{\text{Cu}-\text{Cu}}$  is the Cu pair potential. The parameters are given in table 1.

**Table 1.** The MEAM parameters of copper [15], copper–tin [15] and tin [14].  $E_c$  is the cohesive energy,  $r_0$  is the nearest-neighbour distance and  $\alpha^2 = 9\Omega B/E_c$ , where  $B$  is the bulk modulus and  $\Omega$  is the atomic volume of the reference structure (fcc for Cu and Sn and L1<sub>2</sub> Cu<sub>3</sub>Sn for the alloy).

Composition	$E_c$ (eV)	$A$	$r_0$ (Å)	$\alpha$	$\beta^{(0)}$	$\beta^{(1)}$	$\beta^{(2)}$	$\beta^{(3)}$	$t^{(1)}$	$t^{(2)}$	$t^{(3)}$	$\rho_0$
Cu	3.62	1.07	2.50	5.106	3.62	2.2	6.0	2.2	3.14	2.49	2.95	1.0
Sn	3.08	1.0	3.44	6.20	6.2	6.0	6.0	6.0	4.5	6.5	-0.183	1.0
Cu <sub>3</sub> Sn	3.5	—	2.68	5.38	—	—	—	—	—	—	—	—

The MEAM incorporates a many-body screening function [16], so that the potential is short ranged for close-packed structures such as fcc and long ranged in open structures such as at a free surface. The physical justification for this screening is that if an atom  $j$  is between two atoms  $i$  and  $k$  it is able to screen the interaction between the  $i$  and  $k$  atoms, while if the atom  $j$  is not between the atoms  $i$  and  $k$ , the interaction is unscreened. The amount of screening is dependent upon the relative geometry, not just the distance between atoms  $i$  and  $k$ . The many-body screening is implemented through the use of a screening parameter  $C$  which determines the extent of screening. An atom  $j$  with  $C > C_{\max}$  does not screen atoms  $i$  and  $k$ , while an atom with  $C < C_{\min}$  totally screens atoms  $i$  and  $k$ .

In our system the angular screening was implemented using the method described in [16]. Values of  $C_{\min}$  and  $C_{\max}$  are given in table 2.

**Table 2.** Values of the screening parameters,  $C_{ijk}$ . Note that 1 refers to Cu atoms and 2 refers to Sn atoms.

$ijk$					
	111	112	212	121	221
$C_{\max}$	2.8	2.8	2.8	2.8	2.8
$C_{\min}$	2.0	0.8	0.8	0.8	0.8

For the Cu–Sn interactions, we modified the parameter  $C_{\min}$  from those used in [15] in order to optimize quantities such as the vacancy migration energy, vacancy formation energy and the activation energy of Sn in Cu and Cu in Sn. These quantities are crucial to alloy formation. The details of these calculations are given in [11].

### 3. Methodology

The calculations employed slab geometries with two non-interacting free surfaces in the  $Z$  direction. Periodic boundary conditions were imposed in the directions in the plane of the free surfaces ( $X$  and  $Y$ ). The number of atoms in the computational cell depends on the

surface geometry: the (111) simulations employed 1440 atoms with 90 atoms per layer. The (100) surface simulations comprised up to 6200 atoms with 200 atoms per layer. These values correspond to slabs with surfaces of  $127 \text{ \AA}^2$  for the (111) and  $326 \text{ \AA}^2$  for the (100) surface.

The equilibrated starting configurations were obtained employing Monte Carlo (MC) simulations at a temperature of 100 K. The simulations were performed with a fixed number of atoms and a fixed coverage (fixed number of Sn atoms). In addition to incorporating spatial displacements that accommodate strain effects, the MC simulations allow Cu and Sn atoms to exchange chemical identities while maintaining the total number of each chemical species to be fixed.

At low coverages and for both Sn/Cu(111) and Sn/Cu(100), the Sn atoms incorporate into the topmost layer rather than migrating into the bulk or remaining on the surface. At coverages of 0.33 for Sn/Cu(111) and 0.25 for Sn/Cu(100), the incorporation of Sn atoms into the topmost layer results in the formation of well ordered 2D Sn–Cu structures.

The stability and dynamics of the equilibrated structures resulting from the MC simulations were investigated employing molecular dynamics (MD) simulations. First a representative total energy was obtained by using calculations with a fixed number of atoms, volume and temperature. These calculations were followed by similar calculations with a fixed number of atoms, volume and energy. The configurations were annealed and equilibrated at various temperatures in the range of 300–1250 K for times in the range of 10–160 ps. We monitored the dynamical evolution and structure of the overlayer by looking at the radial distribution function (RDF), atomic trajectories and atomic density profiles.

#### 4. Results

During the initial stages of deposition, one can examine the sample to determine whether the Sn atoms will: form a top layer on the Cu substrate, create a surface alloy phase by incorporation in the surface layer, mix with the Cu atoms within the topmost layers to create a bulk alloy or diffuse into the bulk. Some of these issues have been addressed here by: (a) calculating the segregation energies of Sn to the Cu(111) and Cu(100) surfaces and (b) evaluating the energy difference between placing a single Sn atom on the (100) or (111) surfaces of Cu or incorporating it into the surface layer substitutionally with a Cu atom, which is then exchanged with the Sn atom and placed on the surface. From the latter type of calculations, we find that the incorporation of the Sn into the surface layer is favoured by 0.546 eV for the Cu(100) surface and by 0.424 eV for the Cu(111) surface. This means that for these low-index surfaces, the energetics favour incorporation of deposited Sn into the surface layer.

We also computed the segregation energies in the dilute limit. By definition, the segregation energy is obtained by calculating the total energy of the slab with a single solute atom for different atomic planes near the surface relative to the energy of placing that atom in the bulk. The results for the (100) and (111) low-index surfaces are presented in table 3. These results indicate that there is a strong tendency for the Sn impurities to bind to the surface layer of Cu(100) (0.823 eV) and Cu(111) (0.407 eV). Recent experimental values estimate the segregation energies to be 0.715 eV and 0.736 eV for Cu(100) and Cu(111), respectively [5]. Even though the experimental values represent averages over a range of temperatures and concentrations, the agreement with our calculated values is reasonably good.

The MC simulations predict that at 100 K and for low coverages, the Sn atoms are almost entirely incorporated in the topmost surface plane for both the (100) and (111) surfaces. For a coverage of one-third of a monolayer, a 2D alloy phase is formed on the Cu(111) surface with a  $p(\sqrt{3} \times \sqrt{3})\text{-R } 30^\circ$  structure. This structure is in agreement with both deposition [1] and segregation experiments [3–6]. On the (100) surface and for coverages of one-quarter

**Table 3.** Calculated segregation energies  $Q_i$ , in electronvolts, of a single Sn impurity (dilute limit) to the  $i$ th surface layer in a Cu slab at  $T = 0$  K. The experimental values are from [5].

System	$Q_1$	$Q_2$	$Q_3$	$Q_4$	Experimental value
Sn/Cu(111)	-0.41	-0.24	-0.36	-0.01	-0.736
Sn/Cu(100)	-0.82	-0.26	-0.55	-0.02	-0.715

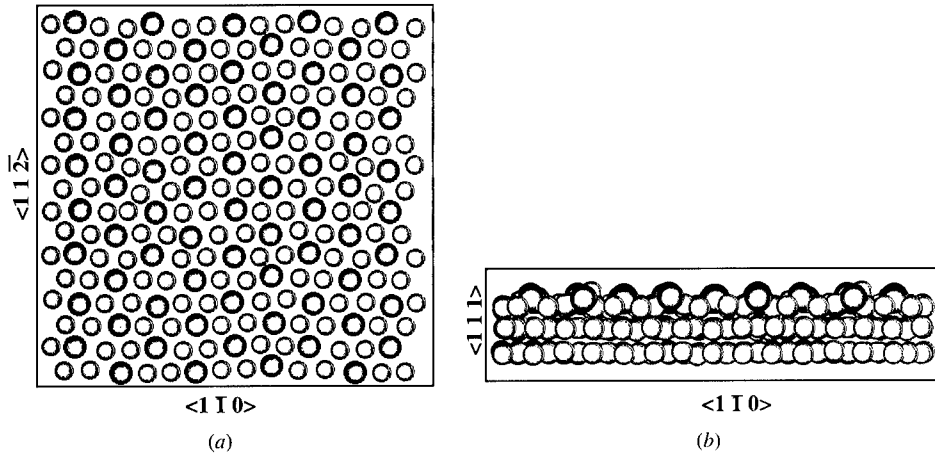


**Figure 1.** Sn/Cu(111) system. The 2D surface alloy structure  $p(\sqrt{3} \times \sqrt{3})\text{-R } 30^\circ$  on Cu(111) at 506 K. The red circles are Sn atoms and the green circles are Cu atoms. (a) Top view and (b) side view showing the first three layers.

of a monolayer, the most stable phase is also a 2D alloy phase with the  $p(2 \times 2)$  structure. This structure is also seen at 25% coverage in deposition [2] and segregation experiments [3, 5].

The stability and dynamical evolution of these structures were investigated employing MD simulations over a range of temperatures. Figure 1 shows top and side views of the  $p(\sqrt{3} \times \sqrt{3})\text{-R } 30^\circ$  ordered structure found on the Cu(111) surface. The atomic arrangement corresponds to a time snapshot at a temperature of 500 K. The 2D surface alloy is rippled, with the Sn atoms located 0.45–0.48 Å above the Cu atoms. This value is in excellent agreement with the value of 0.39 Å obtained from ion-scattering measurements [1]. Recent STM images failed to show this rippling, but this was perhaps due to the relief of the surface strain by the existence of surface steps [7].

Figure 2 shows the atomic density profile near the surface for the structure shown in figure 1 at a temperature of 508 K. The plotted densities represent averages over 20 ps. At temperatures above 508 K a small number of Cu atoms diffuse above the Sn atoms (0.8 Å). The structure remains stable up to a temperature of 900 K. The stability is confirmed through the calculation of the 2D RDF of the surface layer at 508 K (figure 3) and at 900 K. In both cases the first-, second- and third-neighbour distances between the Sn atoms are approximately 4.3, 7.6 and 8.8 Å, which are in the ratio of 1:1.7:2.0 and agree well with what is expected of a 2D hexagonal structure with six-fold symmetry. The first-, second- and third-neighbour distances between the Cu atoms in the surface layer are in the ratio of 1:1.8:2.0, which also corresponds to a 2D hexagonal structure. Figure 3 also shows the 2D RDF of the topmost layer of Cu(111) which keeps its six-fold symmetry characteristic of the Cu(111) structure, without any perturbation in its structure due to the presence of the 2D alloy.

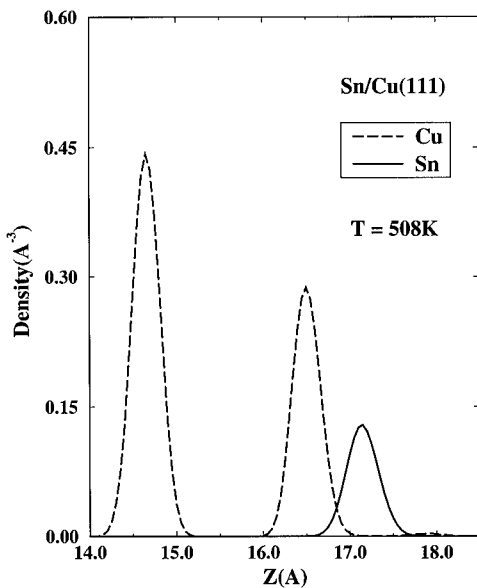


**Figure 2.** Atomic density profile for the Sn/Cu(111) system shown in figure 1 as a function of the distance from the centre of the slab. The profiles represent a time average over 20 ps. The temperature is 508 K. The rippling of Sn atoms above the Cu atoms is clearly visible.

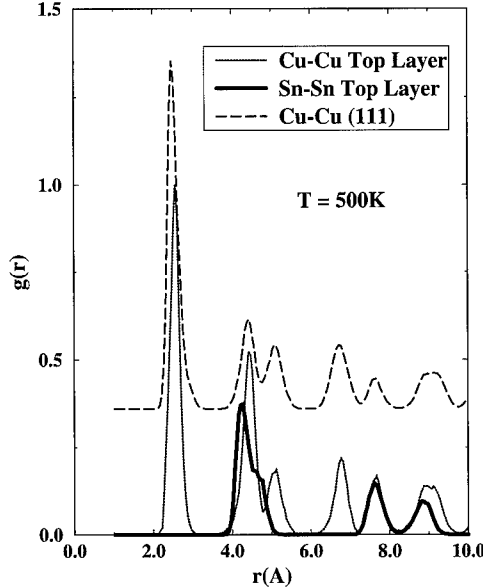


**Figure 3.** Sn/Cu(111) system. The 2D RDF for the structure shown in figure 1 at  $T = 508$  K. The plotted RDFs represent averages over 20 ps. The curves show the Sn–Sn and Cu–Cu interactions for the atoms in the surface layer and of the Cu–Cu interactions in the second layer (below the surface). The RDF of the second layer has been displaced for clarity.

The limiting surface composition of 33% Sn seen in segregation measurements can be explained by comparing the energy cost of replacing a Cu atom with a Sn atom in the  $p(\sqrt{3} \times \sqrt{3})\text{-R } 30^\circ$  alloy overlayer with the energy of placing the Sn impurity substitutionally in a bulk site. We find that the energy of adding an extra Sn impurity substitutionally on the alloy surface is 1.6 eV higher than the energy of placing the Sn impurity in the bulk. Similarly, exchanging a surface Sn atom with a Cu atom in the bulk is unfavourable by 2.6 eV. Thus, an increase or decrease of the Sn composition at the surface is energetically unfavourable with respect to diffusion of Sn into or out of the bulk.

The resulting structure obtained for one-quarter monolayer Sn coverage on Cu(100) also agrees with segregation [3, 5] and deposition experiments [2] namely a 2D alloy with a  $p(2 \times 2)$  structure. MD simulations indicate that the structure is stable up to about 600 K. The structure of the Cu atoms with the alloy overlayer is modified from ideal (100) positions to accommodate the strain caused by the larger Sn atoms. As in the case of the (111) surface, the 2D alloy formed on the (100) surface exhibits a ripple, with the Sn atoms located 0.65–0.68 Å above the Cu atoms at 100 K. The rippling decreases at higher temperatures (300–600 K). The  $p(2 \times 2)$  structure (top and side views) is shown in figure 4. The location of the Sn atoms is more clearly seen in figure 5 which shows the atomic density profile of the first few layers. The rippling of the alloy phase has not been confirmed experimentally. Ion-scattering or STM measurements should allow its determination.

The configuration of the Cu atoms in the alloy phase is distorted with respect to ideal (100) positions. Figure 6 shows the 2D RDF of the  $p(2 \times 2)$  alloy phase (surface layer) and of the Cu atoms immediately below (second layer) at a temperature of 353 K. The curves represent

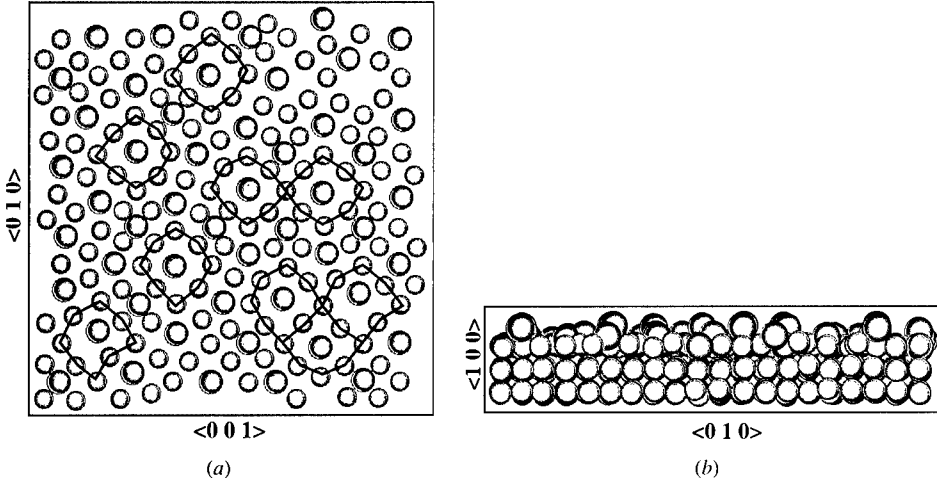


**Figure 4.** Sn/Cu(100) system. The red circles are the Sn atoms and the green circles are the Cu atoms. (a) Top view of the Sn overlayer and the topmost layer of Cu(100) atoms, at 353 K. The octagonal arrangement of Cu atoms around a number of Sn atoms is shown. (b) The side view of (a) showing the rippled p( $2 \times 2$ ) 2D ordered alloy structure.

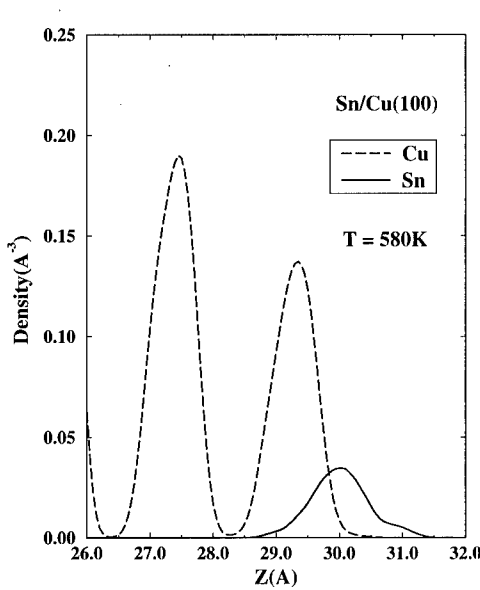


**Figure 5.** Sn/Cu(100) system. The atomic density profile of the p( $2 \times 2$ ) structure at 580 K as a function of distance from the centre of the slab. The profiles represent time averages over 20 ps. The rippling of the alloy surface layer is smaller than in the Cu(111) case.

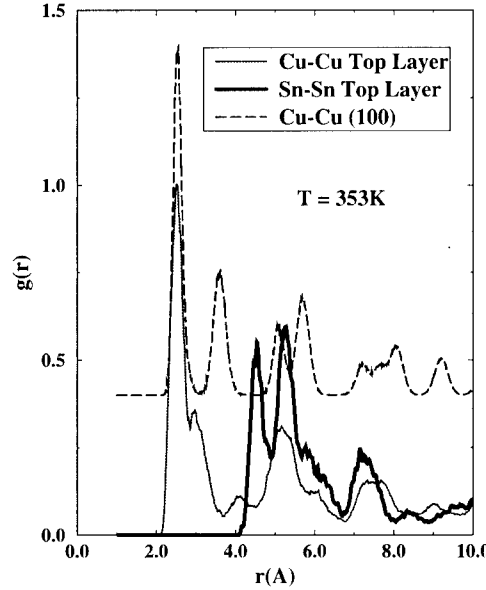


**Figure 6.** Sn/Cu(100) system. The 2D RDF of the first two layers of the p( $2 \times 2$ ) structure at 580 K. The plotted RDFs represent averages over 20 ps. The curves show the 2D RDFs of the Sn-Sn and Cu-Cu interactions on the alloy layer (surface layer) and of the Cu-Cu interactions on the layer below the alloy structure (second layer). The RDF of the second layer has been displaced for clarity.

averages over 20 ps. The first-, second- and third-neighbour distances between the Sn atoms are approximately 4.3, 5.1 and 7.5 Å, which are in the ratios 1:1.2:1.8 and agree well with what is expected of a 2D square structure with four-fold symmetry. On the other hand, the

first-, second- and third-neighbour distances between the Cu atoms in the alloy phase are in the ratio 1:2:3, which corresponds to a distorted octagonal structure. These ratios have also been observed in the Sn–Sn RDF of Sn/Cu(100) at higher coverages and temperatures (1100 K) [11]. The Cu atoms suffer a rearrangement resulting in an octagonal geometry around the Sn atoms as is shown in figure 4(a).

RBS/channelling data reported by Abell *et al* [2] showed that the deposited Sn atoms displaces at least one Cu atom from its regular lattice site. These Cu atoms are randomly distributed, whatever the deposition temperature. However, due to the crude pictures obtained by the mean of RBS/channelling, the experimental results were not capable of elucidating the octagonal rearrangement of the Cu atoms in the alloy [2]. The alloy structure does not significantly modify the structure of the Cu atoms in the second layer. The RDF of the second layer is consistent with that of an undistorted (100) surface structure.

## 5. Conclusions

The calculations presented here show that Sn deposition on (111) and (100) surfaces of Cu results in the formation of 2D ordered alloy structures. On the (111) surface, the one-third monolayer coverage leads to the formation of a 2D alloy phase with a  $p(\sqrt{3} \times \sqrt{3})\text{-R } 30^\circ$  structure that is stable up to temperatures of 900 K. This result is in agreement with deposition and segregation experiments. On the (100) surface and for one-quarter monolayer coverage, the resulting 2D alloy phase has a  $p(2 \times 2)$  structure. This result is in agreement with LEED measurements and segregation experiments. Both of these alloy phases are rippled, with the Sn atoms located above the Cu atoms. The calculated value of this rippling is 0.45–0.48 Å for the  $p(\sqrt{3} \times \sqrt{3})\text{-R } 30^\circ$  structure in close agreement with the experimental value of 0.39 Å. The rippling on the  $p(2 \times 2)$  structure is about 0.65–0.68 Å. Segregation energy calculations show that one-third monolayer coverage on the (111) surface should be the maximum equilibrium surface composition. Incorporation of more or less Sn atoms in the surface layer is energetically unfavourable with respect to incorporation of Sn atoms in the bulk. These values are consistent with segregation experiments. Finally, in the (111) case, the Cu atoms belonging to the 2D alloy phase do not suffer any change in their structure with temperature or coverage changes. This is not the case for the (100) surface, where the alloy Cu atoms rearrange into an octagonal structure via Cu–Sn interactions. This rearrangement is observed for all of the different temperatures and coverages tried.

## References

- [1] Overbury S H and Ku Yi-sha 1992 *Phys. Rev. B* **46** 7868
- [2] Abell F, Cohen C, Davies J A, Moulin J and Schmaus D 1990 *Appl. Surf. Sci.* **44** 17
- [3] Erlewein J and Hofmann S 1977 *Surf. Sci.* **68** 71
- [4] Viljoen C, du Plessis J, Swart H C and van Wyk G N 1995 *Surf. Sci.* **342** 1
- [5] du Plessis J and Viljoen E C 1996 *Appl. Surf. Sci.* **100/101** 222
- [6] du Plessis J, Viljoen P E and van Wyk G N 1991 *Surf. Sci.* **244** 277
- [7] Contini G, Di Castro V, Motta N and Sgarlata A 1998 *Surf. Sci.* **405** L509
- [8] Argile G and Rhead G E 1983 *Surf. Sci.* **135** 18
- [9] Baskes M I 1987 *Phys. Rev. Lett.* **59** 2666
- [10] Baskes M I 1992 *Phys. Rev. B* **46** 2727
- [11] Ravelo R, Aguilar J and Baskes M I 1998 Microscopic simulation of interfacial phenomena in solids and liquids  
*Mater. Res. Soc. Symp. Proc.* **492** 43
- [12] Daw M S and Baskes M I 1983 *Phys. Rev. Lett.* **50** 1285
- [13] Daw M S and Baskes M I 1984 *Phys. Rev. B* **29** 6443
- [14] Ravelo R and Baskes M 1997 *Phys. Rev. Lett.* **79** 2482

- [15] Ravelo R and Baskes M 1996 Thermodynamics and kinetics of phase transformations *Mater. Res. Soc. Symp. Proc.* **398** 287
- [16] Baskes M I, Angelo J E and Bisson C L 1994 *Modelling Simul. Mater. Sci. Eng.* **2** 505  
For a more complete description of the effect of MEAM potential parameters on properties of solids see  
Baskes M I 1997 *Mater. Chem. Phys.* **50** 152
- [17] Rose J H, Smith J R, Guinea F and Ferrante J 1984 *Phys. Rev. B* **29** 2963

## Interfacial free energy calculations via virtual slip

J V Lill<sup>†</sup> and Jeremy Q Broughton<sup>‡</sup>

Naval Research Laboratory, Washington, DC 20315, USA

Received 30 August 1999, accepted for publication 24 January 2000

**Abstract.** The computation of a solid–solid interfacial free energy requires the calculation of the work required to form the interface from the perfect crystal along any reversible pathway. The practical difficulty lies in finding a computational path connecting the perfect crystal to the defective crystal that is *reversible*. We present a method for calculating the interfacial free energy of any solid–solid interface defined geometrically by a slip on a specified crystallographic surface, for example, a stacking fault or an antiphase boundary. A non-physical pathway is defined using a ‘virtual slip’ of the system in which atoms can exist in two places at once. This avoids any ‘hard collisions’ between atoms, and assures that the pathway is reversible. This connects the perfect and defective crystals directly, as described by a given interatomic potential, without recourse to any harmonic approximations.

### 1. Introduction

The development of methods to calculate solid–solid interfacial free energies is motivated by the importance of such quantities to several areas of materials science and technology. For example, nucleation theory relates the rate of precipitate formation, and thus the thermodynamic stability of solid solutions, to the interfacial free energy between two phases. Furthermore, the passage of a dislocation through a crystal can create various extended defects, such as antiphase boundaries (APBs) and complex stacking faults (CSFs), and the difference in free energy between such interfaces and the perfect crystal can have important consequences for dislocation motion, and thus affect the macroscopic mechanical properties of the solid.

Thermodynamics informs us that the interfacial free energy is equivalent to the work done along any *reversible* pathway connecting the perfect and defective crystal. In atomistic terms, reversibility implies the absence of ‘hard’ collisions between the atoms, and it is this aspect of the problem that is responsible for the greatest computational difficulties. The goal of avoiding hard collisions often necessitates the formulation of *non-physical* pathways, using the general ‘ $\lambda$ -integration’ technique, where  $\lambda$  parametrizes the path connecting the reference state and the state whose relative free energy is desired.

The basic idea behind  $\lambda$ -integration goes back to Kirkwood [1], but the first application to the calculation of solid–liquid interfacial free energies was performed by Broughton and Gilmer [2]. The method employed continuous classical interatomic potentials to describe the solid and liquid phases. Later, Frenkel and Ladd [3] devised a  $\lambda$ -integration method to determine the difference in free energy between cph and fcc crystals [3]. Here the pathway connected hard sphere crystals to the corresponding harmonic solids, whose free energies

<sup>†</sup> Present address: Portland State University, Department of Engineering and Technology Management, PO Box 751, Portland, OR 97207, USA.

<sup>‡</sup> Present address: Yale School of Management, 135 Prospect Street, PO Box 20820, New Haven, CT 06520, USA.

were known analytically. This pathway was later extended to connect crystals described by continuous classical potentials to the corresponding harmonic crystals [4]. There have been many applications of similar  $\lambda$ -integration methods using harmonic and quasiharmonic reference states to compute free energies of solids, including chemical disorder [5]. The virtual slip pathway presented here *cannot* include the important effects of chemical disorder near an interface, and we will consider only *perfectly ordered* interfaces in the numerical examples. Possibilities of combining this technique with other methods for treating chemical disorder are considered briefly in the discussion.

Previously, we presented the first application of  $\lambda$ -integration methods to the calculation of solid–solid interfacial free energies [6, 7]. This problem is qualitatively different from calculating liquid–solid interfacial free energies, where the liquid can continuously deform in response to changes in the solid. The ‘stiffness’ of solid–solid interfaces requires that much care be exercised in designing a pathway connecting the perfect and defective crystals that avoids hard collisions. In ‘simulated alchemy’, we took advantage of the particular geometry of APBs, which can be described by either a slip of one half of the crystal with respect to the other half, or a change in the chemical identity of certain of the atoms in one half of the crystal. This is possible because the slip vector takes one lattice site into another. The alchemical pathway then changes the chemical identity of certain of the atoms in half of the simulation cell, thus creating an APB while avoiding any hard collisions.

However, simulated alchemy cannot be applied to CSFs. While a CSF can be described by a slip of one half of the crystal with respect to the other half, the slip vector does not translate one lattice site into another, and a CSF cannot be described by a change of chemical identity of certain of the atoms in half the crystal. The purpose of this article is to present a  $\lambda$ -integration pathway which is applicable to computing the interfacial free energy of CSFs, or of any interface that can be defined by a translation in a particular crystallographic plane of one half of the crystal, including APBs.

The basic idea is to perform a ‘virtual’ slip of the system along a pathway where the atoms in half the crystal can exist at two places at once, the relative separation a given atom and its ‘virtual’ partner being given by the (constant) slip vector that defines the interface. At  $\lambda = 0$  the atom exists ‘completely’ at the initial site, and at  $\lambda = 1$  the atom exits ‘completely’ at the translated site. At intermediate values of  $\lambda$ , the atom exists at both sites at once. At all times, all atoms (and their virtual partners) can execute thermal motion, and the simulation cell can deform, as in standard simulations. The interface is thus created under the given conditions of temperature and stress, while avoiding hard collisions.

In the following sections we describe the implementation of the virtual slip pathway, present numerical results for APBs and CSFs in Ni<sub>3</sub>Al using a second-moment potential, and end with a brief discussion.

## 2. Theory

The interfacial Gibbs free energy is evaluated using the  $\lambda$ -integration method as

$$\Delta G_I = \int_0^1 d\lambda \frac{\partial G_I(\lambda)}{\partial \lambda} = \int_0^1 d\lambda \left\langle \frac{1}{J\alpha} \frac{\partial H(\lambda)}{\partial \lambda} \right\rangle_{\lambda}^{N s_{ij} T} = \int_0^1 d\lambda \Psi(\lambda) \quad (1)$$

where the brackets  $\langle F \rangle_{\lambda}^{N s_{ij} T}$  imply an ensemble average of the phase space function  $F$  using the ensemble characterized by the number of atoms  $N$ , the stress  $s_{ij}$ , the temperature  $T$  and by the parameter  $\lambda$ . The interfacial area is  $\alpha$ , and we assume there are  $J$  such interfaces created simultaneously in the simulation cell along the pathway specified by  $\lambda$ . In practice, we evaluate equation (1) by performing simulations at several discrete values of  $\lambda$  to obtain

$\Psi(\lambda) = \langle [1/(2\alpha)](\partial H(\lambda)/\partial \lambda) \rangle_{\lambda}^{Ns_{ij}T}$  as an average over molecular dynamics or Monte Carlo trajectories, and then perform a numerical integration.

The Hamiltonian is split into two parts according to

$$H = (1 - \lambda)H_0 + \lambda H_1.$$

The only portion of  $H$  that depends on  $\lambda$  is the interatomic potential,  $\Phi\{r_{nm}\}$ , where for simplicity we have assumed a pair form for the potential depending on the distances between atoms  $n$  and  $m$ ,  $r_{nm} = [(q_i^{(n)} - q_i^{(m)})g_{ij}(q_i^{(n)} - q_i^{(m)})]^{1/2}$ , and where the dimensionless coordinates of atom  $n$ ,  $q_i^{(n)}$ , have been scaled by the matrix of lattice vectors,  $a_{ij}$ , and where the metric is  $g_{ij} = a_{ki}a_{kj}$ . We employ a simple matrix notation where the first index labels rows, the second index labels columns and repeated indices imply summation. We can write  $H$  using a Nosé–Hoover thermostat as

$$H = \left[ \left( \sum_{n=1}^N \frac{p_i^{(n)\prime} g_{ij}^{-1} p_j^{(n)\prime}}{2\mu_n s^2} \right) + \frac{1}{2} \sum_{n=1}^N \sum_{m \neq n}^N [(1 - \lambda)\Phi\{r_{nm}^0\} + \lambda\Phi\{r_{nm}^1\}] \right] + (N_1 N_2 N_3) \left( \frac{p'_{ij} p'_{ij}}{2W s^2} - |A|(S_{ij} E_{ij}) \right) + \left( \frac{1}{2} \frac{\theta^2}{Q} + (f_{\text{atom}} k_B T) \ln(s) \right). \quad (2)$$

Here  $s^{-1} p_i^{(n)\prime} = p_i^{(n)}$  are the scaled components of atomic momenta of atom  $n$ ,  $\mu_n$  is the atomic mass of atom  $n$ ,  $s^{-1} p'_{ij} = p_{ij}$  are the momenta of the lattice vector matrix elements,  $s$  is the Nosé time scale,  $\theta$  is the momentum of the time scale,  $f_{\text{atom}}$  is the number of atomic degrees of freedom, including centre of mass constraints,  $k_B$  is Boltzmann's constant,  $T$  is the absolute temperature and  $W$  and  $Q$  are fictitious masses. The stress and strain are measured with respect to the initial configuration, and may be related to the stress and strain measures referred to the system at time  $t$  ( $s_{ij}$  and  $e_{ij}$ ) by:

$$S_{ij} = |F|(F_{ik}^{-1} s_{kp} F_{jp}^{-1}) \quad (3)$$

$$E_{ij} = \frac{1}{2}(F_{ki} F_{kj} - \delta_{ij}) = F_{ki} e_{kp} F_{pj} \quad (4)$$

where the deformation gradient is

$$F_{ij}(t) = a_{ik}(t) A_{kj}^{-1}. \quad (5)$$

We use the special notation  $A_{ij}$  to denote the matrix of lattice vectors at time zero:

$$A_{ij} = a_{ij}(0). \quad (6)$$

The volume of the unit cell at time zero is denoted by the determinant,  $|A|$ . The expression  $-|A|(S_{ij} E_{ij})$  then serves as the nonlinear elastic analogue of the 'PV' term encountered in standard discussions of switching between ensembles using Legendre transformations. The numerical factors ( $N_1 N_2 N_3$ ) give the number of crystalline cells (unit or primitive cells) along each lattice vector in the entire system, and arise because we have referred all strains back to the crystalline cell defined by  $a_{ij}$ . This is possible because the work term  $|A|(S_{ij} E_{ij})$  describes only *homogeneous* deformations, because only one set of lattice vectors is employed.

Physically, what all this means is that integrating trajectories generated from  $H_0$  and assuming ergodicity implies that time averages are equivalent to averages over the Gibbs ensemble characterized by the partition function in the phase space of lattice vectors, scaled coordinates and momenta, and using a nonlinear elastic work term:

$$\begin{aligned} \Xi(Ns_{ij}T) = & \gamma \int d\{q_i^{(n)}\} \int d\{p_i^{(n)}\} \int d\{a_{ij}\} \exp \frac{-1}{k_B T} \left[ \left( \sum_{n=1}^N \frac{1}{2\mu_n} p_i^{(n)} g_{ij}^{-1} p_j^{(n)} \right) \right. \\ & \left. + \frac{1}{2} \sum_{n=1}^N \sum_{m \neq n}^N \Phi\{r_{nm}^0\} - |A|(S_{ij} E_{ij}) \right] \end{aligned} \quad (7)$$

where  $\gamma$  is a normalization constant and  $\int d\{q_i^{(n)}\}$  implies integration over all dimensionless atomic coordinates, etc. The lattice vector momenta, fictitious masses and Nosé thermostat variables have been integrated out of the expression. Readers are referred to [8] for details.

The slip vector which characterizes the interface is  $s_i = a_{ij}(0)\sigma_j$ , where  $a_{ij}(0)$  is the matrix of lattice vectors at time zero, and  $\sigma_j$  are the dimensionless components of the slip vector with respect to these lattice vectors. Similarly, we write the dimensionless components of atom  $n$  at time  $t$  as  $q_j^{(n)}(t)$ , where the Cartesian components of the atom are given by  $r_i^{(n)}(t) = a_{ij}(t)q_j^{(n)}(t)$ .

In the reference state ( $\lambda = 0$ ) the interatomic potential is evaluated using the standard expression for interatomic distances

$$r_{nm}^0 = \sqrt{q_i^{(nm)} g_{ij} q_j^{(nm)}} \quad (8)$$

where the metric is

$$g_{ij}(t) = a_{ki}(t)a_{kj}(t) \quad (9)$$

and the interparticle separation includes the nearest image transformation:

$$q_i^{(nm)} = (q_i^{(n)} - q_i^{(m)}) - N_i \text{NI} \left[ \frac{1}{N_i} (q_i^{(n)} - q_i^{(m)}) \right] \quad (10)$$

where  $N_i$  is the number of crystalline cells along the  $i$ th lattice vector in the simulation cell.

We take a somewhat more general approach than simply allowing one interface in the middle of the simulation cell and another at the periodic boundaries. In the defective state ( $\lambda = 1$ ) we define a one-to-one mapping between the atoms and their translated ‘virtual’ partners

$$h_i^{(n)} = q_i^{(n)} + k_n \sigma_i \quad (11)$$

where  $k_n$  is the number of translations of atom  $n$  by the slip vector  $\sigma_i$ . We must insure that the number of interfaces in the simulation cell, including the effects of periodic boundary conditions, is consistent with the total number of atomic planes in the simulation cell parallel to the interface,  $M$ , and with the ‘modularity’ of the translation,  $m$ . This latter quantity is the number of translations required to map  $q_i^{(n)}$  into itself, i.e.

$$q_i^{(n)} = q_i^{(n)} + m \sigma_i. \quad (12)$$

Thus

$$0 \leq k_n < m \quad (13)$$

and consistency demands that

$$\text{mod}[mJ, M] = 0. \quad (14)$$

The interatomic distances in the defective state are then specified by  $r_{nm}^1$ :

$$r_{nm}^1 = \sqrt{h_i^{(nm)} g_{ij} h_j^{(nm)}}. \quad (15)$$

A crucial point common to both the simulated alchemy and virtual slip pathways is the existence of a one-to-one mapping between the atoms in the reference and defective states. In the simulated alchemy pathway, the mapping is provided by the specification of which atoms change their chemical identity and which do not; in the virtual slip pathway, the mapping is provided by the virtual slips undergone by each atom over the course of the  $\lambda$ -integration. This insures the consistent evaluation of the free energy derivatives in the isothermal-isostress ensemble, characterized by the variables  $(Ns_{ij}T)$ . It must also be emphasized that the periodic

images  $q_i^{(nm)}$  and  $h_i^{(nm)}$  are each consistent with the periodicity of the simulation cell in the plane of the interface. Thus as long as we insure that (14) is satisfied, there are no anomalous effects as the size of the simulation cell is increased. In practice, we choose  $M$  sufficiently large so that the distinct interfaces created within the simulation cell have a minimal influence upon one another.

In principle, the interfacial entropies may also be computed, using the equation:

$$\Delta S_I = \int_0^1 d\lambda \frac{\partial S_I(\lambda)}{\partial \lambda} = -\frac{1}{k_B T^2} \int_0^1 d\lambda \left[ \left\langle H \left( \frac{1}{J\alpha} \frac{\partial H}{\partial \lambda} \right) \right\rangle_{\lambda}^{N_{Sij}T} - \langle H \rangle_{N_{Sij}T} \left\langle \frac{1}{J\alpha} \frac{\partial H}{\partial \lambda} \right\rangle_{\lambda}^{N_{Sij}T} \right]. \quad (16)$$

However, for the *perfectly ordered* interfaces studied here, the numerical noise in the trajectories swamps the small differences in the integrand of equation (16).

### 3. Results and discussion

We employ the same second-moment potential, Vitek *et al* [9], which was used in the previous alchemical calculations of APB free energies in Ni<sub>3</sub>Al [6]. Originally, this potential was fit in three steps. First, the Ni–Ni and Al–Al terms were fit to the cohesive energy and elastic constants for the bulk elemental systems. Next, the Ni–Al terms were fit to the Ni<sub>3</sub>Al (L1<sub>2</sub>) and NiAl (B2) alloying energies and lattice constants. Finally, further adjustments were made to yield a value of the (111) APB energy of 226 mJ m<sup>-2</sup> at 0 K. However, the parameters have since been adjusted, and the (111) APB energy at 0 K is now 246 mJ m<sup>-2</sup>. The final set used for these calculations are given in the appendix.

As a test, we compare results for the calculation of an APB free energy via virtual slip and simulated alchemy. The particular APB is on the (111) plane of L1<sub>2</sub> (fcc-based binary) alloys, and is characterized by a translation of  $\frac{1}{2}[\bar{1}10]a$  of the atoms on one side of the interface from their original lattice sites, where  $a$  is the lattice constant for the underlying cubic lattice. In the simulated alchemy and virtual slip simulations, a system of 2304 atoms having a total of 36 (111) planes was transformed to have three equally spaced APBs. The (111) interplane spacing is approximately 2.06 Å, and the separation between interfaces is approximately 24.72 Å.

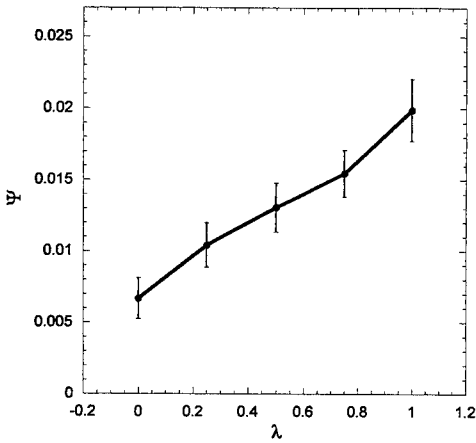


**Figure 1.** Simulated alchemy pathway for the (111) $\frac{1}{2}[-1, 1, 0]a$  APB in Ni<sub>3</sub>Al at 600 K. The integral of  $\Psi = \langle (1/J\alpha)(\partial H(\lambda)/\partial \lambda) \rangle_{\lambda}$  over  $\lambda$  gives an interfacial free energy of  $209.1 \pm 12.5$  mJ m<sup>-2</sup>.

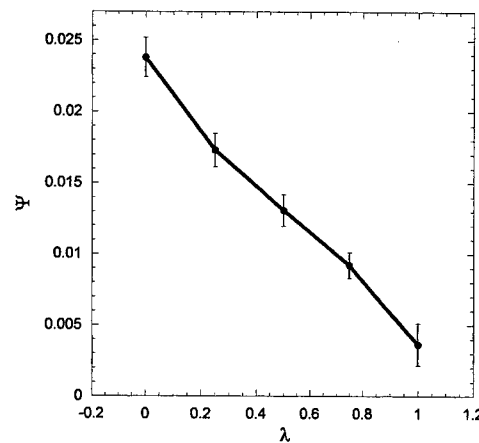


**Figure 2.** Virtual slip pathway for the (111) $\frac{1}{2}[-1, 1, 0]a$  APB in Ni<sub>3</sub>Al at 600 K. The integral of  $\Psi = \langle (1/J\alpha)(\partial H(\lambda)/\partial \lambda) \rangle_{\lambda}$  over  $\lambda$  gives an interfacial free energy of  $213.6 \pm 8.5$  mJ m<sup>-2</sup>.

**Table 1.** Antiphase boundary energies; comparison of simulated alchemy and virtual slip pathways for  $T = 600$  K.

Method	$\Delta G$ (mJ m $^{-2}$ )
Alchemy	$209.1 \pm 12.5$
Virtual slip	$213.6 \pm 8.5$

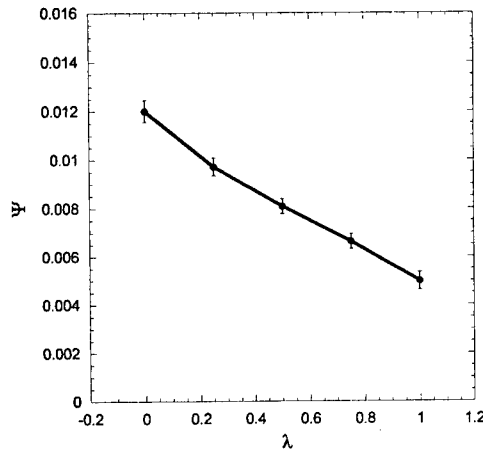


**Figure 3.** Virtual slip pathway for the  $(111)_{\bar{6}}^1[1, 1, -2]a$  CSF in  $\text{Ni}_3\text{Al}$  at 300 K. The integral of  $\Psi = ((1/J\alpha)(\partial H(\lambda)/\partial\lambda))_\lambda$  over  $\lambda$  gives an interfacial free energy of  $132.0 \pm 2.6$  mJ m $^{-2}$ .

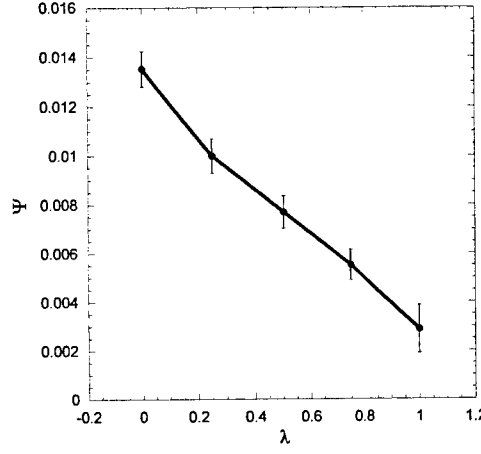


**Figure 4.** Virtual slip pathway for the  $(111)_{\bar{6}}^1[1, 1, -2]a$  CSF in  $\text{Ni}_3\text{Al}$  at 600 K. The integral of  $\Psi = ((1/J\alpha)(\partial H(\lambda)/\partial\lambda))_\lambda$  over  $\lambda$  gives an interfacial free energy of  $125.9 \pm 5.2$  mJ m $^{-2}$ .

The cut-off length for the potential is 6.0 Å, so the APBs are about four cut-off lengths apart in each simulation. The values of  $\Psi = (1/J\alpha)(\partial H(\lambda)/\partial\lambda)$  obtained from simulated alchemy and virtual slip simulations of the APB at 600 K are shown in figures 1 and 2. The discrete values of the dimensionless parameter used are  $\lambda = 0.0, 0.25, 0.5, 0.75$  and  $1.0$ . The interfacial free energies were then obtained using five-point numerical integrations. The behaviour of  $\Psi = (1/J\alpha)(\partial H(\lambda)/\partial\lambda)$  in the simulated annealing and virtual slip pathways differs qualitatively, but there is no reason why they should agree. However, their integrals and the resulting values for the interfacial Gibbs energy (in table 1) agree to within the numerical noise. In these small calculations, the statistical noise along each pathway is comparable.

Having demonstrated the compatibility of the simulated alchemy and virtual slip simulations for APBs, we next use the virtual slip pathway to compute a CSF energy, where the use of simulated alchemy is prohibited because of the change in coordination of the atoms near the interface. The CSF simulated is also on the (111) plane of L1<sub>2</sub> alloys, and is characterized by a translation of  $\frac{1}{6}[1\bar{1}2]a$  of the atoms on one side of the interface from their original lattice sites, where  $a$  is the lattice constant for the underlying cubic lattice. The fitting procedure described above yielded a (111) CSF energy of 142 mJ m $^{-2}$  at 0 K, considerably lower than the APB energy. Aside from the slip vector, the same basic geometry as in the evaluation of the APB free energy was employed. The values of  $\Psi = (1/J\alpha)(\partial H(\lambda)/\partial\lambda)$  for the virtual slip simulations at  $T = 300, 600$  and  $800$  K are shown in figures 3–5, and the results of integrating these curves to obtain the interfacial Gibbs free energies are in table 2. We attempted simulations at 900 K, but that temperature was sufficient to generate defects in the simulation with  $\lambda = 1$ , and the

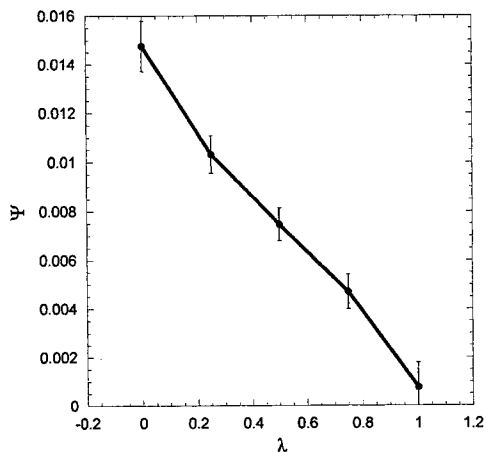


**Figure 5.** Virtual slip pathway for the  $(111)_{\frac{1}{6}}[1, 1, -2]a$  CSF in  $\text{Ni}_3\text{Al}$  at 800 K. The integral of  $\Psi = \langle (1/J\alpha)(\partial H(\lambda)/\partial\lambda) \rangle_\lambda$  over  $\lambda$  gives an interfacial free energy of  $121.2 \pm 5.8 \text{ mJ m}^{-2}$ .

**Table 2.** Stacking fault energies at  $T = 300, 600$  and  $800$  K using the virtual slip pathway.

$T$ (K)	$\Delta G$ (mJ m $^{-2}$ )
0	142
300	$132.0 \pm 2.6$
600	$125.9 \pm 5.2$
800	$121.2 \pm 5.8$

resulting noise swamped the difference in free energy. The entropic effects in these calculations involving perfect interfaces with no chemical disorder are small, but they are observable in the small decrease of the CSF interfacial free energy with temperature over the range 300–800 K.

In conclusion, we have presented results for a new pathway for computing solid–solid interfacial free energies. Although the simulated alchemy and virtual slip pathways are redundant for the case of APBs, the methods are in fact complimentary. The simulated alchemy path can be applied to systems having chemical disorder, and the virtual slip path can be applied to any interface characterized by a relative slip of the crystal on a particular surface. We have demonstrated agreement in the case of APBs, and have applied the virtual slip method to a CSF on (111) in  $\text{Ni}_3\text{Al}$ .

Each method is ‘direct’ in that no reference is made to any harmonic or quasi-harmonic limit; the calculation only requires an interatomic potential, and the quality of the computed interfacial free energy is then consistent with the accuracy of that potential. While the methods are immune to limitations of the sort encountered in the use of harmonic and quasi-harmonic approximations [5], the temperature regime in which accurate interfacial free energies may be computed is similarly limited. If the temperature is sufficiently high to generate a defect during the simulation, as in the case of the CSF at 900 K, the resulting statistical noise will swamp the calculation. The small calculations performed to date indicate that the statistical noise present is sufficiently low to allow determination of interfacial free energies; however, the noise is large enough to preclude calculation of the interfacial entropies in the non-disordered systems studied so far.

In principle, the alchemical pathway [6] could also be applied to chemically disordered systems. For example, it would be straightforward to chose a set of atoms in the simulation

at random and then calculate the change in free energy as the chemical identities of these specific atoms were changed. This alchemical procedure could also be applied to a simulation having an interface created by either a simulated alchemy or virtual slip pathway, thus adding a degree of chemical disorder to a CSF or APB. Another possibility would be the combination of alchemical and cluster-variation methods [10], with separate alchemical pathways for each distinct cluster in an expansion.

The classical potential used here has been fit to give reasonable energies for (111) interfaces; energies for other interfaces can be poor. In particular, the energy of the APB on (001) is very low [6]. The inability of classical potentials to simultaneously fit different interfacial energies is a commonly encountered problem, and any discussion of the *anomalous flow* in Ni<sub>3</sub>Al, which is thought to involve the relative free energies of various (111) and (001) interfaces [11], will require more realistic potentials.

### Acknowledgments

This work was supported by ONR, and by a grant of HPC time from the DOD HPC Shared Resource Centers, CEWES and NRL.

### Appendix. SMA (second moment approximation) potential parameters

The centrosymmetric form taken for the interatomic interaction in the second moment approximation for Ni<sub>3</sub>Al is

$$\Phi = \sum_{n=1}^{N_{\text{atom}}} \sum_{m \neq n} \left\{ \begin{array}{l} V_{\text{Ni-Ni}}(r_{nm}) \\ V_{\text{Al-Al}}(r_{nm}) \\ V_{\text{Ni-Al}}(r_{nm}) \end{array} \right\} - \left( \sum_{n=1}^{N_{\text{atom}}} \sum_{m \neq n} \left\{ \begin{array}{l} H_{\text{Ni-Ni}}(r_{nm}) \\ H_{\text{Al-Al}}(r_{nm}) \\ H_{\text{Ni-Al}}(r_{nm}) \end{array} \right\} \right)^{1/2} \quad (17)$$

where  $r_{nm}$  is the interatomic distance; the brackets indicate the possible chemical interactions. The parametrization employed here has been ‘massaged’ to give reasonable (111) APB and CSF energies in Ni<sub>3</sub>Al at 0 K (figures 6 and 7). The distinct pair potentials for Ni<sub>3</sub>Al are given by three forms for three ranges of interaction (see also tables 3–7):

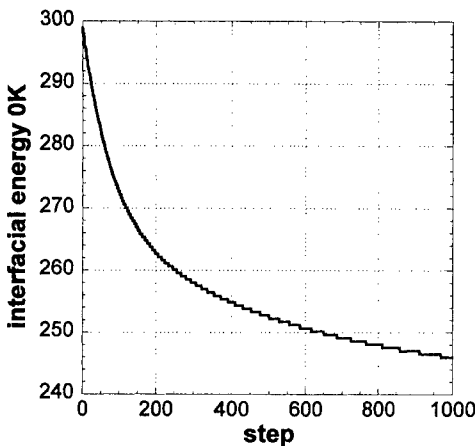


**Figure 6.** Steepest descent for (111)<sub>1/2</sub>[-1, 1, 0]a APB energy at 0 K; the atomic coordinates and lattice vectors were varied.

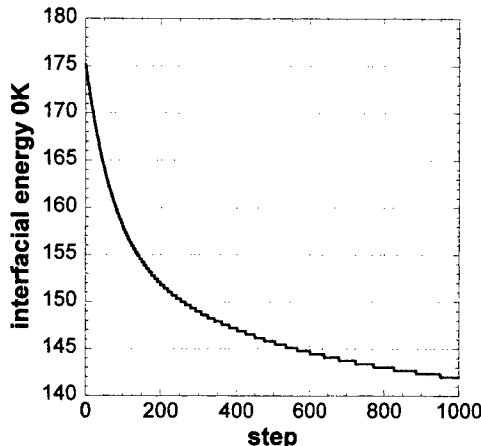


**Figure 7.** Steepest descent for (111)<sub>1/6</sub>[1, 1, -2]a CSF energy at 0 K; the atomic coordinates and lattice vectors were varied.

**Table 3.** SMA parameters, distances defining distinct regions of the pair potential; see the appendix for details.

Parameter	Distance (Å)
$a_{\text{Ni-Ni}}$	0.61
$b_{\text{Ni-Ni}}$	1.465
$a_{\text{Al-Al}}$	0.61
$b_{\text{Al-Al}}$	1.45
$a_{\text{Ni-Al}}$	0.61
$b_{\text{Ni-Al}}$	1.48

**Table 4.** SMA parameters, expansion coefficients in pair potential; see the Appendix for details.

$k$	$r_k^{\text{Ni-Ni}}$ (Å)	$r_k^{\text{Al-Al}}$ (Å)	$r_k^{\text{Ni-Al}}$ (Å)
1	4.317 1695	4.961 6175	4.351 74
2	4.236 112 44	4.779 354	4.244 73
3	3.876 642	4.414 827	3.888 03
4	3.171 798	4.252 815	2.960 61
5	2.889 8604	3.645 27	2.522 23
6	2.431 7118	2.863 994 59	0.700 000

**Table 5.** SMA parameters, expansion coefficients in pair potential; see the appendix for details.

$k$	$\alpha_k^{\text{Ni-Ni}}$ (eV Å <sup>-3</sup> )	$\alpha_k^{\text{Al-Al}}$ (eV Å <sup>-3</sup> )	$\alpha_k^{\text{Ni-Al}}$ (eV Å <sup>-3</sup> )
1	0.751 863 19	0.485 497 15	-0.646 920 88
2	-1.173 09138	-1.122 14795	1.139 269 28
3	0.895 745 43	2.107 195 59	-0.665 510 61
4	-2.015 344 24	-1.619 069 74	1.468 021 93
5	2.996 036 51	0.443 144 85	3.000 0000
6	4.569 2083	1.528 3343	0.000 0000

**Table 6.** SMA parameters, expansion coefficients in pair potential; see the appendix for details.

	$\beta_k^{\text{Ni-Ni}}$	$\beta_k^{\text{Al-Al}}$	$\beta_k^{\text{Ni-Al}}$
0	7.658 30	7.678 10	8.013 00
1	3.3339	-1.582 60	-0.493 200
2	-10.6003	-4.634 10	-5.933 20
3	3.900 90	2.107 60	2.388 90

$$V_{\text{Ni-Ni}}(r_{nm}) = \begin{cases} \sum_{k=1}^6 [\alpha_k^{\text{Ni-Ni}} (r_k^{\text{Ni-Ni}} - r_{nm})^3] & r_{\text{cut}} > r_{nm} > b_{\text{Ni-Ni}} \\ \exp \left[ \sum_{k=0}^3 (\beta_k^{\text{Ni-Ni}} (r_{nm})^k) \right] & a_{\text{Ni-Ni}} \leq r_{nm} \leq b_{\text{Ni-Ni}} \\ \left[ (Z_{\text{Ni}} e)^2 \frac{1}{r_{nm}} \phi_{\text{Ni-Ni}} \right] & r_{nm} < a_{\text{Ni-Ni}} \end{cases} \quad (18)$$

**Table 7.** SMA parameters, expansion coefficients in band energy; see the appendix for details.

Parameter	Distance (Å)
$\rho_1^{\text{Ni-Ni}}$	4.860 360
$\rho_2^{\text{Ni-Ni}}$	3.766 779
$\gamma_1^{\text{Ni-Ni}}$	0.289 298 31
$\gamma_2^{\text{Ni-Ni}}$	0.074 6414
$\rho_1^{\text{Al-Al}}$	4.317 1695
$\rho_2^{\text{Al-Al}}$	3.277 5246
$\gamma_1^{\text{Al-Al}}$	0.657 319 92
$\gamma_2^{\text{Al-Al}}$	-2.148 234 53

$$V_{\text{Al-Al}}(r_{nm}) = \begin{cases} \sum_{k=1}^6 [\alpha_k^{\text{Al-Al}} (r_k^{\text{Al-Al}} - r_{nm})^3] & r_{\text{cut}} > r_{nm} > b_{\text{Al-Al}} \\ \exp \left[ \sum_{k=0}^3 (\beta_k^{\text{Al-Al}} (r_{nm})^k) \right] & a_{\text{Al-Al}} \leq r_{nm} \leq b_{\text{Al-Al}} \\ \left[ (Z_{\text{Al}} e)^2 \frac{1}{r_{nm}} \phi_{\text{Al-Al}} \right] & r_{nm} < a_{\text{Al-Al}} \end{cases} \quad (19)$$

$$V_{\text{Ni-Al}}(r_{nm}) = \begin{cases} \sum_{k=1}^6 [\alpha_k^{\text{Ni-Al}} (r_{\text{Ni-Al}}^k - r_{nm})^3] & r_{\text{cut}} > r_{nm} > b_{\text{Ni-Al}} \\ \exp \left[ \sum_{k=0}^3 (\beta_k^{\text{Ni-Al}} (r_{nm})^k) \right] & a_{\text{Ni-Al}} \leq r_{nm} \leq b_{\text{Ni-Al}} \\ \left[ (Z_{\text{Al}} e) (Z_{\text{Ni}} e) \frac{1}{r_{nm}} \phi_{\text{Ni-Al}} \right] & r_{nm} < a_{\text{Ni-Al}} \end{cases} \quad (20)$$

where the screened Coulomb functions are

$$\begin{aligned} \phi_{\text{Ni-Ni}} = & 0.1818 \exp[-(3.2)r_{nm}/\rho_{\text{Ni-Ni}}] + 0.5099 \exp[-(0.9423)r_{nm}/\rho_{\text{Ni-Ni}}] \\ & + 0.2802 \exp[-(0.4029)r_{nm}/\rho_{\text{Ni-Ni}}] \\ & + 0.02817 \exp[-(0.2016)r_{nm}/\rho_{\text{Ni-Ni}}]. \end{aligned} \quad (21)$$

$$\begin{aligned} \phi_{\text{Al-Al}} = & 0.1818 \exp[-(3.2)r_{nm}/\rho_{\text{Al-Al}}] + 0.5099 \exp[-(0.9423)r_{nm}/\rho_{\text{Al-Al}}] \\ & + 0.2802 \exp[-(0.4029)r_{nm}/\rho_{\text{Al-Al}}] \\ & + 0.02817 \exp[-(0.2016)r_{nm}/\rho_{\text{Al-Al}}]. \end{aligned} \quad (22)$$

$$\begin{aligned} \phi_{\text{Ni-Al}} = & 0.1818 \exp[-(3.2)r_{nm}/\rho_{\text{Ni-Al}}] + 0.5099 \exp[-(0.9423)r_{nm}/\rho_{\text{Ni-Al}}] \\ & + 0.2802 \exp[-(0.4029)r_{nm}/\rho_{\text{Ni-Al}}] \\ & + 0.02817 \exp[-(0.2016)r_{nm}/\rho_{\text{Ni-Al}}] \end{aligned} \quad (23)$$

and the scaled distance factors are

$$\rho_{\text{Ni-Ni}} = [(0.88534)(529\,177\,249)]/[(Z_{\text{Ni}} + Z_{\text{Ni}})] \quad (24)$$

$$\rho_{\text{Al-Al}} = [(0.88534)(529\,177\,249)]/[(Z_{\text{Al}} + Z_{\text{Al}})] \quad (25)$$

$$\rho_{\text{Ni-Al}} = [(0.88534)(529\,177\,249)]/[(Z_{\text{Ni}} + Z_{\text{Al}})]. \quad (26)$$

The atomic numbers are  $Z_{\text{Ni}} = 28$  and  $Z_{\text{Al}} = 13$ ,  $e = \sqrt{\frac{1}{137}\hbar c}$ , and the cut-off length is  $r_{\text{cut}} = 6.0$  K. The distinct contribution to the band energy from the hopping integrals for  $\text{Ni}_3\text{Al}$

are:

$$H_{\text{Ni-Ni}}(r_{nm}) \begin{cases} \sum_{k=1}^2 [\gamma_k^{\text{Ni-Ni}} (\rho_k^{\text{Ni-Ni}} - r_{nm})^3] & r_{\text{cut}} > r_{nm} > b_{\text{Ni-Ni}} \\ 0 & r_{nm} < b_{\text{Ni-Ni}} \end{cases} \quad (27)$$

$$H_{\text{Al-Al}}(r_{nm}) \begin{cases} \sum_{k=1}^2 [\gamma_k^{\text{Al-Al}} (\rho_k^{\text{Al-Al}} - r_{nm})^3] & r_{\text{cut}} > r_{nm} > b_{\text{Al-Al}} \\ 0 & r_{nm} < b_{\text{Al-Al}} \end{cases} \quad (28)$$

$$H_{\text{Ni-Al}}(r_{nm}) = \sqrt{H_{\text{Ni-Ni}}(r_{nm}) H_{\text{Al-Al}}(r_{nm})} = 0. \quad (29)$$

The cross terms in the band energy are taken to be the geometric mean of the corresponding direct terms.

## References

- [1] Kirkwood J G 1935 *J. Chem. Phys.* **3** 300
- [2] Broughton J Q and Gilmer G H 1983 *J. Chem. Phys.* **79** 5095
- [3] Frenkel D and Ladd A J C 1984 *J. Chem. Phys.* **81** 3188
- [4] Frenkel D 1986 *Phys. Rev. Lett.* **56** 856
- [5] Foiles S M 1994 *Phys. Rev. B* **49** 14930
- [6] Skinner A J, Lill J V and Broughton J Q 1995 *Modelling Simulation Mater. Sci. Eng.* **3** 359
- [7] Lill J V, Skinner A J and Broughton J Q 1997 *J. Phase Equilibria* **18** 495
- [8] Lill J V and Broughton J Q 1992 *Phys. Rev. B* **46** 12068
- [9] Vitek V, Ackland G J and Cseri J 1991 *Mater. Res. Soc. Symp. Proc.* **186** 237
- [10] de Fontaine D and Wolverton C 1994 *Prog. Theor. Phys.* **115** 115
- [11] Paxton A T 1992 Point, line and planar defects *Electron Theory and Alloy Design* ed D G Pettifor and A H Cottrell (London: The Institute of Materials) ch 6, p 158

## Linear and nonlinear elasticity in atomistic simulations

J V Lill<sup>†</sup> and Jeremy Q Broughton<sup>‡</sup>

Naval Research Laboratory, Washington, DC 20315, USA

Received 30 August 1999, accepted for publication 24 January 2000

**Abstract.** The use of either linear or nonlinear elastic theory in deriving methodologies for atomistic simulations is shown to be based on two very different views of the interaction of the ‘system’ with the ‘reservoir’. These views may be related through the definition of a phenomenological relaxation time, which describes how the reservoir responds to changes in stress of the system. A general procedure for introducing a finite relaxation time of the reservoir into atomistic simulations is described, and numerical results are presented which demonstrate how the linear and nonlinear simulations can be brought into agreement. A discussion of the underlying thermodynamic assumptions is given, and the benefits of using Nosé–Hoover chains in simulating structural transformations are demonstrated.

### 1. Introduction

The simulation methods of Andersen [1] and of Parrinello and Rahman [2–4] are based, in part, upon the underlying assumption of linearity in the interaction between the atomic system and the ‘reservoir’ which exerts a stress on the system and causes it to deform. There were early attempts at introducing nonlinear elastic effects [5, 6], the motivation being that macroscopically, nonlinearity is important during large, rapid deformations, and this is the regime most suited to direct atomistic simulations. More recently, we presented an alternative nonlinear treatment [7], the principal result of which was the appearance of an effective external pressure that changed as the system deformed, and that was dynamically balanced by the atomic virial pressure in accordance with a nonlinear extension to the virial theorem. The distinction drawn between the linear and nonlinear simulations involved the presumed relaxation of the stress reservoir [7]: in the linear case, the relaxation was instantaneous, whereas in the nonlinear case, the reservoir never relaxed. However, at present there is no computational formalism for unifying atomistic simulations based on linear and nonlinear elasticity, and the connection to continuum mechanics remains obscure.

The purpose of this article is to present an explicit formalism that allows one to continuously switch between the familiar linear and less familiar nonlinear equations of motion for molecular dynamics simulations with varying cell size and shape. Furthermore, in bridging this gap, a more intimate connection between atomistic simulations and continuum mechanics will be established. The only new parameters that must be introduced is a phenomenological relaxation time of the stress reservoir,  $\tau_{\text{relax}}$ , and a strain threshold for the relaxation to take effect. This will be justified thermodynamically by appealing to the equations of nonlinear

<sup>†</sup> Present address: Portland State University, Department of Engineering and Technology Management, PO Box 751, Portland, OR 97207, USA.

<sup>‡</sup> Present address: Yale School of Management, 135 Prospect Street, PO Box 20820, New Haven, CT 06520, USA.

elasticity, including mechanical dissipation [8]. We will also demonstrate that substantial benefits of employing Nosé–Hoover chains [9] when structural transformations are simulated. We will first summarize some relevant macroscopic formulae from continuum mechanics.

In nonlinear elasticity [10, 11], one must distinguish between strains measured relative to some reference state at time zero, or to the current (deformed) state at time  $t$ . The standard expressions for strain are

$$E_{ij} = \frac{1}{2}(F_{ki}F_{kj} - \delta_{ij}) \quad (1)$$

$$e_{ij} = \frac{1}{2}(\delta_{ij} - F_{ki}^{-1}F_{kj}^{-1}) \quad (2)$$

and the corresponding expressions for stress are

$$S_{ij} = |F|(F_{ik}^{-1}s_{kp}F_{jp}^{-1}) \quad (3)$$

$$s_{ij} = |F|^{-1}(F_{ik}S_{kp}F_{jp}). \quad (4)$$

Here  $S_{ij}$  and  $E_{ij}$  are the stress and strain in the system at time zero, and  $s_{ij}$  and  $e_{ij}$  are the stress and strain in the system at time  $t$ . We use a matrix notation for the Cartesian tensors; the first index labels rows, the second index labels columns and a summation convention for repeated indices is implied. Transposes may be identified by the order of the indices, for example in equation (4),  $S_{kp}F_{jp}$  implies ‘the  $k$ th row and  $j$ th column of the product of the matrix  $\mathbf{S}$  times the transpose of the matrix  $\mathbf{F}$ . In continuum theories,  $E_{ij} = E_{ij}(t, \{R_k\})$  and  $e_{ij} = e_{ij}(t, \{r_i\})$ —as well as  $S_{ij} = S_{ij}(t, \{R_k\})$  and  $s_{ij} = s_{ij}(t, \{r_i\})$ —are functions of coordinates, referring to the initial axes  $\{R_i\}$  or to the current axes  $\{r_i\}$ ; the mapping between the initial and current (i.e. the reference and deformed) coordinates near  $\{R_k\}$  and  $\{r_p\}$  is

$$F_{ij}(t, \{r_p\}, \{R_k\}) = \left. \frac{\partial r_i}{\partial R_j} \right|_{\{r_p\}, \{R_k\}}. \quad (5)$$

Typically,  $\{R_i\}$  and  $\{r_i\}$ —as well as the corresponding upper case and lower case tensorial functions of these variables—are referred to as ‘Lagrangian’ (or ‘material’) and ‘Eulerian’ (or ‘spatial’), respectively. Certain of these quantities have commonly accepted names:  $E_{ij}$  is the ‘Green–Lagrange’ strain,  $S_{ij}$  is the ‘second Piola–Kirchoff’ stress,  $s_{ij}$  is the ‘Cauchy’ stress and  $F_{ij}$  is the ‘deformation gradient’.

One obvious distinction between the material and spatial descriptions occurs in the time dependence of quantities defined with respect to the material or spatial coordinates. If  $X = X(t, R_i)$  is a function of the material coordinates, then  $(d/dt)X = (\partial/\partial t)X$ . However, if  $x = x(t, r_i)$  is a function of the spatial coordinates, then  $(d/dt)x = (\partial/\partial t)x + ((\partial/\partial t)r_i)(\partial/\partial r_i)x$ . A less obvious distinction is the difficulty of defining a boundary condition problem in the Eulerian frame, because of, for example, the inability of specifying the Cauchy stress  $s_{ij}$  on the (unknown) boundary of the deforming solid [11].

When deriving equations of motion for atomistic simulations, we typically view equation (5) as describing some interior region of a solid initially near  $\{r_p\}$  and  $\{R_k\}$ , which is sufficiently small so that variations in strain and temperature across the region may be ignored. Furthermore, assume that the atomic lattice near  $\{r_p\}$  and  $\{R_k\}$  can be described by sets of lattice vectors  $a_{ij}(t, \{r_p\})$  and  $A_{ij}(\{R_k\})$ , where  $A_{ij}(\{R_k\}) = a_{ij}(0, \{r_k\})$  and  $\{r_k(0)\} = \{R_k\}$ . The deformation gradient is then

$$F_{ij}(t, \{r_p\}, \{R_k\}) = a_{ik}(t, \{r_p\})A_{kj}^{-1}(\{R_k\}). \quad (6)$$

If we restrict our attention to just this one region and ignore ‘convective’ terms such as

$$\frac{\partial a_{ik}(t, \{r_p\})}{\partial r_i} \frac{\partial r_i}{\partial t}$$

we can drop  $\{r_p\}$  and  $\{R_k\}$ , and write

$$F_{ij}(t) = a_{ik}(t)A_{kj}^{-1}. \quad (7)$$

This is equivalent to viewing as equation (7) as describing the entire crystal undergoing a homogeneous deformation, but we prefer to retain the interpretation of equation (6) as describing a sufficiently small interior region of a solid. This latter view is suggestive of a ‘coarse-graining’ approach based on the size of the atomistic simulation itself, and is consistent with the common use of periodic boundary conditions in atomistic simulations. We adopt a continuum rather than atomistic viewpoint, and refer to such simulations as ‘homogeneous’ because there is only one deformation gradient (equation (7)) in the problem, even though the atomic configuration can become highly defective within the simulation cell.

The lattice vectors  $a_{ij}(t)$  can then serve as scaling factors to define the dimensionless coordinates of atom  $n$  through

$$r_i^{(n)}(t) = a_{ij}(t)q_j^{(n)}(t). \quad (8)$$

Here  $q_j^{(n)}$  is then the projection of atom  $n$  onto the  $i$ th lattice vector (i.e. the  $i$ th column of  $a_{ij}$ ), scaled by the length of the  $i$ th lattice vector. Equation (8) is typically the starting point for formulations of atomistic simulations with varying cell size and shape [1–4]. This scaling allows for the identification of microscopic quantities that have as their limits the corresponding macroscopic thermodynamic variables, for example the microscopic virial expression for the pressure and the thermodynamic pressure [12]. We will continue the microscopic analysis in the following section, but first we must obtain a few more definitions from continuum mechanics.

The nonlinear expression for the virtual work done in an infinitesimal deformation of the material is obtained by consideration of an infinitesimal deformation of a material already in a state of finite strain [10]. First define a quantity we shall call the ‘infinitesimal strain rate’:

$$\varepsilon_{kp} = \left( \frac{d}{dt} F_{kn} \right) F_{np}^{-1} = \left( \frac{d}{dt} a_{kn} \right) a_{np}^{-1} \quad (9)$$

and its symmetrized version:

$$\bar{\varepsilon}_{kp} = \frac{1}{2}[\varepsilon_{kp} + \varepsilon_{pk}]. \quad (10)$$

We call  $\varepsilon_{ij}$  an *infinitesimal* strain rate because from equation (9) we obtain the approximate relations  $F_{ij}(t + \lambda) \approx (\delta_{ik} + \lambda\varepsilon_{ik})F_{kj}(t)$ , or equivalently  $a_{ij}(t + \lambda) \approx (\delta_{ik} + \lambda\varepsilon_{ik})a_{kj}(t)$ , for some small time step  $\lambda$ ; rigid rotations of the system are eliminated using the symmetrized infinitesimal strain rate,  $\bar{\varepsilon}_{ij}$ . Note, in particular, that we are *not* decomposing the deformation gradient as  $F_{ij} = (\delta_{ij} + \epsilon_{ij})$  [13]; furthermore, the infinitesimal strain rate  $\varepsilon_{ij}$  remains well defined and equation (9) is satisfied regardless of the magnitude of the deformation. The time derivative of the Green–Lagrange strain can then be written in the simple form:

$$\frac{d}{dt} E_{ij} = F_{kj} \bar{\varepsilon}_{kp} F_{pi}. \quad (11)$$

We refer all strains and stresses to the reference system at time zero, and write the infinitesimal change in strain as  $\lambda[(d/dt)E_{ij}]$ , where  $\lambda$  is a small time step: the virtual work done in further deforming the system, already in a state of finite strain specified by  $F_{ij}$ , is then

$$|A|S_{ij} \left( \lambda \frac{d}{dt} E_{ij} \right) = |a|s_{kp}(\lambda \bar{\varepsilon}_{kp}) \quad (12)$$

where  $|A|$  and  $|a|$  are determinants of the lattice vectors at time zero and time  $t$ , and serve as a reference volumes. The dependence of the work on the strain history of the material

arises implicitly in equation (12) through the deformation gradient because we have computed the work required to further deform a material in a state of finite strain. This suggests the following equivalent forms for the ‘work term’, i.e. that part of the Legendre transformation used in switching between various thermodynamic potentials:

$$W_{\text{strain}} = -|A|(S_{ij} E_{ij}) = -|a|(s_{ij} e_{ij}). \quad (13)$$

We can make the Legendre transformations more formal by noting that  $\partial W_{\text{strain}}/\partial E_{ij} = |A|S_{ij}$ , and this guarantees the correct change of independent variables from  $E_{ij}$  to  $S_{ij}$  [14]. Thurston [15] summarized the standard thermodynamic potentials and their exact differentials for materials subjected to stress or to hydrostatic pressure. Our expressions are consistent with these except for the minor difference of using reference volumes.

The thermodynamic states subject to general stress are not only characterized by an entropy or temperature, and by a strain or stress, but also by a reference state with respect to which the strain is measured. Formally, how do we change from one reference state to another, and what is the thermodynamic significance of so doing? The answer involves an explicitly dissipative procedure which we will implement in accordance with the ‘principle of fading memory’ [16]. This is a formalization of the observation that it is not necessary to know the entire strain history of a material to determine its present state. Before describing the numerical technique for continuously changing reference states during a simulation, we must summarize the phenomenological treatment of mechanical dissipation in continuum mechanics.

As discussed by Lemaitre and Chaboche [8], the treatment of finite deformations often requires the introduction of ideas from *irreversible* thermodynamics, and this is also true in the present analysis. The goal is to break the problem into a reversible ‘elastic’ part and an irreversible ‘plastic’ part. While it is possible to write the infinitesimal strain as the sum of separate elastic and plastic strains, this is found to be impossible when finite strains are considered. Instead, the deformation gradient is written as the product of an elastic ( $\Gamma_{ij}$ ) and a plastic ( $\Theta_{ij}$ ) transformation as:

$$F_{ij} = \Gamma_{ij} \Theta_{ij}. \quad (14)$$

The interpretation of equation (14) assumes the existence in strain space of some ‘intermediate relaxed’ state; see the figure in [8, p 48]. This intermediate state has relaxed from the initial reference state through an irreversible plastic deformation; further small deformations of this intermediate relaxed state are reversible and elastic. The finite strain cannot be separated into elastic and plastic parts; however, the strain rate can be decomposed as a sum of plastic and elastic strain rates as

$$\varepsilon_{ij}(t) = \gamma_{ij}(t) + \varphi_{ij}(t) \quad (15)$$

where  $\gamma_{ij}(t)$  is the elastic strain rate and  $\varphi_{ij}(t)$  is the plastic strain rate. This naturally leads to expressions for the elastic and plastic powers as  $|a|s_{kp}\bar{\gamma}_{kp}$  and  $|a|s_{kp}\bar{\varphi}_{kp}$ , respectively. Explicit formulae for these quantities are given in the following section. The plastic power is necessarily positive,

$$|a|s_{kp}\bar{\varphi}_{kp} \geq 0 \quad (16)$$

and is indicative of the entropy produced during an irreversible process [8].

The difficulty of defining a boundary condition problem in the Eulerian frame, mentioned above, can manifest itself in atomistic simulations with periodic boundary conditions through the inability of predicting the Cauchy stress in the simulation after a finite deformation. In continuum analysis, one simply cannot know the boundary conditions for the appropriate boundary condition problem. In molecular dynamics simulations, one can always run trajectories; however, the internal virial pressure tensor does not, in general, balance the

negative of the Cauchy stress, but rather the effective external pressure [7]. This latter quantity contains a dependence on the strain history, and manifests itself through a splitting of the pressure fields during structural transformations; this splitting, in turn, is a consequence of the change in symmetry during the transformation. In a purely mechanical sense, the goal of the present analysis is to demonstrate how the formalism of irreversible thermodynamics of solids [8] may be incorporated into molecular dynamics simulations to ensure that the virial pressure tensor and the negative of the Cauchy stress (eventually) coincide. This allows for the greatest degree of consistency between the atomistic and continuum formulations, given the present ‘coarse-grained’ approach.

In the following section, we summarize the equations of motion used in the molecular dynamics simulations, and derive an explicit connection between the linear and nonlinear methods through the introduction of a relaxation time. This allows for evaluation of the elastic and plastic factors for the deformation gradient and the elastic and plastic strain rates. The next section contrasts linear, nonlinear and ‘relaxed’ simulations of a structural phase transformation, and demonstrates how the relaxed simulations connect the linear and nonlinear results. Agreement of the virial pressure with the negative of the Cauchy stress is demonstrated upon relaxation, and energy dissipation is observed during relaxation. Furthermore, the introduction of a strain threshold, above which relaxation is allowed, will be seen to further bring the microscopic and macroscopic analyses into conformity. Finally, the use of Nosé–Hoover chains to thermostat the lattice degrees of freedom is shown to significantly improve the treatment of temperature in simulations of structural transformations.

## 2. Theory

Begin with the Hamiltonian written in scaled time and using scaled momenta [17, 18]:

$$\begin{aligned} H = & \left[ \left( \sum_{n=1}^N \frac{p_i^{(n)\prime} g_{ij}^{-1} p_j^{(n)\prime}}{2\mu_n s^2} \right) + \frac{1}{2} \sum_{n=1}^N \sum_{m \neq n}^N \Phi\{r_{nm}\} \right] + \left[ \frac{1}{2} \frac{\pi^2}{Q} + (f_{\text{atom}} k_B T) \ln(s) \right] \\ & + (N_1 N_2 N_3) \left[ \frac{p'_{ij} p'_{ij}}{2W(s_1)^2} + W_{\text{strain}} \right] + \left[ \frac{1}{2} \frac{(\pi_1)^2}{Q_1} + (f_{\text{cell}} k_B T) \ln(s_1) \right] \\ & + \sum_{n=2}^{N_{\text{chain}}} \left[ \frac{1}{2} \frac{(\pi_n)^2}{Q_n} + (k_B T) \ln(s_n) \right]. \end{aligned} \quad (17)$$

The negative sign in equation (13) is consistent with the sign conventions for pressure and stress and for measuring the work done by the atomic system on its surroundings. The relation between the scaled and physical atomic momenta and velocities is  $\mu_n^{-1} g_{ij}^{-1} s^{-1} p_j^{(n)\prime} = \mu_n^{-1} g_{ij}^{-1} p_j^{(n)} = v_i^{(n)}$ . Similarly, the scaled and physical momenta and velocities for the lattice vectors are related by  $W^{-1} s_1^{-1} p'_{ij} = W^{-1} p_{ij} = v_{ij}$ . Here  $s$  is the Nosé time scale that thermostats the atomic degrees of freedom and  $s_1$  is the first time scale in the Nosé–Hoover chain that thermostats the cell degrees of freedom. The subscripted Nosé time scales  $s_n$  and their conjugate momenta  $\pi_n$ , constitute the Nosé–Hoover chain. Following the usual arguments [1, 9, 17, 18], equation (17) may be shown to imply the following partition function for the isothermal-isostress ensemble:

$$\begin{aligned} \Xi(Ns_{ij}T) = c \int d\{q_i^{(n)}\} \int d\{p_i^{(n)}\} \int d\{a_{ij}\} \exp \frac{-1}{k_B T} \left[ \left( \sum_{n=1}^N \frac{1}{2\mu_n} p_i^{(n)} g_{ij}^{-1} p_j^{(n)} \right) \right. \\ \left. + \frac{1}{2} \sum_{n=1}^N \sum_{m \neq n}^N \Phi\{r_{nm}\} + W_{\text{strain}} \right] \end{aligned} \quad (18)$$

where  $c$  is a normalization constant, and  $\int d\{q_i^{(n)}\}$  implies integration over all components of all the dimensionless atomic coordinates,  $q_i^{(n)} = a_{ij}^{-1} r_j^{(n)}$ , etc. Here, for simplicity, we assume the interatomic potential  $\Phi\{r_{nm}\}$  depends only on the interatomic distance,  $r_{nm} = \sqrt{q_i^{(n)} g_{ij} q_j^{(n)}}$ , where the metric is  $g_{ij} = a_{ki} a_{kj}$ .

Previously, we have used equation (17) with equation (13) to derive the equations of motion based on the dimensionless atomic coordinates and the deformation gradient equation (7). We will re-write the equations here in a different form, using a slightly different notation. We do so for two reasons. First, we employ Nosé–Hoover chains [9] to thermostat the cell degrees of freedom; this will be seen to be of practical importance in the following section. Second, we will re-write the cell dynamics in a symmetrical form that allows for a closer connection to continuum mechanics and a more intuitive discussion of the source of the nonlinearity in the problem.

The equations governing the atoms are as given before [7]:

$$\frac{d}{dt} v_i^{(n)} = \frac{1}{\mu_n} F_i^{(n)} - (\xi \delta_{ij} + \omega_{ij}) v_j^{(n)} \quad (19)$$

where the  $i$ th component of force on atom  $n$  is

$$\frac{1}{\mu_n} F_i^{(n)} = \frac{1}{\mu_n} \sum_{m \neq n} \left( \frac{-1}{r_{nm}} \frac{d\Phi}{dr_{nm}} \right) q_i^{(nm)}$$

$q_i^{(nm)}$  is the dimensionless nearest image difference between atoms  $n$  and  $m$ , and the atomic velocities and momenta in physical time are related by  $v_i^{(n)} = \mu_n^{-1} g_{ij}^{-1} p_j^{(n)}$ . The Coriolis frictional term can be written as  $\omega_{ij} = a_{ip}^{-1} (\varepsilon_{kp} + \varepsilon_{pk}) a_{kj}$ , where  $\varepsilon_{ij}$  is the infinitesimal strain rate defined in equation (9). Because  $\{q_i^{(n)}\}$  are dimensionless,  $\xi$  and  $\{v_i^{(n)}\}$  have units of time<sup>-1</sup> and  $\{\mu_n^{-1} F_i^{(n)}\}$  and  $\omega_{ij}$  have units of time<sup>-2</sup>.

We include only atomic degrees of freedom in the feedback equation for the Nosé–Hoover thermostat [17–19]:

$$\frac{d\xi}{dt} = \frac{1}{Q_{\text{atom}}} \left[ \sum_{n=1}^N \mu_n (v_i^{(n)} g_{ij} v_j^{(n)}) - f_{\text{atom}} k_B T \right] \quad (20)$$

where  $f_{\text{atom}} = 3N - 3$  is the number of atomic degrees of freedom, assuming elimination of the centre-of-mass motion, for the  $N$ -atom system. The fictitious mass  $Q_{\text{atom}}$  has units of energy time.

The cell dynamics are then given by [7]:

$$\frac{d}{dt} v_{ij} = \frac{1}{W} (P_{ik} - \Omega_{ik}) |a| F_{jk}^{-1} - \xi_1 v_{ij} \quad (21)$$

where the velocity and momentum of the deformation gradient are related by  $(d/dt)F_{ij} = v_{ij} = W^{-1} p_{ij}$  and  $\xi_1$  is the first friction in the Nosé–Hoover chain [9]. We have used the deformation gradient equation (7) as a canonical variable in the derivation in order to insure modular invariance [7, 13], i.e. to make the kinetic term  $[1/(2W)] p_{ij} p_{ij}$  in equation (17) invariant to the arbitrary choice of lattice vectors  $a_{ij}$ . The deformation gradient velocities  $\{v_{ij}\}$  and Nosé–Hoover friction  $\xi_1$  have units of time<sup>-1</sup>,  $P_{ij}$  and  $\Omega_{ij}$  have units of pressure, and the fictitious mass  $W$  has units of mass length<sup>2</sup>. The external pressure,  $\Omega_{ij}$ , will be described below.

The dynamics for the  $N_{\text{chain}}$  links in the chain are then given by the equations [9]:

$$\frac{d}{dt} \xi_1 = \frac{1}{Q_1} [W(\varepsilon_{ik} G_{kp} \varepsilon_{ip}) - f_{\text{cell}} k_B T] - \xi_1 \xi_2 \quad (22)$$

$$\frac{d}{dt}\xi_n = \frac{1}{Q_n}[Q_{n-1}(\xi_{n-1})^2 - k_B T] - \xi_n \xi_{n+1} \quad (23)$$

$$\frac{d}{dt}\xi_{N_{\text{chain}}} = \frac{1}{Q_{N_{\text{chain}}}}[Q_{N_{\text{chain}}-1}(\xi_{N_{\text{chain}}-1})^2 - k_B T]. \quad (24)$$

The fictitious masses  $Q_n$  have units of energy time. The number of degrees of freedom for the cell dynamics, after elimination of rigid body rotations [7], is  $f_{\text{cell}} = 6$ .

We now re-write equation (21) by using the infinitesimal strain rate, equation (9), to obtain:

$$\frac{d}{dt}\varepsilon_{ij} = \frac{1}{W}[P_{ik} - \Omega_{ik}]|a|G_{kj}^{-1} - \varepsilon_{ik}\varepsilon_{kj} - \xi_1\varepsilon_{ij} \quad (25)$$

where

$$G_{ij} = F_{ik}F_{jk}. \quad (26)$$

We are free to symmetrize  $\varepsilon_{ij}$  at every time step, and thus eliminate rigid rotations of the system from the dynamics in equation (25). Also, equation (25) is quite close in form to the equations of Wentzcovitch [13]; the only differences arise in the expressions for  $\Omega_{ik}$ . The choice of the deformation gradient elements as canonical variables assures the modular invariance [13] of equation (25), regardless of the magnitude of the deformation [7], but this is a separate question from the inclusion of nonlinear effects. It might appear that dependence on the strain history has been erased from the problem by switching variables from  $F_{ij}$  to  $\varepsilon_{ij}$ , but such is not the case; equation (25) includes the strain history through  $G_{ij}$ , and most importantly, through  $\Omega_{ij}$ .

The effective external pressure  $\Omega_{ij}$  arises naturally in canonical derivations using equation (13) in equation (17) through the derivative

$$-\frac{\partial W_{\text{strain}}}{\partial F_{ij}} = \Omega_{ik}|a|F_{jk}^{-1} \quad (27)$$

which yields

$$\Omega_{ij} = -[\delta_{ij}(s_{nm}e_{nm}) + (F_{ki}^{-1}F_{kp}^{-1})s_{pj}]. \quad (28)$$

If one uses the lattice vectors  $a_{ij}$  as dynamical variables and equation (13), one obtains  $-(\partial/\partial a_{ij})W_{\text{strain}} = \Omega_{ik}h_{kj}$ , where  $h_{ij} = |a|a_{ji}^{-1}$  is the surface area tensor;  $-(\partial/\partial a_{ij})W_{\text{strain}}$  then gives the components of force acting on the three unique surfaces of the crystalline cell  $a_{ij}$ . In contrast, linear simulations [3] use the external pressure

$$\Omega_{ij} = -s_{ij}. \quad (29)$$

We can obtain equation (29) from equation (28) by demanding that  $F_{ij} = \delta_{ij}$ , and hence  $e_{ij} = 0$ ; this amounts to setting the reference lattice equal to the current lattice,  $A_{ij} = a_{ij}(t)$  [3]. If one uses the lattice vectors as canonical variables, one can first derive a conservative set of equations and then set  $F_{ij} = \delta_{ij}$  [3], despite the fact that this implies  $W_{\text{strain}} = 0$  identically. Similarly, one can use either lattice vectors or elements of the deformation gradient as canonical variables and derive conservative equations of motion [7]; retention of a constant reference lattice then yields the nonlinear simulation. The distinction between the ‘linear’ and ‘nonlinear’ simulations thus do *not* arise from any linear approximation to the total strain of the system, nor from any linear approximation to the work term  $W_{\text{strain}}$  used to derive the equations governing the simulation. The distinction between the ‘linear’ and ‘nonlinear’ simulations is *not* perturbative. Rather, the difference lies in the specification of the stress exerted on the system by the reservoir; the term ‘nonlinear’ implies the applied pressure depends on the strain history of the system, while the term ‘linear’ implies the applied pressure has no such dependence. The only term in equation (17) where strain history-dependence can arise is in

$W_{\text{strain}}$ . Comparing the treatment of stress in various simulations can be confusing because of the different possible definitions for stress, strain and pressure; for example, a constant diagonal part of the stress matrix is often treated as a ‘hydrostatic’ contribution [3]. However, such distinctions should not cloud the fundamental source of nonlinearity, which is inclusion of a dependence upon the strain history of the reservoir.

While the procedure employed in deriving the standard Parrinello–Rahman equations is *ad hoc*, it is nonetheless very useful. It guarantees that the negative of the Cauchy stress balances the virial pressure tensor. The underlying assumption of an infinitely fast relaxation time of the stress reservoir is a good approximation when the experiment being simulated is that of a small crystal undergoing a finite homogeneous deformation while suspended in a fluid in a diamond anvil cell. However, it is not a good approximation when a small internal region of a crystal undergoes a phase transformation. In this case, the nonlinear equations, which assume an infinitely long relaxation time because of the constant reference lattice and a dependence on the strain history, offers an alternative. The problem with the nonlinear formulation is that it retains a relatively large amount of strain energy. We will now dissipate this strain energy in a manner consistent with the nonlinear continuum formulation of the irreversible thermodynamics of solids [8].

Begin by assuming a slowly varying time dependence in the reference lattice vectors  $A_{ij}$ . Further, assume that this time dependence is sufficiently slow so that we may take it to be constant when deriving the equations of motion for all the atomic, lattice and thermostating variables. It should be emphasized that the equilibrium condition expressed by the partition function, equation (18), is about all we can rigorously say about the dynamics. When incorporating elements of the irreversible thermodynamics of solids, we try to build on this by assuming the time dependence of the reference lattice to be sufficiently slowly varying so that the equations derived under the equilibrium assumptions remain valid. Write the reference lattice vectors in this case as

$$A_{ij}(t) = \int_{t-w}^t dt' \Psi(t' - t) a_{ij}(t') = \{\tau_{\text{relax}}[1 - \exp(-w/\tau_{\text{relax}})]\}^{-1} \times \int_{t-w}^t dt' \exp[(t' - t)/\tau_{\text{relax}}] a_{ij}(t'). \quad (30)$$

In practice, we can guarantee that the reference lattice is sufficiently slowly varying by choosing an appropriately long relaxation time  $\tau_{\text{relax}}$  and monitoring the conserved energy of the simulation. The time  $w$  in equation (30) provides a ‘window’ over which we average the lattice vectors to obtain the new reference lattice at time  $t$ , and the exponential function in the integrand weights the most recent sets of lattice vectors most heavily; those lattice vectors farther in the past than the window  $w$  are not included in the average. In this manner, the system ‘forgets’ its original shape. Adopting the language of Truesdell and Noll [16], we call  $\Psi(t' - t)$  an ‘obliterator’, and quantities which employ equation (30) rather than  $A_{ij}(0)$  we shall refer to as having been ‘obliterated’.

The time derivative of the reference lattice vectors is

$$\frac{d}{dt} A_{ij}(t) = \{\tau_{\text{relax}}[1 - \exp(-w/\tau_{\text{relax}})]\}^{-1} [a_{ij}(t) - \exp[-w/\tau_{\text{relax}}] a_{ij}(t - w)] - \frac{1}{\tau_{\text{relax}}} A_{ij}(t). \quad (31)$$

We can then define a ‘reference’ deformation gradient for  $A_{ij}(t)$ , using  $A_{ij}(0)$  as the reference state:

$$\Theta_{ij}(t) = A_{ik}(t) A_{kj}^{-1}(0) \quad (32)$$

and an ‘obligated’ deformation gradient for  $A_{ij}(t)$ , using  $A_{ij}(t)$  as the reference state:

$$\Gamma_{ij}(t) = a_{ik}(t)A_{kj}^{-1}(t). \quad (33)$$

Obviously, the ‘complete’ deformation gradient can be recovered as

$$F_{ij}(t) = \Gamma_{ik}(t)\Theta_{kj}(t) \quad (34)$$

in agreement with equation (14). By construction, the time dependence of  $\Theta_{ij}(t)$  is slow compared to that of  $\Gamma_{ij}(t)$  and  $F_{ij}(t)$ . The notation here implies identification of  $\Gamma_{ij}(t)$  and  $\Theta_{ij}(t)$  with the elastic and plastic factors of the deformation gradient as in equation (14). We will continue this analogy, and postpone a discussion until after the numerical results have been presented.

We can define an infinitesimal strain rate for  $A_{ij}(t)$  by analogy with equation (9) as

$$\vartheta_{ij}(t) = \left( \frac{dA_{ik}(t)}{dt} \right) A_{kj}^{-1}(t) = \left( \frac{d}{dt} \Theta(t) \right) \Theta_{kj}^{-1}(t) \quad (35)$$

and an infinitesimal strain rate for  $\Gamma_{ik}(t)$  as

$$\gamma_{ij}(t) = \left( \frac{d}{dt} \Gamma_{ik}(t) \right) \Gamma_{kj}^{-1}(t). \quad (36)$$

Then defining

$$\varphi_{ij}(t) = \Gamma_{ik}(t)\vartheta_{kp}(t)\Gamma_{pj}^{-1}(t) \quad (37)$$

we can obtain the obligated strain rate as

$$\gamma_{ij}(t) = \varepsilon_{ij}(t) - \varphi_{ij}(t) \quad (38)$$

where the total strain rate  $\varepsilon_{ij}(t)$  is given by equation (9). Rearrangement of equation (38) then yields equation (15).

We can define the obligated Green–Lagrange strain

$$E_{ij}^{\Gamma} = \frac{1}{2}(\Gamma_{ki}\Gamma_{kj} - \delta_{ij}) \quad (39)$$

and an obligated work term,

$$W_{\text{strain}}^{\Gamma} = -|A|(S_{ij}E_{ij}^{\Gamma}) \quad (40)$$

etc, and re-derive all the molecular dynamics results under the assumption of a slow time variation of the reference lattice vectors,  $A_{ik}(t)$ . The result would be the same equations quoted above, but with the understanding that the obligated quantities are used, for example

$$\frac{d}{dt} \gamma_{ij} = \frac{1}{W} (P_{ik} - \Omega_{ik}^{\Gamma}) |a| G_{kj}^{\Gamma-1} - \gamma_{ik} \gamma_{kj} - \xi_1 \gamma_{ij} \quad (41)$$

and

$$\varepsilon_{ij}^{\Gamma}(t) = \gamma_{ij}(t) \quad (42)$$

where

$$G_{ij}^{\Gamma} = \Gamma_{ik}\Gamma_{jk} \quad (43)$$

$$\Omega_{ij}^{\Gamma} = -[\delta_{ij}(s_{nm}e_{nm}^{\Gamma}) + (\Gamma_{ki}^{-1}\Gamma_{kj}^{-1})s_{pj}] \quad (44)$$

$$e_{ij}^{\Gamma} = \frac{1}{2}(\delta_{ij} - \Gamma_{ki}^{-1}\Gamma_{kj}^{-1}) \quad (45)$$

etc. The elastic and plastic powers can then be written as:

$$|a|s_{kp}\bar{\gamma}_{kp} \quad (46)$$

$$|a|s_{kp}\bar{\varphi}_{kp}. \quad (47)$$

The use of the ‘obligated’ reference lattice is thus seen to yield a deformation gradient that factors into the product of two transformations, a strain rate that decomposes into the sum of two rates and an ‘intermediate relaxed’ reference state described by the obligated reference lattice vectors  $A_{ij}(t)$ , all in agreement with the phenomenological equations of continuum mechanics including mechanical dissipation. We have identified the ‘elastic’ and ‘plastic’ quantities according to whether or not their time dependence is due to that of the reference lattice vectors; i.e. it is the variation of some of the parameters that characterize the equilibrium ensemble that gives rise to the ‘plastic’ quantities. But does this *mathematical* identification of the plastic and elastic strain rates make sense *physically*? We will next compare linear and nonlinear simulations with relaxed simulations employing the obligator, and show that the mathematical identification of the plastic strain rate may be made to conform to physical ideas of plasticity through the inclusion of a ‘strain threshold’ above which relaxation is allowed to take place.

### 3. Numerical results

We have performed a series of linear, nonlinear and obligated simulations of a bcc to close packed structural transformation, using a smooth, short-ranged, two-parameter pair potential employed in previous tests of simulation methodology [5–7]. The potential yields a bcc ground state at low density, and nearly degenerate fcc and hcp ground states at higher density; the imposed temperature is kept sufficiently low so that the metastable bcc phase remains intact for times comparable to that of the simulation. Details of the potential can be found in [7]. The simulations consist of starting in the bcc state, increasing the applied pressure  $P$ , where ( $-s_{ij} = P\delta_{ij}$ ), and observing the transformation. The only differences between the various simulations described below is the use of either the linear (equation (29)), nonlinear (equation (28)) or obligated (equation (44)) expressions for the external pressure, and equations (26) or (43). Integrations were performed over 180 ps, the number of atoms in each case was 720, the temperature was thermostatted at 50 K and the imposed pressure was varied from 0 to 5.25 GPa.

Four basic simulations were performed: a linear Parrinello–Rahman simulation with no memory and a single Nosé thermostat for both the atoms and lattice vectors; a nonlinear simulation with perfect memory, a Nosé thermostat for the atoms and a separate Nosé–Hoover chain having nine links for the lattice vectors; an obligated simulation having a relaxation time of  $\tau_{\text{relax}} = 60$  ps, a Nosé thermostat for the atoms and a separate Nosé–Hoover chain having one link for the lattice vectors; and an obligated simulation having a relaxation time of  $\tau_{\text{relax}} = 60$  ps, a Nosé thermostat for the atoms and a separate Nosé–Hoover chain having nine links for the lattice vectors. The simulation using only a single link in the Nosé–Hoover chain is equivalent to simply using separate Nosé thermostats for the atomic and lattice degrees of freedom. Selected trajectories for these simulations are shown in figures 1–6.

The most dramatic differences between the linear and nonlinear simulations are seen in the trajectories of the virial and external pressures, shown in figures 1 and 2. In the linear simulation, the diagonal elements of virial pressure  $P_{kk}$  fluctuate about  $\Omega_{kk} = P$ . (The off-diagonal elements fluctuate about zero.) In the nonlinear simulation, the diagonal elements of virial pressure  $P_{ij}$  fluctuate about  $\Omega_{ij}$ , which in turn depend upon the strain history of the system. The diagonal elements of  $\Omega_{ij}$  are initially degenerate, but are seen to ‘bifurcate’ when the transformation occurs, reflecting the change in symmetry that occurs when the new close packed phase finds itself in the old bcc matrix. The virial and external pressures in the ‘obligated’ simulations are seen to relax from the nonlinear to the linear results over the time  $\tau_{\text{relax}}$ , and thus provide a connection between the linear (Parrinello–Rahman) and nonlinear

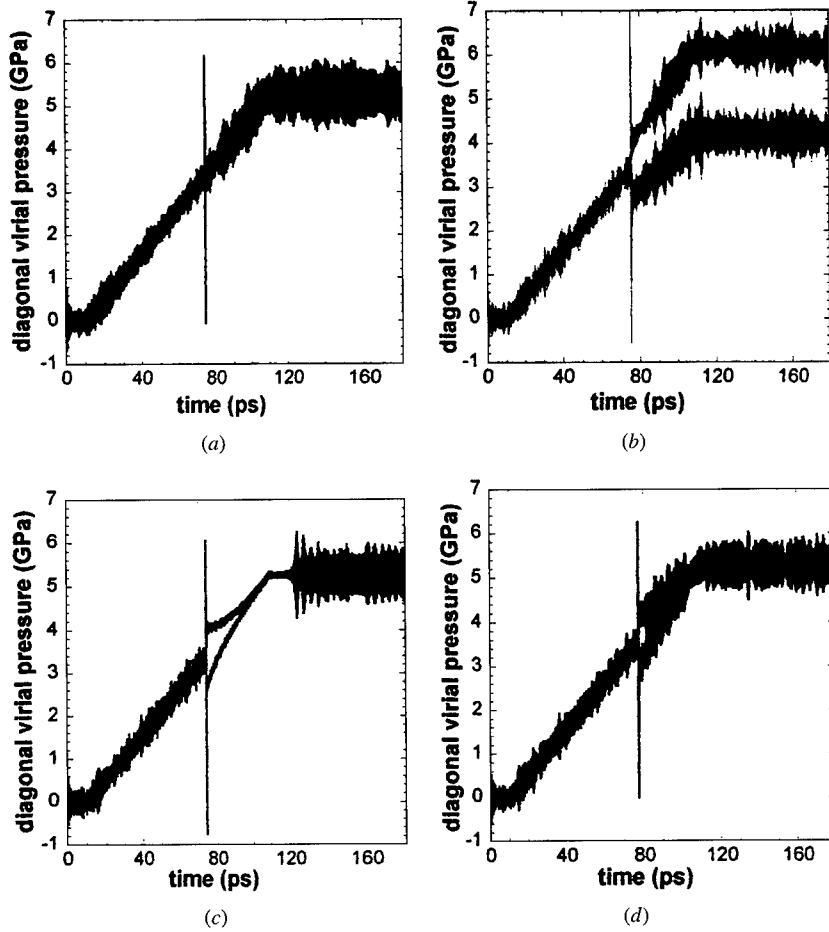


**Figure 1.** Diagonal elements of virial pressure ( $P_{ij}$ ) in GPa against the simulation time: (a) linear simulation with no memory and a single Nosé thermostat for the atoms and lattice vectors; (b) nonlinear simulation with perfect memory, a Nosé thermostat for the atoms and a Nosé–Hoover chain with nine links for the lattice vectors; (c) oblivious simulation with a relaxation time of  $\tau_{\text{relax}} = 60$  ps, a Nosé thermostat for the atoms and a Nosé–Hoover chain with one link for the lattice vectors; (d) oblivious simulation with a relaxation time of  $\tau_{\text{relax}} = 60$  ps, a Nosé thermostat for the atoms and a Nosé–Hoover chain with nine links for the lattice vectors.

formalisms. In all cases, the virial pressure  $P_{ij}$  is seen to fluctuate about the external pressure  $\Omega_{ij}$  as defined above, in accordance with the (nonlinear) virial theorem [7].

The plastic and elastic powers per atom, and their integrals, are shown in figures 3 and 4. The elastic powers oscillate about zero in each case; however, their integrals reveal small negative values, consistent with the crystal undergoing compression. The plastic powers show a sharp increase at the time of the phase transformation, implying the large amount of strain energy being dissipated after the finite homogeneous deformation of the original lattice; this is confirmed by their integrals. The fluctuations of the (rapid) elastic powers are much larger in magnitude than those of the (slow) plastic powers. In the simulation with separate Nosé thermostats, the fluctuations in the elastic power (figure 3(c)) show a dramatic decrease immediately after the transformation. To understand this behaviour, we examine the kinetic temperature in the simulations.

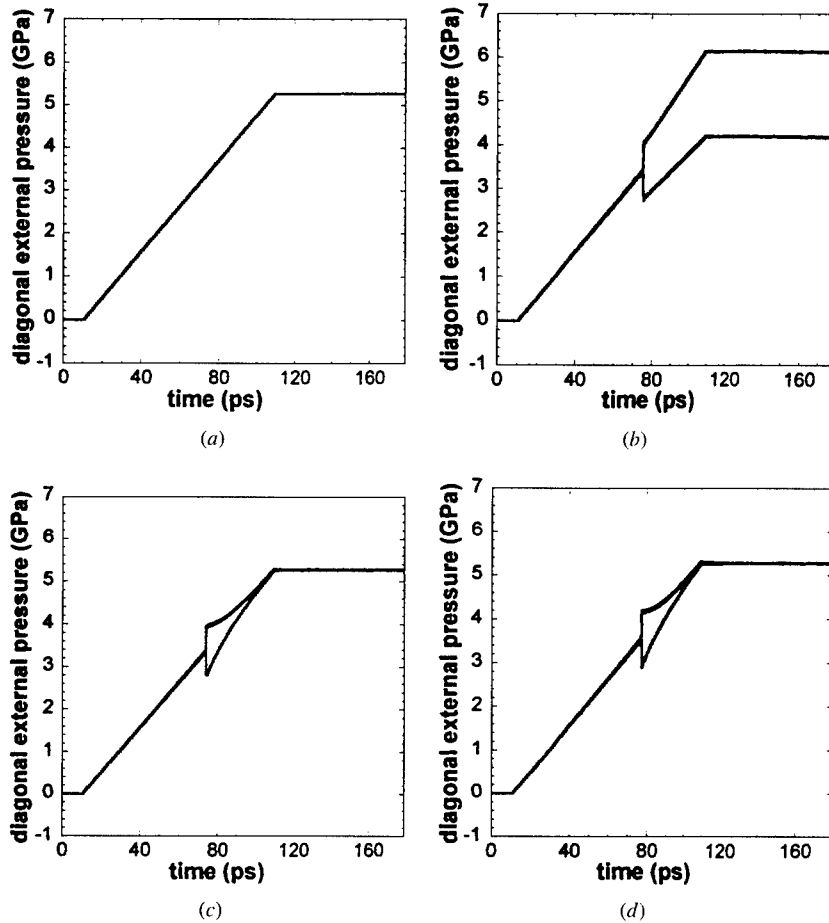


**Figure 2.** Diagonal elements of external pressure ( $\Omega_{ij}$ ) in GPa against the simulation time: (a) linear simulation with no memory and a single Nosé thermostat for the atoms and lattice vectors; (b) nonlinear simulation with perfect memory, a Nosé thermostat for the atoms and a Nosé–Hoover chain with nine links for the lattice vectors; (c) oblivious simulation with a relaxation time of  $\tau_{\text{relax}} = 60$  ps, a Nosé thermostat for the atoms and a Nosé–Hoover chain with one link for the lattice vectors; (d) oblivious simulation with a relaxation time of  $\tau_{\text{relax}} = 60$  ps, a Nosé thermostat for the atoms and a Nosé–Hoover chain with nine links for the lattice vectors.

The atomic and lattice vector kinetic temperatures are shown in figures 5 and 6. Not much difference can be discerned between the various atomic kinetic temperatures, however the lattice vector kinetic temperatures show distinct differences. After suppression of rigid rotations of the simulation, there are only six degrees of freedom remaining in the lattice vector dynamics; it is therefore to be expected that the fluctuations in kinetic temperature should be greater than those observed in the atomic kinetic temperature. Furthermore, in each simulation, the lattice vector kinetic temperature is seen to ‘spike’ at the time of the transformation. This is due to the large and rapid collective motion of the lattice vectors executing a Bain deformation, and is unavoidable. However, this can cause trouble for the thermostats. In the simulation with no memory and only a single Nosé thermostat, figure 6(a), the nature of the fluctuations changes after the phase transformation, substantially increasing in wavelength. This suggests that the single Nosé thermostat has trouble partitioning energy between the atoms and the lattice vectors, when the lattice vectors alone receive a substantial

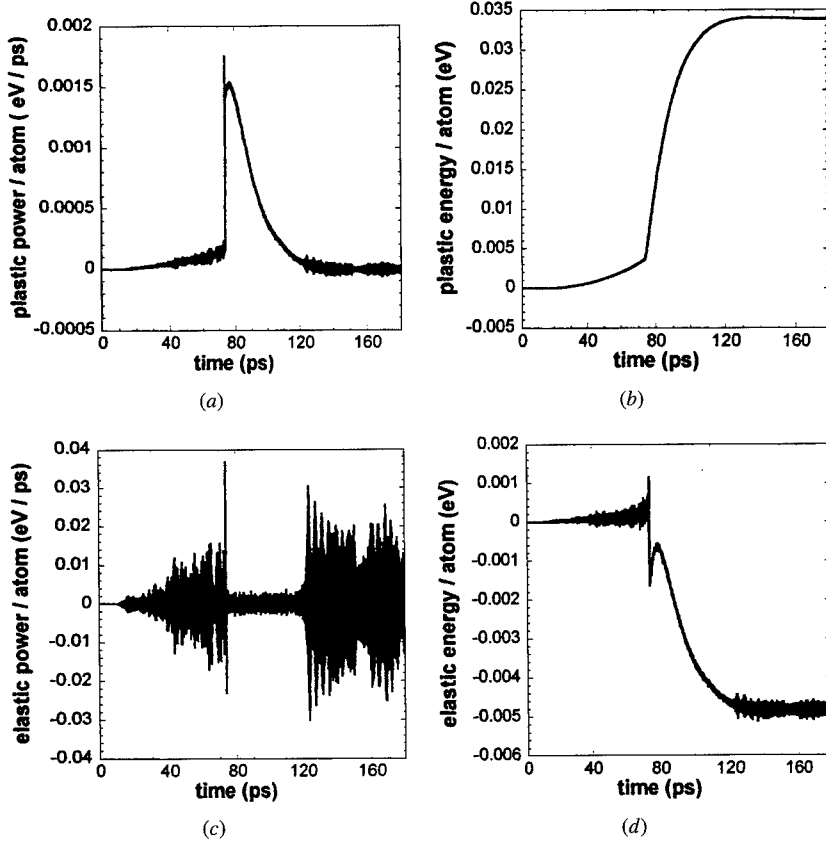


**Figure 3.** Obliterated simulation with a relaxation time of  $\tau_{\text{relax}} = 60$  ps, a Nosé thermostat for the atoms and a Nosé–Hoover chain with one link for the lattice vector: (a) plastic power per atom, equation (47) (in  $\text{eV ps}^{-1}$ ); (b) integrated plastic power per atom (in electronvolts); (c) elastic power per atom, equation (46) (in  $\text{eV ps}^{-1}$ ); and (d) integrated elastic power per atom (in electronvolts).

increase of kinetic energy during the phase transformation. If one attempts to correct this by using separate Nosé thermostats for the atoms and the lattice vectors, figure 6(c), the situation in fact becomes worse. The single Nosé thermostat drastically overcompensates, suppressing fluctuations in the kinetic temperature as well as the virial pressure, figure 1(c), and the plastic power, figure 3(c).

These difficulties raise serious questions regarding the presumed ergodicity of the lattice vector trajectories. The use of a separate Nosé–Hoover chain to thermostat the lattice vectors is seen to eliminate these problems. This serves as a specific application of the original arguments of Martyna *et al* [9] regarding the use of Nosé–Hoover chains to promote ergodicity. However, consideration of the trajectories for the plastic power suggest that a different problem remains. The simulations can be viewed as occurring in three steps. First, the initial bcc crystal suffers a series of small deformations; there are essentially no difference between the pressure fields in the linear, nonlinear and obliterated simulations. However, the obliterated simulations slowly dissipate energy as the deformations accumulate. Second, the structural transformation occurs; here, the differences between the simulations become manifest in the pressure fields. Third, the final close packed crystal suffers a series of small deformations; differences remain between the linear and nonlinear simulations, and the obliterated simulations relax from the latter to the former.

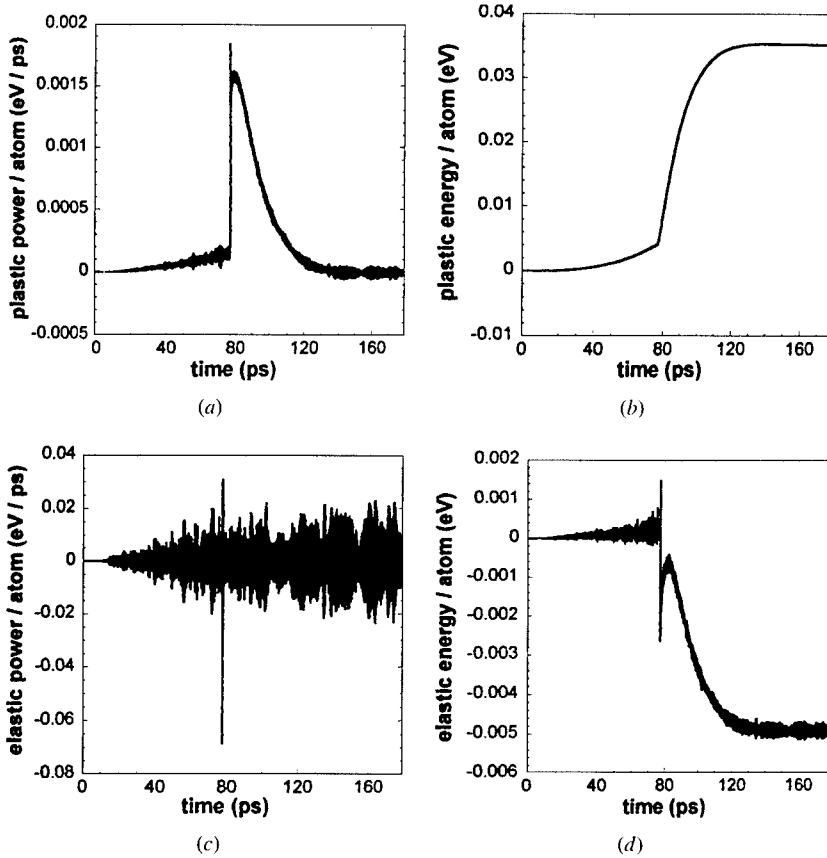


**Figure 4.** Obliviated simulation with a relaxation time of  $\tau_{\text{relax}} = 60$  ps, a Nosé thermostat for the atoms and a Nosé–Hoover chain with nine links for the lattice vectors: (a) plastic power per atom, equation (47) (in  $\text{eV ps}^{-1}$ ); (b) integrated plastic power per atom (in electronvolts); (c) elastic power per atom, equation (46) (in  $\text{eV ps}^{-1}$ ); and (d) integrated elastic power per atom (in electronvolts).

The remaining problem is that energy is dissipated as the crystal suffers a series of infinitesimal deformations. While this is consistent with our definition of the obliterated reference lattice, it occurs in a regime we would consider to be elastic. An approximate solution is to only allow for relaxation after the lattice has changed volume by some specified percentage. We have therefore performed an obliterated simulation having a relaxation time of  $\tau_{\text{relax}} = 60$  ps, a Nosé thermostat for the atoms, a separate Nosé–Hoover chain having nine links for the lattice vectors and a strain threshold of  $\delta_{\text{relax}} = 0.05$ . Trajectories for the pressures and temperatures are shown in figure 7, and trajectories for the plastic and elastic powers are shown in figure 8. The plastic power and energy reveal that now energy is dissipated only after the finite deformation associated with the phase transformation, and the temperature equilibration is reasonable, however a small difference remains between the ‘bifurcated’ branches of the internal and external pressures due to the incomplete relaxation caused by the threshold.

#### 4. Summary

In summary, the linear and nonlinear methods simulate distinct equilibrium ensembles; this distinction arises from the different interaction between the ‘system’ and the ‘reservoir’. In

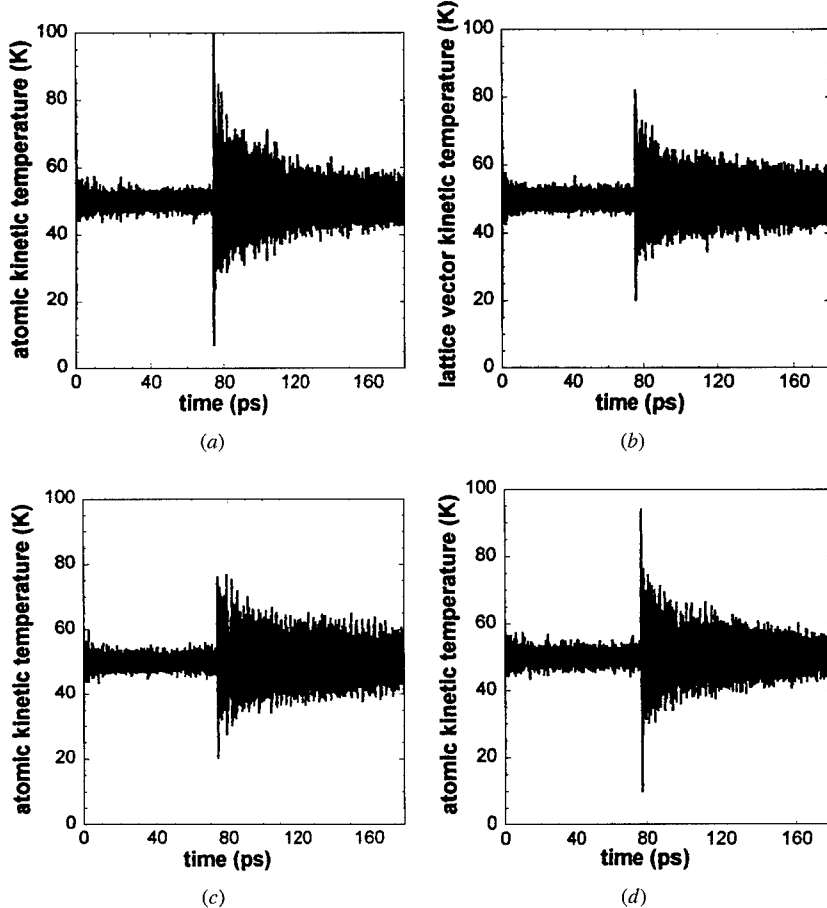


**Figure 5.** Atomic kinetic temperature (K): (a) linear simulation with no memory and a single Nosé thermostat for the atoms and lattice vectors; (b) nonlinear simulation with perfect memory, a Nosé thermostat for the atoms and a Nosé–Hoover chain with nine links for the lattice vectors; (c) obliterated simulation with a relaxation time of  $\tau_{\text{relax}} = 60$  ps, a Nosé thermostat for the atoms and a Nosé–Hoover chain with one link for the lattice vectors; and (d) obliterated simulation with a relaxation time of  $\tau_{\text{relax}} = 60$  ps, a Nosé thermostat for the atoms and a Nosé–Hoover chain with nine links for the lattice vectors.

the linear case, this interaction is a one-way street; the reservoir proposes, and the simulation disposes. In the nonlinear case, the situation is more democratic, and more complicated. While each ensemble may be characterized by the total number of particles ( $N$ ), the stress ( $s_{ij}$ ) and the temperature ( $T$ ), the meaning of the stress is slightly different in each case. In the linear case, the atoms and lattice vectors arrange themselves so that the virial pressure dynamically balances the (negative) Cauchy stress  $-s_{ij}$  at all times. In the nonlinear case, the virial pressure balances the effective external pressure  $\Omega_{ij}(t)$ , which can change upon a finite deformation of the system. This is consistent with the view that we cannot specify the stress on the (unknown) surface of the deforming body; in the nonlinear case, one must view  $s_{ij}$  as the stress that would be balanced in the absence of a deformation of the system. In the absence of any finite deformation, this distinction disappears and the effective external pressure fluctuates about the negative Cauchy stress. Physically, linear simulations are most appropriate when the entire crystal is undergoing a homogeneous deformation, for

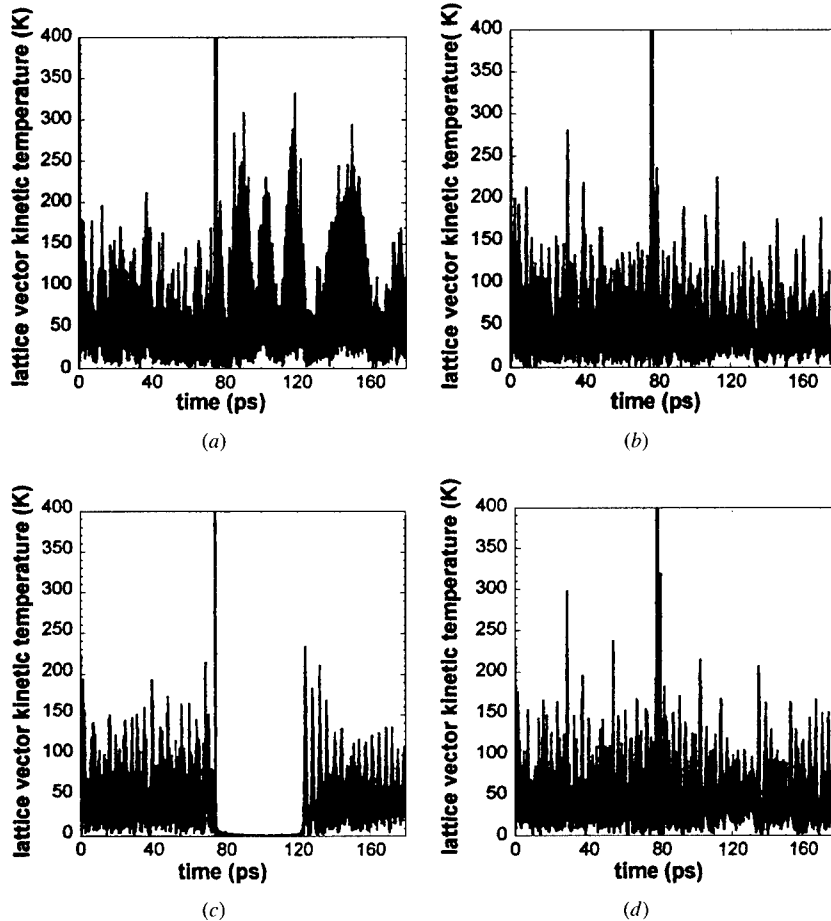


**Figure 6.** Lattice vector kinetic temperature (K): (a) linear simulation with no memory and a single Nosé thermostat for the atoms and lattice vectors; (b) nonlinear simulation with perfect memory, a Nosé thermostat for the atoms and a Nosé–Hoover chain with nine links for the lattice vectors; (c) obliterated simulation with a relaxation time of  $\tau_{\text{relax}} = 60$  ps, a Nosé thermostat for the atoms and a Nosé–Hoover chain with one link for the lattice vectors; and (d) obliterated simulation with a relaxation time of  $\tau_{\text{relax}} = 60$  ps, a Nosé thermostat for the atoms and a Nosé–Hoover chain with nine links for the lattice vectors.

example during the hydrostatic compression of a small crystal in a diamond anvil cell. In this case the stress reservoir is a fluid, which can relax very rapidly to accommodate the deformation of the sample. By contrast, nonlinear simulations are more appropriate when only a portion of the material is transforming and the new phase must do work on the surrounding matrix to include itself. Here the stress reservoir represents the matrix; and this might or might not relax on a sufficiently rapid time scale for the linear simulation to remain valid. For small deformations, one can imagine that an acoustic wave carries away the energy required to deform the matrix; the linear and nonlinear simulations become equivalent in this limit.

In order to connect these two ensembles, we must consider an explicit non-equilibrium procedure, in which some of the quantities that characterize the ensembles are changed. We have therefore introduced a dissipative pathway parametrized by a phenomenological

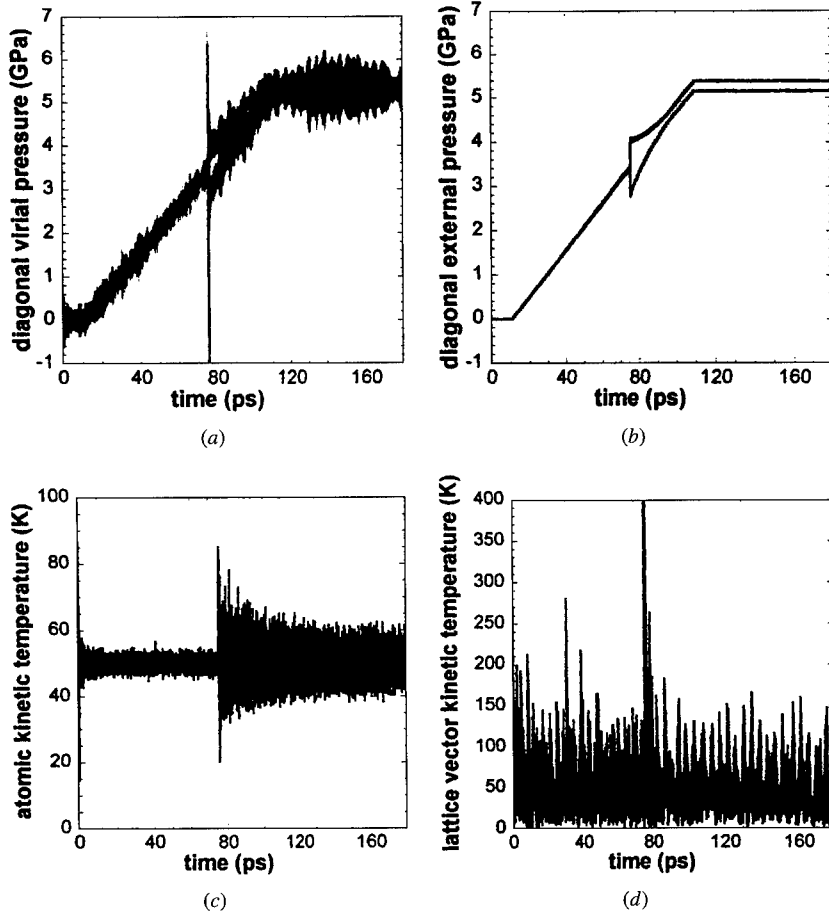


**Figure 7.** Obliviated simulations with a relaxation time of  $\tau_{\text{relax}} = 60$  ps, a strain threshold of  $\delta_{\text{relax}} = 0.05$ , a Nosé thermostat for the atoms and a Nosé–Hoover chain with nine links for the lattice vectors: (a) diagonal elements of virial pressure ( $P_{ij}$ ) (in GPa) against simulation time; (b) diagonal elements of external pressure ( $\Omega_{ij}$ ) (in GPa) against simulation time; (c) atomic kinetic temperature (K); and (d) lattice vector kinetic temperature (K).

relaxation time and a strain threshold, along which the reference lattice vectors are allowed to change slowly with time. Using the obliterated reference lattice, the virial pressure balances  $\Omega_{ij}^{\Gamma}$ , which approaches  $s_{ij}$  over the relaxation time  $\tau_{\text{relax}}$ . The degree of nonlinearity—i.e. strain history dependence—in the problem can then be controlled with  $\tau_{\text{relax}}$ . The deformation gradient is seen to factor into elastic and plastic transformations, and the strain rate can be decomposed into the sum of elastic and plastic terms. The plastic quantities are characterized by the variation of the parameters that distinguish between the equilibrium ensembles, namely the reference lattice vectors. The definition of the intermediate relaxed state with the obliterated reference lattice dissipates a portion of the energy built up in the reservoir from the work performed on it by the atomic system, and causes the nonlinear ensemble to approach its linear counterpart over the specified relaxation time. Numerically, the connection of the two ensembles is greatly facilitated by the use of separate thermostats for the atoms and lattice vectors and, in particular, by the use of a Nosé–Hoover chain to thermostat the latter degrees of freedom.

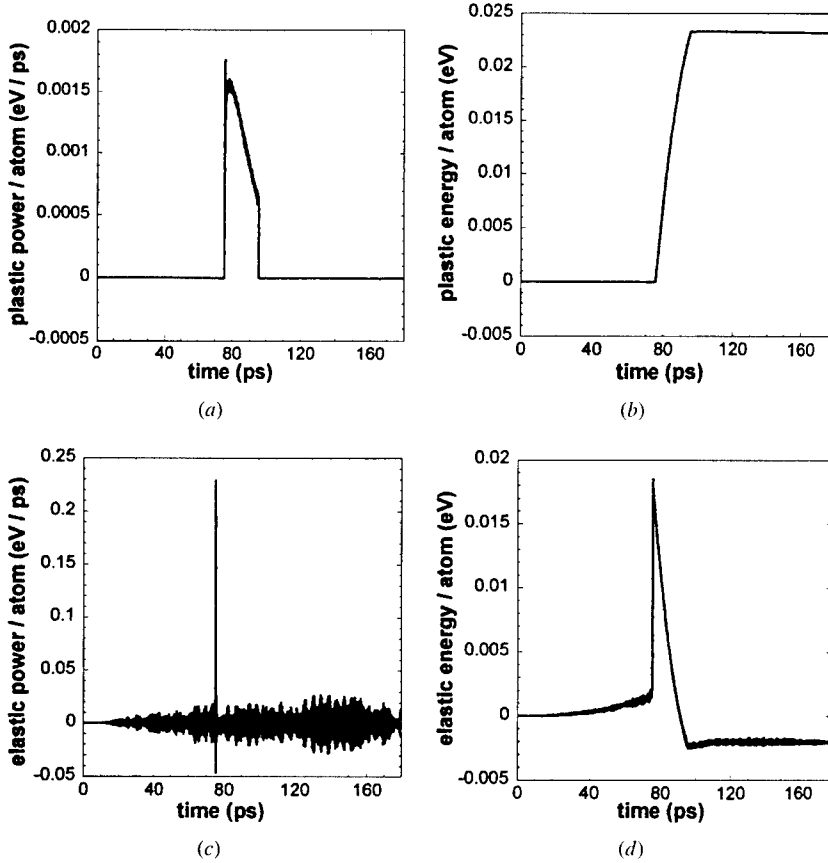


**Figure 8.** Obliviated simulation with a relaxation time of  $\tau_{\text{relax}} = 60$  ps, strain threshold of  $\delta_{\text{relax}} = 0.05$ , a Nosé thermostat for the atoms and a Nosé–Hoover chain with nine links for the lattice vectors: (a) plastic power per atom, equation (47) (in  $\text{eV ps}^{-1}$ ); (b) integrated plastic power per atom (in electronvolts); (c) elastic power per atom, equation (46) (in  $\text{eV ps}^{-1}$ ); (d) integrated elastic power per atom (in electronvolts).

The identification of the elastic and plastic factors of the deformation gradient with  $\Gamma_{ij}$  and  $\Theta_{ij}$ , and the elastic and plastic strain rates with  $\gamma_{ij}$  and  $\varphi_{ij}$ , is consistent with the macroscopic analysis given earlier provided that we understand that it is the time average of these quantities that must obey the corresponding macroscopic equations and inequalities. For example, the plastic ‘rate-work’ equation (47) can fluctuate about zero, and therefore violate equation (16) on an *atomic* time scale. However, the time integral or ensemble average of equation (47) obeys equation (16). This is consistent with the ‘local state hypothesis’ [8], which presumes that the thermodynamic state of the material at a given point and at a given instant of time depends only on the values of certain variables and not on their time-derivatives. This is equivalent to assuming that the system evolves as a series of equilibrium states, consistent with our assumption of a slow time variation of the reference lattice vectors and with the ‘coarse-grained’ view of the simulation representing a small interior region of material. Also, the inclusion of the strain threshold is necessary for the elastic and plastic powers to correspond to reversible and irreversible processes. Physically, specifying the connection of these two limiting ensembles with a relaxation time and strain threshold amounts to ‘bootstrapping’ a constitutive model for the material being simulated. However, the only deformations possible within the current

formulation are homogeneous, from the continuum point of view. Also, all the dissipative quantities in the simulation are *not predicted*, but are treated as parameters of the system through the specification of the relaxation time and threshold. The actual physical pathway responsible for the stress relaxation *cannot be addressed* within the present phenomenological formalism.

This raises the more fundamental question of whether it is possible to dissipate the work required to include the new phase through some specific physical mechanism. Real systems accommodate the inclusion of a new structural phase and dissipate strain energy on a very large length scale by forming interfaces—typically, slip or twin interfaces—in *non-homogeneous* distortions which effect the strain relief [20]. However, all previous molecular dynamics methodologies involving variable simulation cell shape and based on rigorous scaling arguments have been essentially homogeneous [1–7, 13]. In another article [21] we present an *inhomogeneous* method that incorporates the formation of slip interfaces.

### Acknowledgment

This research was supported by ONR.

### References

- [1] Andersen H C 1980 *J. Chem. Phys.* **72** 2384
- [2] Parrinello M and Rahman A 1980 *Phys. Rev. Lett.* **45** 1196
- [3] Parrinello M and Rahman A 1981 *J. Appl. Phys.* **52** 7182
- [4] Parrinello M and Rahman A 1982 *J. Chem. Phys.* **76** 2662
- [5] Ray J R and Rahman A 1984 *J. Chem. Phys.* **80** 4423
- [6] Ray J R and Rahman A 1985 *J. Chem. Phys.* **82** 4243
- [7] Lill J V and Broughton J Q 1992 *Phys. Rev. B* **46** 12 068
- [8] Lemaitre J and Chaboche J-L 1994 *Mechanics of Solid Materials* (Cambridge: Cambridge University Press)
- [9] Martyna G J, Klein M L and Tuckerman M 1992 *J. Chem. Phys.* **97** 2635
- [10] Murnaghan F D 1951 *Finite Deformations of an Elastic Solid* (New York: Wiley)
- [11] Eringen A C 1989 *Mechanics of Continua* (Malabar: Kreiger)
- [12] Abraham F F 1986 *Adv. Phys.* **35** 1
- [13] Wentzcovitch R M 1991 *Phys. Rev. B* **44** 2358
- [14] McQuarrie D A 1976 *Statistical Mechanics* (New York: Harper and Row)
- [15] Thurston R N 1964 Wave propagation in fluids and normal solids *Physical Acoustics: Principles and Methods* ed W P Mason (New York: Academic) pp 1–110
- [16] Truesdell C and Noll W 1965 The non-linear field theories of mechanics *Encyclopedia of Physics* vol III/3, ed S Flügge (Berlin: Springer) (see sections 38 and 39 for discussions of the principle of fading memory and stress relaxation)
- [17] Nosé S 1984 *J. Chem. Phys.* **81** 511
- [18] Nosé S 1984 *Mol. Phys.* **52** 2
- [19] Hoover W G 1985 *Phys. Rev. A* **31** 1695
- [20] Porter D A and Easterling K E 1993 *Phase Transformations in Metals and Alloys* (London: Chapman and Hall) ch 6
- [21] Lill J V and Broughton J Q *Phys. Rev. Lett.* submitted

## Modelling bulk viscosity of powder aggregate during sintering

D Bouvard and T Meister

Laboratoire Génie Physique et Mécanique des Matériaux, Institut National Polytechnique de Grenoble, UMR CNRS 5010, BP 46, 38402 Saint Martin d'Hères cedex, France

Received 14 October 1999, accepted for publication 10 February 2000

**Abstract.** A model of sintering by coupled surface diffusion and grain-boundary diffusion is presented, which is based on the numerical simulation of interparticle neck changes. This model is used to investigate the bulk viscosity of particle aggregates through densification. The results obtained suggest that a sintering powder has a Newtonian behaviour. The neck size is found to be the parameter that better controls the viscosity. However, as density is the most convenient parameter to be introduced in constitutive equations, two expressions of viscosity against density are proposed for the cases when surface diffusion is faster or slower than grain-boundary diffusion. It is shown that the models proposed in the literature for the initial sintering stage predict the same evolution as numerical results in the case of slow surface diffusion, even at high density. On the other hand the models proposed for the intermediate stage predict the same evolution as numerical results in the case of fast surface diffusion, even at low density.

### 1. Introduction

Modelling of the sintering of metal or ceramic powders has been extensively developed in the few past decades [1, 2]. Two approaches have been proposed. Physical models are based on the description of the mechanisms arising in the material during sintering [3–5]. Most often such a description requires a drastic schematization of the microstructure and a simplification of the mechanisms involved. Thus this approach is not efficient for the quantitative prediction of the behaviour of real materials. However, it can allow understanding the physics of sintering, identifying the main operating phenomena and anticipating the microstructural evolution of the material. The second method consists of fitting analytical equations directly from experimental data [6]. Such a phenomenological approach, based on the behaviour of the real material, seems to be more useful for practical applications.

Investigating the effect of stresses on the sintering process becomes more meaningful as new problems are tackled, such as pressure sintering processes, sintering of composite materials [7], analysis of shape changes due to a heterogeneous green density field [8–10]. A constitutive equation describing the response of the material to thermo-mechanical loading is then required. The phenomenological approach is still adapted to this purpose. However, the experimental data are necessarily limited since testing the mechanical behaviour of powders in sintering conditions (high temperature, controlled atmosphere) is delicate. For example, investigating the densification kinetics under low isotropic pressure is almost impossible since it would require canning the powder within a soft material that supports high temperature and does not hinder the densification of the powder. Thus physical modelling is certainly beneficial for completing the experimental information or extrapolating it to unexplored mechanical loading cases. This is the main motivation of this paper, which will present a model developed for

investigating the bulk viscosity of particle aggregates during sintering. With this model we will investigate the evolution of viscosity through densification. Also, we will try to verify if the viscosity is independent of pressure, i.e. if a sintering powder behaves as a Newtonian fluid. Such a property is always assumed in constitutive equations for the reason that diffusion kinetics is linear versus stress [8–13]. However nonlinear effects may arise from neck geometry. Also, the symmetry between tension and compression is worth being investigated since particulate materials often present asymmetric behaviour. We will show that physical modelling can help solve such problems, which are difficult to analyse from experimental data because the material constantly changes due to densification and grain growth [14].

Sintering models usually include two steps. First the evolution of contact between two particles is modelled in terms of shrinkage and area growth. For this purpose analytical or numerical methods can be used, depending on whether a rough description of particle geometry is sufficient or not. Classical models assume simple interparticle neck geometry or pore geometry and uncoupled sintering mechanisms [15]. To describe more realistic geometry and take into account several mechanisms simultaneously, numerical techniques are necessary [16, 17]. The second step of the modelling process consists of deriving the macroscopic deformation of the sintering body from interparticle contact evolution. Once again analytical or numerical methods are possible. For a homogeneous powder that does not exhibit significant rearrangement, analytical ‘homogenization’ expressions have been proposed. For more complex problems, ‘discrete element methods’, based on the numerical simulation of random particle assembly, may be required [18–20].

The model presented in this paper is based on the numerical simulation of interparticle neck changes by coupled surface diffusion and grain-boundary diffusion, which are often the preponderant sintering mechanics. An analytical homogenization method is next used to derive the densification kinetics. To find the viscosity we applied short loading sequences during sintering, as performed by Cai *et al* [21] for experimental characterization of the viscosity of alumina powder. Analytical expressions are proposed to describe the evolution of viscosity as function of density. The numerical results are finally compared with the predictions of several models.

## 2. Basic equations and methods

### 2.1. Two-sphere problem

Two identical spheres of radius  $R$  are in contact through a plane circular contact of radius  $x$ , which is treated as a grain boundary (figure 1). Since the system is symmetrical about the axis perpendicular to the contact, the cylindrical coordinates  $(r, z)$  are used. A curvilinear coordinate  $s$  is also defined along the intersection of the particles’ free surface with the meridian plane. The dihedral angle at the neck is  $\psi$ . The gradient of the chemical potential in the contact results in a radial diffusion flux at the edge of the neck,  $j_r$ , defined as the volume of material passing out of the grain boundary through a unit area in unit time. This radial flux is classically calculated as

$$j_r = \frac{4D_g\Omega}{xkT} \left( \sigma + \gamma_s K(x) + 2\frac{\gamma_s}{x} \sin\left(\frac{\psi}{2}\right) \right) \quad (1)$$

where  $D_g$  is the diffusivity in the grain boundary,  $\Omega$  is the atomic volume,  $k$  is Boltzmann’s constant,  $\gamma_s$  is the surface energy,  $T$  is the absolute temperature,  $\sigma$  is the average compressive stress on the neck and  $K(x)$  is the curvature at the edge of the neck [22]. Curvature is defined to be positive when the centre of curvature is outside the particle. The total volume of material

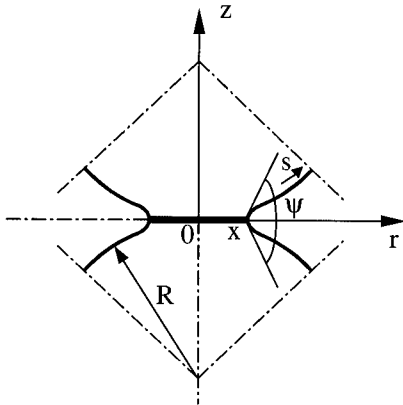


**Figure 1.** Schematic diagram of particle contact.

delivered to the edge of the neck in unit time is then

$$V = 2\pi x \delta_g j_r(x) \quad (2)$$

where  $\delta_g$  is grain-boundary thickness. The shrinkage rate, i.e. half of the rate of approach of one particle towards the other, is

$$\dot{w} = \frac{2\delta_g j_r}{x}. \quad (3)$$

The matter flowing out of the grain boundary is redistributed on the free surface of the particle by surface diffusion. This diffusion flux,  $j_s$ , which is entirely in the meridional direction, is expressed as:

$$j_s = \frac{\delta_s D_s \Omega \gamma_s}{kT} \frac{dK}{ds} \quad (4)$$

where  $\delta_s$  is the thickness of the surface layer in which diffusion takes place,  $D_s$  is the diffusion coefficient on the surface,  $K(s)$  is the curvature of the free surface. The surface flux results in the deposition or removal of material leading to a displacement rate normal to the surface:

$$v = -\frac{1}{r} \frac{d(r j_s)}{ds}. \quad (5)$$

From this equation a new particle boundary created by diffusion during any time increment can be calculated.

The grain-boundary diffusion analysis (equations (1) and (2)) and the dihedral angle at the neck provides two boundary conditions. Another condition is obtained from the following assumption: the angle between the tangent to the surface and  $r$  axis is equal to  $\pi/4$  and this angle is forced to remain  $\pi/4$  for that point, as if there was a band of contact all around the equator of the particle. This condition is supposed to represent, on average, the surrounding of a contact in a random packing of spheres during sintering. We assume that it is realistic from 0.64 to 0.9 of relative density, which corresponds to a coordination number between 7 and 10 [23]. For higher densities, the interactions between neighbouring contacts become important and this model is certainly not relevant.

This problem of neck deformation has been solved with a one-dimensional finite-difference calculation using a curvilinear array of points representing the current shape of the free-surface

particle, as proposed by Nichols and Mullins [16] and Bross and Exner [17]. Details of the numerical analysis can be found elsewhere [24]. In these calculations a critical parameter is

$$d_s = \frac{\delta_s D_s}{\delta_g D_g}. \quad (6)$$

This parameter will be referred to as the ‘diffusion ratio’ in the following.

## 2.2. Homogenization

Consider an isotropic homogeneous aggregate of monosized spherical particles with radius  $R$ , which is sintered under an isotropic external pressure  $p$ , possibly varying with time. It is assumed that at every time all interparticle contacts within the aggregate experience the same contact force and deform with the same neck growth and shrinkage rates. The densification rate can simply be calculated from the shrinkage rate,  $\dot{w}$ :

$$\frac{\dot{D}}{D} = 3 \frac{\dot{w}}{R - w} \quad (7)$$

which is integrated as

$$D = D_0 \left(1 - \frac{w}{R}\right)^{-3} \quad (8)$$

where  $D_0$  is the initial relative density, about 0.64 for random close packing. The average compressive axial stress transmitted to a neck is classically expressed as [25]

$$\sigma = \frac{4R^2}{ZDx^2} p \quad (9)$$

where  $Z$  is the number of necks per particle, which was calculated as a function of  $D$  by Arzt [23]. The relation found by Arzt for the densification by diffusion mechanisms can be approximated as  $Z = 11D$ .

These equations have been used to deduce the densification kinetics under any sintering cycle with constant or varying pressure from the numerical model of neck deformation. At time  $t$ , consider the actual neck geometry, characterized, in particular, by the neck radius  $x$ , and the shrinkage  $w$ . The relative density of the aggregate is deduced from  $w$  through equation (8). The external stress acting on the neck is calculated from equation (9) with the actual value of the pressure,  $p(t)$ . Then the numerical model is run to compute the free-surface changes and the shrinkage occurring during time increment,  $\delta t$ . The average shrinkage rate during  $\delta t$  is calculated and the average densification rate is deduced through equation (7). This process is iterated so that the densification rate is obtained as a function of time.

## 3. Numerical results

### 3.1. Free sintering

Free sintering was simulated first. The dihedral angle was assumed to be equal to  $130^\circ$ . A study of the influence of the dihedral angle can be found in [24]. The calculation started with an initial neck radius  $x = 0.01R$  and a surface that was spherical everywhere, except in the vicinity of the neck. It was stopped when the relative density reached 0.9. Four values of the diffusion ratio were investigated, 0.1, 1, 10 and 100. Note that the case  $d_s = 0.1$  was run with much difficulty. It is difficult to redistribute the matter arriving at the neck with such a low surface diffusion coefficient. To perform a simulation it was necessary to start from a higher neck radius,  $x = 0.1R$ .

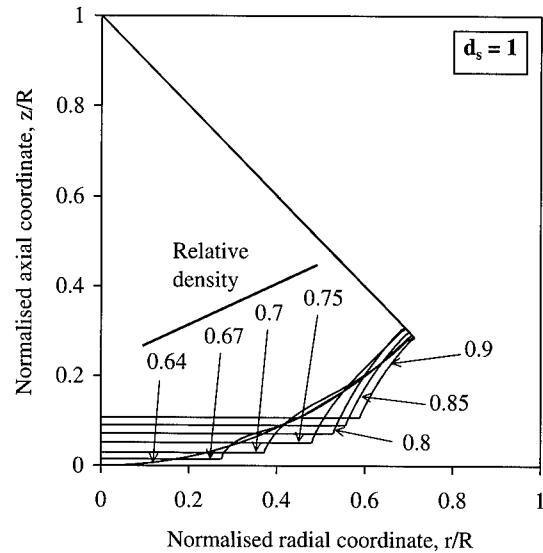


Figure 2. Evolution of the free surface contour during free sintering with  $d_s = 1$ .

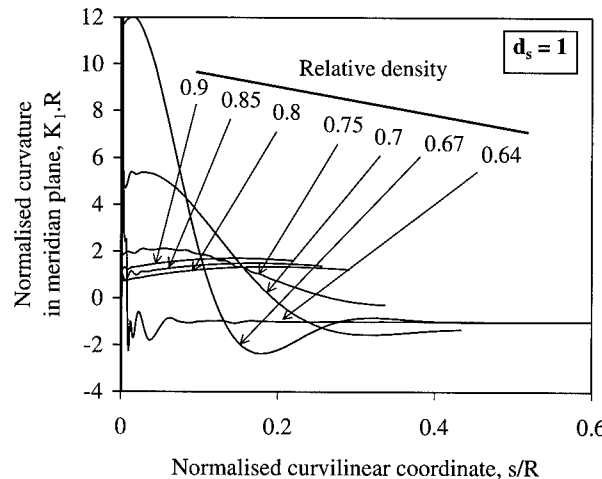
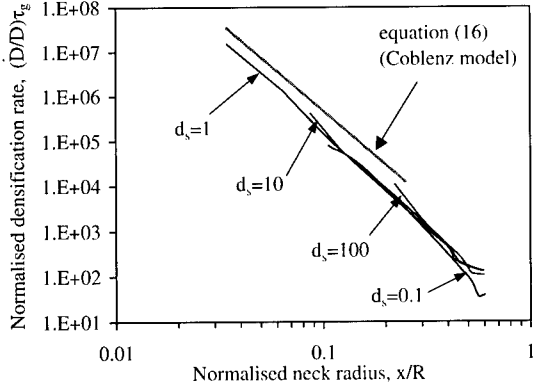


Figure 3. Curvature in the meridian plane as a function of the curvilinear coordinate during free sintering with  $d_s = 1$ . The values for  $D = 0.64$  and  $s \approx 0$  are off-scale.

Examples of the free-surface contour obtained at seven values of the density during sintering with  $d_s = 1$  are shown in figure 2. For the final density ( $D = 0.9$ ), the neck radius is  $0.6R$  and the shrinkage is  $0.1R$ . Figure 3 shows the curvature in the meridian plane as a function of curvilinear coordinate. For the initial density, the curvature is very high (off-scale) close by the neck and equal to  $-1/R$ , everywhere else. During densification, curvature gradients progressively vanish. From  $D = 0.8$ , the curvature is almost uniform along the free surface.

The densification rates obtained for each value of the diffusion ratio are represented in figures 4 and 5 as functions of two parameters, respectively, the neck radius, which is the



**Figure 4.** The densification rate as a function of the neck radius: effect of the diffusion ratio and comparison with equation (16).

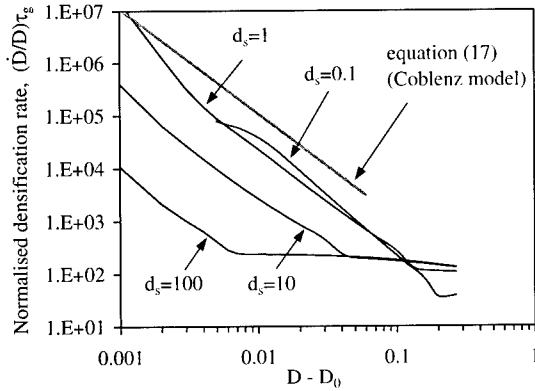


**Figure 5.** The densification rate as a function of the increase in density: effect of the diffusion ratio and comparison with equation (17).

microscopic parameter characterizing the progress of sintering, and the relative density, which is the only possible macroscopic parameter. As a normalization, the densification rate was multiplied by the characteristic time of grain boundary diffusion, defined as

$$\tau_g = \frac{kT R^4}{\delta_g D_g \Omega \gamma_s}. \quad (10)$$

As suggested by physical models (see section 4), the initial density was subtracted from the density in figure 5 and logarithmic scales were used in both figures.

Figure 4 shows that the densification rate decreases with increasing neck radius, following a power law with an exponent between  $-5$  and  $-4$ . There is almost no influence of the diffusion ratio on this evolution. Figure 5 is more complicated. Two stages are clearly observed. At low density the densification rate strongly decreases as density increases. It is higher when  $d_s$  is lower and apparently reaches a limiting curve as  $d_s$  reaches its lowest values. At a certain value of density, we observe a sharp transition leading to a gentle decrease of the densification rate. During this second stage, which Svoboda *et al* [26] named quasi-equilibrium sintering, the curvature is quasi-uniform along the free surface of the particles. The normalized densification rate at a given density is then almost independent of the diffusion ratio, i.e. the densification

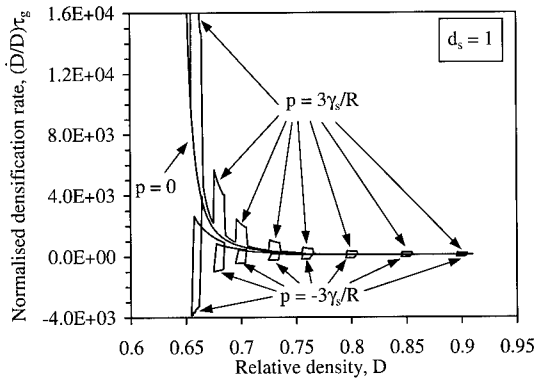


**Figure 6.** Comparison of densification rate curves obtained during free sintering and sintering with compressive or tensile loading sequences for  $d_s = 1$ .

rate is proportional to  $D_g$  and independent of  $D_s$ . The transition between both stages appears at a lower density when the surface diffusion is faster. For example, it occurs at  $D = 0.84$  when  $d_s = 0.1$  and between 0.75 and 0.8 when  $d_s = 1$ , which is consistent with figure 3. For the highest diffusion ration,  $d_s = 100$ , the second stage starts at a relative density of about 0.65. At this density the neck radius is already equal to  $0.425R$ . It means that most of the neck growth occurred by surface diffusion only, without significant densification.

### 3.2. Sintering with loading sequences

To evaluate the viscosity of a particle assembly at various densities, short isotropic loading sequences were introduced during sintering simulations. This pressure was either positive (compression) or negative (tension). Examples of results are shown in figure 6. The densification rates obtained during three simulations with  $d_s = 1$  are compared: free sintering, sintering with eight compressive loading sequences and sintering with eight tensile loading sequences. The loading was applied during a prescribed density interval  $+0.01$  or  $-0.01$ . The application of a pressure,  $p = 3\gamma_s/R$ , leads to an instantaneous increase in the densification rate. When the stress is removed, the densification rate suddenly lowers to about the free-sintering curve. This suggests that the effect of the former loading sequence on the sintering process rapidly vanishes. The viscosity,  $\eta$ , can directly be deduced from the jump in the densification rate,  $\Delta(\dot{D}/D)$  when the loading is applied or removed:

$$\eta = \frac{p}{\Delta(\dot{D}/D)}. \quad (11)$$

When a ‘tensile pressure’,  $p = -3\gamma_s/R$ , is applied, the densification rate becomes negative and thus the density decreases. It proves that this pressure—in absolute value—is higher than the sintering stress, usually defined as the opposite of the isotropic stress that should be applied to get no densification. After the end of the first tensile loading, there is a significant transitory period before the densification rate returns to the free-sintering curve. This transitory effect is much less pronounced for the following loading sequences, which are applied during ‘second stage’ sintering.

Similar simulations were performed with several values of  $d_s$ , between 0.1 and 100, and several values of  $p$ , between  $-3\gamma_s/R$  and  $10\gamma_s/R$ . Figures 7 and 8 show the viscosity multiplied by  $\tau_g R/\gamma_s$  as function of  $x$  and  $D - D_0$ , respectively. Each curve corresponds to particular values of  $d_s$  and  $p$ , which makes the drawing somewhat confused. However it

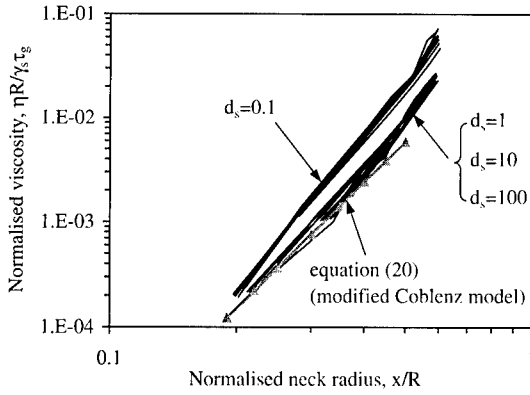


**Figure 7.** Bulk viscosity as a function of the neck radius: effect of the diffusion ratio and comparison with equation (20).

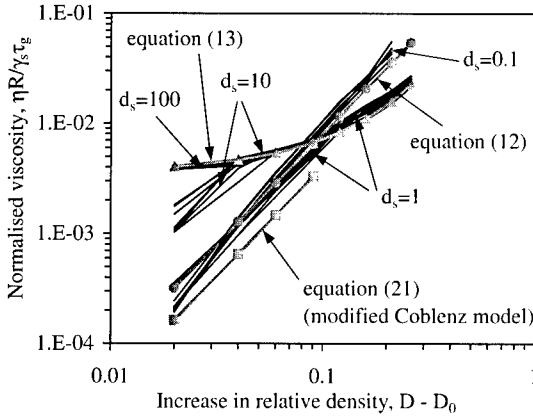


**Figure 8.** Bulk viscosity as a function of the increase in density: effect of the diffusion ratio and comparison with equations (12), (13) and (21).

clearly shows that the influence of the stress is insignificant. Whatever the stress, whether it is tensile or compressive, the viscosity is about the same at a given neck size or density. In figure 7 it appears that the viscosity varies as the neck size to a power between four and five. The viscosity is almost independent of  $d_s$ , except for  $d_s = 0.1$ . In this case the viscosity is twice as large for the same neck radius. In figure 8, two zones can be distinguished, as in figure 5. In the first sintering stage (high-curvature gradients), the viscosity increases with increasing relative density and diffusion ratio. In the second stage (quasi-uniform curvature), it is almost independent of the diffusion ratio. For the highest value of  $d_s$ , only the second stage is observed because curvature gradients disappear early during the densification.

Two analytical expressions were adjusted to these data (figure 5). The following power relation corresponds to  $d_s = 0.1$  (slow surface diffusion):

$$K = 0.8 \frac{\tau_g \gamma_s}{R} (D - D_0)^2 \quad (12)$$

whereas an exponential law describes the case  $d_s = 100$  (fast surface diffusion):

$$K = 3.610^{-5} \frac{\tau_g \gamma_s}{R} e^{7.16D}. \quad (13)$$

#### 4. Comparison with physical models

Many models have been proposed in the last few decades to describe densification rate and bulk viscosity during sintering by grain-boundary diffusion. Most of these models distinguish between the initial stage of sintering, when interparticle necks are small, and the final stage, when pores are isolated from each other. Some authors have also proposed an intermediate stage with interconnected cylindrical pores. In the following we first describe and adapt the model by Coblenz *et al* [15], which has the advantage of being simple. We will then examine the prediction of other models.

When grain-boundary diffusion is the main sintering mechanism, Coblenz *et al* [15] proposed the following approximations for free sintering, with the assumption  $w \ll x \ll R$  (initial stage):

$$K(x) = \frac{4R}{x^2} = \frac{1}{w}. \quad (14)$$

From equations (1), (3) and (10), with  $\gamma = 0$  and  $\psi = 180^\circ$ , we obtain

$$\dot{w} = \frac{16R^5}{x^4\tau_g} = \frac{R^3}{w^2\tau_g}. \quad (15)$$

Using equations (7) and (8) and the assumption  $(D - D_0)/D_0 \ll 1$ , we deduce the free sintering densification rate as a function of  $x$ :

$$\left(\frac{\dot{D}}{D}\right)_s = \frac{48R^4}{x^4\tau_g} \quad (16)$$

or as a function of  $D$ :

$$\left(\frac{\dot{D}}{D}\right)_s = \frac{27D_0^2}{(D - D_0)^2\tau_g}. \quad (17)$$

This relation is supposed to be valid for a small neck, let us say less than  $R/4$ , and a relative density close to  $D_0$ , let us say  $0.64 < D_0 < 0.7$ . Figures 4 and 5 show that equations (16) and (17) overestimate the densification rate calculated by numerical simulation, although the predicted variations as  $1/x^4$  and  $(D - D_0)^{-2}$ , respectively, are reasonable up to large necks.

The Coblenz model can easily be adapted to take into account an isotropic external pressure. If an average compressive stress,  $\sigma$ , is applied upon the contact during sintering, the shrinkage rate is obtained from equations (1), (3) and (14):

$$\dot{w} = \frac{R^3}{w^2\tau_g} \left(1 + \frac{x^2\sigma}{4R\gamma_s}\right). \quad (18)$$

Using equations (7) and (9) and assuming  $w \ll R$ , one gets

$$\frac{\dot{D}}{D} = \left(\frac{\dot{D}}{D}\right)_s \left(1 + \frac{pR}{ZD\gamma_s}\right). \quad (19)$$

Finally, with Arzt's approximation [23],  $Z = 11D$ ;  $D \approx D_0$ ; and with equation (14), the viscosity is written as

$$\eta = \frac{p}{\dot{D}/D - (\dot{D}/D)_s} = \frac{11D_0^2\tau_g\gamma_s}{48R^5} x^4. \quad (20)$$

Using equation (15), we obtain an alternative expression:

$$\eta = \frac{11\tau_g\gamma_s}{27R} (D - D_0)^2. \quad (21)$$

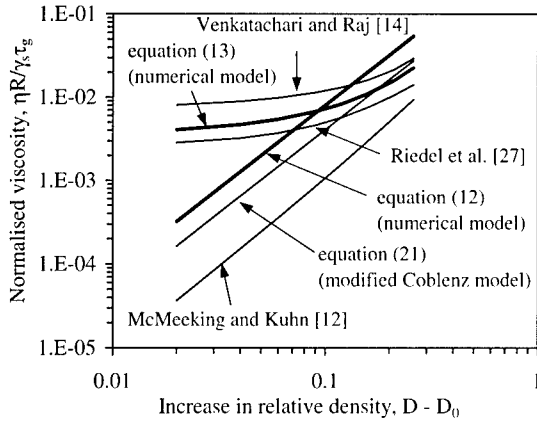


**Figure 9.** Comparison of equations (12), (13) and (21) with the predictions of various models.

Both expressions are compared with the numerical results in figures 7 and 8, respectively. Although the modified Coblenz model is supposed to be valid only for small neck radii, it correctly predicts the evolution of the viscosity as a function of the neck radius (figure 7) up to  $x = R/2$ , except for the lowest value of  $d_s$ . The evolution of viscosity against the relative density (figure 8) is not so well described, but the increase of  $\eta$  with  $(D - D_0)^2$  is verified during the first stage.

Finally, in figure 9 we plot, together with the curves resulting from equations (12), (13) and (21), the prediction of other models of sintering by grain-boundary diffusion. McMeeking and Kuhn [12] described neck growth and shrinkage during the initial stage, assuming that surface diffusion is fast enough to redistribute instantaneously the matter flowing out of the grain boundary. Riedel *et al* [27] obtained a constitutive equation for the intermediate stage from equilibrium particle surfaces computed for several values of the coordination number [26]. Venkatachari and Raj [14] modelled the closing of isolated spherical pores. Figure 9 shows that initial-stage model predicts the same type of evolution as the numerical results obtained with slow surface diffusion, whereas intermediate- and final-stage models give the same type of evolution as the numerical results with fast surface diffusion.

## 5. Discussion and conclusions

The proposed model mixes numerical and analytical methods for analysing the densification kinetics of a particle assembly during solid-state sintering by coupled grain-boundary diffusion and surface diffusion. In this paper it has principally been used to investigate the evolution of bulk viscosity through densification.

Preliminary free-sintering calculations showed that the main parameter driving the densification is the neck radius. For a given neck radius the densification rate is proportional to the grain-boundary diffusion coefficient and independent of the surface diffusion coefficient. The evolution of the densification rate as a function of relative density shows two successive stages. In the first stage, curvature gradients on the free surface of the particles are significant and the densification rate continuously drops as the particle geometry changes. During the second stage the curvature is quasi-uniform and the densification rate gently decreases. The transition between both stages occurs at a lower density when the surface diffusion is faster.

Bulk viscosity was estimated at various densities by introducing compressive or tensile loading sequences during sintering. It appeared that the viscosity was almost independent of the stress, whether it was compressive or tensile. This confirms that the material behaviour is Newtonian, as verified by Venkatachari and Raj [14] from data obtained with alumina powder. Once again the neck radius is the parameter which better controls the viscosity. The viscosity varies as the neck radius at a power between four and five. Surprisingly, the Coblenz model for grain-boundary diffusion, which was modified to take into account a external pressure, compared rather well with these results, even when particle geometry was far away from the geometry assumed in this model. Concerning viscosity against density evolution, two stages are observed as for free sintering. In the first stage the viscosity varies as  $(D - D_0)^2$ , as predicted by the modified Coblenz model, whereas in the second stage we adjusted an exponential law that gives about the same type of evolution as the models proposed in the literature for intermediate- and final-stage sintering.

At first sight, it seems surprising that the models describing initial-stage sintering by grain-boundary diffusion better match the numerical simulations when surface diffusion is slower, whereas these models assume that surface diffusion is not a limiting mechanism. Actually, when surface diffusion is slow, interparticle necks grow mainly by grain-boundary diffusion and curvature gradients remain significant; hence the assumptions of initial-stage models are relevant up to high densities. On the other hand, when surface diffusion is fast, it causes neck growth without significant densification and curvature gradients rapidly disappear. Grain-boundary diffusion starts being active in a second step, when neck geometry is close to that assumed by intermediate- or final-stage models, although density is still low (near the initial density).

Indeed, the above results cannot directly be compared with experimental data because the microstructure of real materials is much more complex than that assumed in the model and, also, direct measurement of bulk viscosity is difficult. However, we believe that our results can be helpful for the formulation of constitutive equations and for the analysis of experimental data. Our study confirms, in particular, that the description of the viscous behaviour of a sintering powder with a Newtonian law is reasonable. Also, it suggests different kinds of evolution of the viscosity as a function of the relative density depending on the diffusion ratio. However, we found that the relative density, which is the only variable describing powder changes during sintering in classical constitutive equations, is not the most interesting parameter. Neck radius appears to be more appropriate, but this is a microscopic parameter, which is difficult to estimate in real systems, whereas relative density can be quite easily measured.

## References

- [1] Olevski E 1998 *Mater. Sci. Eng.* **23** R41–100
- [2] Exner H E and Kraft T 1998 *Proc. Powder Metallurgy World Congress* vol 2 (Shrewsbury, UK: EPMA) pp 278–83
- [3] Coble R L 1958 *J. Am. Ceram. Soc.* **41** 55–62
- [4] Swinkels F B and Ashby M F 1983 *Acta Metall.* **29** 259–81
- [5] Johnson J L and German R M 1996 *Metall. Mater. Trans. A* **27** 441–50
- [6] Su H and Johnson D L 1996 *J. Am. Ceram. Soc.* **79** 3211–17
- [7] Bordia R K and Scherer G W 1988 *Acta Metall.* **36** 2399–408
- [8] Riedel H, Meyer D, Svoboda J and Zipse H 1993–94 *Int. J. Refractory Metals Hard Materials* **12** 55–60
- [9] Brandt J and Nilsson L 1998 *Mech. Cohes. Frict. Mater.* **3** 181–205
- [10] Gillia O and Bouvard D 1998 *Proc. Powder Metallurgy World Congress, Fundamentals of Sintering Special Seminar* (Shrewsbury, UK: EPMA) pp 16–23
- [11] Jagota A, Dawson P R and Jenkins J T 1988 *Mech. Mater.* **7** 255–69
- [12] McMeeking R M and Kuhn L T 1992 *Acta Metall.* **40** 961–9
- [13] Cocks A C F 1994 *Acta Metall.* **42** 2191

- [14] Venkatachari R and Raj R 1986 *J. Am. Ceram. Soc.* **69** 499–506
- [15] Coblenz W S, Dyns J M, Cannon R M and Coble R L 1980 *Proc. 5th Int. Conf. on Sintering and Related Phenomena* ed G C Kuczynski (New York: Plenum) pp 141–57
- [16] Nichols F A and Mullins W W 1965 *J. Appl. Phys.* **36** 1826–35
- [17] Bross P and Exner H E 1979 *Acta Metall.* **27** 1013–20
- [18] Jagota A and Dawson P R 1988 *Acta Metall. Mater.* **36** 2563–74
- [19] Parhami F and McMeeking R M 1998 *Mech. Mater.* **27** 111–24
- [20] Ross J W, Miller W A and Weatherly G C 1982 *Acta Metall.* **30** 203–12
- [21] Cai P Z, Messing G L and Jenkins J T 1997 *J. Am. Ceram. Soc.* **80** 445–52
- [22] Johnson D L 1969 *J. Appl. Phys.* **40** 192–200
- [23] Arzt E 1982 *Acta Metall.* **30** 1883–90
- [24] Bouvard D and McMeeking R M 1996 *J. Am. Ceram. Soc.* **79** 66–72
- [25] Molerus O 1975 *Powder Technol.* **12** 259–75
- [26] Svoboda J, Zipse H and Riedel H 1995 *Acta Metall. Mater.* **42** 435–44
- [27] Riedel H, Zipse H and Svoboda J 1994 *Acta Metall. Mater.* **42** 445–52

## Structure and energetics of Cu–Au alloys

G D Barrera<sup>†</sup>, R H de Tendler<sup>‡</sup> and E P Isoardi<sup>§</sup>

<sup>†</sup> Departamento de Química, Facultad de Ciencias Naturales, Universidad Nacional de la Patagonia San Juan Bosco, Ciudad Universitaria, (9000) Comodoro Rivadavia, Argentina

<sup>‡</sup> Instituto Universitario de Estudios Nucleares, Centro Atómico Ezeiza, Comisión Nacional de Energía Atómica, Avda. del Libertador 8250, (1429) Buenos Aires, Argentina

<sup>§</sup> Departamento de Química Inorgánica, Analítica y Química Física, Facultad de Ciencias Exactas y Naturales, Universidad de Buenos Aires, Pabellón 2, Ciudad Universitaria, (1428) Buenos Aires, Argentina

Received 7 November 1999, accepted for publication 16 February 2000

**Abstract.** The structures and energetics of Cu–Au alloys over a wide range of temperatures are studied using a combination of quasi-harmonic (QH) lattice dynamics and Monte Carlo (MC) simulations at constant temperature and constant pressure. The many-body potential used is fitted to room-temperature experimental data taking vibrational contributions into account. Transitions to the disordered phases are studied using MC simulations in which not only anisotropic deformation of the unit cell and atomic movements are allowed, but also exchange of atoms of different type is explicitly considered. Our calculations reproduce all characteristic features of the order-disorder transitions, including the characteristic peaks in the plots of heat capacity as a function of temperature.

### 1. Introduction

Cu–Au alloys are an interesting ‘model’ system due to the existence of three intermetallic compounds, namely  $\text{Cu}_3\text{Au}$ ,  $\text{CuAu}$  and  $\text{CuAu}_3$ , the temperature-induced order–disorder transitions and the capability of forming thermodynamically stable long period superlattice structures. Accordingly, a broad range of properties have been studied for this system, both experimentally and theoretically [1–8], and for both ordered and disordered phases. Nevertheless few workers have considered the three intermetallic solids, namely  $\text{Cu}_3\text{Au}$ ,  $\text{CuAu}$  and  $\text{CuAu}_3$ , using the same theoretical approach and identical interatomic potentials. Several authors have restricted themselves to only one of these compounds (see, for instance, [1–4]), and, because of the empirical origin of the interatomic potentials employed, there is no guarantee that these potentials are transferable to the other intermetallic compounds. In addition little attention has been paid to the relative stability of the three stoichiometric compounds [5–7]. Accordingly, in this paper we study the relative stability of the intermetallic solids  $\text{Cu}_3\text{Au}$ ,  $\text{CuAu}$  and  $\text{CuAu}_3$ . We find that the potentials available in the literature are not suitable for this purpose and so develop a new potential, which is then used to study the energetics of the ordered and disordered phases and the main characteristics of the order–disorder transitions. This is the main aim of the present work.

A potential commonly used is that proposed by Foiles *et al* [8]. The parameters of this potential have been obtained by fitting the results of static calculations to the room-temperature

elastic constants, lattice parameters, cohesive energy and vacancy formation energies of the pure metals, and to the heats of solution of binary alloys. Hence, when this potential is used to calculate these same properties at finite temperature, it is clear that they will not reproduce the experimental data to which they were fitted, due to the neglect of vibrational effects during the fitting procedure. Other potentials, for instance those proposed by Dumez *et al* [6] and by Cai and Ye [5], have been fitted to low-temperature data using only static calculations, and so neglecting zero point vibrational effects. In order to make the calculations consistent, here we use a potential in which the parameters are obtained by fitting to low-temperature experimental data taking vibrational contributions into account. This is now possible because we can calculate thermodynamic and elastic properties of alloys at finite temperatures using quasi-harmonic (QH) lattice dynamics in a very efficient and rapid way as implemented in the computer code EAMLD [9]. We then use both QH lattice dynamics and Monte Carlo (MC) simulations to study the structures and energetics of Cu–Au alloys over a wide range of temperatures. The ordered and disordered phases of Cu<sub>3</sub>Au, CuAu and CuAu<sub>3</sub> are studied using MC simulations at constant temperature and pressure, in which the explicit exchange of atoms of different type allows the transition to the disordered state to take place in a feasible amount of computer time.

Space restricts our comments here to previous work which has considered the three intermetallic compounds, Cu<sub>3</sub>Au, CuAu and CuAu<sub>3</sub>, and atomistic models that are physically different, neglecting small differences from previous model potentials due to the use of slightly different parametrization schemes. Ackland and Vitek [10] and Vitek *et al* [11] have also proposed a potential model for the alloy system Cu–Au. However, this model uses cubic splines to represent the pair potentials and so cannot be used to study the temperature dependence of the lattice parameters, heat capacities or phonon spectra in general, which depend on higher-order derivatives of the potentials.

In the ordered phase, CuAu has a tetragonal structure and consists of alternate planes of Cu and Au atoms perpendicular to the c-axis, as shown in figure 1. The observed structure can be thought of as a distorted face-centred cubic lattice, in which the experimental value of  $c/a \sim 0.926$  [12] is mainly a consequence of the different size of the Cu and Au atoms. Although Cheong and Laughlin [13] have shown that the thermodynamic stability of the ordered phase of CuAu may be significantly influenced by this tetragonal lattice distortion, the preliminary calculations of Cai and Ye [5] have been carried out with  $c/a = 1$ . Consequently, a further objective of this paper is to study the importance of the tetragonal distortion on the relative stability of CuAu.

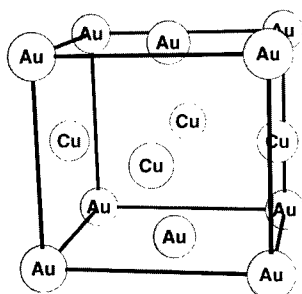


**Figure 1.** Structure of CuAu in the ordered phase. In the disordered phase all lattice positions are occupied at random by Cu or Au atoms.

## 2. Relative stability of the intermetallic solids

In figure 2 we show the enthalpies of mixing calculated from the results of atomistic simulations by a number of authors [5–8] together with the experimental values reported by Smith [14] extrapolated to  $T = 0$ . These have been calculated from the reported cohesive energies according to

$$\Delta H_{\text{mix}}(\text{Cu}_x\text{Au}_{1-x}) = H(\text{Cu}_x\text{Au}_{1-x}) - xH(\text{Cu}) - (1-x)H(\text{Au}). \quad (1)$$

It is clear that the agreement of these calculations with the experimental values is not satisfactory. In the static limit,  $\Delta H_{\text{mix}} = \Delta G_{\text{mix}}$  and it can be seen that the calculations of Cai and Ye and Dumez *et al* predict, in this limit, that  $\text{CuAu}_3$  is unstable with respect to disproportionation to  $\text{CuAu}$  and  $\text{Au}$ , in disagreement with experiment. A similar result is obtained from the results obtained from the calculation of Foiles *et al* [8], although in this case the difference in energy involved is too small to allow a definite conclusion. At this stage, it is not clear if this problem is a limitation of the static approximation, the interatomic models proposed or the particular potentials used.

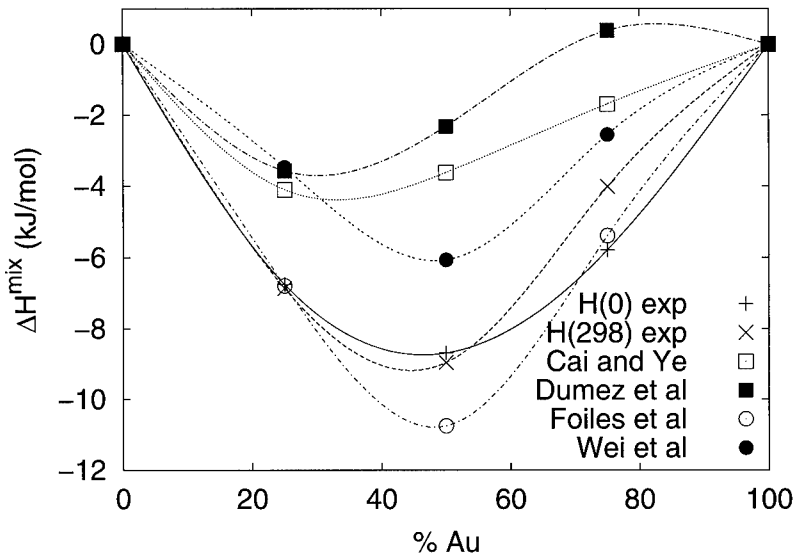


**Figure 2.** Enthalpies of mixing obtained from the static cohesive energies calculated by Dumez *et al* [6] (full squares), Cai and Ye [5] (open squares), Wei *et al* [7] (full circles), Foiles *et al* [8] (open circles) and from experimental data (crosses). The curves have no physical meaning and are included only as a guide to the eye.

Wei *et al* [7] have carried out first-principles calculations of the ordered structures and energetics of  $\text{Cu}_n\text{Au}_{4-n}$  ( $0 \leq n \leq 4$ ). In table 1 we list their calculated values for the cohesive energies of  $\text{Cu}_n\text{Au}_{4-n}$ . From these data we can calculate the change in internal energy for the reaction



to be equal to  $+1.9 \text{ kJ mol}^{-1}$ , again predicting  $\text{CuAu}_3$  is unstable with respect to disproportionation to  $\text{CuAu}$  and  $\text{Au}$  in disagreement with experiment. The relative stability of  $\text{CuAu}_3$  thus appears to be a very stringent test of both interatomic potential and *ab initio* first-principles calculations.

**Table 1.** Cohesive energies of Cu<sub>n</sub>Au<sub>4-n</sub> (0 ≤ n ≤ 4) calculated from the results of Wei *et al* [7].

	Cu	Cu <sub>3</sub> Au	CuAu	CuAu <sub>3</sub>	Au
ΔE (kJ mol <sup>-1</sup> )	-417.782	-421.641	-424.536	-421.641	-419.711

### 3. Methods

#### 3.1. Interatomic potentials

It is well known that the use of two-body interatomic potentials has serious limitations, for example the impossibility of accounting for the observed failure of the Cauchy relations or the differences between vacancy and cohesive energies. These limitations can be overcome by using many-body potentials such as those proposed by Daw and Baskes [15], Finnis and Sinclair [16] and Ercolessi *et al* [17]. Although the physical motivation in proposing each of these potentials is different, the crystal energy in all of these models can be written as

$$E_{\text{stat}} = \sum_i F_i(\rho_i) + \frac{1}{2} \sum_i \sum_j' \phi_{ij}(r_{ij}) \quad (3)$$

where, within the embedded atom method,  $F_i(\rho_i)$  is negative and represents the energy of ‘embedding’ atom  $i$  in the electronic density  $\rho_i$  created by all other atoms in the crystal, and  $\phi_{ij}$  is the core–core repulsion between atoms  $i$  and  $j$ , which is assumed to depend only on the type of atoms  $i$  and  $j$  and the distance between them. The electron density  $\rho_i$  is assumed to be the sum of the electron densities of all other atoms at the nucleus of atom  $i$ :

$$\rho_i = \sum_j' f_j(r_{ij}) \quad (4)$$

where  $f_j(r_{ij})$ , assumed to be isotropic about atom  $j$ , is the electron density due to basis functions centred on atom  $j$  at a distance  $r_{ij}$ . The prime on the summations in equations (3) and (4) indicates that terms with  $r_{ij} = 0$  are not included. This model has the advantage that it includes certain many-body contributions to the crystal energy while the computational effort is not as large as in those approaches where angular contributions are explicitly included.

#### 3.2. Quasi-harmonic lattice dynamics

In the quasi-harmonic approximation it is assumed that the Helmholtz energy of a crystal,  $F$ , at a temperature  $T$  can be written as the sum of static and vibrational contributions,

$$F = E_{\text{stat}} + F_{\text{vib}}(T). \quad (5)$$

$E_{\text{stat}}$  is the potential energy of the static lattice in a given configuration and  $F_{\text{vib}}$  is the sum of harmonic vibrational contributions from all the normal modes. For a periodic structure, the frequencies  $v_j(\mathbf{q})$  are obtained by diagonalization of the dynamical matrix in the usual way [18], so that  $F_{\text{vib}}$  is given by

$$F_{\text{vib}} = \sum_{j=1}^{3N} \sum_q \frac{1}{2} h v_j(\mathbf{q}) + kT \ln(1 - e^{hv_j/kT}) \quad (6)$$

where the first term is the zero-point energy at  $T = 0$ . For a macroscopic crystal the sum over  $\mathbf{q}$  becomes an integral over a cell in reciprocal space, which can be evaluated by taking successively finer uniform grids until convergence is achieved. Vibrational frequencies do not depend on temperature explicitly, but do so implicitly through the position of the atoms in the

unit cell which determines the dynamical matrix. The free energy thus obtained is a function of both some external coordinates,  $\mathcal{R}_{\text{ext}}$ , which are taken here as the lattice parameters ( $a$  for a cubic crystal,  $a$  and  $c$  for a hexagonal crystal, etc) and a set of internal coordinates which gives the position of the atoms within the unit cell  $\mathcal{R}_{\text{int}} = \{r\}$ ; this whole set of coordinates is denoted collectively as  $\mathcal{R}$ . For a given temperature and applied pressure,  $P_{\text{ext}}$ , the crystal structure is that which minimizes the availability  $\tilde{G}$  [19]:

$$\tilde{G}(\mathcal{R}) = F(\mathcal{R}) + P_{\text{ext}} V(\mathcal{R}^{\text{ext}}). \quad (7)$$

At the equilibrium configuration  $P = P_{\text{ext}}$  and the availability equals the Gibbs energy:

$$\tilde{G} = G \equiv F + PV. \quad (8)$$

A particularly efficient method to minimize  $\tilde{G}$  is described in detail elsewhere [9].

### 3.3. Monte Carlo simulations

We have carried out two different types of Monte Carlo simulations, with and without atom exchanges, denoted as MC and MCX, respectively. To facilitate comparison with experiment, both of these were carried out at constant temperature and constant pressure.

In the first approach, which we call MC, vibrational effects are taken into account by allowing random moves of the atoms, chosen at random, in the range  $[-r_{\text{max}}, r_{\text{max}}]$ . To determine whether the displacement is accepted or rejected, the Metropolis algorithm is used. In order to carry out the simulation at constant pressure, random changes in the volume, for cubic crystals, or in the lattice parameters  $a$ ,  $b$  and  $c$ , for orthorhombic crystals, are also made and the Metropolis algorithm is used again to decide whether to accept or reject the attempted distortion of the unit cell.

In order to study the order-disorder transition of Cu–Au alloys it is crucial to sample different atomic configurations. Allowing both for atom displacements and distortions of the unit cell as indicated above, it is possible to study both the pure metals and the ordered alloys. However, in this way, the ordering of the alloy is maintained at temperatures much higher than the observed transition temperature, usually up to temperatures very close to the melting point. A better sampling of different atomic configurations can be obtained by also exchanging atoms at random, and accepting or rejecting the new configurations according to the usual Metropolis algorithm.

The maximum displacement for the atoms as well as the maximum changes in the volume or lattice parameters are determined during the ‘equilibration’ run in such a way as to produce an acceptance rate of approximately 0.3. Detailed balance is achieved, at any stage of the simulations, by deciding whether to carry out an atom displacement, a cell distortion or an exchange at random with a probability of N:1:1, respectively, where N is the number of atoms in the simulation box. In order to get well equilibrated starting configurations, especially for the disordered alloys, it is necessary to carry out the equilibration runs for approximately  $10^6$  steps. A typical number of different configurations sampled is  $10^7$ .

By carrying out simulations with and without atom interchanges it is then possible to estimate the effects of the disorder on the calculated thermodynamic properties. Here we present results for the lattice parameters, enthalpies and heat capacities as a function of temperature, for a wide range of temperatures. Heat capacities are calculated using standard formulae from fluctuation theory [20].

#### 4. Applications: Cu–Au alloys

##### 4.1. Parametrization

One aim of this work is to verify if a simple potential of the EAM form is capable of reproducing the main features of the order-disorder transition of Cu–Au alloys as well as giving a suitable description of the relative energies of different intermetallic compounds. For this reason, we have chosen to use a simple potential form. For the electronic densities we use exponential functions:

$$f_j(r) = A_j \exp(-r/\sigma_j^e) \quad (9)$$

with different parameters  $A_j$  and  $\sigma_j^e$  for each metal ( $j = \text{Cu}, \text{Au}$ ) and with a cut-off of 6.0 Å. The repulsive potential is also assumed to have the simple form

$$\phi_{ij}(r) = B_{ij} \exp(-r_{ij}/\sigma_{ij}^r) \quad (10)$$

with parameters  $B_{ij}$  and  $\sigma_{ij}^r$  for each type of interaction (Cu–Cu, Au–Au and Cu–Au). For the embedding energy we use

$$F_j(\rho_j) = -C_j \sqrt{\rho_j} \quad (11)$$

again, with different parameters  $C_j$  for each atom type.

For pure Cu, five parameters need to be determined:  $B_{\text{CuCu}}$ ,  $\sigma_{\text{CuCu}}^r$ ,  $A_{\text{Cu}}$ ,  $\sigma_{\text{Cu}}^e$  and  $C_{\text{Cu}}$ . Because the energy of any given configuration depends only on  $C_{\text{Cu}}\sqrt{A_{\text{Cu}}^e}$  and not on the separate values of  $A_{\text{Cu}}$  and  $C_{\text{Cu}}$ , only four of these parameters can be determined by fitting to properties of the pure metals. Without loss of generality, we take  $C_{\text{Cu}} = 1$ . The remaining four parameters are fitted so as to reproduce the experimental lattice parameter, sublimation energy, elastic constants and frequencies of vibration of pure Cu at the X-point at room temperature. In table 2 we show the experimental data used in the fitting together with the values obtained from the present model. With this simple model it is not possible to reproduce the experimental values exactly. The same procedure was followed for Au. Although the parameters  $C_{\text{Cu}}$  and  $C_{\text{Au}}$  can be taken as 1 for the pure metals, the energies of Cu–Au alloys depend on their relative values. Here, we take  $C_{\text{Cu}} = 1$  while the parameter  $C_{\text{Au}}$ , together with the cross interaction parameters  $B_{\text{CuAu}}$  and  $\sigma_{\text{CuAu}}^r$ , are fitted to reproduce the lattice parameters  $a$  and  $c$  and the sublimation energy of CuAu(I) at room temperature. Experimental and calculated values are given in table 2. In table 3 we collect together the parameters of the present potential.

Inclusion of the frequencies of vibration in the fitting procedure proved to be necessary in order to obtain a good description of the phonon spectra. Without this, the resulting

**Table 2.** Experimental data at 298 K used to determine the model parameters and corresponding calculated values.

	Cu		Au		CuAu	
	Experiment	Calculated	Experiment	Calculated	Experiment	Calculated
$a$ (Å)	3.6150	3.6149	4.0785	4.0799	3.966	3.966
$c$ (Å)					3.673	3.673
$\Delta G_{\text{sub}}$ (kJ mol <sup>-1</sup> )	-350.938	-350.936	-392.773	-392.766	-380.810	-380.810
$C_{11}$ (GPa)	170.0	165.9	192.5	185.7	—	—
$C_{12}$ (GPa)	122.5	122.7	163.0	150.2	—	—
$C_{44}$ (GPa)	75.8	72.6	42.4	48.27	—	—
$v_T(X)$ (THz)	5.09	5.06	2.75	2.48	—	—
$v_L(X)$ (THz)	7.20	7.50	4.61	3.54	—	—

**Table 3.** Parameters of the potential model used in this work.

$i/j$	$B_{ij}$ (eV)	$\sigma_{ij}^r$ ( $\text{\AA}$ )	$A_i$	$\sigma_{ij}^e$ ( $\text{\AA}$ )	$C_i$ (eV)
Cu	7076.56	0.241 535	188.542	0.536 562	1
Au	14 759.9	0.272 639	4162.93	0.366 085	1.421 97
Cu/Au	10 153.2	0.258 268	—	—	—

potentials slightly overestimate the vibration frequencies of Cu (by  $\sim 10\%$ ) and underestimate the vibration frequencies of Au by as much as 40%. As a consequence of this, the thermal expansion of Au is severely overestimated, leading eventually to a breakdown of the quasi-harmonic approximation at  $\sim 400$  K. This problem is partially solved by including some vibration frequencies in the fitting procedure, although it is obvious that this is at the cost of a poorer reproduction of the elastic constants. This could possibly be improved by the use of a more sophisticated approach, such as the modified embedded atom method proposed by Baskes *et al* [21].

The use of room-temperature experimental values in the fitting procedure differs from previous work where experimental values have been extrapolated to  $T = 0$ . One advantage of our procedure is that vibrational effects, including zero point energy contributions, are readily taken into account. In addition the precision of measurements at room temperature is usually superior to that obtained at low temperatures. When fitting potential parameters using low-temperature data and static calculations, corrections due to zero point energy contributions are required, but have been ignored by most workers.

#### 4.2. Structures and cohesive energies of Cu–Au alloys

As a representative example of the temperature dependence of the lattice parameters we show the variation of the calculated lattice parameters of Cu and CuAu in figures 3 and 4. Also plotted are those calculated from the experimental lattice parameters reported by Pearson [12] and the thermal expansion coefficients tabulated by Touloukian *et al* [22], for Cu, and the lattice parameters of CuAu reported by Bjerkelund *et al* [23], for CuAu. As expected, at low temperatures results from QH lattice dynamics and (classical) MC simulations differ due to the neglect of quantum effects in the latter. We have verified that using the classical expression for the free energy in the QH calculations,

$$F_{\text{vib}} = kT \sum_{j=1}^{3N} \sum_q \ln \left( \frac{h\nu_j(q)}{kT} \right) \quad (12)$$

we obtain results in excellent agreement with those from the MC simulations up to temperatures near the Debye temperature ( $\theta_D$ ) of each solid (345, 163, 282, 205 and 183 K, for Cu, Au, Cu<sub>3</sub>Au, CuAu and CuAu<sub>3</sub> at low temperatures, respectively [24–26]). The importance of quantum effects decreases with temperature and above  $\theta_D$  there is a small range of temperatures in each case where QH and MC results are in good agreement. At still higher temperatures the QH approximation is less successful because of its neglect of further anharmonic effects and it eventually breaks down, as in Au at  $T \sim 700$  K, where the lattice parameter is greatly overestimated.

As mentioned above, an interesting property of Cu–Au alloys is the capability of forming thermodynamically stable long period superlattice structures. For instance, CuAu is known to exist in two different crystal structures. At low temperatures the structure of CuAu, CuAu(I), has the tetragonal unit cell shown in figure 1. Between 658 and 683 K the thermodynamically

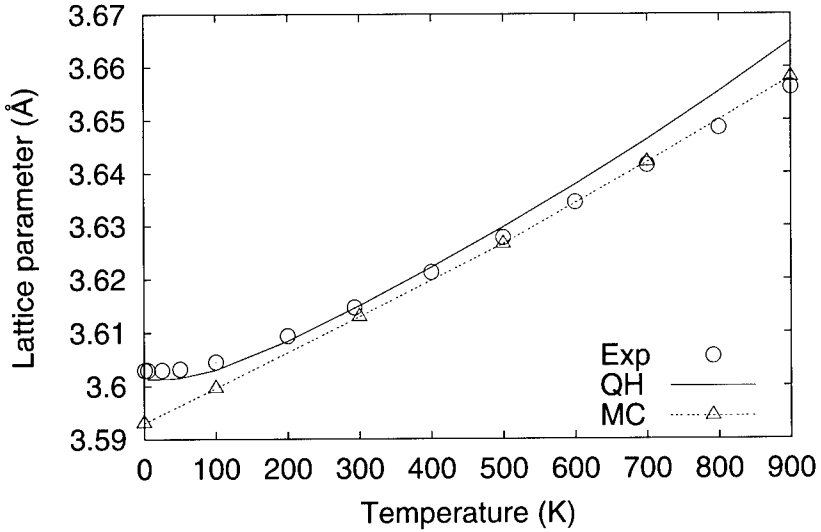


**Figure 3.** Cu: lattice parameter versus temperature. The labels Exp, QH and MC refer to the experimental data, and the results of the calculations of quasi-harmonic lattice dynamics and Monte Carlo simulations, respectively.

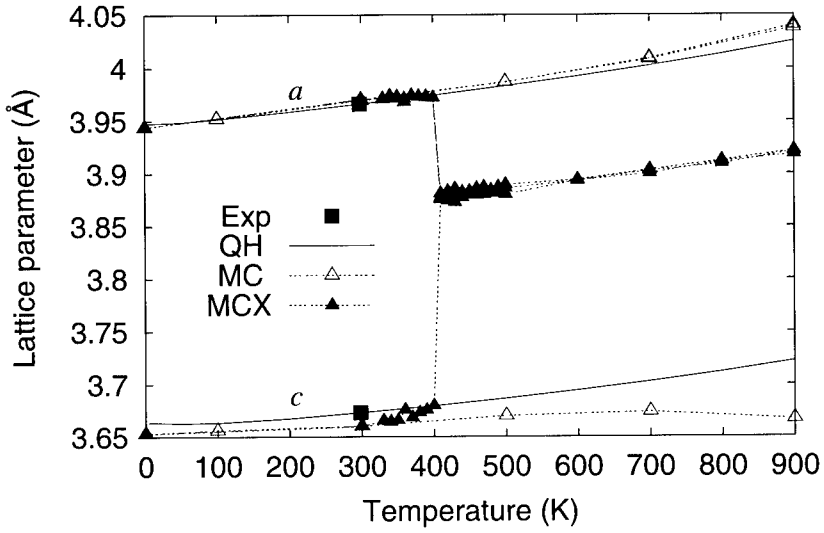


**Figure 4.** CuAu: lattice parameters versus temperature. The labels Exp, QH, MC and MCX refer to the experimental data, and the results of the calculations of quasi-harmonic lattice dynamics and Monte Carlo simulations without and with exchange of atoms of different type, respectively.

stable structure of CuAu, CuAu(II), has a 40 atom unit cell with a  $\frac{1}{2}\langle 110 \rangle$  antiphase boundary on the [100] planes. The energy of formation of this antiphase boundary calculated with our model in the static limit is  $55.8 \text{ mJ m}^{-2}$ , which compares well with the experimental estimates [27, 28] of  $40\text{--}60 \text{ mJ m}^{-2}$ . No further attempts to consider the superstructures with antiphase domains were carried out because this is an effect due to details in the electronic structure of the solids that cannot be explained with our atomistic model [29].

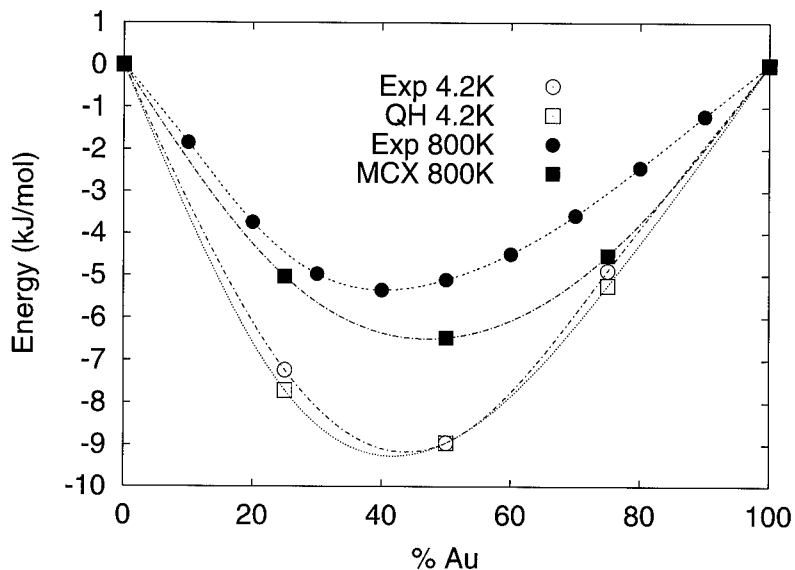


**Figure 5.** Gibbs energies of mixing at 4.2 K and enthalpies of mixing at 800 K of Cu–Au alloys versus composition. QH: quasi-harmonic lattice dynamics calculations at 4.2 K for the ordered phase. MCX: Monte Carlo simulations with exchange of atoms at 800 K for the disordered phase. The curves have no physical meaning and are included only as a guide to the eye.

All QH lattice dynamics calculations, including those at high temperatures, were carried out only on the ordered compounds. The values shown as MC at  $T = 0$  in figures 3 and 4 correspond to static calculations. These are included in the plots to show that the static values are indeed the limiting results of the MC calculations as  $T \rightarrow 0$ . The difference between the results of the static and QH calculations at  $T = 0$  are due to the zero point contributions. This difference is larger for Cu than for Au, due to its smaller atomic mass. The increase in the lattice parameters due to quantum effects is of the same order as the entire linear thermal expansion between 0 and 300 K. This result clearly highlights the need to include quantum effects at low temperatures in cases when quantitative studies of structural parameters are attempted.

For CuAu, we show in figure 4, in addition, the results of Monte Carlo calculations in which interchange of atoms of different types is explicitly included (MCX), as described above. The Monte Carlo runs without exchange of atoms (MC) maintain the ordered structures up to temperatures very close to the melting point. The transition to the disorder state in the MC runs with interchange of atoms produces a rapid change in the lattice parameters of the intermetallic solids with increasing  $T$ , as shown in figure 4. We cannot expect a discontinuity in the lattice parameters as observed experimentally due to the finite size of the unit cells utilized in the simulations (256 atoms). Cu<sub>3</sub>Au, CuAu and CuAu<sub>3</sub> transform to the disordered state at approximately 370, 430 and 320 K, respectively. In all cases the calculated transition temperatures are lower than the experimental values, and we return to this in the next section. The differences between the lattice parameters of the ordered and disordered structures of Cu<sub>3</sub>Au and CuAu<sub>3</sub> are in good agreement with experiment. The transition to the disordered phase of CuAu is particularly interesting because it is associated with a change of symmetry in the crystal structure.

In figure 5 we show the enthalpies of mixing of Cu<sub>3</sub>Au, CuAu and CuAu<sub>3</sub> obtained using our interatomic potentials, together with low-temperature experimental data [7] for the

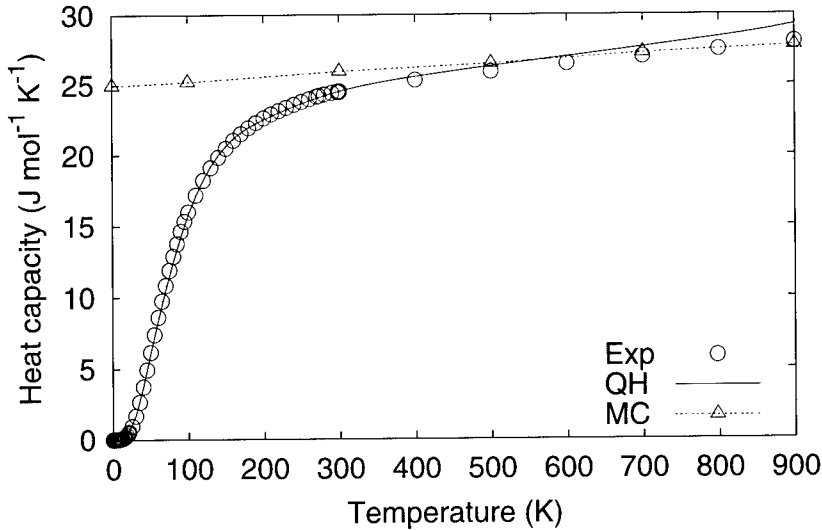


**Figure 6.** Cu: Heat capacity at constant pressure versus temperature. Labels have the same meaning as in figure 3.

ordered solids and high-temperature experimental data for the disordered materials [30]. At low temperatures we used QH lattice dynamics, where quantum effects are taken into account, to calculate the enthalpies of mixing of the ordered solids. While at high temperatures quantum contributions are negligible, the sampling of different configurations is essential, and so we determine the enthalpies of mixing using MCX simulations (with exchange of atoms). In particular, the enthalpies of mixing of the ordered solids agree very well with the experimental data. Although it is important to remember that the cohesive energies of Cu, Au and CuAu were used to fit the potential parameters, CuAu<sub>3</sub> is now predicted to be stable in agreement with experiment, unlike results obtained with previous potentials [5, 6].

#### 4.3. Heat capacities and order-disorder transitions

The first investigations of the order-disorder transitions in alloys included measurements of heat capacity as a function of temperature. In order to assess the feasibility of calculating heat capacities from MC simulations at constant pressure, we carried out MC simulations both with and without exchange of atoms of different type, in which the heat capacity was evaluated directly from fluctuations in the enthalpy. The results are shown in figures 6 and 7 together with those obtained from QH lattice dynamics and experimental data [30]. At low temperatures, the importance of quantum effects is much more evident here than in the calculation of structural parameters. The results indicated as MC at  $T = 0$  correspond to the classical limit of  $3R$ . No physical meaning should be ascribed to the results of classical simulations at temperatures below  $\theta_D$ ; these are included in the graphs only to show that the correct limiting values of  $C_P$  at low temperatures were obtained. From the plots of heat capacity versus temperature it is possible to estimate the order-disorder transition temperatures of Cu<sub>3</sub>Au, CuAu and CuAu<sub>3</sub> as 370, 430 and 320 K, which agree with those obtained earlier from the lattice parameter plots, and are appreciably lower than the experimental values of 663, 683 and  $\sim 500$  K, respectively. The underestimation of the transition temperatures is not a consequence of the particular parametrization used in this work. We have verified that when using different functional forms for the electronic densities, the repulsive potentials and/or the embedding function the results

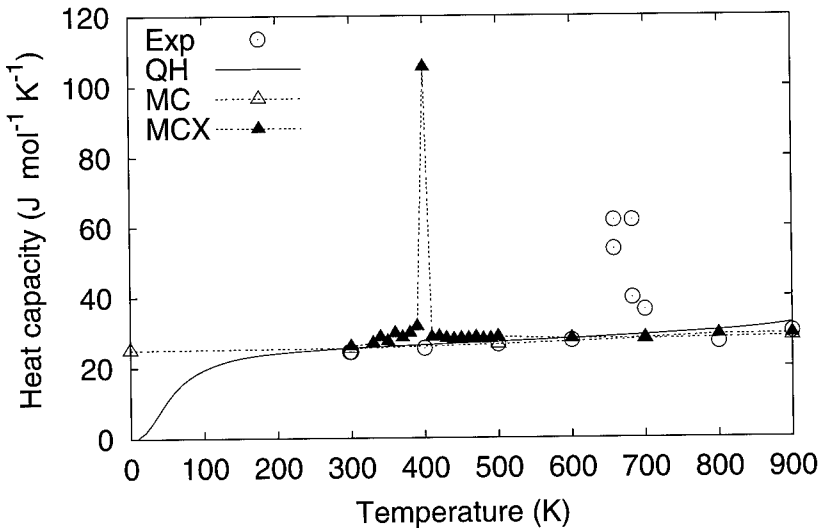


**Figure 7.** CuAu: Heat capacity at constant pressure versus temperature. Labels have the same meaning as in figure 3.

presented here do not change appreciably. Neither does the use of a different cut-off for both the electronic densities and the repulsive potentials increase the transition temperatures. Previous works, such as that by Polatoglou and Bleris [4] have obtained better agreement with the experimental transition temperatures but have used a model in which local relaxation and atomic vibration are neglected. We have already shown that these effects are expected to decrease the calculated transition temperatures and so the better agreement found with these models should be considered fortuitous [31].

## 5. Conclusions

We propose a new interatomic potential for Cu–Au alloys fitted to room-temperature data, in which zero point effects are explicitly accounted for by using QH lattice dynamics calculations. This potential compares favourably with previous potentials. There is a good agreement between calculated and experimental data of structural and energetic parameters at low temperatures. Another distinguishing feature of this new potential is that it gives a good description of the tetragonal distortion of CuAu. Our model predicts that CuAu<sub>3</sub> is stable with respect to disproportionation to CuAu and Au, in agreement with experiment.

From the calculations of lattice parameters and enthalpies as a function of temperature we have established the existence of a small range of temperatures where QH lattice dynamics calculations and classical MC simulations agree. This is of great practical importance because QH calculations, as opposed to MC simulations, provide a very efficient way of calculating entropies and free energies. The values of free energies over the range where both techniques agree can then be used as a starting point to calculate free energies of both ordered and disordered states as a function of temperature by using thermodynamic integration. This provides a relatively simple way of calculating free energies at high temperatures where MC simulations are most suitable.

We have also calculated isobaric heat capacities from the fluctuations in the enthalpy for all the solids considered. Our results show that present computational resources are sufficient

to reproduce the characteristic peaks in the plots of heat capacity as a function of temperature at temperatures near  $T_C$ , in spite of the relatively small size of the unit cells employed. The most demanding simulations are those for CuAu, where there are two independent lattice parameters  $a$  and  $c$ . In spite of this, the plots of lattice parameter versus temperature show all the characteristic features of the transition to the cubic disordered phase.

The enthalpies of mixing at low temperatures for the intermetallic compounds considered here agree very well with available experimental data. The results for the disordered phase at 800 K, however, reproduce the experimental data only qualitatively. Although the agreement with the experimental data is very good for 75% Au, our calculations overestimate the enthalpy of mixing at 25% Au by approximately 60%. This is unexpected, particularly considering that our potential reproduces correctly the enthalpy of mixing at low temperatures. This clearly shows that there is still room for improvement in the quality of the interatomic potentials, even for systems as comparatively simple as that considered in this work.

Our methodology for fitting interatomic potentials using room-temperature experimental data should be generally applicable, especially for those systems where low-temperature data are scarce or not available.

### Acknowledgments

GDB greatly acknowledges financial support from the Consejo Nacional de Investigaciones Científicas y Técnicas de la República Argentina. This work has been made possible by means of a grant from the Fundación Antorchas.

### References

- [1] Rey Losada C, Hayoun M and Pontikis V 1993 *Mater. Res. Soc. Symp. Proc.* **291** 549
- [2] Cleri F and Rosato V 1993 *Phil. Mag. Lett.* **67** 369
- [3] Nagel L J, Anthony L and Fultz B 1995 *Phil. Mag. Lett.* **72** 421
- [4] Polatoglu H M and Bleris G L 1994 *Solid State Commun.* **90** 425
- [5] Cai J and Ye Y Y 1996 *Phys. Rev. B* **54** 8398
- [6] Dumez C, Hayoun M, Losada C R and Pontikis V 1994 *Interface Sci.* **2** 45
- [7] Wei S H, Mbaye A A, Ferreira L G and Zunger A 1987 *Phys. Rev. B* **36** 4163
- [8] Foiles S M, Baskes M I and Daw M S 1986 *Phys. Rev. B* **33** 7983
- [9] Barrera G D and de Tendler R H 1997 *Comput. Phys. Commun.* **105** 159
- [10] Ackland G J and Vitek V 1990 *Phys. Rev. B* **41** 10324
- [11] Vitek V, Ackland G J and Cserti J 1991 *Mater. Res. Soc. Symp. Proc.* **186** 237
- [12] Pearson W B 1985 *Pearson's Handbook of Crystallographic Data for Intermetallic Phases* (Metals Park, OH: American Society for Metals)
- [13] Cheong B and Laughlin D E 1994 *Acta Metall. Mater.* **42** 2123
- [14] Smith C J (ed) 1976 *Metals Reference Book* (London: Butterworths)
- [15] Daw M S and Baskes M I 1984 *Phys. Rev. B* **29** 6443
- [16] Finnis M W and Sinclair J E 1984 *Phil. Mag. A* **50** 45
- [17] Ercolessi F, Parrinello M and Tosatti E 1988 *Phil. Mag. A* **58** 213
- [18] Wallace D C 1972 *Thermodynamic of Crystals* (New York: Wiley)
- [19] Pippard A B 1964 *The Elements of Classical Thermodynamics* (Cambridge: Cambridge University Press)
- [20] Allen M P and Tildesley D J 1987 *Computer Simulation of Liquids* (New York: Oxford University Press)
- [21] Baskes M I, Nelson J S and Wright 1989 *Phys. Rev. B* **40** 6085
- [22] Touloukian Y S, Kirby R K, Taylor R E and Lee T Y R 1977 *Thermophysical Properties of Matter* vols 4, 13 (New York: Plenum)
- [23] Bjerkelund E, Pearson W B, Selte K and Kjekshus A 1967 *Acta Chem. Scand.* **21** 2900
- [24] Overton W C and Gaffney J 1955 *Phys. Rev. B* **98** 969
- [25] Neighbours J R and Alers G A 1958 *Phys. Rev. B* **111** 707
- [26] Martin D L 1976 *Phys. Rev. B* **14** 369

- [27] Matcinkowski M J, Brown N and Fisher R M 1961 *Acta Metall.* **9** 129
- [28] Sastry S M L and Ramaswami B 1976 *Phil. Mag.* **33** 375
- [29] Pearson W B 1972 *The Crystal Chemistry and Physics of Metals and Alloys* (New York: Wiley–Interscience) p 90
- [30] Hultgren R, Desai R D, Hawkins D T, Gleiser H G and Kelley K K 1973 *Selected Values of the Thermodynamic Properties of Binary Alloys* (Cleveland, OH: American Society for Metals)
- [31] Purton J A, Barrera G D, Allan N L and Blundy J D 1998 *J. Phys. Chem.* **102** 5202

## Influence of cage structures on the vibrational modes and Raman activity of methane

J Kortus<sup>†‡§</sup>, G Irmert<sup>†</sup>, J Monecke<sup>†</sup> and Mark R Pederson<sup>‡</sup>

<sup>†</sup> Institute of Theoretical Physics, Freiberg University of Mining and Technology,  
B.-v.-Cotta-Strasse 4, 09596 Freiberg, Germany

<sup>‡</sup> Center for Computational Materials Science—6392, Naval Research Laboratory,  
Washington DC 20375-5000, USA

Received 24 January 2000, in final form 20 March 2000

**Abstract.** Melanophlogite is a naturally occurring  $\text{SiO}_2$ -based clathrate structure which has the same structure of type I gas hydrates. Two types of voids are found in melanophlogite. Furthermore, as in the case of the gas hydrates, melanophlogite traps gas molecules within the voids. In this work we present a joint theoretical and experimental investigation of the  $\text{CH}_4$  Raman spectra associated with the enclathrated  $\text{CH}_4$  molecules. We find that the Raman intensities of the totally symmetric hydrogen stretch modes are significantly perturbed by the presence of the clathrate cage and show that the calculated Raman spectra may be used to determine the concentration and location of the enclathrated gas molecules. Relative to the gas-phase structure we identify two effects which are responsible for the change in intensity of the enclathrated molecules relative to the gas phase. The polarizability of the surrounding cage acts to increase the Raman spectra of the stretch mode in the pentagondodecahedra cage. However, in the lower-symmetry tetrakaidecahedra cage, mixing between the hydrogen stretch mode and other optically silent molecular vibrations counteracts this effect and accounts for the different Raman intensities observed for the two types of voids. We suggest that similar calculations and experiments on the gas hydrates may provide an *in situ* diagnostic tool for determining the amount of natural gas contained within the gas hydrates on the sea floor.

(Some figures in this article are in colour only in the electronic version; see [www.iop.org](http://www.iop.org))

### 1. Introduction

Structures containing large voids of free space have been the subject of great scientific interest due to their large-scale application in the chemical industry and the possibility for studying basic interactions between the host structure and the guests which fill the voids. Examples of these cage structures are fullerenes [1, 2], clathrate structures such as gas hydrates [3] or zeolites.

Zeolites are of interest because they serve as shape and size selective catalysts and molecular sieves. However, the possibility of using these materials as hosts for the synthesis of small clusters has only recently been explored [4, 5]. Similar to the well known semiconductor superlattices, zeolite frameworks provide a method for creating new three-dimensional periodic arrays of guest molecules enclosed in the zeolite voids.

The experimental effort in this area, driven partially by potential applications to nonlinear optical devices and solar elements has resulted in several zeolite-based materials, which include

§ Present address: Center for Computational Materials Science—6392, Naval Research Laboratory, Washington DC 20375-5000, USA.

small semiconductor clusters. Some specific examples are CdS [6], GaP [7] and Se [8] clusters. More information about other systems can be found elsewhere in review articles [4, 5] and references therein. In addition to experimental efforts there have also been theoretical studies, which have investigated the structural and electronic properties of zeolites [9, 10] or the simulation of small silicon clusters in sodalite [11]. Some of the most interesting questions about these systems pertain to the guest–guest and guest–host interactions. The guest–host interaction seems to be dominant, because in typical zeolites guests are separated by more than ten angstroms. The experimentally observed blue shift of the optical absorption threshold [8] compared with free clusters suggest similar quantum confinement effects that occur in layered semiconductor superlattices, due to changes of electronic states in the system by guest–host interactions.

The present paper will discuss a similar clathrate structure known as melanophlogite. Melanophlogite is a naturally occurring, low-density form of silica, which is always found to contain some organic matter. The  $\text{SiO}_4$  tetrahedra of the host form a three-dimensional framework consisting of two different kinds of cages. One of these cages is the naturally occurring silica equivalent of a  $\text{C}_{20}$  fullerene. In fact, melanophlogite was the first known example of a silicate framework structure with the pentagonal dodecahedron as a framework element [12].

The main goal of the present work is to investigate the interesting guest–host interactions of the host framework and the methane included in this material. Raman spectroscopy provides a non-destructive method for obtaining information about the kind of guests by observing their vibrational fingerprints. Furthermore, if the Raman activity of the guest molecules is known, the density of the guests may be determined. Since, density-functional calculations provide a cost-effective *ab initio* means for determining the Raman activity of molecules the two methods combined give us a powerful tool for analysing and characterizing the above-mentioned structures.

From a technological standpoint, the secondary goal of this work is to demonstrate, by way of example, that techniques similar to those used here may be helpful for obtaining information about the concentration and type of natural gas contained within the gas hydrates. One of the clathrate structures of the gas hydrates is, in fact, identical to the structure of melanophlogite. The work discussed in the following shows that *in situ* Raman measurements of gas hydrates in conjunction with theoretically determined Raman spectra could be used to determine the location, type and concentration of such molecules.

In the following sections we provide more information about this not so well known material and give experimental and theoretical details. In section 3 we discuss the experimental and theoretical details. In section 4 we present and discuss our results and conclusions are given in the last section.

## 2. Melanophlogite

Melanophlogite is a white and colourless mineral, which is found only at a few localities (Sicily [13], Fortullino [14], Chvaletice [15], Mount Hamilton [16] and Tsekur-Koyash [17]). Although melanophlogite is quite rare in nature it has been synthesized at 443 K from an aqueous solution of silica acids under a high pressure of different gases [18].

This silica polymorph usually contains several guest molecules (e.g.  $\text{CH}_4$ ,  $\text{N}_2$  and  $\text{CO}_2$ ) in varying amounts. Kamb [12] first suggested that this low-density cubic form<sup>†</sup> of silica, which may also incorporate long, straight-chain hydrocarbons, is isostructural to the cubic gas

<sup>†</sup> The reported tetragonal forms, with a doubled unit cell in one direction, will not be discussed here.

hydrates [3] of type I. The  $\text{SiO}_4$  tetraheders form a three-dimensional framework by sharing corners. This framework contains two types of cages: two pentagondodecahedra (cage I) and six tetrakaidecahedra (cage II) per unit cell. Figure 1 displays a schematic diagram of the crystal structure of three by three unit cells parallel to the [100] direction. The highlighted part presents four cages of type I on the corners and two cages of type II in the middle. The structure of the smaller cage I shown in figure 2 is well known from recent interest in carbon fullerenes. It is the natural occurring silica equivalent of a  $\text{C}_{20}$  fullerene. However, due to the tetrahedral coordination preferred by Si atoms the cages share faces to satisfy the  $\text{sp}^3$  bonding. The corners are occupied by silicon atoms, whereas the oxygen atoms are located on the middle of the edges. The free space within cage I can be approximately described by a sphere-like void with diameter  $d \sim 5.7 \text{ \AA}$  and a volume  $V \sim 97 \text{ \AA}^3$ .

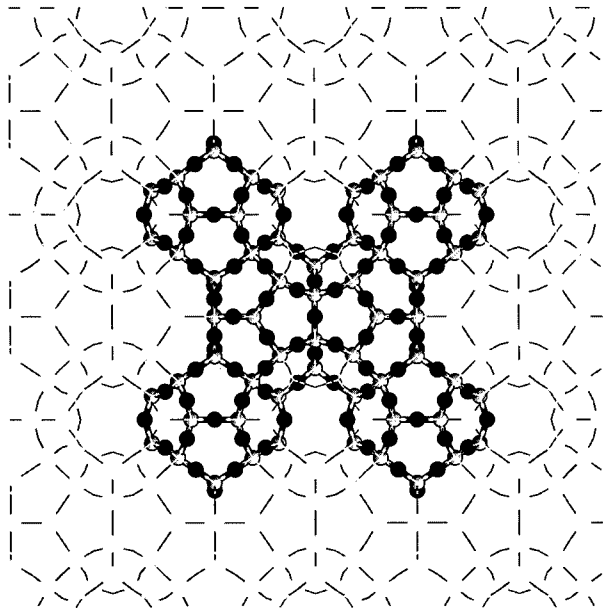


**Figure 1.** View of three by three unit cells of melanophlogite in the [100] direction. The corners of the emphasized section displays four cages of type I and two cages of type II in the middle. The lighter atoms are silicon atoms which are connected by oxygen atoms (dark circles). There are no guest molecules displayed.

The structure of cage type II is presented in figure 3. The top and bottom faces are hexagons and the remaining faces are pentagons. The free space within can be approximated by an ellipsoid with  $d_1 \sim d_2 \sim 5.8 \text{ \AA}$ ,  $d_3 \sim 7.7 \text{ \AA}$  and a volume of  $136 \text{ \AA}^3$ . An interesting feature of cage II is that the stacking of cages lead to nanotube-like structures, which may contain long chain-like molecules. The open circular objects seen in figure 1 represent a top view of the stacked cages of type II. The entire crystal structure may also be described as a three-dimensional array of stacked cages of type II.

### 3. Experimental and theoretical details

#### 3.1. Raman measurements

Small crystallites of melanophlogite from Furtullino without visible fluid inclusions were carefully selected under an optical microscope from Olympus. The measurements were

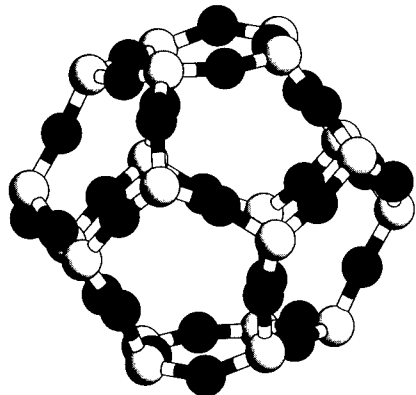


**Figure 2.** Cage I consists of 12 pentagonal faces. It is the natural occurring silica equivalent of a  $C_{20}$  fullerene. The atoms on the corners are silicon atoms (light circles), whereas the atoms between are oxygen atoms (dark circles). The guest molecule (methane) located inside this cage is not shown.

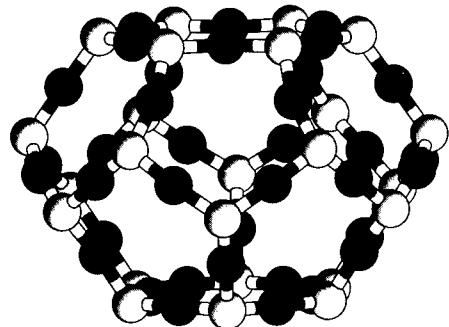


**Figure 3.** Cage II has a total of twelve pentagonal faces and two hexagonal faces (top and bottom). The atoms on the vertices are silicon atoms (light circles), which are connected to one another by bridging oxygen atoms (dark circles). The guest molecule (methane) located inside is not shown.

performed with the 514 nm line of an  $Ar^+$  laser employing a triple-stage Jobin Yvon monochromator and a liquid nitrogen cooled CCD for detection. The scattered light was measured in subtractive mode. All experiments were carried out at room temperature with special care: using low power density of the laser in order to prevent the influence of illumination on the measurement results. The Raman spectra shown in figure 4 are typical of several obtained from different spots on the crystallite.

The spectral resolution in the C–H stretching vibration range was about  $2\text{ cm}^{-1}$  due to the finite slit width of the spectrometer. Using this value in order to deconvolute the measured halfwidths the corrected halfwidths of the two observed  $CH_4$  vibration bands are about  $6\text{ cm}^{-1}$ .

### 3.2. Theoretical considerations

There are several current limitations which make it difficult to perform such calculations on periodic systems. First, the system is very large and contains a total of 143–178 atoms

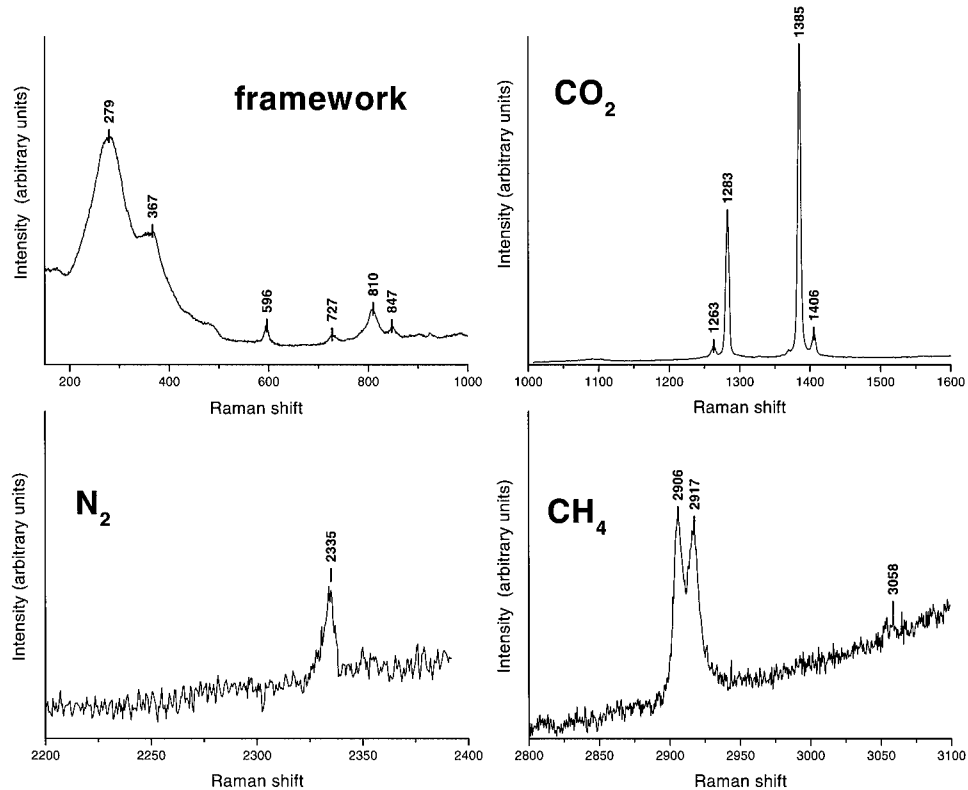


**Figure 4.** Raman spectra of melanophlogite: framework vibrations,  $\text{CO}_2$  vibrations,  $\text{N}_2$  vibrations and the totally symmetric breathing vibration of the guest molecule methane,  $\text{CH}_4$ .

depending on how many clathrate voids contain  $\text{CH}_4$  molecules. Including the guest molecules in the void of the cages significantly lowers the symmetry of the unit cell. Second, the short C–H bond length would require extremely small muffin-tin spheres for a linearized augmented plane wave (LAPW) calculation which implies a very large value of  $R * k_{\max}$ . Even without this complication all-electron calculations on unit cells of this size are not currently an option.

Another frequently used numerical method for *ab initio* calculations of large unit and super cells would be a plane-wave expansion of the electronic wavefunctions, and non-local pseudopotentials to replace the effect of the core electrons. However, for the particular problem we are concerned with here, this approach is numerically very expensive for the following reason. The oxygen valence wavefunctions are strongly localized which results in a high plane-wave cutoff energy (typically about 60–70 Ryd). Together with the large volume of the complete unit cell, this makes plane-wave calculations too expensive.

There is also a more fundamental reason for using cluster-based models for this study. To date, the Raman spectra of periodic systems has only been studied for very simple periodic systems. This is primarily due to the problem of dealing with a uniform or extremely long-period electric field in another extremely short-period system. The calculation of Raman spectra for periodic systems remains an active area of research.

The calculation of the vibrational spectra of the whole unit cell together with different guest molecules by first-principle *ab initio* methods is currently still beyond present computing

possibilities. Therefore, in order to calculate the Raman frequencies and intensities of interest, we used some approximations based on experimental observations. The basic assumption is that no mixing of the vibrational modes of the framework and of guest molecules occur. This assumption is supported by experiment, because the framework vibrations are more than  $2000\text{ cm}^{-1}$  lower than the investigated totally symmetric  $1A_1$  mode of methane. Further possible changes of the molecule geometry due to charge transfer between guests and framework is neglected, although we allow for full relaxation of all electronic degrees of freedom and we account for breathing of the methane molecule. Using these assumptions the influence of the different cages can be considered as a small perturbation of a nearly free vibrating molecule.

Based on x-ray data [12] we generated the unit cell of melanophlogite and removed the two different cage types. The dangling bonds were then resaturated with hydrogen atoms. Holding the cage atoms fixed we allowed the methane to vibrate. This does not introduce a large error because, as already mentioned, the framework vibrations are slow compared to the totally symmetric  $1A_1$  mode of methane.

The orientation of methane inside the cage has not been experimentally determined. Due to the space available there is no *a priori* reason for excluding the possibility that the methane can rotate within the cage at room temperature. For our calculations we restricted ourselves to an orientation of the methane molecule, which was adapted to the symmetry of cage I. There is no orientation of the  $T_d$  methane molecule which is compatible with the symmetry of cage II, therefore we have chosen the same orientation as for cage I. That means that all methane molecules would have the same orientation in the entire crystal framework of melanophlogite. This special choice certainly is not satisfactory and could be avoided by using, for example, molecular dynamic techniques including the relaxation of the entire unit cell together with the included guest molecules. To address this point we carried out some preliminary tight-binding calculations allowing for full relaxation of the unit cell and the included methane. The initial placement of methane is not a special case for which the forces acting on the molecule vanish by symmetry. With the initial placement of methane described above we did not observe a rotation of methane during these simulations. The results of these tight-binding calculations will not be discussed here, although they agree well with the *ab initio* results. The use of the computationally more demanding *ab initio* methods was required, because the tight-binding method did not allow for the calculation of Raman intensities.

To determine the changes in the Raman frequencies and intensities, we displaced the hydrogen atoms of methane by a small distance (0.05 au) according to the positive and negative direction of the normal vibration of the methane  $A_1$  mode and calculated the total energy and the forces of the corresponding geometry for both cages. Using the information of the forces acting on the relaxed free methane placed in both cages allowed for the calculation of the new equilibrium geometry of methane in the cages. In order to calculate the Raman intensities we applied an external electric field of 0.005 au to our cage structures with the methane as an included guest. The total energy for the frequency calculations was converged to  $10^{-6}$  Hartree and for intensities to  $10^{-8}$  Hartree.

The calculations were performed using the all-electron, full potential Gaussian-orbital cluster code NRMOL [19]. The potential is calculated analytically on a variational integration mesh which allows for the determination of the electronic structure, total energies and Pulay-corrected Hellmann–Feynman forces with any desired numerical precision. We used the Perdew–Zunger parameterization of the standard Ceperly–Alder [20] functional within local density approximation (LDA). A more detailed description of the technique used and of computational problems associated with calculation of Raman scattering activities within density functional theory can be found elsewhere [21].

## 4. Results and discussion

### 4.1. Raman measurements

Figure 4 presents the results of Raman measurements of melanophlogite. The vibrational spectra shown in figure 4(a) was identified as the framework vibrations of melanophlogite. The higher peaks at 727, 810 and 847  $\text{cm}^{-1}$  are not due to melanophlogite but probably due to dolomite, which was present in the investigated samples. This observation was supported by an absence of these peaks in samples from a different origin. Figures 4(b) and 4(c) are associated with the vibrations of  $\text{CO}_2$  and  $\text{N}_2$ , respectively. Due to the larger halfwidths of these peaks than that of free molecules in air, we concluded that these molecules are an integral part of melanophlogite. The most interesting results used for further discussion of the Raman measurements are displayed in figure (d). The peak found at 2917  $\text{cm}^{-1}$  is located at the same position as the totally symmetric  $A_1$  mode of methane. Further support that the observed vibration is connected with methane comes from the higher peak found at about 3058  $\text{cm}^{-1}$ , which is assigned to be asymmetric stretching  $T_2$  mode of methane. The lower peak at 2906  $\text{cm}^{-1}$  ( $\Delta = 11 \text{ cm}^{-1}$ ) is somewhat unexpected, since the total symmetric mode of methane is non-degenerate.

### 4.2. Theoretical calculation

As described above, we calculated the frequencies and Raman activities of the modes of methane in both cages. Due to the symmetry compatible orientation of methane in cage I the force constant matrix is diagonal for the investigated totally symmetric mode of methane. This further supports our chosen orientation, because within our numerical accuracy we found no torque components acting to rotate the methane molecule. The case of methane in cage II is more complicated, because the normal vibration of the totally symmetric mode of free methane is broken in cage II. Therefore our force constant matrix is no longer diagonal, which results in a mixing of other modes with the totally symmetric  $A_1$  mode. After diagonalization of the force constant matrix we found a mixing of the totally symmetric mode with the threefold degenerate  $T_2$  mode above 3000  $\text{cm}^{-1}$ . This mode splits in a single vibrational mode and a twofold degenerated mode separated by 9  $\text{cm}^{-1}$ . Eventually this could be found in experiment as a broad structure, because the unsplit threefold degenerate mode of the methane in cage I is found between the split modes of cage II. However, the current available experimental data do not allow for reliable investigation of this effect.

The results including only harmonic effects compared with the calculation of the free methane molecule using the same numerical approximations are summarized in table 1. Compared with the experimental results all calculated frequencies are slightly too high, which is a well known behaviour of LDA calculations. Using the free methane vibrations as a reference the  $A_1$  mode in both cages is shifted downwards, but by different amounts. The perturbation of methane in the smaller cage I is larger, which results in the observed splitting of the totally symmetric mode of methane. The calculated splitting of only 3  $\text{cm}^{-1}$  is too small compared with the experimentally measured value of 11  $\text{cm}^{-1}$ . The previously mentioned tight-binding calculations of an entire unit cell of melanophlogite resulted in a splitting of 4.5  $\text{cm}^{-1}$ .

In order to improve the theoretical results we included anharmonic effects in our calculations. Using all available energies and forces we fitted the data to a third-order polynomial of the total energy as a function of the displacement of the totally symmetric mode. Because we are still confined to the subspace of only one normal mode this problem reduces to a one-dimensional quantum mechanical problem of a particle in the resulting potential, which we solved numerically. This gives an additional splitting of 2  $\text{cm}^{-1}$  due to anharmonic

**Table 1.** Raman frequency  $\omega$  and activity  $R$  of the totally symmetric mode of methane in cages I and II compared with free methane including only harmonic effects.

	$\omega$ (cm $^{-1}$ )	$R$ (Å $^4$ amu $^{-1}$ )
Free CH <sub>4</sub>	2934	248
Cage I	2928	480
Cage II	2931	153

effects, which is additive to the harmonic splitting. Repeating the same calculations with a fourth-order polynomial lead to the same splitting as previously obtained. Therefore, our calculations give a totally splitting of the total symmetric mode of methane in melanophlogite of 5 cm $^{-1}$ . The agreement with experiment is still not perfect, and we attribute this to the approximate configuration of the CH<sub>4</sub> and the crystallographic data used for the generation of the cages. However, we believe that the qualitative description of this system is satisfactory. The basic interaction between the cage and methane leads to a weakening of the bonding of the hydrogens to the carbons, which results in the downward shift of frequencies caused by an elongation of the carbon–hydrogen bond. This is an effect that is well known since zeolites are used for the cracking of long-chained hydrocarbons.

In addition to the calculations of vibrational frequencies the NRMOL code allows for the calculation of Raman activities. The results presented in table 1 are, at first sight, confusing. Compared with the free molecule, the Raman activity of methane in cage I is enhanced, but decreased in cage II. This behaviour can be understood by the observed mixing of the totally symmetric  $A_1$  mode and the  $T_2$  mode above 3000 cm $^{-1}$ , which caused by the cage II induced broken symmetry. Due to this mixing the Raman activity of the totally symmetric  $A_1$  mode is decreased and increased for the  $T_2$  mode above 3000 cm $^{-1}$ . In the case of cage I this mixing does not occur, because cage I and methane share a common set of symmetry operations, so that the symmetry of cage I is compatible with that of methane for the totally symmetric vibrational mode.

As the final result we obtained a ratio of Raman activities of 3:1 for cage I and II. Bearing in mind that a unit cell of melanophlogite has a cage I:cage II ratio of 1:3, the observed, nearly equal, Raman intensities of both peaks are in good agreement with our calculations, assuming that the probability of methane as a guest molecule in both cage types is the same.

## 5. Conclusions

We have presented experimental and theoretical results for a vibration of a guest molecule in different cage structures. The applied methods are not confined to the discussed sample, but should be useful tools for investigations of a broader class of materials such as zeolites or other clathrates with guest molecules. The limiting condition for application should always be a careful check of the framework and guest interactions.

The calculations performed here qualitatively explain the splitting of the CH<sub>4</sub> symmetric vibrational  $A_1$  mode that has been experimentally measured. Furthermore, the comparison between the calculated Raman-intensity ratios and the experimentally observed ratios suggests that, for this sample, the methane molecules occupy the two different types of cages with equal probability.

If such materials could be used to engineer arrays of weakly interacting encapsulated molecules or clusters, it would be useful to use Raman spectroscopy to determine the density of encapsulants and the relative probabilities of finding a given encapsulant in the different cages.

We have shown that the Raman intensities of the encapsulated molecule differ significantly from that of the gas-phase molecule and exhibit a sensitive dependence on the cage structure. This means that a quantitative determination of the relative populations cannot be achieved by borrowing gas-phase intensities. However, density-functional calculations provide a cost-effective means for determining how the encapsulant Raman intensities depend on the cage and could provide a mean for characterizing future samples.

Indeed melanophlogite samples from another location lead to experimentally observed ratios that are different from those discussed here. It would be interesting if an alternative experimental means could be used to confirm that the two samples do indeed have different ratios of cage I:cage II methane densities.

We hope this work will encourage some research on melanophlogite as an interesting material for basic studies of guest–host interactions and, possibly, as a means for developing arrays of weakly interacting particles.

### Acknowledgments

We gratefully acknowledge S Köhler for making available and preparing the investigated melanophlogite samples. One of us (JK) would like to thank the Deutsche Forschungsgemeinschaft and the Michael-Jürgen-Leisler-Kiep Stiftung for financial support. MRP was supported, in part, by the ONR Molecular Design Institute N0001498WX20709.

### References

- [1] Kroto H W, Heath J R, O'Brien S C and Smalley R E 1985 *Nature* **318** 162
- [2] Kratschmar W, Lamb L D, Fostopoulos K and Huffman D R 1990 *Nature* **347** 254
- [3] von Stackelberg M and Müller H R 1954 *Z. Elektrochem.* **58** 25
- [4] Stucky G D and MacDougall J E 1990 *Science* **247** 669
- [5] Ozin G A, Kuperman A and Stein A 1989 *Angew. Chem.* **28** 359
- [6] Wang Y and Herron N 1988 *J. Phys. Chem.* **92** 4988
- [7] MacDougall J E, Eckert H, Stucky G D, Herron N, Wang Y, Moller K, Bein T and Cox D 1989 *J. Am. Chem. Soc.* **111** 8006
- [8] Bogomolov V N, Khodkevich S V, Romanov S G and Agroskin L S 1981 *Solid State Commun.* **47** 181
- [9] Ursenbach C U, Madden P A, Stich I and Payne M C 1995 *J. Phys. Chem.* **99** 6697
- [10] Sun Q, Ye L and Xie X 1998 *Phys. Status Solidi b* **207** 357
- [11] Demkov A A and Sankey O F 1997 *Phys. Rev. B* **56** 10497
- [12] Kamb B 1965 *Science* **148** 232
- [13] von Lasaulx A 1876 *N. Jb. Mineral.* 250  
Skinner B J and Appleman D E 1963 *Am. Mineral.* **48** 854
- [14] Grasselini Troysi M and Orlandi P 1972 *Atti Soc. Tosc. Sci. Nat., Mem., Serie A* **79** 245
- [15] Žák L 1967 *Am. Mineral.* **57** 779
- [16] Cooper J F Jr and Dunning G E 1972 *Am. Mineral.* **57** 1494
- [17] Kropatsheva S K and Markov J J 1975 *Dokl. Akad. Nauk* **224** 905
- [18] Giess H, Gerke H and Liebau F 1982 *N. Jb. Mineral. Mh.* **3** 119
- [19] Jackson K A and Pederson M R 1990 *Phys. Rev. B* **42** 3276  
Pederson M R and Jackson K A 1991 *Phys. Rev. B* **43** 7312  
Pederson M R and Jackson K A 1991 *Density Functional Methods in Chemistry* ed J K Labanowski and J W Andzelm (Berlin: Springer)
- [20] Perdew J P and Zunger A 1981 *Phys. Rev. B* **23** 5048
- [21] Porezag D and Pederson M R 1996 *Phys. Rev. B* **54** 7830

## **14th U.S. National Congress of Applied Mechanics**

The 14th U.S. National Congress of Applied Mechanics will be hosted by the Department of Engineering Science and Mechanics, Virginia Tech, on 23-28 June 2002, and will be held on the campus of Virginia Polytechnic Institute and State University (Virginia Tech) in Blacksburg, VA. Virginia Tech is the largest comprehensive university (with approximately 25,780 students) in the Commonwealth of Virginia. The College of Engineering awards nearly 840 B.S. degrees, 390 M.S. degrees and 175 Ph.D. degrees every year. The Department of Engineering Science and Mechanics enrolled 89 graduate students in 1998-99, awarded 15 Masters and 12 Doctoral degrees in 1998-99, and had a research expenditure of \$6.8M dollars in 1998-99. The graduate program of the College of Engineering has been ranked 25th in the country in the 1999 U.S. News & World Report.

**SPONSORS:** U.S. National Congress of Applied Mechanics and its sponsoring societies: Acoustical Society of America, American Institute of Aeronautics and Astronautics, American Institute of Chemical Engineers, American Mathematical Society, American Physical Society, American Society of Testing and Materials, American Society of Civil Engineers, American Society of Mechanical Engineers, Society for Experimental Mechanics, Society for Industrial and Applied Mathematics, Society for Naval Architects and Marine Engineers, Society of Engineering Science, Society of Rheology.

**GOALS:** The conference will bring together mechanicians, and provide a forum for exchanging ideas, and promoting interaction among them. Scientists and researchers from all over the world are welcome to participate in the conference. **All areas of applied mechanics, including Smart Materials & Structures, will be covered. Each speaker will be allotted 22 minutes for presentation and discussion of the paper.**

**ORGANIZING COMMITTEE:** Gen. Co-Chairs: E. Henneke ([henneke@vt.edu](mailto:henneke@vt.edu)) and R. Batra ([rbatra@vt.edu](mailto:rbatra@vt.edu)); Scientific Prog. Comm. Co-Chairs: F. Hussain ([FHussain@uh.edu](mailto:FHussain@uh.edu)) and M. Hyer ([hyerm@vt.edu](mailto:hyerm@vt.edu)).

**SPECIAL SYMPOSIA:** Several colleagues have kindly agreed to organize symposia; please see the Conference website. Those interested in organizing a symposium should contact a member of the organizing committee.

**ABSTRACT FORMAT AND OTHER INFO:** See the conference website [www.esm.vt.edu/usncam14/](http://www.esm.vt.edu/usncam14/)

**TRAVEL TO BLACKSBURG:** The closest airport is in Roanoke and is 45 miles from the Virginia Tech campus. It is presently served by U.S. Airways, Delta, United, and Northwest. Rental cars are available at the airport. A limousine service from the airport to Blacksburg and back is also available. The local organizing committee will make additional arrangements to facilitate travel between Roanoke Airport and Blacksburg. Information about Blacksburg community is available at the website <http://www.bev.net/>.

### **IMPORTANT DATES:**

31 January 2002 (Submission of Abstracts)	1 May 2002 (Deadline for reduced registration fee)
28 February 2002 (Acceptance/Declination Letters mailed)	23-28 June 2002 (Conference Program)
31 March 2002 (Preliminary Program mailed)	

**MAILING ADDRESS FOR ABSTRACTS:** USNCAM14, ESM Dept., MC 0219, Virginia Tech, Blacksburg, VA 24061, USA; e-mail [usncam14@vt.edu](mailto:usncam14@vt.edu); fax +1 540-231-4574.

**CONTACT FOR INFORMATION ON HOUSING, TRAVEL ETC.:** Wanda Hylton, Continuing Education, Mail Code 0364, Virginia Tech, Blacksburg, VA 24060, USA; e-mail [whylton@vt.edu](mailto:whylton@vt.edu); tel. +1 540-231-9617; fax +1 540-231-9886.

**REGISTRATION FEE:** \$375.00 if paid by 1 May 2002; \$450 after 1 May 2002. The registration fee covers the book of abstracts, two coffee/refreshment breaks every day of the conference, a reception on 24 June 2002, a banquet on 29 June 2002, and admission to all sessions.

**FINANCIAL ASSISTANCE:** The organizing committee does **not** have funds to support even the partial travel of any potential participant.

*(Continued from outside back cover)*

- 357 **Linear and nonlinear elasticity in atomistic simulations**  
J V Lill and J Q Broughton
- 377 **Modelling bulk viscosity of powder aggregate during sintering**  
D Bouvard and T Meister
- 389 **Structure and energetics of Cu–Au alloys**  
G D Barrera, R H de Tendler and E P Isoardi
- 403 **Influence of cage structures on the vibrational modes and Raman activity of methane**  
J Kortus, G Irmer, J Monecke and M R Pederson

# Modelling and Simulation in Materials Science and Engineering

Volume 8 Number 3 May 2000

Special Feature: Papers from the Workshop on Thermodynamic and Structural Properties of Alloy Materials, 20–24 June 1999, Oranjestad, Aruba

## Preface

## PAPERS

- 211 Long-range versus short-range interactions and the configurational energies of Ba( $B, B'$ )O<sub>3</sub> and Pb( $B, B'$ )O<sub>3</sub> perovskites  
B P Burton
- 221 Prediction of solution enthalpies of substitutional impurities in aluminium  
M H F Sluiter and Y Kawazoe
- 233 *Ab initio* study of transitory metastable phases solidified by drop-tube processing  
C Berne, A Pasturel, M Sluiter and B Vinet
- 239 Pseudo-critical slowing down within the cluster variation method and the path probability method  
T Mohri
- 251 Infinitesimal lattice-constant treatment of liquid  
R Kikuchi and C M van Baal
- 261 Electron and positron states in amorphous Ni<sub>0.4</sub>Pd<sub>0.4</sub>P<sub>0.2</sub>  
D M C Nicholson, P A Sterne, J C Swihart, Jeffry Tran and Yang Wang
- 269 Change from a bulk discontinuous phase transition in V<sub>2</sub>H to a continuous transition in a defective near-surface skin layer  
J Trenkler, H Abe, P Wochner, D Haeffner, J Bai, H D Carstanjen and S C Moss
- 277 The Ni–Ni<sub>3</sub>Al phase diagram: thermodynamic modelling and the requirements of coherent equilibrium  
A J Ardell
- 287 The energetics of surface-alloy formation: an embedded-atom-method, second-order-expansion study  
M Asta, V Ozoliņš and J J Hoyt
- 295 Vibrational thermodynamics: coupling of chemical order and size effects  
D Morgan, A van de Walle, G Ceder, J D Althoff and D de Fontaine
- 311 First-principles alloy theory in oxides  
G Ceder, A Van der Ven, C Marianetti and D Morgan
- 323 First-principles theory of 250 000-atom coherent alloy microstructure  
C Wolverton
- REGULAR PAPERS**
- 335 Morphology and dynamics of 2D Sn–Cu alloys on (100) and (111) Cu surfaces  
J F Aguilar, R Ravelo and M I Baskes
- 345 Interfacial free energy calculations via virtual slip  
J V Lill and J Q Broughton

(Continued on inside back cover)